INSTITUTO POTOSINO DE INVESTIGACIÓN CIENTÍFICA Y TECNOLÓGICA A.C.

ADVANCED MATERIALS DIVISION

CARBON NANOSTRUCTURES AND LAMINAR SYSTEMS LABORATORY

DISSERTATION:

“SYNTHESIS, CHARACTERIZATION AND PHYSICAL PROPERTIES OF NITROGEN DOPED 3D CARBON NANOSTRUCTURES GROWN OVER SUBSTRATES BY THE CHEMICAL VAPOR DEPOSITION TECHNIQUE”

Presented by:

M. Sc. JUAN LUIS FAJARDO DÍAZ

Candidate for the degree of:

PhD in NANOSCIENCE AND MATERIALS

Advisor:
Dr. EMILIO MUÑOZ SANDOVAL

San Luis Potosí, S.L.P., July of 2020

IPICYT

Constancia de aprobación de la tesis

La tesis "**Synthesis, characterization and physical properties of nitrogen doped 3D carbon nanostructures grown over substrates by the chemical vapor deposition technique**" presentada para obtener el Grado de Doctor(a) en Nanociencias y Materiales fue elaborada por **Juan Luis Fajardo Díaz** y aprobada el **día 10 de Julio del 2020** por los suscritos, designados por el Colegio de Profesores de la División de Materiales Avanzados del Instituto Potosino de Investigación Científica y Tecnológica, A.C.

Dr. Emilio Muñoz Sandoval
Director/Codirectores de la tesis

Florentino López Urías

Dr. Florentino López Urías
Miembro del Comité Tutoral

Dr. Horacio Flores Zúñiga
Miembro del Comité Tutoral

Dr. Armando Encinas Oropesa
Miembro del Comité Tutoral

Institutional Acknowledgments

This research was developed in the Carbon Nanostructures and Laminar System Laboratory associated to the Advanced Material Division from the Instituto Potosino de Investigación Científica y Tecnologica A.C. (IPICYT).

Thanks to the
Consejo Nacional de Ciencia y Tecnología (CONACYT) for the PhD scholarship (253091) and CONACYT Projects grant #CB-2013-220744 and grant #2016-01-4148 Problemas Nacionales.

Also thank to the LINAN department and its members Dra. Gladis Judith Labrada Delgado, Dr. Hector Gabriel Silva Pereira, M.Sc. Beatriz Adriana Rivera Scoto, and M.Sc. Ana Iris Pena Maldonado. To the LAMBAMA department and its members M.Sc. Dulce Partida Gutierrez, Dra. Elizabeth Diane Isaacs Páez, M.Sc. Guillermo Vidriales Escobar, I.Q. Ma. Del Carmen Rocha Medina. To the administrative department and its members Diana Minerva Gomez Rivera, Lic. Juana Edith Rodriguez Delgadillo and M.E Ivonne Lizette Cuevas Vélez. Thanks also to the Dr. Vicente Rodriguez González for the use of their facilities and Dr. Sergio Miguel Durón Torres from the Autonomous University of Zacatecas for the use of their facilities.

IPICYT

Instituto Potosino de Investigación Científica y Tecnológica, A.C.

Acta de Examen de Grado

El Secretario Académico del Instituto Potosino de Investigación Científica y Tecnológica, A.C., certifica que en el Acta 016 del Libro Primero de Actas de Exámenes de Grado del Programa de Doctorado en Nanociencias y Materiales está asentado lo siguiente:

En la ciudad de San Luis Potosí a los 17 días del mes de julio del año 2020, se reunió a las 17:00 horas en las instalaciones del Instituto Potosino de Investigación Científica y Tecnológica, A.C., el Jurado integrado por:

Dr. Armando Encinas Oropesa	**Presidente**	**IPICYT**
Dr. Horacio Flores Zúñiga	**Secretario**	**IPICYT**
Dr. Emilio Muñoz Sandoval	**Sinodal**	**IPICYT**
Dr. Florentino López Urías	**Sinodal**	**IPICYT**

a fin de efectuar el examen, que para obtener el Grado de:

DOCTOR EN NANOCIENCIAS Y MATERIALES

sustentó el C.

Juan Luis Fajardo Díaz

sobre la Tesis intitulada:

Fabricación, caracterización y propiedades físicas de nanoestructuras de carbono dopadas con nitrogeno crecidas en sustratos usando el método de deposición química de vapor

que se desarrolló bajo la dirección de

Dr. Emilio Muñoz Sandoval

El Jurado, después de deliberar, determinó

APROBARLO

Dándose por terminado el acto a las 19:40 horas, procediendo a la firma del Acta los integrantes del Jurado. Dando fe el Secretario Académico del Instituto.

A petición del interesado y para los fines que al mismo convengan, se extiende el presente documento en la ciudad de San Luis Potosí, S.L.P., México, a los 17 días del mes de julio de 2020.

Dr. Marcial Bonilla Marín
Secretario Académico

Mtra. Ivonne Lizette Cuevas Vélez
Jefa del Departamento del Posgrado

IPICYT
SECRETARIA ACADEMICA

THANKS TO

To God for all opportunities in my entire life and give me the strength and encouragement to follow this path, the science path.

To my mom *Maria Concepción Díaz García.* Wherever you are, I know that you are seeing this achievement. This is all for you.

To my dad *José Luis Fajardo Trejo.* I know that these times are tough, and you have all my love and strength to continue along life. Thank you for being so supportive.

To my wife *Claudia Erika Pro Martinez.* Thank you for all your love and support every time that it was difficult and for making my life full of happiness. You know that all this is for our family. Thanks also for giving me our beautiful daughter *Jazmin*.

To my sisters and brother *Yolanda, Lucero, Mayra y Marco,* for always be there when I need it.

To my friend *Alan Quezada*, what a surprise find you here, was very nice that at the end, we will work in such similar things.

To my lab partners and friends *Alex, Vero, Cristina, Luis, Gaby, Felipe, Roque, Brenda, Paco, Pancho* for all the good talks and for being so supportive. I've learned a lot from you guys, hope you have learned a little bit from me.

ACKNOWLEDGMENTS

To my tutoring committee for all the comments in these four years with the intention that everything came out the best.

To professor Dr. *Florentino López Urías*. You not only were an advisor, but you were also a mentor that taught me that in science, the more important things are keep doing it with conviction, goodwill, good moral values and a lot of work, a lot. I hope in the future be as a good researcher and person like you.

Special thanks to professor Dr. *Emilio Muñoz Sandoval*. If there is any type of an excellent researcher, concern by their students, giving them opportunities to grow as a researcher, giving them a lot of things to think, solve and work and at the end of the day wanna spend time talking about theories and experiments with a beer or coffee…it is you. I came here to obtain a degree, and I'm leaving with a co-worker and a friend. I know that we can do very interesting things in the future. I'll always be thankful to be part of this group.

SYNTHESIS, CHARACTERIZATION AND PHYSICAL PROPERTIES OF NITROGEN DOPED 3D CARBON NANOSTRUCTURES GROWN OVER SUBSTRATES BY THE CHEMICAL VAPOR DEPOSITION TECHNIQUE

Abstract

The growth of a variety of carbon nanostructures is still a hot topic, especially those that involve the growth of structures as building blocks to create 3D carbon materials. This doctoral dissertation project focused on techniques, catalysts, and precursors needed to grow these types of 3D carbon structures that are highly associated with a variety of applications in electronics, energy, chemistry, environmental remediation, medicine, and others.

We described the state of the art associated with the growth techniques, catalyst characteristics, parameters, and precursors needed for the growth of carbon nanotubes, graphene, and other types of carbon nanostructures like helical structures, nanobelts, and highly defective carbon nanofibers. Also, it is explored the influence of bimetallic catalysts in the growth of carbon nanostructures by a chemical vapor deposition technique.

The growth parameters of Co-Cu bimetallic thin films by a sputtering technique is investigated. Following the mixture of precursors used in our group for the growth of nitrogen-doped 3D carbon nanotube sponges, these were tested in a chemical vapor deposition system using the Co-Cu bimetallic thin film as a catalyst with a direct variation of temperature. Interesting interlaced and wrinkled carbon nanofibers were found. Besides, the growth of carbon nanobelts over Co-Cu thin films by the CVD technique was studied. This 3D carbon nanostructure is explored in their physical and chemical characteristics to determine a growth mechanism and the influence of Co and Cu nanoparticles. Tests with Ag and Au are also described.

An exciting aspect is that Cu plays a crucial role in the growth of these types of structures. This work includes an exploration of a series of experiments using Cu thin films to grow carbon nanostructures to determine the influence and effect of Cu NPS during the growth of the carbon nanobelts. It was found that Cu NPS can nucleate a highly defective CNT and helical carbon nanostructures depending on size and shape. The growth mechanism is discussed.

Finally, it is described the growth of 3D carbon nanostructures named “carbon nanotube sponges” using Fe as a catalyst and the quartz tube as a substrate with different precursors in a CVD system. The carbon nanotube sponges where physico-chemical characterized to determine potential applications.

Keywords: Cu-Co catalyst, carbon nanobelts, carbon nanostructures, carbon nanotube sponges.

SYNTHESIS, CHARACTERIZATION AND PHYSICAL PROPERTIES OF NITROGEN DOPED 3D CARBON NANOSTRUCTURES GROWN OVER SUBSTRATES BY THE CHEMICAL VAPOR DEPOSITION TECHNIQUE

Resumen

El crecimiento de una variedad de nanoestructuras de carbono es aún considerado un tema relevante, en especial aquellos tópicos relacionados con el crecimiento de estructuras 3D de carbono en la que se emplean unidades constructoras. Este proyecto de tesis doctoral se enfoca en las técnicas de síntesis, así como en los catalizadores y precursores necesarios para el crecimiento de estructuras 3D de carbono, que están altamente asociadas a una variedad de aplicaciones en campos como electrónica, energía, química, remediación ambiental, medicina y otros.

A lo largo de la tesis, describimos el estado del arte asociado a las técnicas de crecimiento, características de los catalizadores, parámetros y precursores necesarios para el crecimiento de nanotubos de carbono, grafeno, y otro tipo de estructuras como estructuras helicoidales, nanocinturones y nanofibras de carbono estructuralmente defectuosas. Además, se explora la influencia de catalizadores bimetálicos en el crecimiento de nanoestructuras de carbono por la técnica de deposición química de vapor.

Se investigan los parámetros de crecimiento de láminas delgadas de un catalizador bimetálico a base de Co y Cu por la técnica de devanado catódico o sputtering. Esta lámina delgada es probada como catalizador bajo condiciones variantes de temperatura y empleando una mezcla de precursores anteriormente empleada en el grupo para la síntesis de estructuras 3D como esponjas de carbono nanoestructuradas y dopadas con nitrógeno. De forma interesante se observa la formación de nanofibras corrugadas y entrelazadas. Asimismo, se estudia el crecimiento de nanocinturones de carbono crecidos sobre la lámina delgada de Co-Cu. Se exploran las características físicas y químicas con el fin de determinar el mecanismo de crecimiento y la influencia de las nanopartículas de Co y Cu en el crecimiento de estas nanoestrucutras 3D de carbono. Pruebas con Ag y Au también son realizadas.

En el desarrollo de esta tesis se encuentra aspectos interesantes sobre el rol del Cu ene el crecimiento de este tipo de nanoestructuras. Este trabajo de tesis incluye una serie de experimentos exploratorios empleando láminas delgadas de Cu, con el fin de determinar la influencia y efecto de las nanopartículas de Cu en el crecimiento de los cinturones de carbono. Se encontró que dependiendo de la forma y tamaño de las nanopartículas de Cu se favorece el crecimiento de nanotubos de carbono altamente defectuosos y nanoestructuras helicoidales de carbono. Se discute el mecanismo de crecimiento de estas nanoestructuras.

Finalmente, se describe el crecimiento de nanoestructuras 3D de carbono llamadas “esponjas de carbono” en las que se emplea Fe como catalizador y un tubo de cuarzo como un substrato empleando una variedad de precursores en un sistema de descomposición química de vapor. Las esponjas nanoestructuradas de carbono fueren caracterizadas fisicoquímicamente con el fin de determinar alguna aplicación potencial.

Palabras clave: Catalizador Co-Cu, nanocinturones de carbono, nanoestructuras de carbono, esponjas nanoestructuradas de carbono.

INDEX

CHAPTER ONE:

Hypothesis, Justification, and Objectives

CHAPTER TWO

CHAPTER THREE

CHAPTER FOUR:

CHAPTER FIVE:

CONCLUSIONS:

Annexe (Publications):

Figure Index

CHAPTER ONE:

CHAPTER TWO:

CHAPTER THREE:

CHAPTER FOUR:

CHAPTER FIVE:

Table index

CHAPTER TWO:

CHAPTER THREE:

CHAPTER FOUR:

CHAPTER FIVE:

CHAPTER ONE:

CHEMICAL VAPOR DEPOSITION AS A TECHNIQUE FOR THE GROWTH OF NEW 3D CARBON NANOSTRUCTURES (INTRODUCTION)

1.1 Chemical vapor deposition for the growth of carbon nanostructures

In the last twenty years, the development of carbon nanomaterials like nanotubes, nanofibers, and graphene has developed considerably due to the progress of new techniques and technologies for their use and synthesis. The first discoveries developed by Sumio Ijima in 1991 associated with the carbon nanotubes (CNT) synthesis, described them as enrolled graphitic layers. They obtained these CNT structures with a DC- filament arc-discharge vapor deposition system [1]. The synthesis developed by Sir. Harold Kroto (1989), where they synthesize the buckminsterfullerene that consists of semi-spherical nanocages completely closed with Cn atoms (n = 60, 240 or higher) using an arc discharge process [2]. The famous "scotch tape" graphene isolation technique used by Andrea Geim and Konstantine Novoselov in 2004 [3] marked the way and encouraged an increase in the research associated with nanocarbon materials. Since then, some variety of carbon allotropes like nanoonions [4,5], carbon nanofibers (CNF) [6,7], nanocones [8,9], helical CNT [10,11] and others have been reported [12].

Different production methods are employed to produce CNT like laser ablation flame synthesis [13–15](figure 1.1a), high pressure carbon monoxide (HiPCo) [16–18], electrolysis [19,20], chemical vapor deposition (CVD) [21–23] (figure 1.1d). For instance, Zhang et al. [24] described the synthesis of single-walled carbon nanotubes (SWCNT) and multiwalled CNT (figure 1.1b) by an electrical tube furnace at 1300 °C and 560 Torr where a graphite target (1.2% Ni-Co) was irradiated using a laser beam of Nd-yttrium-aluminum-garnet (YAG) with an energy density of about 3 J/cm^2 per pulse. Nikolaev et al. [25] synthesize SWCNT by a gas phase catalytic process (HiPCO) at temperatures between 800 °C to 1200 °C, pressures of 1 atm to 10 atm, and $Fe(CO)_5$ as catalyst (figure 1.1c). Dimitrov et al. [26] describe the conditions for the use of electrolysis to produce CNT. A graphite cell working as anode is used as a container to support temperatures above 700 °C and as cathode is used graphite electrodes of approximately 6.5 mm isolated. LiCl or $SnCl_2$-LiCl salts pre-dried are used as the electrolyte. The process is developed at high temperatures (1600 °C) combined with constant voltages of 4.0 V to 8.4 V. Couteau et al.[27] produced multiwalled CNT with high purity in a continuous rotary CVD system. They used a mixture of $CaCO_3$ with Fe(III), Fe(II), and Co as a catalyst at temperatures of 720 °C with acetylene as precursor and nitrogen as carrier gas in a continuous fixed-bed flow reactor (quartz) with a diameter of 80 mm and heating area of 750 mm.

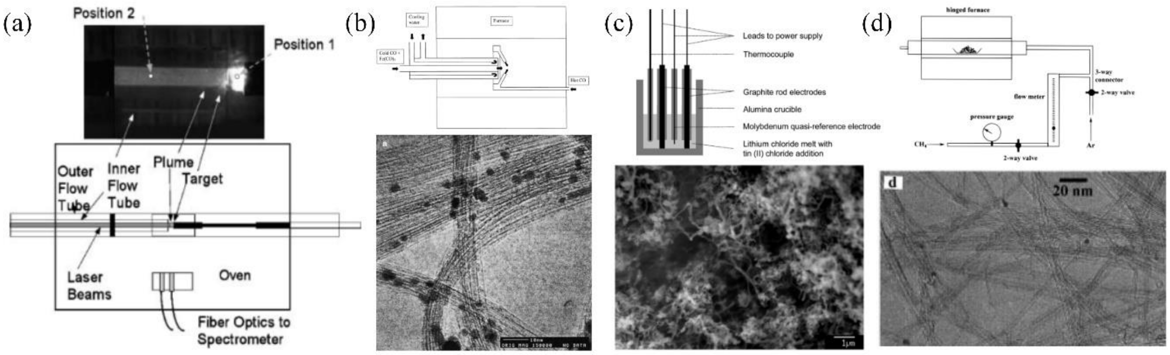

Figure 1.1: Schematic representation of common techniques used to produce CNT. (a) Laser ablation flame synthesis [14], (b) high pressure carbon monoxide [modified from [25]. (c) Salt assisted electrolysis [modified [19]]. (d) Chemical vapor deposition [modified from [23]].

In the case of the growth of CNF, similar techniques to those employed for CNT are used. The CNF can be described as sp^2-linear filaments with diameter sizes around 100 nm where no hollow core is appreciated, and truncated conical structures or planar layers are commonly observed [28]. The more common technique used to produce them is vapor-grown, which consists of the pyrolysis or thermal decomposition of organic compounds. Different types of catalysts, temperatures, precursors considerably modify the growth mechanism and the carbon deposition over the nanoparticle. Also, it has been reported that bimetallic structures highly promote the formation of carbon nanofibers. Fan et al. [29] described the influence of sulfur by the incorporation of thiophene in a benzene/hydrogen mixture at 1200 °C for 45 min with ferrocene as a catalyst. They produced nanoscaled and high yields of CNF influenced by a high concentration of thiophene (figure 1.2a). Rodriguez et al. [30] described the use of bimetallic particles based on Fe-Cu in order to modify the growth mechanism of CTN and produce CNF. The type of structure of the CNF varies influenced by the shape of the metallic nanoparticle, where planar layers (figure 1.2b) and herringbone structure (figure

1.2c) can grow over the planar and conical shapes of metallic nanoparticles (NPS), respectively.

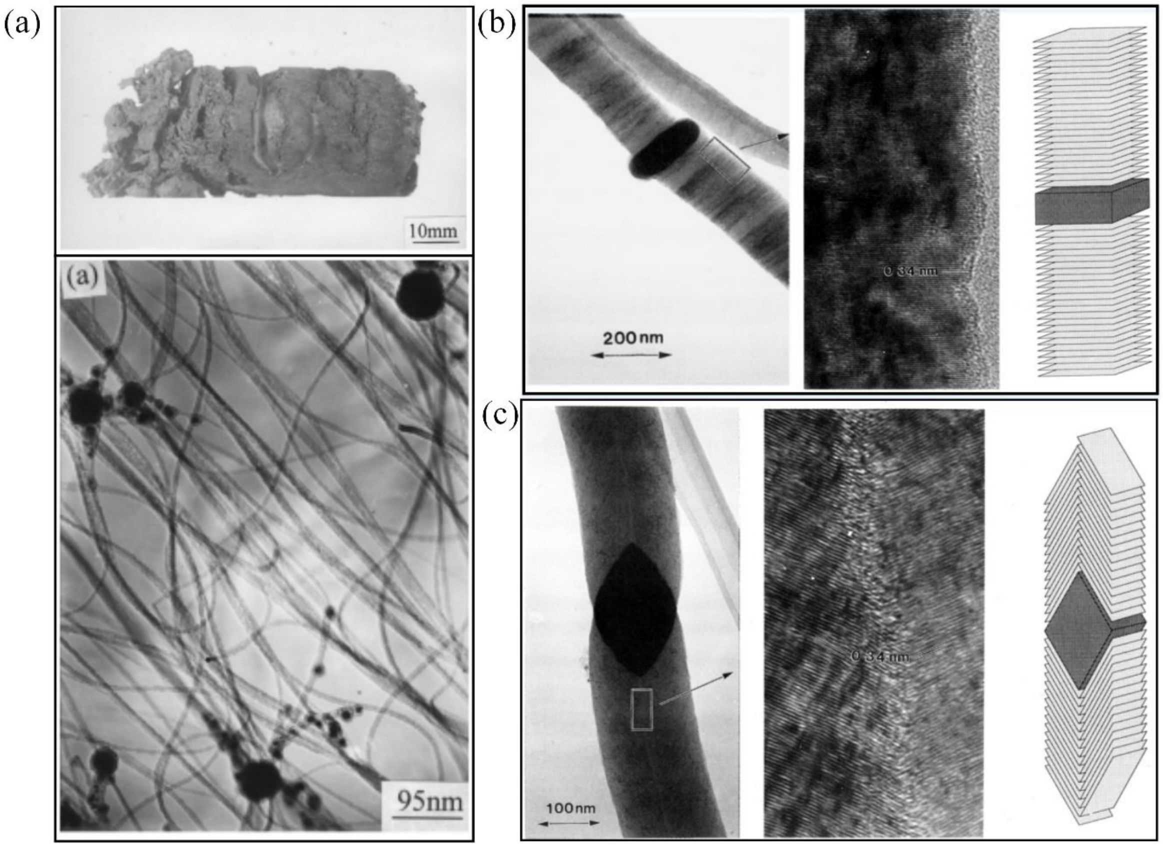

Figure 1.2: (a) Large production of CNF by the incorporation of thiophene in a benzene/hydrogen mixture used in a CVD system [modified from [29]]. (b) In-plane and (c) herringbone CNF growth by the use of a bimetallic catalyst (Fe-Cu) in CVD[30].

In the case of graphene, two approaches used to describe the synthesis of graphene: the top-down and the bottom-up approaches. In the case for top-down methods we can find electrochemical exfoliation [31–33] (figure 1.3a), micromechanical cleavage [34,35] (figure 1.3b), exfoliation by solvent interaction [36,37](figure 1.3c), carbon nanotube unzipping [38] (figure 1.3d) and arc discharge [39] (figure 1.3e). Also, mixed techniques are usually employed for the synthesis of graphene. For example, Peng et al. [40] described a graphene nanoribbon aerogel obtained by the unzipping of carbon nanotubes sponge. By an aggressive oxidation process, a transversal cutting effect was obtained in order to obtain the graphene sheets from CNT. In the case of the bottom-up techniques, the more developed are epitaxial growth over silicon carbide and chemical vapor deposition. Son et al. [41] described the growth mechanism of graphene over the surface of Si nanoparticles without the formation of silicon carbide. The graphene synthesis was taken by a chemical vapor deposition process at temperatures of 900 °C to 1100 °C and a mixture of CH_4 and CO_2 as a precursor. The deposited graphitic materials over the Si spheres are reduced with H_2 at 1000 °C to reduce the Si nanospheres and graphitic structure.

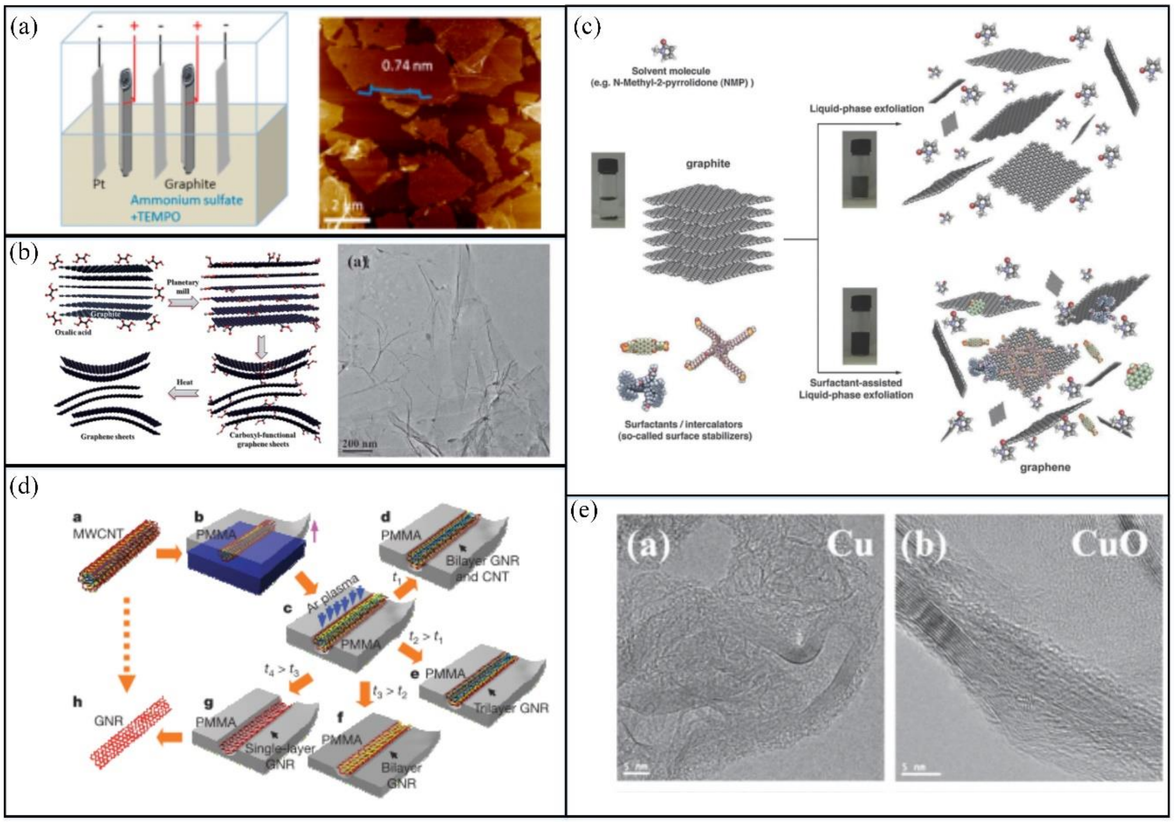

Figure 1.3: (a) Electrochemical graphite exfoliation using Pt and ammonium sulfate [modified from [31]]. (b) Mechanical graphene exfoliation using oxalic acid and heat [modified from [35]]. (c) Liquid phase exfoliation using N-methyl-2-pyrrolidone (NMP) and surfactants [37]. (d) CNT unzipping using a PMMA coating and Ar plasma to a transversal cut [38]. (e) Graphene sheets grew by arc discharge using Cu and CuO electrodes [39].

The chemical vapor deposition system is more commonly used for the synthesis of all types of carbon nanostructures. Compared with other techniques, the CVD technique had some advantages:

- The process is simple and economical.
- It is easily scalable for mass production of carbon nanofibers and nanotubes.
- A variety of carbon nanostructures can be produced, even for the same type of structure. For example: can be produced single-walled CNT, multiwalled CNT, aligned CNT, entangled CTN, helical CNT.
- A variety of catalysts can be applied.
- Mixed-effects can be obtained in one step.
- Defined carbon nanostructures can be obtained by a specific pre-treatment of the catalyst and substrates.

More recently, there is a lot of attention over the synthesis and growth of mixed carbon nanostructures to create 3D-macroscopic carbon nanostructures by the chemical vapor deposition technique[42–44]. For instance, Figure 1.4a described the carbon nanotube sponge synthesized by CVD technique and using 1,2-dichlorobenzene as a precursor; a 3D CNT arrangement described first time by Gui et al. [44]. Dong et al. [45] described a procedure to create a hybrid CNT-graphene. By the use of a bimetallic structure that consists of a Cu-thin film layer decorated with Si-NPS, it is possible to create a graphene surface catalyzed by the Si-NPS and the formation CNT catalyzed by copper nanoparticles that were diffused from the thin film. Figure 1.4b described the CVD procedure and the hybrid carbon structure obtained by one-step CVD synthesis compared with one prepared in two steps by spin coating had better results in a field-effect transistors test. Yan et al. [46] create a hybrid graphene-CNT structure by multiple CVD steps. First, the graphene was grown over a Ni-matrix, then Fe and Al_2O_3 thin layers were deposited by e-beam evaporation, finally by CVD at 750 °C and using a mixture of ethylene and Ar/H_2 gas the CNT were synthesized over the graphene structure (Figure 1.4c).

With all the types of techniques described previously and the type of carbon nanostructure that can be synthesized, the chemical vapor deposition technique seems to be highly reliable to produce quality carbon nanostructures, a variety of structures, and even 3D carbon nanostructures in one-step synthesis.

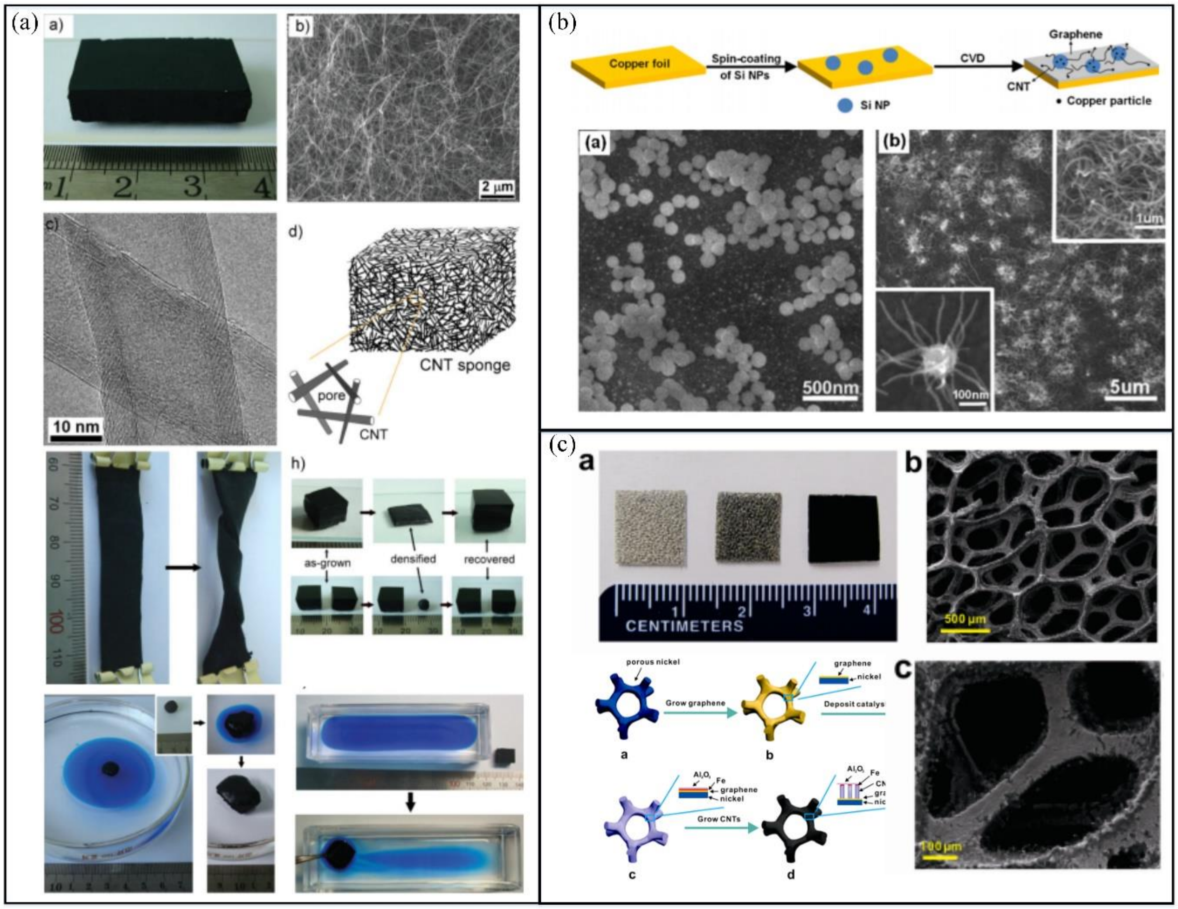

Figure 1.4: (a) Carbon nanotube sponge described as a 3D arrangement of CNT with outstanding mechanical and oil sorption properties [modified from [44]]. (b) Cu-Si Bimetallic catalyst used to grow a hybrid graphene-CNT growing over Si NPS [modified from [modified from [45]]. Hybrid CNT-graphene structure obtained by the CVD system using Ni, Fe, and Al_2O_3 [modified from [46]].

1.2 The catalyst used for carbon nanostructures synthesis

Despite all the applications enrolled in the CVD technique, the size and shape of the carbon nanostructures strongly depend on the type and shape of the catalytic surface and particles.

The more commonly used catalyst for the growth carbon nanotubes are Co [47], Fe [48], and Ni [49], while for the production of graphene, the more common substrates used are Cu [50] and SiO_2 [51]. However, many reports are testing a variety of such elements like Al, In, Pt, Ti, Mg, Pd, K, Cs, Na, W, Mn, Mo, Ir [52], Au, Ag [53], and some oxides like $CaCO_3$ [27], SiO_2 [54], MgO, Al_2O_3 [55], TiO_2 [56]and ZnO [57] as catalyst or substrate.

Nevertheless, what makes that every metallic or non-metallic nanoparticle promotes the growth of carbon nanotube, graphene, or a CNF? The affinity of the crystal structure of metallic and non-metallic nanoparticles plays a crucial role in the growth mechanism. The diffusion capacity of C atoms into the crystal structure and the formation of carbides structures has a crucial role in the formation of CNT or CNF. Figure 1.5a shows the diffusion of diffusion constant (cm^2/s) versus temperature (K) for some typical metals [58]. In the case of the carbide structures, the diffusion of carbon is limited to surface interaction or by the precipitation of carbon atoms or the diffusion trough the substitutional process. That is the reason for the lower diffusion rates for carbides compared with their basal metal structure. For instance, in the case of $Fe_{(FCC)}$ or $Fe_{(BCC)}$, both crystal structures had high diffusion constant; however, the diffusion decreases sharply for $Fe_{(FCC)}$ structure with low temperature (< 1173 °C) associated to an interstitial diffusion in BCC geometry. The metals with a higher diffusion constant below 1273 °C are Co, Ni, Fe, Pd, V, Fe, and Mo. Jourdain et al.[58] described that for Zn and Cu, there is a low affinity to carbon. The affinity with Fe, Co, and Ni is finite, and for transition metals like Ti and Mo, there is a strong bond between C and the metal.

Another exciting aspect associated with the growth of the graphitic network is related to the interaction of carbon atoms over a specific crystal phase of the metallic nanoparticle. Yazyev et al. [53] described by the first-principles technique how the atoms of carbon interact with a specific surface of metallic nanoparticles like Cu, Ag, Au, Ni, Pd, and Pt, specifically over the (111) crystal direction (Figure 1.5b). They found that the surface diffusion of carbon adatoms (surface atom) over crystalline structures is preferable over carbon dimer when it is used as a diatomic atom precursor that mono atom diffusion (Figure 1.5c). Also, they described that the interaction of carbon adatoms is preferable over the (100) for Ag, Au, Pd, and Pt, while it is preferable over the (111) in Cu and Ni.

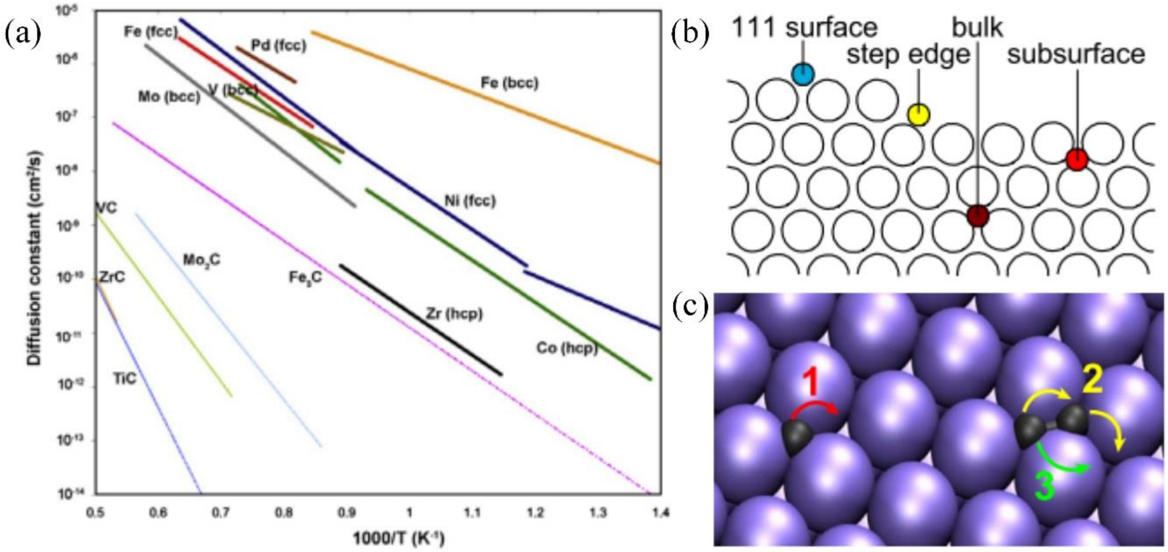

Figure 1.5: (a) Diffusion constants for metals and metals carbides as a function of temperature[58]. (b) Interaction of carbon with metal surfaces. (c) Interaction of carbon 1. Adatom, 2 and 3, carbon dimer with Fe (111) metal surface[53].

Lin et al.[59] described fours steps that happened during the growth of a CNT using a Ni NPS:

- There is a time lag of around 774s before the catalysis of a CNT after the synthesis begins.
- At 650 °C in Ni NPS, the nucleation is dominated by surface and bulk diffusion, while the formation of inner graphitic layers is related to interfacial diffusion.
- For the continuous growth of graphitic layers, this is dominated by a surface carbon diffusion that nucleates at the base of the symmetric Ni catalytic particle.
- As carbon is incorporated into the surface nucleation, the NPS becomes asymmetric and more graphitic layers stretch to the bottom, forming a cap that covers the particle.

In the case of graphene growth, there are also differences associated with the growth mechanism in the crystal surface. For instance, the growth of graphene over a Cu layer considerably changes depending on the crystal direction. Ogawa et al. [60] found that in the case of a Cu (100) film, the graphene synthesized had a multi-domain structure revealing a higher defective structure leaving domain boundaries and growing in a different direction. However, in the case of Cu(111) film, the graphitic structure grows homogeneously over the surface. This effect is probably associated with the surface deposition and lower activation energies for the incorporation of adatoms over the surface of Cu(111) [58].

1.3 Carbon nanotubes using Co: Growth characteristics

As we described early, there are three metals commonly used for the synthesis of CNT, such as Ni, Co, and Fe in a CVD system. However, the growth of CTN varies considerably in these three cases. Huang et al. [61] report a comparative study of the catalytic potential of Ni, Co, and Fe for carbon nanotube growth. They found that Co metals promote the growth of CNT with a smaller diameter and lower growth rate compared with Ni and Fe. Also, they found that in the case of the graphitic layers synthesized by Co, this tends to have open walls over the graphitic structure and thinner walls compared for those synthesized by Fe and Ni. A similar result was obtained by Lee et al. [62] Where Co was used to produce thinner and defective CNT. Contrary, Hernadi et al. [63] explains that Co catalyst promotes the growth of highly homogeneously diameters and structure, and when it is deposited over the Yttrium substrate, the quality of the CNT is better compared with Fe. They also described that when using ethylene and n-pentane, the Co nanoparticles provoke non-homogeneous CNT. Gohier et al. [64] by a CVD technique using Co, Ni, and Fe found that the growth mechanism changes from “growth base” for small NPS (~ 5nm) to base-growth for nanoparticles above 20 nm. Also found that Co tent to promote a dense deposit of CNT compared with Fe and Ni, which produce lower density depositions.

Different experimental conditions are described for the growth of CNT using Co catalyst. For instance, Chai et al. [65] used CoO supported over different substrates like Al_2O_3 and SiO_2 to grow CNT using methane. They found that the better temperature to grow CNT over SiO_2 is 550 °C; however, when alumina is used, a better quality can be obtained from a range of temperatures between 550°C to 700 °C. Zheng et al. [66] uses a cobalt nitrate catalyzed mixed with ethanol and subsequently dispersed on alumina disk as a catalyst in a CVD system. They found that the growth of CNT from Co NPS is influenced strongly by the temperature where a temperature of 600 °C is suitable for the growth of CNT. They also described that with a higher concentration of precursor (ethanol), the synthesis of amorphous carbon increases.

1.4 Carbon nanostructures using Cu: Growth characteristics

Cu metal has mainly been used as a catalyst for the growth of graphene due to the low diffusion of carbon atoms into the Cu crystal structure and the high energy need for the carbon saturation into Cu material. Li et al. [67] described a method to grow large-area graphene over a Cu foil. The experiment was developed at 1000 °C in a CVD system using methane and hydrogen as precursors. They described that the self-limited growth process of graphene over Cu is influenced by the high temperature, low C diffusion, and the poor C saturation of Cu film. However, no all surface of Cu in thin films is suitable to grow uniform graphene layers. Ogawa et al. [60] did a comparative study associated with the influence of the Cu(111) and Cu(100) orientations over the growth of graphene (figure 1.6a). They found that the Cu(111) direction promotes a highly uniform and single-crystal graphene sheet while the Cu(100) direction promotes the multi-domain graphene. This effect is related to the formation of C-C bonds adatoms in Cu structure that are aligned parallel to Cu surface in two major orientations $[10]_{graphene}/[011]_{Cu}$ and $[01]_{graphene}/[011]_{Cu}$. Similar results were obtained by Rasool et al.[68] where they found that Cu(100) crystal produce grain boundaries leading to the growth of graphene sheets in a variety of orientations.

Another way to control the grain boundaries formation of graphene an obtain single graphene crystals can be obtained by controlled surface oxidation of the copper foil. Duong et al. [69] described a process where multi-domain graphene sheets can be obtained after a selective oxidation treatment of the Graphene-Cu foil. By an ultraviolet oxidation process, the grain boundaries of graphene sheets promote the formation of a highly oxidized surface with C-O and C-OH bonds, this interaction with Cu surface promotes the formation of oxidized copper. This treatment helps to observe the graphene-CuO surface by an optical microscope (figure 1.6b).

Interestingly, Cu nanoparticles have been used to grow helical carbon nanostructures and CNT. Xia et al. [70] explains the shape and size characteristics of Cu NPS to growth helical carbon nanostructures by the CVD technique. It is described that octahedrons and triangular prisms NPS of size around 40 nm and 70 nm respectively showing the [110] crystal direction tent to grow helical carbon nanostructures (figure 1.6c). This effect is associated with an anisotropic diffusion process and a non-homogenous precipitation process that induces differences over the growth of graphitic layers and finally variations on morphologies. In the case where Cu NPS are used to grow CNT, Xia et al. [70] described that nanoparticles with a size around 80 nm to 200 nm could synthesize CNT. Zhu et al. [71] also described that the growth of CNT in the CVD system using Cu foils is need temperatures between 700 °C a 1000 °C. They found that Cu migrates from the foil, and Cu NPS diffuses over the graphitic network in order to provoke the growth of CNT. At temperatures of 700 °C, the nanoparticle is found at the tip, while for higher temperatures, small Cu NPS can be found inside the CNT.

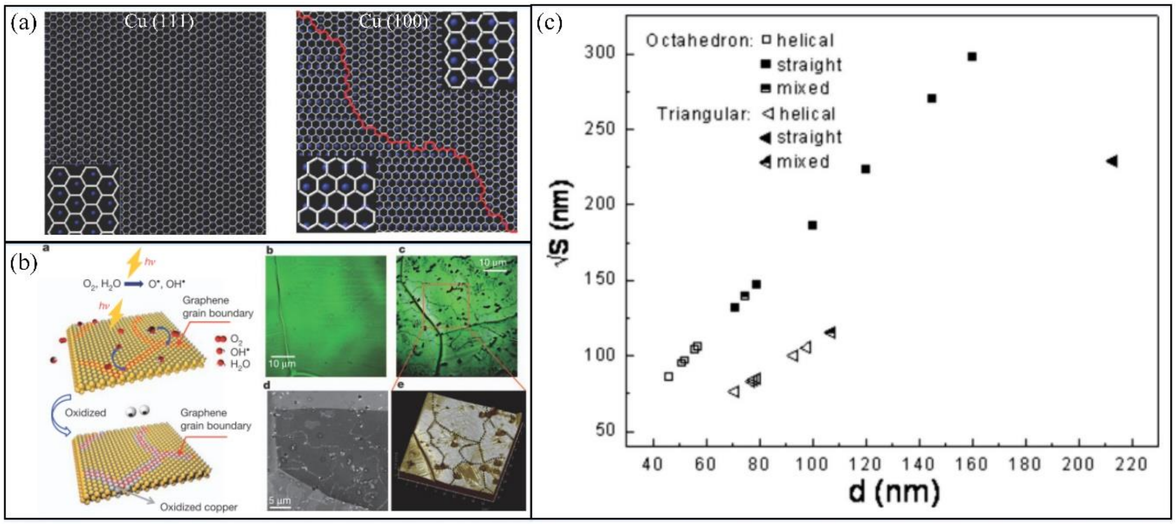

Figure 1.6: (a) Representative models for the growth of uniform graphene in Cu (111) and multi-domain graphene in Cu(100) [60]. (b) Growth of graphene influenced by CuO grain boundaries after ultraviolet oxidation [69]. (c) Influence of size and shape of Cu nanoparticles over the growth of helical, straight, and mixed CNT [70].

1.5 Non-typical carbon nanostructures using mixed catalyst

There are a few reports about the influence of bimetallic catalyst in the growth of carbon nanostructures. Rodriguez et al.[30] report the influence of Cu in Fe catalyst activity in a CVD system at 600°C using ethylene as a carbon precursor. They found a considerable modification of the growth mechanism where highly defective carbon nanostructures were obtained, like herringbone structures, stacked platelets, and defective surface CNF. Furthemore, a related research of Chambers et al. [72] test the effect of Cu over the behavior of Co during the growth of CNF. They found that Cu ratio impacts considerably over the growth rate and type of carbon nanostructures. While Cu is maintained low (1:3 in Cu:Co), the yield production maintains almost invariable. However, in higher concentrations (3:1 in Cu:Co), the production of carbon nanostructures decreases considerably. They observed intertwined agglomerates and highly defective CNT generated by big metallic particles, they attribute the defective structure to the influence of copper during Co catalytic growth.

Mixture using Ni has also been done already. Guevera et al. [73] developed a procedure where Ni and Fe powders where mechanical mixed with Cu powder (30% at) in order to obtain an alloy that could be used as a catalyst in a CVD system. They found that the influence of Cu over the Ni catalyst promotes a higher carbon deposition at 550 °C with no substantial variation of morphology.

Mixed catalysts are commonly used where Fe, Co, or Ni are involved in order to promote a series of effects like doping, morphological changes, or integration between different carbon nanostructures. For instance, Wang et al. [74] developed B-C-N doped SWCNT structures using a Fe-Mo bimetallic catalyst. Du et al. [75] synthesized graphene/vertically aligned CNT 3D structure using SiO_2 and iron phthalocyanine. He et al. [76] developed a hybrid CNF/CNT structure using a carbonized melamine sponge and $Co(NO_3)_2$, $Ni(NO_3)_2$, and $Fe(OH)_2$ as a catalyst for CNT growth process. Kitiyanan et al. [77] developed SWCNT by a Co-Mo catalyst. Okazaki et al. [78] developed MWCNT and nano coils by the use of NPS of Fe-In-Sn-O. Qi et al. [79] synthesized helical CTN and nanobelts structures by the use of a Fe-Cu catalyst at 450°C in a CVD system.

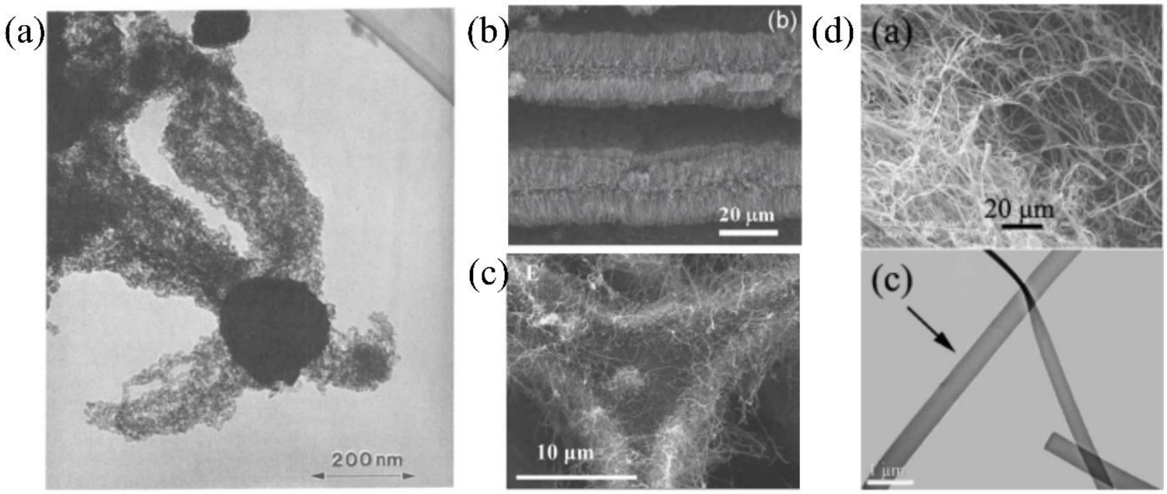

Figure 1.7: (a) Intertwined CNT agglomerates produced by Co-Cu nanoparticle [72]. (b) CNT/graphene hybrid nanostructure produced using SiO_2 and iron phthalocyanine [75]. (c) CNF/CNT hybrid structure grown using a melamine sponge and $Fe(OH)_3$ as a catalyst [76]. (d) Carbon nanobelts produced with a Fe-Cu catalyst [79].

1.6 References

[1] S. Iijima, Helical microtubules of graphitic carbon, Nature. 354 (1991).

[2] H.W. Kroto, The stability of the fullerenes C_n, with n = 24, 28, 32, 36, 50, 60 and 70, Nature. 329 (1987) 529–531. https://doi.org/10.1038/329529a0.

[3] I.V.G. and A.A.F. K. S. Novoselov, A. K. Geim, S. V. Morozov, D. Jiang, Y. Zhang, S. V. Dubonos, Electric Field Effect in Atomically Thin Carbon Films, 306 (2004) 666–669.

[4] K. Bogdanov, A. Fedorov, V. Osipov, T. Enoki, K. Takai, T. Hayashi, V. Ermakov, S. Moshkalev, A. Baranov, Annealing-induced structural changes of carbon onions: High-resolution transmission electron microscopy and Raman studies, Carbon. 73 (2014) 78–86. https://doi.org/10.1016/j.carbon.2014.02.041.

[5] V.L. Kuznetsov, I.L. Zilberberg, Y. V. Butenko, A.L. Chuvilin, B. Segall, Theoretical study of the formation of closed curved graphite-like structures during annealing of diamond surface, Journal of Applied Physics. 86 (1999) 863–870. https://doi.org/10.1063/1.370816.

[6] Z. He, J.L. Maurice, A. Gohier, C.S. Lee, D. Pribat, C.S. Cojocaru, Iron catalysts for the growth of carbon nanofibers: Fe, Fe_3C or both?, Chemistry of Materials. 23 (2011) 5379–5387. https://doi.org/10.1021/cm202315j.

[7] K.P. De Jong, J.W. Geus, Carbon Nanofibers Applications (2).Pdf, Catalytic Review. 42 (2000) 481–510.

[8] S.N. Naess, A. Elgsaeter, G. Helgesen, K.D. Knudsen, Carbon nanocones: Wall structure and morphology, Science and Technology of Advanced Materials. 10 (2009). https://doi.org/10.1088/1468-6996/10/6/065002.

[9] J.X. Wei, K.M. Liew, X.Q. He, Mechanical properties of carbon nanocones, Applied Physics Letters. 91 (2007) 1–4. https://doi.org/10.1063/1.2813017.

[10] A. Shaikjee, N.J. Coville, The synthesis, properties and uses of carbon materials with helical morphology, Journal of Advanced Research. 3 (2012) 195–223. https://doi.org/10.1016/j.jare.2011.05.007.

[11] Z. Ren, P.-X. Gao, A review of helical nanostructures: growth theories, synthesis strategies and properties, Nanoscale. 6 (2014) 9366–9400. https://doi.org/10.1039/C4NR00330F.

[12] J. Zhang, M. Terrones, C.R. Park, R. Mukherjee, M. Monthioux, N. Koratkar, Y.S. Kim, R. Hurt, E. Frackowiak, T. Enoki, Y.Y. Chen, Y.Y. Chen, A. Bianco, Carbon science in 2016: Status, challenges and perspectives, Carbon. 98 (2016) 708–732. https://doi.org/10.1016/j.carbon.2015.11.060.

[13] M. Yudasaka, F. Kokai, K. Takahashi, R. Yamada, N. Sensui, T. Ichihashi, S. Iijima, Formation of single-wall carbon nanotubes: Comparison of CO2 laser ablation and Nd:YAG laser ablation, Journal of Physical Chemistry B. 103 (1999) 3576–3581. https://doi.org/10.1021/jp990072g.

[14] C.D. Scott, S. Arepalli, P. Nikolaev, R.E. Smalley, Growth mechanisms for single-wall carbon nanotubes in a laser-ablation process, Applied Physics A: Materials Science and Processing. 72 (2001) 573–580. https://doi.org/10.1007/s003390100761.

[15] C. Kocabas, M.A. Meitl, A. Gaur, M. Shim, J.A. Rogers, Aligned arrays of single-walled carbon nanotubes generated from random networks by orientationally selective laser ablation, Nano Letters. 4 (2004) 2421–2426. https://doi.org/10.1021/nl048487n.

[16] D.E. Johnston, M.F. Islam, A.G. Yodh, A.T. Johnson, Electronic devices based on purified carbon nanotubes grown by high-pressure decomposition of carbon monoxide, Nature Materials. 4 (2005) 589–592. https://doi.org/10.1038/nmat1427.

[17] C.E. Dateo, T. Gökçen, M. Meyyappan, Modeling of the HiPco Process for Carbon Nanotube Production. I. Chemical Kinetics, Journal of Nanoscience and Nanotechnology. 2 (2002) 523–534. https://doi.org/10.1166/jnn.2002.125.

[18] M.J. Bronikowski, P.A. Willis, D.T. Colbert, K.A. Smith, R.E. Smalley, Gas-phase production of carbon single-walled nanotubes from carbon monoxide via the HiPco process: A parametric study, Journal of Vacuum Science & Technology A: Vacuum, Surfaces, and Films. 19 (2001) 1800–1805. https://doi.org/10.1116/1.1380721.

[19] R. Das Gupta, C. Schwandt, D.J. Fray, Preparation of tin-filled carbon nanotubes and nanoparticles by molten salt electrolysis, Carbon. 70 (2014) 142–148. https://doi.org/10.1016/j.carbon.2013.12.084.

[20] C. Schwandt, A.T. Dimitrov, D.J. Fray, High-yield synthesis of multi-walled carbon nanotubes from graphite by molten salt electrolysis, Carbon. 50 (2012) 1311–1315. https://doi.org/10.1016/j.carbon.2011.10.054.

[21] H. Ohno, D. Takagi, K. Yamada, S. Chiashi, A. Tokura, Y. Homma, Growth of vertically aligned single-walled carbon nanotubes on alumina and sapphire substrates, Japanese Journal of Applied Physics. 47 (2008) 1956–1960. https://doi.org/10.1143/JJAP.47.1956.

[22] C. Veríssimo, S.A. Moshkalyov, A.C.S. Ramos, J.L. Gonçalves, O.L. Alves, J.W. Swart, Different carbon nanostructured materials obtained in catalytic chemical vapor deposition, Journal of the Brazilian Chemical Society. 17 (2006) 1124–1132. https://doi.org/10.1590/S0103-50532006000600009.

[23] A.M. Cassell, J.A. Raymakers, J. Kong, H. Dai, Large Scale CVD Synthesis of Single-Walled Carbon Nanotubes, The Journal of Physical Chemistry B. 103 (1999) 6484–6492. https://doi.org/10.1021/jp990957s.

[24] Y. Zhang, H. Gu, S. Iijima, Single-wall carbon nanotubes synthesized by laser ablation in a nitrogen atmosphere, Applied Physics Letters. 73 (1998) 3827–3829. https://doi.org/10.1063/1.122907.

[25] P. Nikolaev, M.J. Bronikowski, R.K. Bradley, F. Rohmund, D.T. Colbert, K. a Smith, R.E. Smalley, Gas-phase catalytic growth of single-walled carbon nanotubes from carbon monoxide, Chemical Physics Letters. 313 (1999) 91–97. https://doi.org/Doi 10.1016/S0009-2614(99)01029-5.

[26] A.T. Dimitrov, G.Z. Chen, I.A. Kinloch, D.J. Fray, A feasibility study of scaling-up the electrolytic production of carbon nanotubes in molten salts, Electrochimica Acta. 48 (2002) 91–102. https://doi.org/10.1016/S0013-4686(02)00595-9.

[27] E. Couteau, K. Hernadi, J.W. Seo, L. Thiên-Nga, C. Mikó, R. Gaál, L. Forró, CVD synthesis of high-purity multiwalled carbon nanotubes using CaCO 3 catalyst support for large-scale production, Chemical Physics Letters. 378 (2003) 9–17. https://doi.org/10.1016/S0009-2614(03)01218-1.

[28] M.S. Kim, Yoong Ahm; Hayashi, Takuya; Endo, Morinobu; Dresselhaus, Carbon Nanofibers, in: R. Vajtai (Ed.), Springer Handbook of Nanomaterials, Springer, Houston, TX, 2013: p. 1234. https://doi.org/10.1007/978-3-642-20595-8.

[29] Y.Y. Fan, H.M. Cheng, Y.L. Wei, G. Su, Z.H. Shen, Influence of preparation parameters on the mass production of vapor-grown carbon nanofibers, Carbon. 38 (2000) 789–795. https://doi.org/10.1016/S0008-6223(99)00178-5.

[30] N.M. Rodriguez, A. Chambers, R.T.K. Baker, Catalytic Engineering of Carbon Nanostructures, Langmuir. 11 (1995) 3862–3866. https://doi.org/10.1021/la00010a042.

[31] C.Y. Su, A.Y. Lu, Y. Xu, F.R. Chen, A.N. Khlobystov, L.J. Li, High-quality thin graphene films from fast electrochemical exfoliation, ACS Nano. 5 (2011) 2332–2339. https://doi.org/10.1021/nn200025p.

[32] S. Yang, S. Brüller, Z.S. Wu, Z. Liu, K. Parvez, R. Dong, F. Richard, P. Samorì, X. Feng, K. Müllen, Organic Radical-Assisted Electrochemical Exfoliation for the Scalable Production of High-Quality Graphene, Journal of the American Chemical Society. 137 (2015) 13927–13932. https://doi.org/10.1021/jacs.5b09000.

[33] D. Wei, L. Grande, V. Chundi, R. White, C. Bower, P. Andrew, T. Ryhänen, Graphene from electrochemical exfoliation and its direct applications in enhanced energy storage devices, Chemical Communications. 48 (2012) 1239–1241. https://doi.org/10.1039/c2cc16859f.

[34] J. Chen, M. Duan, G. Chen, Continuous mechanical exfoliation of graphene sheets via three-roll mill, Journal of Materials Chemistry. 22 (2012) 19625–19628. https://doi.org/10.1039/c2jm33740a.

[35] T. Lin, J. Chen, H. Bi, D. Wan, F. Huang, X. Xie, M. Jiang, Facile and economical exfoliation of graphite for mass production of high-quality graphene sheets, Journal of Materials Chemistry A. 1 (2013) 500–504. https://doi.org/10.1039/c2ta00518b.

[36] J. Song, X. Wang, C.-T. Chang, Preparation and characterization of graphene oxide paper., Journal of Nanomaterials. 448 (2007) 457–60. https://doi.org/10.1038/nature06016.

[37] A. Ciesielski, P. Samorì, Graphene via sonication assisted liquid-phase exfoliation, Chemical Society Reviews. 43 (2014) 381–398. https://doi.org/10.1039/c3cs60217f.

[38] L. Jiao, L. Zhang, X. Wang, G. Diankov, H. Dai, Narrow graphene nanoribbons from carbon nanotubes, Nature. 458 (2009) 877–880. https://doi.org/10.1038/nature07919.

[39] H. Cho, I.S. Oh, J.H. Kang, S. Park, B. Ku, M. Park, S. Kwak, P. Khanra, J. Hee Lee, M. Jong Kim, Catalyst and doping methods for arc graphene, Nanotechnology. 25 (2014). https://doi.org/10.1088/0957-4484/25/44/445601.

[40] Q. Peng, Y. Li, X. He, X. Gui, Y. Shang, C. Wang, C. Wang, W. Zhao, S. Du, E. Shi, P. Li, D. Wu, A. Cao, Graphene nanoribbon aerogels unzipped from carbon nanotube sponges, Advanced Materials. 26 (2014) 3241–3247. https://doi.org/10.1002/adma.201305274.

[41] I.H. Son, J.H. Park, S. Kwon, S. Park, M.H. Rümmeli, A. Bachmatiuk, H.J. Song, J. Ku, J.W. Choi, J.M. Choi, S.G. Doo, H. Chang, Silicon carbide-free graphene growth on silicon for lithium-ion battery with high volumetric energy density, Nature Communications. 6 (2015) 1–8. https://doi.org/10.1038/ncomms8393.

[42] X. Gui, H. Li, K. Wang, J. Wei, Y. Jia, Z. Li, L. Fan, A. Cao, H. Zhu, D. Wu, Recyclable carbon nanotube sponges for oil absorption, Acta Materialia. 59 (2011) 4798–4804. https://doi.org/10.1016/j.actamat.2011.04.022.

[43] T. Yuan, J. Ruan, C. Peng, H. Sun, Y. Pang, J. Yang, Z.F. Ma, S. Zheng, 3D red phosphorus/sheared CNT sponge for high performance lithium-ion battery anodes, Energy Storage Materials. 13 (2018) 267–273. https://doi.org/10.1016/j.ensm.2018.01.014.

[44] X. Gui, J. Wei, K. Wang, A. Cao, H. Zhu, Y. Jia, Q. Shu, D. Wu, Carbon nanotube

sponges, Advanced Materials. 22 (2010) 617–621. https://doi.org/10.1002/adma.200902986.

[45] X. Dong, B. Li, A. Wei, X. Cao, M.B. Chan-Park, H. Zhang, L.J. Li, W. Huang, P. Chen, One-step growth of graphene-carbon nanotube hybrid materials by chemical vapor deposition, Carbon. 49 (2011) 2944–2949. https://doi.org/10.1016/j.carbon.2011.03.009.

[46] Z. Yan, L. Ma, Y. Zhu, I. Lahiri, M.G. Hahm, Z. Liu, S. Yang, C. Xiang, W. Lu, Z. Peng, Z. Sun, C. Kittrell, J. Lou, W. Choi, P.M. Ajayan, J.M. Tour, Three-dimensional metal- Graphene- Nanotube multifunctional hybrid materials, ACS Nano. 7 (2013) 58–64. https://doi.org/10.1021/nn3015882.

[47] L. Huang, B. White, M.Y. Sfeir, M. Huang, H.X. Huang, S. Wind, J. Hone, S. O'Brien, Cobalt ultrathin film catalyzed ethanol chemical vapor deposition of single-walled carbon nanotubes, Journal of Physical Chemistry B. 110 (2006) 11103–11109. https://doi.org/10.1021/jp060693r.

[48] X. Peng, K. Koczkur, A. Chen, Synthesis of well-aligned bamboo-like carbon nanotube arrays from ethanol and acetone, Journal of Physics D: Applied Physics. 41 (2008) 095409. https://doi.org/10.1088/0022-3727/41/9/095409.

[49] L.M. Ombaka, P. Ndungu, V.O. Nyamori, Usage of carbon nanotubes as platinum and nickel catalyst support in dehydrogenation reactions, Catalysis Today. 217 (2013) 65–75. https://doi.org/10.1016/j.cattod.2013.05.014.

[50] Z. Tu, Z. Liu, Y. Li, F. Yang, L. Zhang, Z. Zhao, C. Xu, S. Wu, H. Liu, H. Yang, P. Richard, Controllable growth of 1-7 layers of graphene by chemical vapour deposition, Carbon. 73 (2014) 252–258. https://doi.org/10.1016/j.carbon.2014.02.061.

[51] S. Park, R.S. Ruoff, Chemical methods for the production of graphenes, Nat Nano. 4 (2009) 217–224. https://doi.org/10.1038/nnano.2009.58.

[52] S. Esconjauregui, C.M. Whelan, K. Maex, The reasons why metals catalyze the nucleation and growth of carbon nanotubes and other carbon nanomorphologies, Carbon. 47 (2009) 659–669. https://doi.org/10.1016/j.carbon.2008.10.047.

[53] O. V. Yazyev, A. Pasquarello, Carbon diffusion in CVD growth of carbon nanotubes on metal nanoparticles, Physica Status Solidi (B) Basic Research. 245 (2008) 2185–2188. https://doi.org/10.1002/pssb.200879573.

[54] A. Bachmatiuk, F. Börrnert, M. Grobosch, F. Schäffel, U. Wolff, A. Scott, M. Zaka, J.H. Warner, R. Klingeler, M. Knupfer, B. Büchner, M.H. Rümmeli, Investigating the graphitization mechanism of SiO2 nanoparticles in chemical vapor deposition, ACS Nano. 3 (2009) 4098–4104. https://doi.org/10.1021/nn9009278.

[55] A. Moisala, A.G. Nasibulin, E.I. Kauppinen, The role of metal nanoparticles in the catalytic production of single-walled carbon nanotubes - a review, Journal of Physics - Condensed Matter. 15 (2003) S3011. https://doi.org/10.1088/0953-8984/15/42/003.

[56] Y. Zhang, I. Utke, J. Michler, G. Ilari, M.D. Rossell, R. Erni, Growth and characterization of CNT-TiO2 heterostructures, Beilstein Journal of Nanotechnology.

5 (2014) 946–955. https://doi.org/10.3762/bjnano.5.108.

[57] M. Law, L.E. Greene, J.C. Johnson, R. Saykally, P. Yang, Nanowire dye-sensitized solar cells., Nature Materials. 4 (2005) 455–459. http://www.chem.uci.edu/~lawm/Nanowire dye-sensitized solar cells.pdf.

[58] V. Jourdain, C. Bichara, Current understanding of the growth of carbon nanotubes in catalytic chemical vapour deposition, Carbon. 58 (2013) 2–39. https://doi.org/10.1016/j.carbon.2013.02.046.

[59] M. Lin, J.P.Y. Tan, C. Boothroyd, K.P. Loh, E.S. Tok, Y.L. Foo, Dynamical observation of bamboo-like carbon nanotube growth, Nano Letters. 7 (2007) 2234–2238. https://doi.org/10.1021/nl070681x.

[60] Y. Ogawa, B. Hu, C.M. Orofeo, M. Tsuji, K.I. Ikeda, S. Mizuno, H. Hibino, H. Ago, Domain structure and boundary in single-layer graphene grown on Cu(111) and Cu(100) films, Journal of Physical Chemistry Letters. 3 (2012) 219–226. https://doi.org/10.1021/jz2015555.

[61] Z.P. Huang, D.Z. Wang, J.G. Wen, M. Sennett, H. Gibson, Z.F. Ren, Effect of nickel, iron and cobalt on growth of aligned carbon nanotubes, Applied Physics A: Materials Science and Processing. 74 (2002) 387–391. https://doi.org/10.1007/s003390101186.

[62] C.J. Lee, J. Park, J.A. Yu, Catalyst effec on carbon nanotubes synthesized by thermal chemical vapor deposition, Chemical Physics Letters. 360 (2002) 250–255.

[63] K. Hernadi, A. Fonseca, J.B. Nagy, A. Siska, I. Kiricsi, Production of nanotubes by the catalytic decomposition of different carbon-containing compounds, Applied Catalysis A: General. 199 (2000) 245–255. https://doi.org/10.1016/S0926-860X(99)00561-X.

[64] A. Gohier, C.P. Ewels, T.M. Minea, M.A. Djouadi, Carbon nanotube growth mechanism switches from tip- to base-growth with decreasing catalyst particle size, Carbon. 46 (2008) 1331–1338. https://doi.org/10.1016/j.carbon.2008.05.016.

[65] S.P. Chai, S.H.S. Zein, A.R. Mohamed, Preparation of carbon nanotubes over cobalt-containing catalysts via catalytic decomposition of methane, Chemical Physics Letters. 426 (2006) 345–350. https://doi.org/10.1016/j.cplett.2006.05.026.

[66] L. Zheng, X. Liao, Y.T. Zhu, Parametric study of carbon nanotube growth via cobalt-catalyzed ethanol decomposition, Materials Letters. 60 (2006) 1968–1972. https://doi.org/10.1016/j.matlet.2005.12.060.

[67] X. Li, W. Cai, J. An, S. Kim, J. Nah, D. Yang, R. Piner, A. Velamakanni, I. Jung, E. Tutuc, S.K. Banerjee, L. Colombo, R.S. Ruoff, Large area synthesis of high quality and uniform graphene films on copper foils, Science. 324 (2009) 1312–1314. https://doi.org/10.1126/science.1171245.

[68] H.I. Rasool, E.B. Song, M. Mecklenburg, B.C. Regan, K.L. Wang, B.H. Weiller, J.K. Gimzewski, Atomic-scale characterization of graphene grown on copper (100) Single Crystals, Journal of the American Chemical Society. 133 (2011) 12536–12543. https://doi.org/10.1021/ja200245p.

[69] D.L. Duong, G.H. Han, S.M. Lee, F. Gunes, E.S. Kim, S.T. Kim, H. Kim, Q.H. Ta, K.P. So, S.J. Yoon, S.J. Chae, Y.W. Jo, M.H. Park, S.H. Chae, S.C. Lim, J.Y. Choi, Y.H. Lee, Probing graphene grain boundaries with optical microscopy, Nature. 490 (2012) 235–239. https://doi.org/10.1038/nature11562.

[70] J.H. Xia, X. Jiang, C.L. Jia, The size effect of catalyst on the growth of helical carbon nanofibers, Applied Physics Letters. 95 (2009) 1–4. https://doi.org/10.1063/1.3271031.

[71] J. Zhu, J. Jia, F.L. Kwong, D.H.L. Ng, Synthesis of bamboo-like carbon nanotubes on a copper foil by catalytic chemical vapor deposition from ethanol, Carbon. 50 (2012) 2504–2512. https://doi.org/10.1016/j.carbon.2012.01.073.

[72] A. Chambers, N.M. Rodriguez, R.T.K. Baker, Modification of the Catalytic Behavior of Cobalt by the Addition of Copper, Society. (1995) 10581–10589.

[73] L. Guevara, C. Wanner, R. Welsh, M.A. Atwater, Using Mechanical Alloying to Create Bimetallic Catalysts for Vapor-Phase Carbon Nanofiber Synthesis, Fibers2. 3 (2015) 394–410. https://doi.org/10.3390/fib3040394.

[74] W.L. Wang, X.D. Bai, K.H. Liu, Z. Xu, D. Golberg, Y. Bando, E.G. Wang, Direct synthesis of B-C-N single-walled nanotubes by bias-assisted hot filament chemical vapor deposition, Journal of the American Chemical Society. 128 (2006) 6530–6531. https://doi.org/10.1021/ja0606733.

[75] F. Du, D. Yu, L. Dai, S. Ganguli, V. Varshney, A.K. Roy, Preparation of Tunable 3D Pillared Carbon Nanotube À Graphene Networks for High-Performance Capacitance, (2011) 4810–4816.

[76] S. He, H. Hou, W. Chen, 3D porous and ultralight carbon hybrid nanostructure fabricated from carbon foam covered by monolayer of nitrogen-doped carbon nanotubes for high performance supercapacitors, Journal of Power Sources. 280 (2015) 678–685. https://doi.org/10.1016/j.jpowsour.2015.01.159.

[77] B. Kitiyanan, W.E. Alvarez, J.H. Harwell, D.E. Resasco, Controlled production of single-wall carbon nanotubes by catalytic decomposition of CO on bimetallic Co-Mo catalysts, Chemical Physics Letters. (2000) 497–503.

[78] N. Okazaki, S. Hosokawa, T. Goto, Y. Nakayama, Synthesis of carbon tubule nanocoils using Fe-In-Sn-O fine particles as catalysts, Journal of Physical Chemistry B. 109 (2005) 17366–17371. https://doi.org/10.1021/jp050786t.

[79] X. Qi, W. Zhong, Y. Deng, C. Au, Y. Du, Characterization and magnetic properties of helical carbon nanotubes and carbon nanobelts synthesized in acetylene decomposition Over Fe-Cu nanoparticles at 450 °C, Journal of Physical Chemistry C. 113 (2009) 15934–15940. https://doi.org/10.1021/jp905387v.

HYPOTHESIS, JUSTIFICATION, AND OBJECTIVES

Hypothesis

It is possible to obtain a coupled graphitic structure into a nitrogen-doped three-dimensional carbon nanostructure with the use of bimetallic catalytic particles (Co: Cu, Au, Ag) deposited over SiO_2 substrate.

Justification

- There are few research works focused on the influence of bimetallic catalytic particles in the synthesis of 3D carbon nanostructures. In previous reports, it is demonstrated that bimetallic catalytic particles considerably modify the growth of CNT promoting defective structure, which could act as an anchor point for 3D networks.
- It is known that Cu is well used for the growth of graphene sheets (In-plane growth) while Co, Ni, or Fe for the growth of CNT (vertical growth).
- Doping and functionalization of carbon nanostructures is a way to modify their structural conditions as well as the electronic and chemical properties.

Main Objective

The growth of 3D carbon nanostructures by chemical vapor deposition strongly depends on the type of catalytic particle, temperature, and precursors. In this thesis, the main objective consists on determinate the influence of a mixed Cobalt (commonly used to growth CNT) and Cu (commonly used to growth graphene) thin film and Fe based catalyst in the growth of doped and functionalized 3D carbon nanostructures as well as determinate the growth mechanism influenced by the interaction of a variety of precursors over the crystal structure of Co, Cu, and Fe. Each chapter will contribute to the resolution associated to the influence of precursors, synthesis time and reduction process, along with the effect associated to the size and shape of metallic nanoparticles and sprayed metallic materials in the growth of a variety of carbon nanostructures that promotes the formation of 3D nanostructured carbon materials.

Objectives by Chapter

Chapter 2:

- Obtain the Co-Cu thin film growth parameters by a sputtering technique.
- Test a variety of precursors in the growth of carbon nanostructures by the use of a Co-Cu thin film as catalysts.

Chapter 3:

- Determine the influence of reduction time before synthesis in the nanoparticle formation.
- Determine the physical and chemical characteristics of the wrinkled carbon nanobelts (N-CBS).
- Evaluate other metals like Ag and Au in the N-CBS growth.
- Present a growth mechanism.

Chapter 4:

- Understand the mechanism developed by Cu substrate and Cu nanoparticle to grow carbon nanostructures in a controlled CVD system.

Chapter 5:

- Use a Fe-based catalyst to grow other 3D carbon nanostructures.
- Determine the influence of different precursors in the growth of 3D carbon nanostructures.
- Evaluate the physical and chemical structure characteristics.
- Determine a growth mechanism approach.

CHAPTER TWO:

BIMETALLIC CATALYTIC MISCIBILITY (CO-CU) IN THE GROWTH OF NEW CARBON NANOSTRUCTURES

2.1 Introduction

The growth of new 2D carbon allotropes and 3D macroscopic carbon architectures is a topic of high interest where graphitic materials like carbon nanotubes networks [1,2], wrinkled graphene sheets [3,4], and nanofibers [5,6] works like unities in the growing of macroscopic systems. These materials can be used in supercapacitors [7], electrodes in lithium batteries [8], catalyst [9], oil sorbents [10], and ORR-reactions [11]. It has been demonstrated that the structure and physical-chemical properties of the 3D carbon nanomaterials depend principally on the synthesis conditions, precursors, and catalyst [12–14]. However, the use of bimetallic catalysts on the growth of this type of material is far to be understood [15]. Chambers et al. [16] reported a multi growth arrangement of carbon nanotubes on specific crystallographic planes of cobalt nanoparticles as a consequence of adding copper during the synthesis. Also, other mixtures like Ag-Co, Fe-Co, and Ni-Cu as a catalyst is reported to favor the growth of unusual morphologies [17,18].

In this chapter would be addressed the results for the synthesis of Co-Cu thin films by magnetron sputtering technique and its use as a catalyst in a chemical vapor deposition system. Mixtures of different precursors like ethanol, thiophene, and benzylamine were used to grow nanostructured 3D carbon materials. Oxygen and sulfur molecules address high structural defects changing the type of growth from a growth-based to a tip-growth mechanism leading to the formation of carbon nanotubes, wrinkled carbon nanofibers, and corrugated macroscopic structures by an interlaced effect of the wrinkled carbon nanofibers.

2.2 Growth of Co-Cu thin film of 20:2 nm thickness

2.2.1 Methodology

Si/SiO_2 substrates of 8 cm x 8 cm and 2 mm thickness were cleaned using acetone (99.974 %, Fermont), ethanol (96.5 %, CTR scientific) and Isopropanol (99.8%, CTR Scientific) in an ultrasonic bath during 30 min each and dried with a flush of N_2 (99.9995 %, Infra). The substrates were cut into pieces of approximately 4 cm x 4 cm an attached to metallic support adequate for the mechanical arm of the physical vapor deposition system (PVD).

The PVD system used for the growth of Co-Cu thin films consists of a sputtering Intercovamex V3 high-vacuum equipment developed by the Intercovamex company. This equipment has a mechanical arm to introduce the sample and a central 304 stainless steel chamber of 14” diameter and 18” high where six metallic electrodes (cathodes) can be attached for the simultaneously or individual use to be deposited. A glow discharge argon cold plasma is generated by a direct current power supply (DC MDX-500) and a pulsed-direct current power supply (Pinnacle-Plus). By two mechanical pumps and two turbomolecular pumps (ATP 80 and ATP 400), a high vacuum is reached ($1x10^{-7}$ torr) at the main chamber. The deposition thickness is linear to time and depends on the vacuum, discharge parameters, and type of power supply. The samples were stored under a nitrogen atmosphere to prevent further oxidation.

2.2.2 Results

Previous works developed by Muñoz-Sandoval et al. [19] determined the initial parameters for the deposition of Co and developed the methodology for the growth of Cu thin films. Figure 2.1a schematizes the PVD process where a Si/SiO_2 substrate was attached to the anode, and Co and Cu electrodes work as a cathode. A high electric field is applied to create a glow discharge plasma in order to sputter the cathode and deposit metallic ions on the Si substrate. Initial tests to corroborate the experimental conditions of Cu deposition were advanced. Figure 2.1b and figure 2.1c illustrate a transversal scanning electronic micrograph of the growth of thin films at 60 min and 75 min. The thickness of the Cu films was measured of 108.8 nm and 126.3 nm, respectively, which gives a deposition rate of 0.030 nm per second. A similar deposition scan was developed for Co. Table 2.1 depicts the specific conditions for each electrode (Co and Cu). For Co, a deposition rate of 0.02 nm per second with direct current at 30 W and the $2x10^{-2}$ torr is established. For the growth of 20 nm of Co, 17 min 7 sec is necessary. In the case of Cu thin film, a deposition rate of 0.03 nm per second was established with a pulsed-direct current power supply at 15 W and $1.2x10^{-2}$ torr.

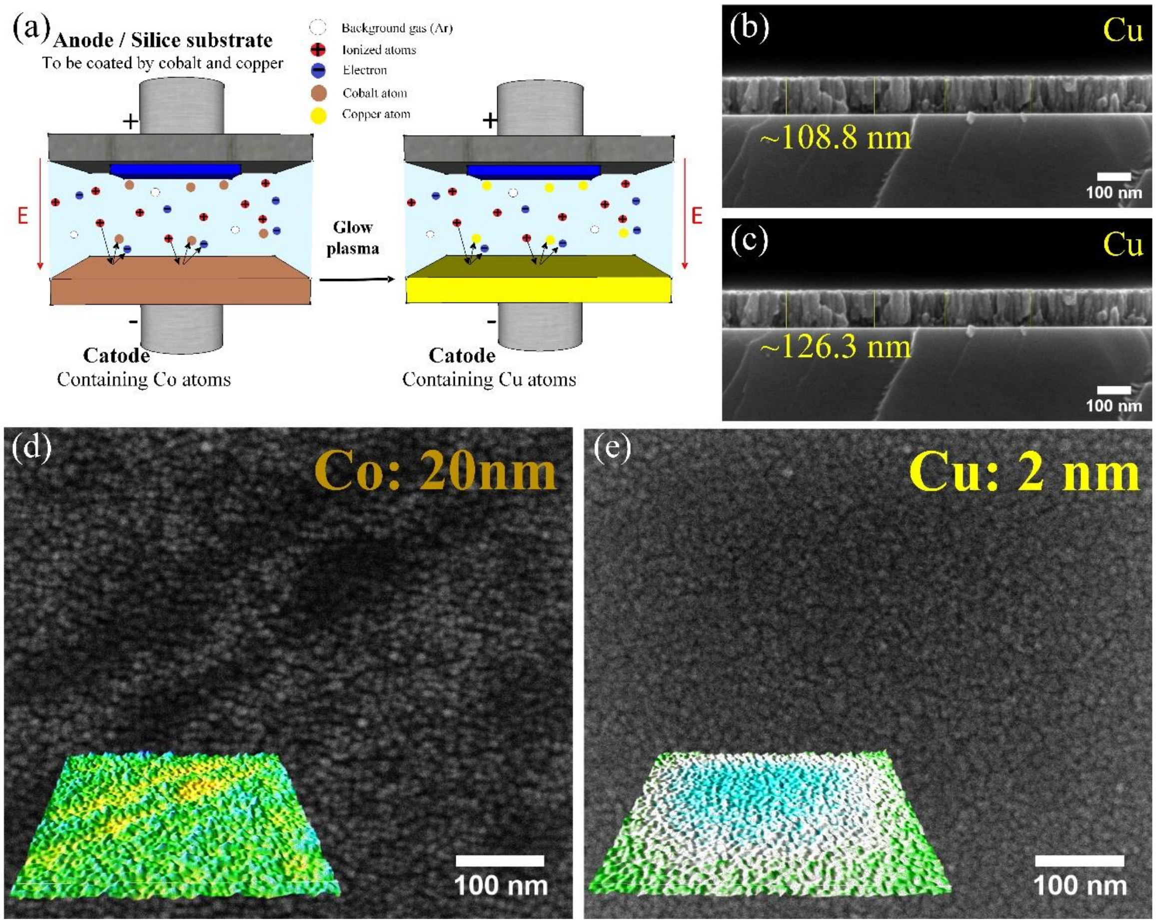

Figure 2.1: (a) Schema for PVD deposition process by a sputtering technique and glow plasma using Co and Cu electrodes. (b) and (c) represents a transversal SEM image and thickness measurement after 60 min and 75 min of Cu deposition, respectively. (d) SEM image after deposition of 20 nm of Co and roughness 3D visualization (inset). (e) SEM image after deposition of 2 nm Cu over Co, and 3D surface plot (inset).

Table 2.1: Operational conditions for Co-Cu thin film deposition

	Cobalt (Co)	**Copper (Cu)**
Power supply	Direct current	Pulsed-direct current
Potential	30 W	15 W
Time for synthesis	17 min 7 seg	1 min 6 seg
Pressure	2 x 10^{-2} torr	1.2 x 10^{-2} torr

Figure 2.1c and figure 2.1d illustrate an SEM image of the Co (20 nm) and after the Cu (2 nm) deposition, respectively. A full covered deposition was obtained over the SiO_2 substrate

in both cases. Nevertheless, considering the contrast changes over the SEM image is possible to perform a surface 3D plot. For Co deposition, surface irregularities are observed after deposition with variations over 5 nm to 10 nm (Figure 2.1c inset). After Cu deposition, fewer surface variations are observed and a more well-distributed surface (Figure 2.1d inset). The behavior associated with the substrate over a reductive atmosphere is described in subsequent chapters.

2.3 Test of Co-Cu thin film in a CVD system with different precursors

2.3.1 Methodology

Co-Cu thin films deposited over Si were used as a substrate in an aerosol assisted chemical vapor deposition system (AACVD). Figure 2.2a depicts the AACVD configuration, which consists of a nebulizer built-in reinforced glass with dimensions of 2.5 in diameter and 40 cm length that contains at the base a piezoelectric transducer (Ø 38 mm). This system is connected to a radiofrequency power supply (RBI Instrumentation) with a supply capacity of 0.8 MHz to obtain precursors droplets of around 8 μm to a few nm [20]. The nebulizer is connected to a quartz tube of 1 in diameter and 1.1 m length. Two tubular furnaces (Tube furnace 21100) were used at different temperatures, the furnace near to the sprayer was set at 750 °C (F1) while the furthest was set at 850 °C (F2). A carrier gas of H_2/Ar at 5%/95% was used. The end of the quartz tube was connected to a Liebig condenser and a solvent trap filled with acetone (~300 ml). Figure 2.2b illustrates a schematic representation of how 20 pieces of 1 cm x 1cm of Co-Cu/Si thin film were positioned from the beginning of the 750 °C furnace to the end of the 850 °C furnace. For practical comparison, the results described in the following chapters would be taken from the middle of F1 (S1), between F1 and F2 furnace (S2), and in the middle of F2 (S3). Figure 2.2c shows the temperature profile generated by the interaction of F1 and F2 temperature flows inside the quartz tube measured with a 60 cm thermocouple bar (type K). The temperature described for S1, S2 and S3 related to its position are 749 °C, 801 °C, and 859 °C, respectively.

In order to get the growth of carbon nanostructures over substrates, a mixture of precursors containing nitrogen, oxygen, and sulfur was addressed. Table 2.2 depicts the variation of volume concentration for benzylamine (C_7H_9N, Aldrich), ethanol (C_2H_6O, CTR Scientific), thiophene (C_4H_4S, Aldrich) used inside nebulizer to be pyrolyzed inside the furnace.

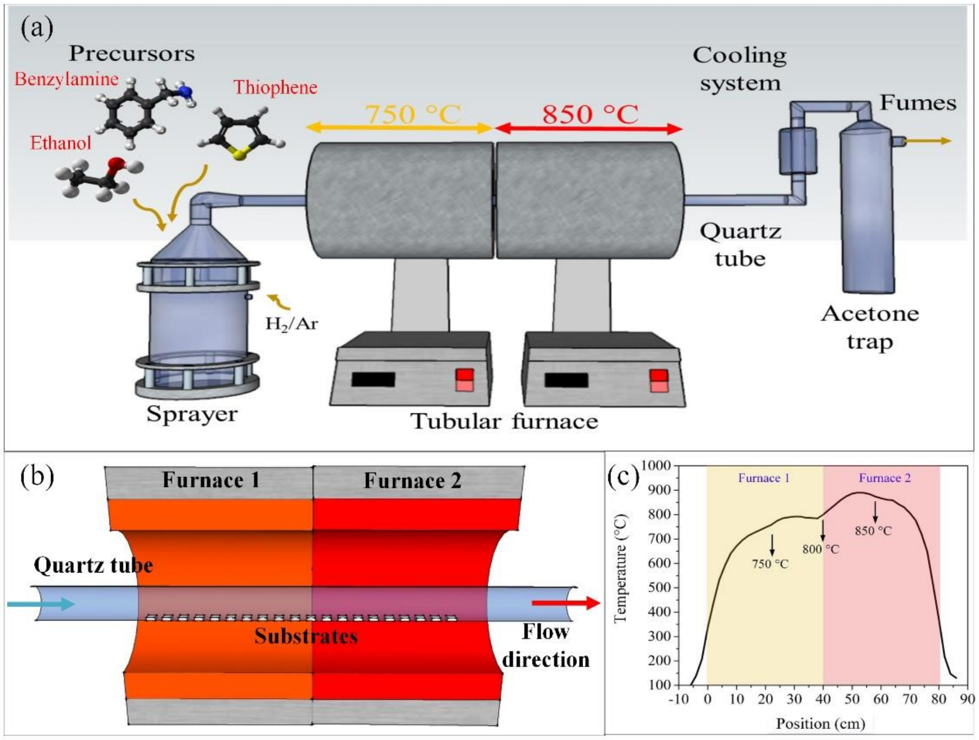

Figure 2.2: (a) Schematic representation of the AACVD system using Co-Cu/Si substrates and two tubular furnaces at different temperatures of 750 °C and 850°C. (b) Scale illustration shows the position of 1 cm x 1 cm substrates inside the quartz tube. (c) Temperature profile inside the quartz tube due to the interaction of F1 and F2.

Table 2.2: Precursor concentration used to grow carbon nanostructures over the Co-Cu substrate.

Solution	*Benzylamine (W/W %)*	*Ethanol (W/W %)*	*Thiophene (W/W %)*
Benzylamine (B)	100	-	-
Benzylamine-Tiophene (BT)	99.48	-	0.51
Ethanol (E)	-	100	-
Ethanol-Thiophene (ET)	-	99.87	0.12
Benzylamine-Ethanol (BE)	49.90	50.09	-
Benzylamine-Ethanol-Thiophene (BET)	49.75	49.93	0.32

It is worth to mention that the concentration of BET solution was taken from the reported by Muñoz-Sandoval et al. [14] used to grow nitrogen-doped carbon nanotube sponges in a chemical vapor deposition system. The other volume concentrations of solutions BT, ET and BE, are the results of eliminating one of the precursors in the mixture and get a 100 % W/W ratio.

2.3.2 Precursor effect in the growth of carbon nanostructures

Figure 2.3 depicts the scanning electron microscope for ethanol used as a precursor. Figure 2.3a illustrates the type of morphology that grew over the Co-Cu substrate at the S1-E position (750 °C). Tubular carbon nanostructures were barely formed, and mainly the structure consists of carbon agglomerates. These agglomerates encapsulate Co-Cu-based nanoparticles (red arrows), and in some cases, these particles promote the growth of non-perfect tubular structures (blue arrows). Figure 2.3b shows the micrograph at the S2-E position (800 °C). This SEM image depicts tubular carbon nanotubes that grew over the Co-Cu substrate. A variety of CNT was observed. The presence of short and highly curved CNT (inset) where walls seem to be highly defective with the formation of knots and elbows promotes the bend of the tubular structures. Also, the presence of long CNTs (~2 μm) was found. Figure 2.3c illustrates the type of carbon structures synthesized in the S3-E sample at 850 °C. Here no presence of long tubular structures was detected. However, agglomerates of carbon material with short CNT (~280 nm length) anchored were observed. These short and non-perfect tubular structures contain in almost all the cases a metallic particle at the tip, presumably Co nanoparticle. A comparison between the size diameters of the tubular structures found in S1, S2, and S3 (figure 2.3d) reveals that at lower temperatures the size of the CNT was lower (23 nm diameter) while, for S2 and S3 broader distributions were obtained with average diameters of 36 nm and 31 nm respectively.

The type of tubular structure considerably changes when the benzylamine was only used. Figure 2.4a shows the type of structure found in the S1-B section. CNTs with a bumped wall structure (red arrows) were observed. Also, due to the curvature effect presented in the structure, some agglomerated of CTN were formed (blue arrows). The tubular structures had an average diameter of 40 nm and an average length of 2.3 μm. Figure 2.4b illustrates the type of tubular structure found in S2-B. Highly curved tubular structures with the not apparently defective arrangement build the sample. This curvature effect in CNT walls is widely related to the incorporation of nitrogen into the graphitic structure [21]. Also, some short defective structures and carbon agglomerates were detected (blue arrow). The tubular structure found had diameters from 20 nm to 160 nm and an average length of ~ 5 µm. For S3-B (figure 2.4c), A mixture of straight-CNT (yellow arrow), carbon agglomerates (blue arrow), defective-CNT (red arrow), and highly curved-CNT (white arrow) is noticed. These tubular structures had diameters from 20 nm to 80 nm and lengths of ~3 µm. An interlaced effect can be obtained due to the rolling effect of highly curved tubular structures (green arrow). Figure 2.4d illustrates a comparison made over the diameter size distribution where at the S2 position (800 °C), a broader diameter distribution was found. This behavior was similar to the found in the sample using only ethanol. However, in this case, the diameters are higher (average of 64 nm), almost two times the found in the ethanol sample (36 nm).

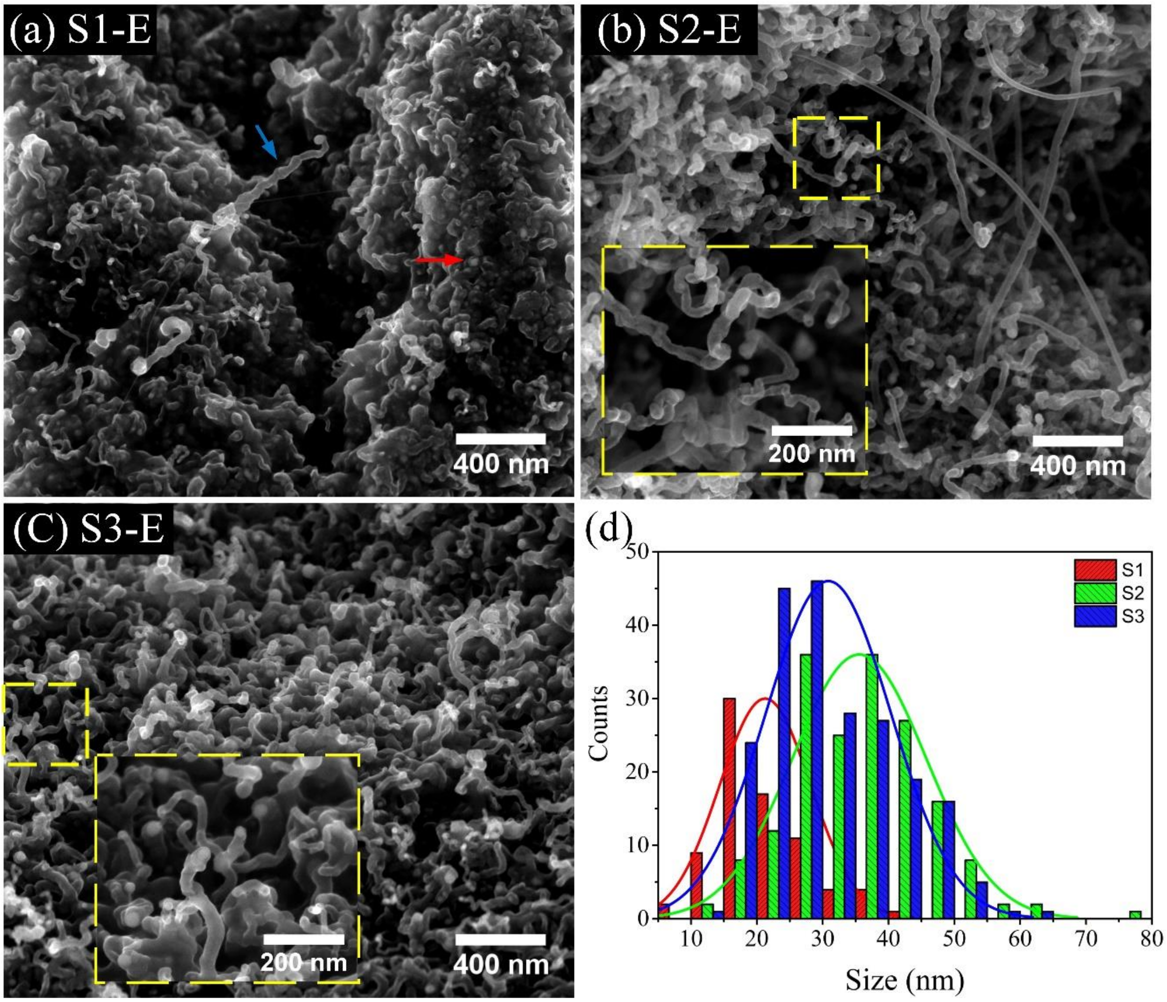

Figure 2.3: SEM image related to the synthesis of carbon nanostructures using ethanol (E) at S1 position (a), S2 position (b), and S3 position (c). (d) Tubular carbon nanostructure histogram for S1, S2, and S3 positions.

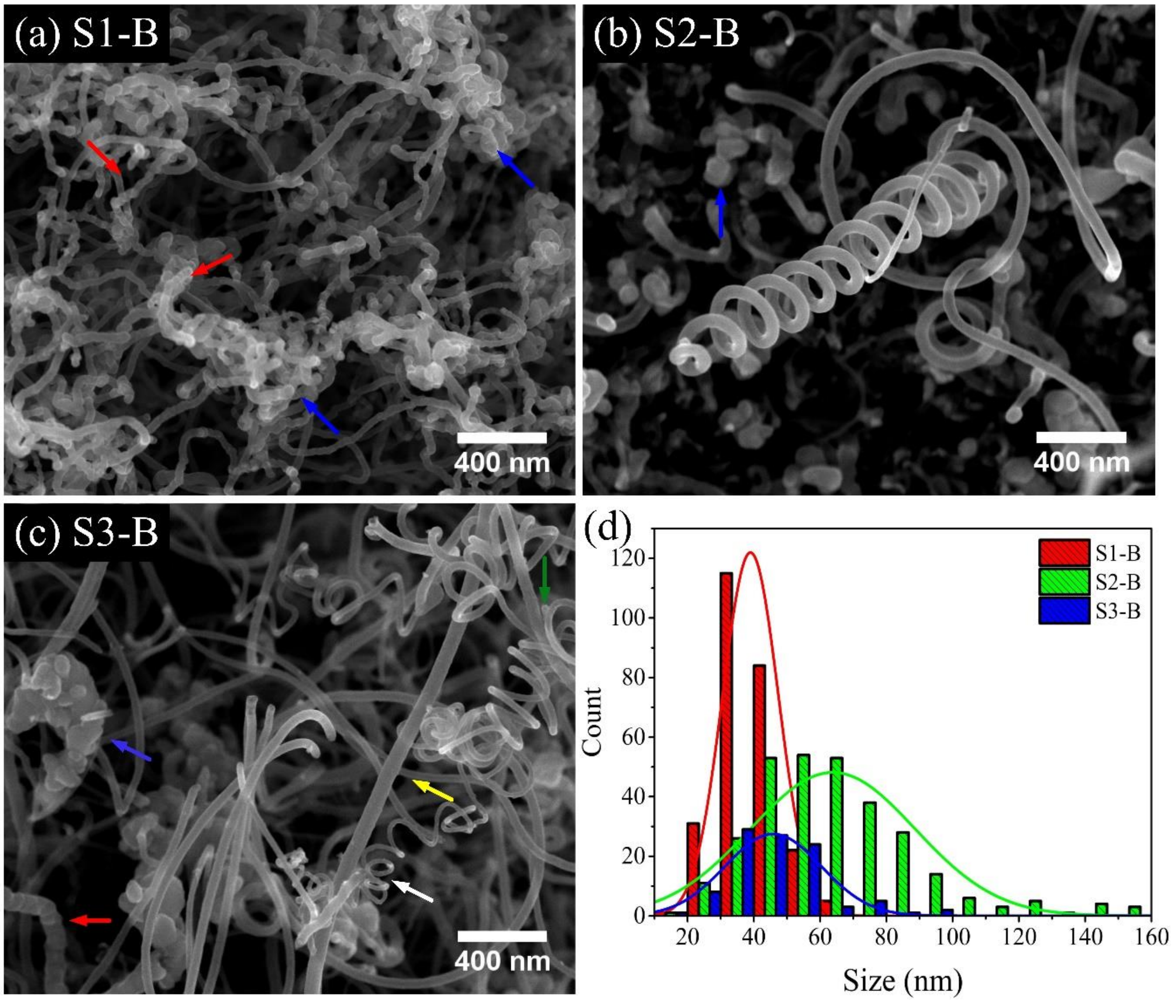

Figure 2.4: SEM image associated with the carbon nanostructures obtained by the use of benzylamine (B) at S1 position (a), S2 position (b), and S3 position (c). (d) Tubular carbon nanostructure histogram for S1, S2, and S3 positions.

Figure 2.5 illustrates the morphologies found in the experiment where a mixture of benzylamine and ethanol (BE) was employed. Figure 2.5a shows the S1-BE sample. At this condition of low temperature, the presence of a variety of tubular structures with considerable diameter and length variations, and carbon agglomerates with short carbon nanotubes attached were identified. Some of the long and thin tubular structures are highly curved, and it was intertwined randomly (red arrow). The thicker tubular structures tend to be less curved.

The inset in figure 2.5a shows a magnification over a section of a carbon agglomerate where it was appreciated short tubular structures with semi-spherical nanoparticles embedded in the structure (blue arrow) and some cases at the tip of the structure (green arrow). Figure 2.5b depicts the tubular morphologies found at S2-BE. In this case, the tubular structures had diameters well-distributed and highly deformed. The tubular structures are randomly arranged, and some of them had elongated and semi-spherical nanoparticles embedded inside (inset). For S3-BE (figure 2.5c), there is no trace of long tubular structures. Conversely, carbon agglomerates showing small tubular structures were observed. These tip sections of what appears to be carbon nanotubes contain metallic semi-spherical and elongated nanoparticles (inset) inside the structure in almost all the cases revealing a tip growth mechanism. Some of the particles also are fully encapsulated in a core-shell structure (red arrow). Figure 2.5d depicts that average diameter increases as the temperature increases being S1-BE the sample with the lowest diameter (22 nm) and S3-BE the sample with the highest diameter (52 nm) and broader distribution (from 10 nm to 120 nm).

The previous results indicate the formation of two types of structures. However, for the ethanol and benzylamine mixture, the growth of carbon nanostructures considerably changes. For S1-E and S3-E, ethanol promotes the encapsulation of metallic nanoparticles in an “onion-like” nanostructure and the formation of thin (between 10nm and 60 nm diameter), short and rugged tubular nanostructures. In contrast, the use of benzylamine promotes the formation of long, thicker (from 20 nm to 160 nm) and highly curved tubular structures. The combination of precursors led to the formation of carbon agglomerates with tubular structures for S1-BE. It also led to the formation of metallic semi-spherical and elongated nanoparticles surrounded by carbon material for S3-BE. However, in all cases, the S2 position promotes the growth of tubular structures. In consequence, this position was taken as the main section to compare the effect of adding thiophene as a precursor and observe the variations reflected in the tubular structures.

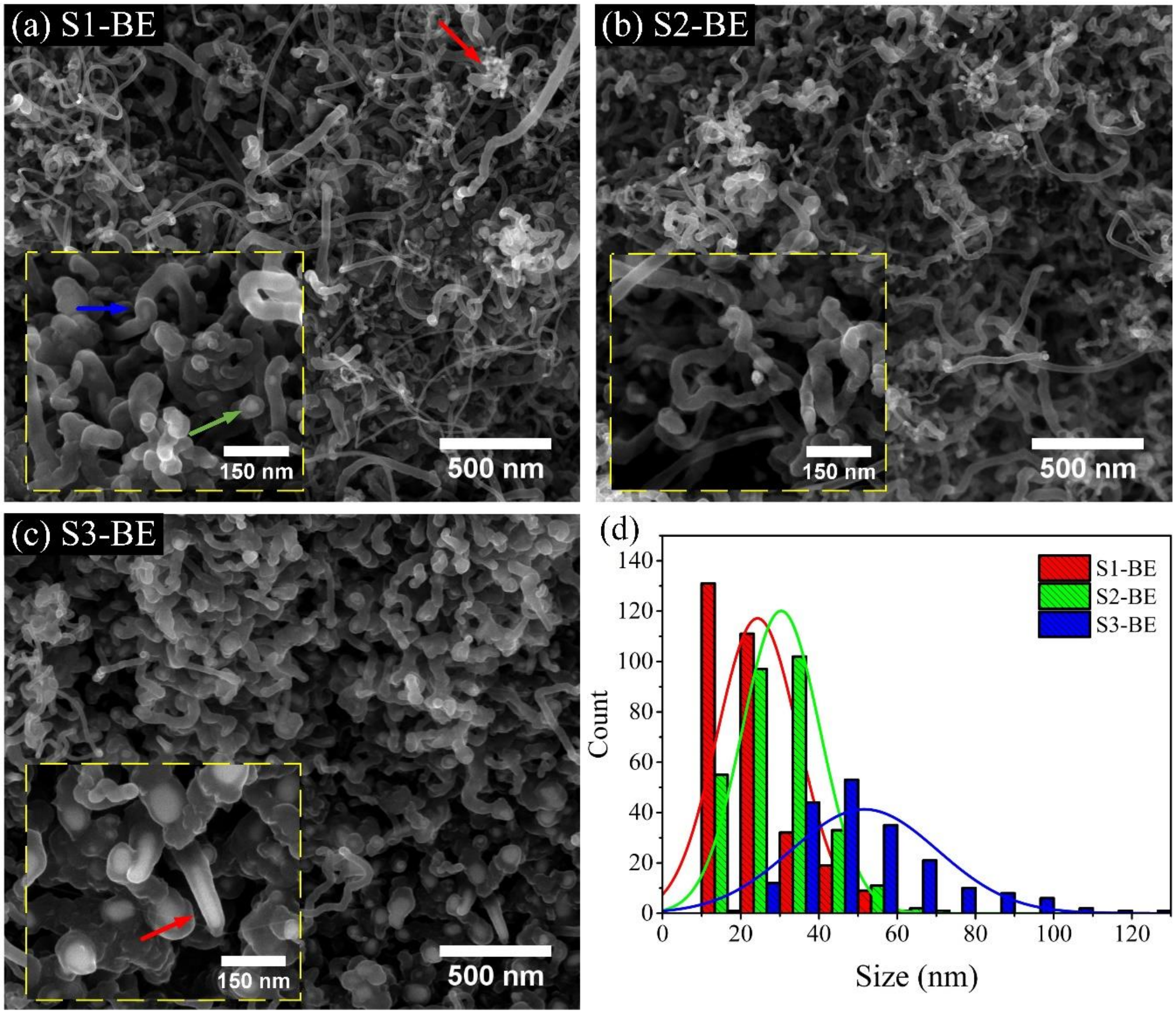

Figure 2.5: SEM image related to the synthesis of carbon nanostructures using a benzylamine-ethanol mixture (BE) at S1 position (a), S2 position (b), and S3 position. (d) Tubular carbon nanostructure histogram for S1, S2, and S3 positions.

Figure 2.6 illustrates a comparison between the synthesis using E, B, and BE and after the incorporation of thiophene in mixtures as ET, BT, and BET. Figure 2.6a-c depicts the tubular structures found in E, BE, and B, respectively described above. After the incorporation of thiophene in E (figure 2.6d), the formation of tubular structures is limited, leading to the formation of short-bumped tubular structures that at the tip or in the main body encapsulates a metallic nanoparticle (red arrow). Figure 2.6e shows the type of nanostructures obtained with the BET solution. The incorporation of thiophene modifies the nature of the tubular structure considerably to the point that there is no more trace of nanotube formation. The metallic nanoparticle changes the growth mechanism, as can be seen outside the structure where corrugated carbon nanofibers are catalyzed from particular spots in metallic particles. The corrugated carbon nanofibers obtained interlaced to create a flat interconnected and corrugated macroscopic structure (red arrow). A similar effect is observed in the BT sample (figure 2.6f), but in this case, the corrugated graphitic structure agglomerates into random morphologies highly defected.

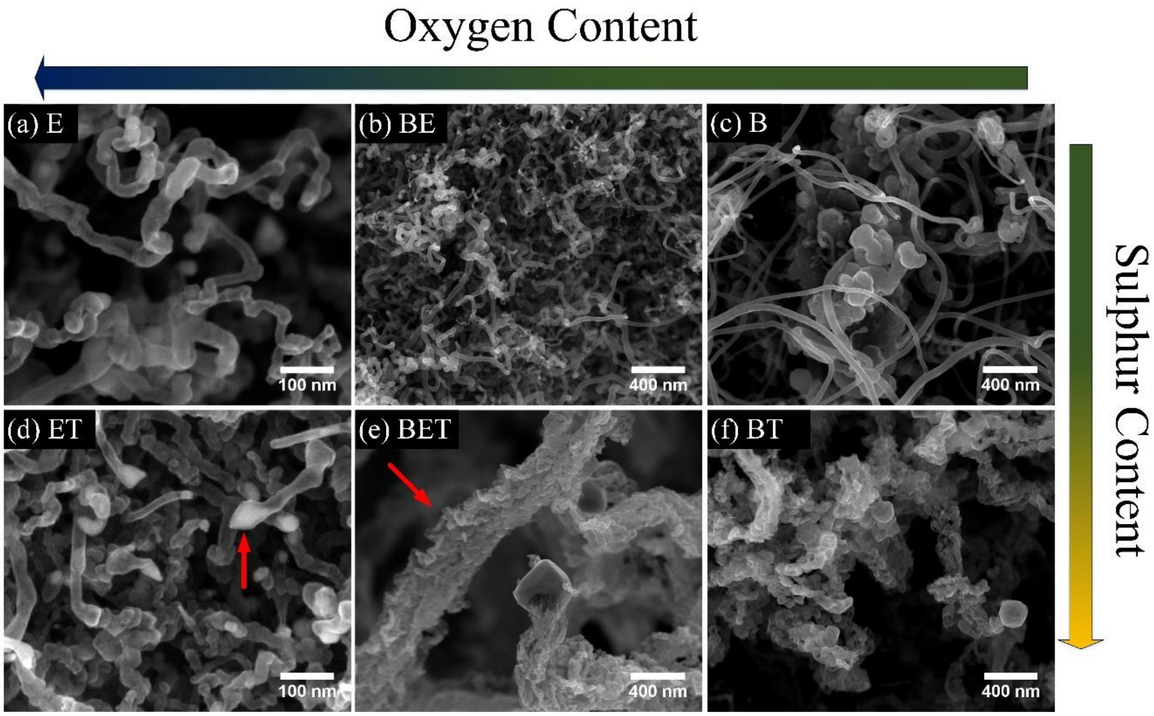

Figure 2.6: Nanostructures that grew at S2 position for (a) E (b) BE, (c) B, and the effect after the incorporation of thiophene in each sample (d) ET, (e) BET and (f) BT.

To have a better understanding related to the type of morphologies found in E, B, and BE without thiophene, TEM was employed. Figure 2.7a shows a low magnification micrograph for the E sample. Three types of morphologies are observed: 1) carbon nanotubes with bamboo shape morphology (yellow arrow), 2) Tubular carbon nanotubes without bamboo shape structure (blue arrow), and 3) encapsulated metallic nanoparticles surrounded by graphitic material. Figure 2.7b depicts the graphitic layers that structures the folded CNT. In this case, the graphitic layers were stacked (white square) similar to the formation of herringbone graphitic structure [22,23]. Also, graphitic layers were folded (white arrow), showing two different directions in the fast Fourier transform analysis (inset). Figure 2.7c illustrates a metallic particle of around 15 nm that is surrounded by graphitic material, a structure that is known as “onion-like” [24]. An EDS analysis over the particle depicts that is mainly structured by Co, Cu, and O.

In the case of the B sample, figure 2.7d depicts a low magnification micrograph where curved carbon nanotubes (red arrow), nanoparticles encapsulated (blue arrow), and particle aggregates presumably SiO_2 from the substrate (green arrow) were observed. The CNT shows a bamboo shape structure and depicts a robust bending effect over the walls (figure 2.7e red arrow). With no apparently defective edge structure, the CNT shows considerable changes over the growing directions leading to the formation of helical structures and highly curved carbon nanotubes. Figure 2.7f illustrates a high-magnification TEM image over the CNT wall, where graphitic layers are well ordered with an interlayer distance of 0.36 nm (inset). Also, the CNT shows a very-thin graphitic section (~12 graphitic layers) that structures the bamboo-shape. Figure 2.7g described the TEM micrograph of the type of morphologies found when benzylamine and ethanol are mixed. This sample is structured mainly by highly defective CNT with an irregular bamboo shape structure. Some of the CNT also contains at the tip metallic semi-spherical and elongated nanoparticles. The CNT shows a defective wall structure (figure 2.7h red arrow), and the bamboo shape does not show a periodic growth. Figure 2.7i illustrates a Z-contrast TEM image over a catalytic nanoparticle at the tip of a CNT structure. The elongated nanoparticle reveals that the main body of the nanoparticle contains Co and is surrounded by Co-Cu oxide as the presence of oxygen increases considerably in the EDX analysis.

Figure 2.8 depicts the type of morphologies found after the use of thiophene in B, E, and BE solutions in the S2 position. Figure 2.8a illustrates the Z-contrast TEM image for the type of structures obtained using an ET mixture. The presence of graphitic carbon material highly defected contains metallic nanoparticles attached, and in almost all the cases are encapsulated. Figure 2.8b described an elongated nanoparticle of 47 nm length, where two different crystalline materials are observed in a core-shell configuration. An EDX line analysis of 10 points was applied in order to determine the nature of the two crystalline material. Figure 2.8c describes de EDX results from P1 to P10. This result reveals that the core and the shell of the particle contain a high concentration of Co, Cu, and O.

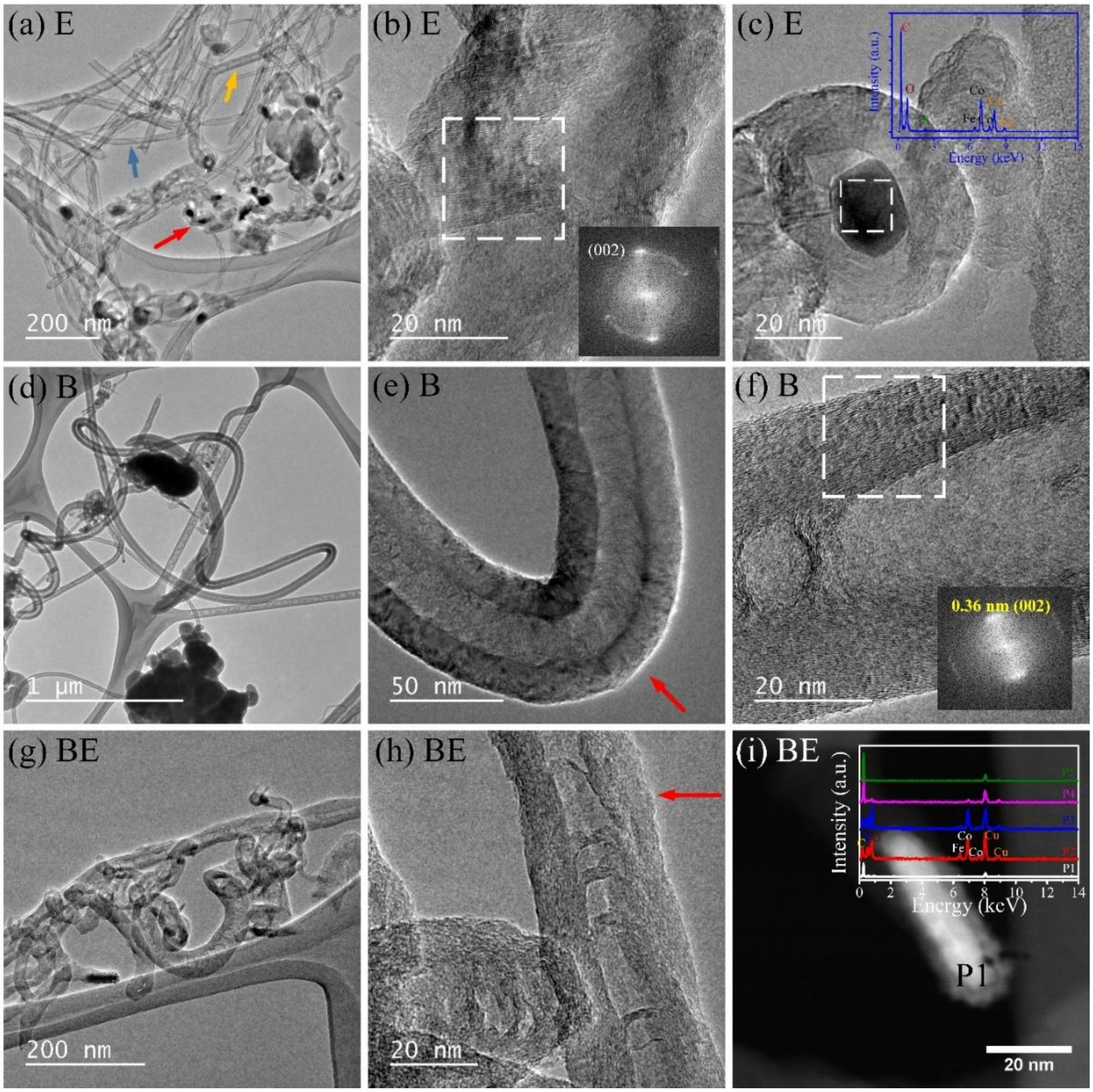

Figure 2.7: TEM micrograph of (a-c) E sample where a variety of morphologies are observed like carbon nanotube with bamboo shape (yellow arrow), carbon nanotube without bamboo shape (blue arrow) and Co-nanoparticle encapsulated (red arrow). (d-f) B sample where curved carbon nanotubes with bamboo shape are observed. (g-i) BE samples where deformed bamboo-shaped carbon nanotubes and Co@CuO were found.

Figure 2.8d shows the type of morphologies obtained in the BT mixture. For this sample, considerably changes over the type of structures are observed compared with the previously reported for the B sample (figure 2.7d-f). Vestiges of CNT formation are observed (yellow arrow). However, the main structure consists of corrugated, sharped, and highly defective graphitic structures (black arrows). Figure 2.8e shows sections of bamboo-like CNT that change morphology along with the structure and graphitic layers folds, leading to loss of the tubular structure. Also, the catalytic particle is encapsulated by corrugated graphitic material (yellow arrow). Figure 2.8f reveals that the wall of this corrugated structure the graphitic layers do not grow parallel in a tubular way; in this case, the graphitic layers stacks and goes transversal to the growth axis leading to high defects formation and sharp edges (red arrow). A similar effect is observed for the BET mixture. Figure 2.8g shows that the incorporation of thiophene to the BE mixture modifies the tubular structure (figure 2.7g-i) and changes entirely to the formation of highly defective carbon nanofibers (CNF) that interlace to create a macroscopic form. It is noticeable how sections of CNF go out of the macroscopic structure. Figure 2.8h depicts a section of a CNF (white square figure 2.8g) where no tubular core is observed, and graphitic sections are wrapped irregularly and randomly, as a consequence, the CNF shows a large number of curved and sharp edges. Figure 2.8i shows the catalytic particle that is responsible for the growth of the previously discussed morphologies. The particle is surrounded by a different type of crystalline material. Though a refinement developed using CrysTBox software [25] that uses the Fast-Fourier Transform to match the obtained information with a reference crystalline matrix, it was possible to determine that the main structure of the particle was structured by Co_3Cu showing the (112) zone axis (inset 1). In contrast, the surrounded material (inset 2) reveals the presence of CuO in the (010) zone axis.

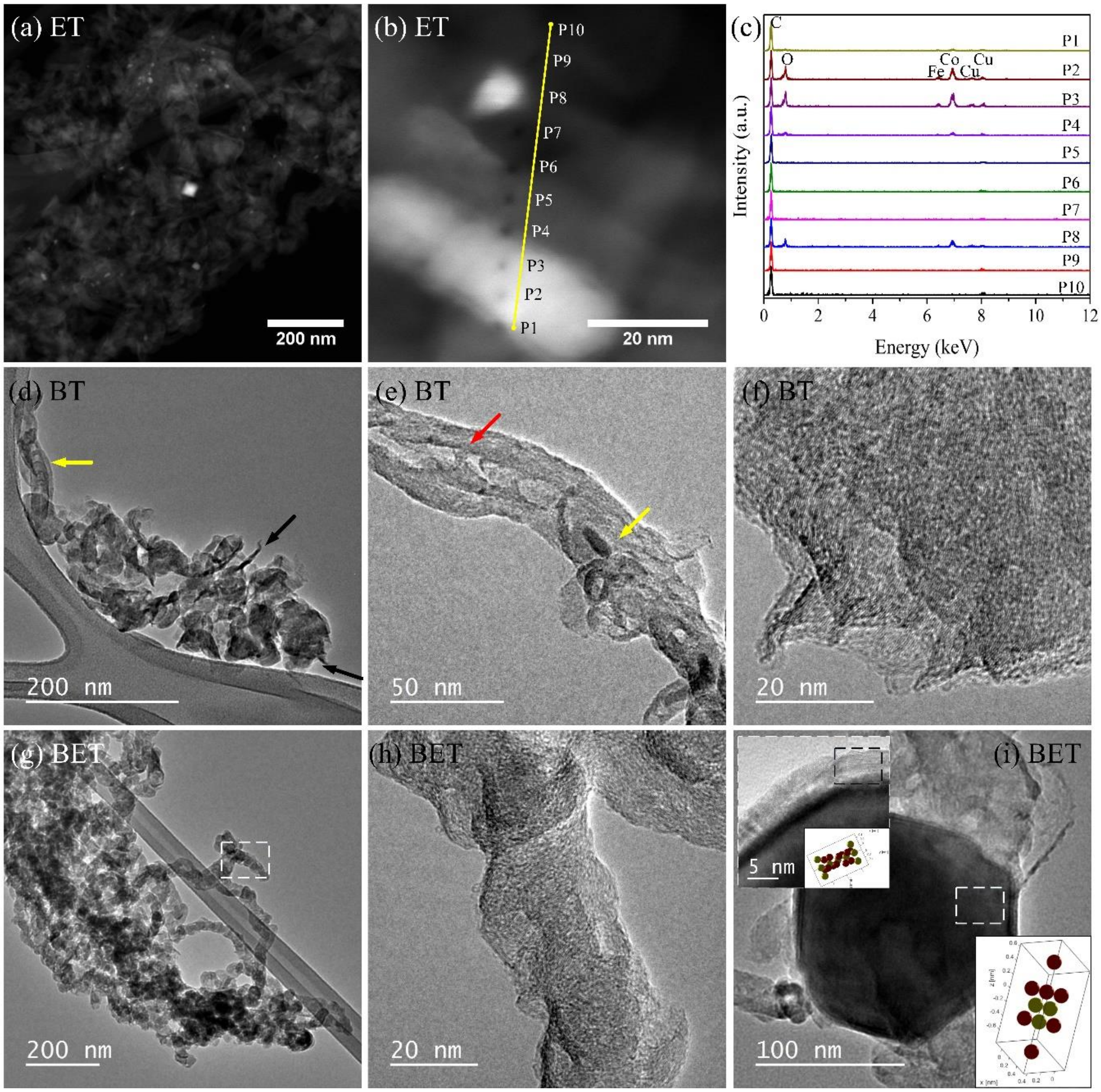

Figure 2.8: Comparative of mixtures after the incorporation of thiophene. ET mixture where: (a) Z-contrast TEM micrograph of graphitic agglomerate where metallic particles are attached and encapsulated. (b) Line EDX analysis over an encapsulated nanoparticle. (c) EDX results from P1 to P10. BT mixture where (d) reveals the presence of highly defective graphitic structure and vestiges of CNT (yellow arrow). (e) the transition from bamboo shape CNT (red arrow) to defective graphitic structure with metallic nanoparticle encapsulated (yellow arrow). (f) Edge formation due to the stacking of graphitic layers. BET mixture reveals (g) interlace corrugated CNF into a macroscopic structure. (h) A section of defective CNF. (i) A catalytic nanoparticle of Co_3Cu (inset 1) surrounded by CuO (inset 2).

To compare the graphitic characteristics of all mixtures, Raman was employed. Raman is highly used to several determinate aspects of the graphitic structure. Information related to the graphitic quality [26], p- and n- doping in the graphitic network [27–30], several graphitic layers [31], and the influence of functionalization and doping into the graphitic structure [32–34]. Figure 2.9a depicts the Raman spectra from B, E, BE, BT, ET, and BET mixtures (in S2 zone). In all cases are noticeable the D band, G band, 2D band, and D+D' band. Also, in the case of the E sample, the presence of Si signals (~510 cm^{-1}) could be related to the Si/SiO$_2$ substrate [35] and the presence of CuO (~650 cm^{-1}) could be related with onion-like Cu-Co metallic particles [36] observed previously on TEM micrographs. The D band is associated with the atom vibration associated with defective graphitic structure due to "breathing modes" (A1g symmetry) observed in sp^2 carbon atoms on hexagonal rings and is commonly positioned at 1350 cm^{-1} for CNT. The G band is associated with the in-plane vibration known as "stretching mode" (E2g symmetry) over the C=C bonds contained in the graphitic network and commonly positioned at 1582 cm^{-1} [37]. The 2D band is a second-order vibration mode that is activated by the resonant vibration due layer numbers [30], and its position is influenced by the surface charge characteristics [28]. The D+D' band is also described as a second-order vibration that its increment is associated with surface roughness due to the formation of wrinkled surface and whisker formation [38,39].

The I_D/I_G ratio is commonly used to determine the degree of defects, as goes above unity [26], while the I_{2D}/I_G ratio is associated with the number of graphitic layers. Figure 2.9b illustrates the variation in the I_D/I_G ratio and the I_{2D}/I_G ratio. It is noticeable how before the use of thiophene, the I_D/I_G ratio for B and BE sample maintains below unity, and for E is lightly above the unity (~1.17). Nevertheless, after the use of thiophene, the I_D/I_G ratio increases considerably, reaching values of 1.69 and 1.72 for ET and BET, respectively. This I_D/I_G behavior is highly linked to the formation of sharp-edged CNF and defective morphologies found in these two samples. Furthermore, the I_{2D}/I_G ratio shows a significant behavior for ET and BET sample, indicating that the number of graphitic layers changes considerably after the incorporation of thiophene. Comparing this information with the described in TEM and SEM characterización, the I_{2D}/I_G ratio for the ET and BET samples can be connected to the low graphitic layers found in edges and folds of the CNT. Thiophene has been widely used to produce unusual carbon nanostructures. Campos Delgado et al. [40] used a mixture of ethanol, ferrocene, and small amounts of thiophene to produce graphitic nanoribbons. The growth of graphene nanoribbons and looped graphene sheets are associated with temperature synthesis. Vallés et al. [41] also described that the use of thiophene during the CVD process promotes the growth of Y intersections in CNT associated with the sulfur content. Also, they described that an increase of sulfur concentration in the gas phase promotes the formation of high defective carbon nanostructure, even in some cases limiting the directional growth of the carbon nanostructure. Following the reported in the literature, sulfur in the form of oligothiophene and thiophene structures can create helical symmetrical and asymmetrical carbon nanostructures due to the incorporation of sulfur atoms at the borders of graphitic structure[42].

More meaningful information can be obtained from the Raman spectra. Figure 2.9c depicts the curve fitting performed over the D and G sections using Lorentz curves. Three more curves can be observed in addition to D (orange) and G (blue) curves. D1 curve (green) is related to the influence of sp^3 carbon hybridization over the C=C vibration modes [43], D2 curve (cyan) can be related to the effect over the C=C due the hydrogenated and –OH functionalities at borders in graphitic structure [34,44]. The D´ is commonly associated with a dispersive vibration mode due to defective structure [45]. Figure 2.9d shows the relative deconvoluted area under the curve for D, D1, D2, G, and D' bands for each sample. It is possible to observe how the area of the D band increases for ET and BET.

Similarly, the D1 band also increases, meaning an increase of defects related to sp^3 C hybridization. In the case of the B and BT sample, the incorporation of thiophene increases the D2 band considerably, possibly attributed to the incorporation of SH and S atoms to the graphitic structure and the degree of defects incorporated to the graphitic structure due to an increase of C-S-C doping or C-S functionalization [46,47]. BET is the sample with higher defects ratio as the D band, and D' band has a higher area.

Figure 2.9e illustrates the deconvolution performed using Lorentz curves over the 2D section. Two more signals beside the 2D (red) and D+D' (blue) peaks were found. The G* is highly associated with surface roughness [38], while de 2D' band is commonly observed over curved and corrugated graphitic structures [39]. For ET and BET samples, there are observed more defined peaks, which could be indicative of higher surface and structures defects due to corrugation, folding, and high roughness. The position of the 2D band compared with the position of the G and D band could give information related to the concentration of electrons on the surface. Das et al. [28] described that the shift of the 2D band to lower values (~2660 cm^{-1}) is related to electron doping while a shift to higher values (~2700 cm^{-1}) corresponds to hole doping. Ferrari et al. [48] depict that a shift to higher values over the G band (~1600 cm^{-1}) is associated with the electron doping while Casiraghi et al. [45] depicts that D band shifts to lower values as dispersion effect of borders increases. Figure 2.9f shows a comparison between the position of D, G with the 2D band. For D band, the samples containing benzylamine have a shift to higher values, which can be linked to an increase of the randomness of the defective structure [49]. For the G band, the BET mixture behaves differently to other mixtures with a shift to higher values (~1584 cm^{-1}) associated with an increase of electrons doping the structure [48]. Similarly, can be appreciated that for B (with nitrogen incorporation) a shift over the 2D band to higher values (~2691 cm^{-1}) indicates a hole doping while for E (with oxygen incorporation) a shift of the 2D band to lower values (~2676 cm^{-1}) is related with electron doping. A work of density functional simulation (DFT) developed by Lopez-Urías et al. [50] over the influence of nitrogen doping and oxygen functionalization at graphitic borders depicts that pyrrolic nitrogen doping promotes a hole doping while quaternary and pyridinic electron doping while mostly all the oxygen functional groups promote an electron doping. In the case of B sample could be mainly associated with the formation of pyrrolic while for E sample with oxygen functional groups. In the case of the BET sample, the shift of the 2D band to lower values indicates an electron doping.

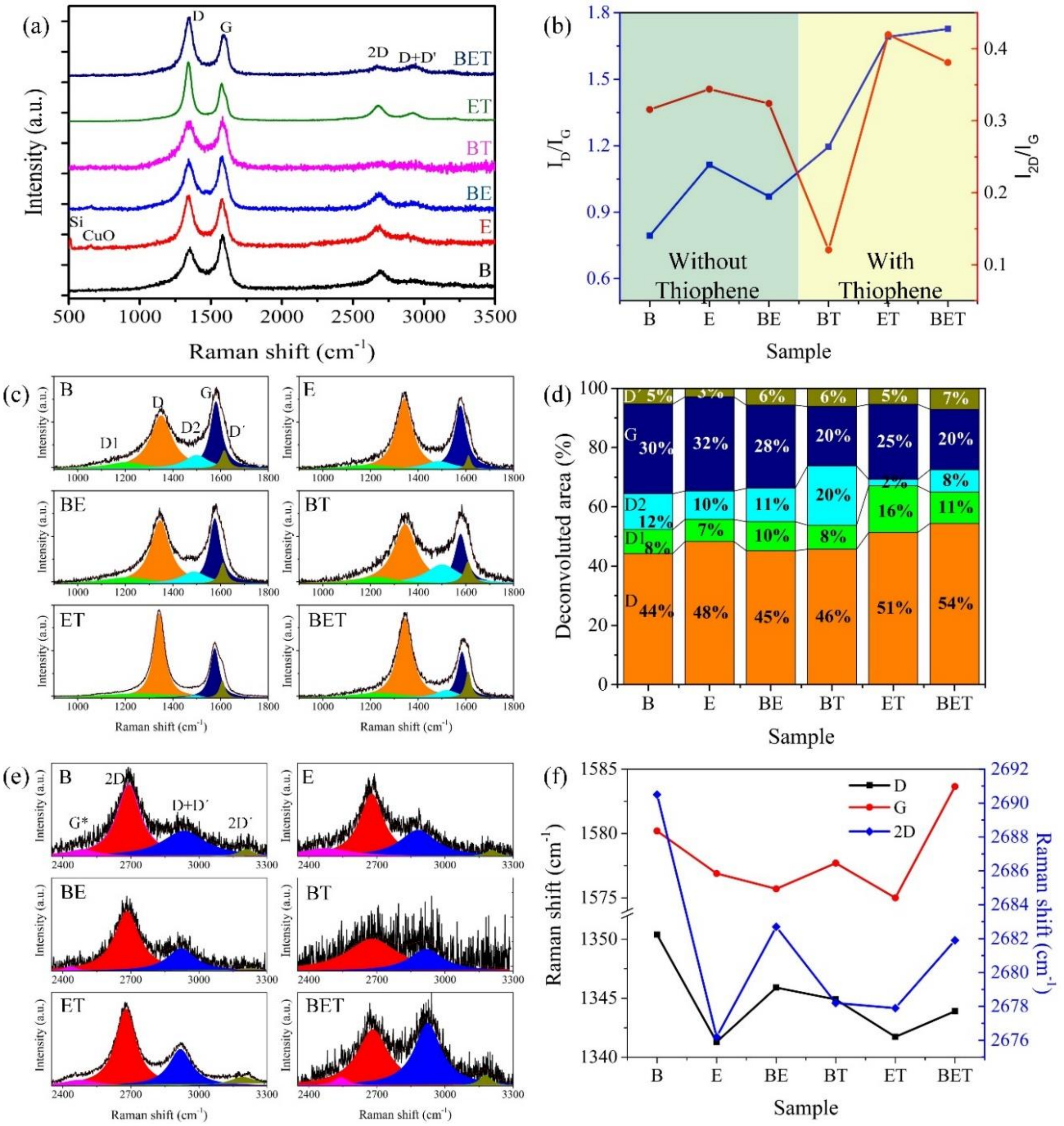

Figure 2.9: (a) Raman spectroscopy comparison for B, E, BE, ET, BT, BET sample. (b) I_D/I_G and I_{2D}/I_G ratio comparison. (c) Lorentz deconvolution over the D and G band section reveals the presence of five peaks: D1, D, D2, G, and D'. (d) Comparison of the relative area obtained in deconvolution for each sample. (e) Lorentz deconvolution over the 2D section reveals the presence of four signals: G*, 2D, D+D´, 2D´ bands.

Figure 2.10 depicts the XRD diffraction patterns for all samples. Figure 2.10a illustrates the section between 2q = 10° to 90°, where it is possible to observe the main signals. In all cases, the presence of the (002) peak is correlated with graphitic carbon. For B and BT samples, clear signals related to SiO_2 are observed. This Si content could be due to a high interaction of SiO_2 with the sample. For all cases, the metallic catalytic particle seems to be structured by Co_{fcc} (COD 9011619, blue line) and Cu_{fcc} (COD 4313211, green line). The interaction between Co_{fcc} and Cu_{fcc} can be presented in the form of a core-shell structure o by crystallographic phase miscibility where Cu or Co atoms can be replaced. Nafria et al. [51] described how, during the growth of Co-Cu nanoparticles and the oxidation-reduction process, the particles change its crystal structure from Cu@Co to Co@Cu in a process where Cu oxidizes. Also, Co covers the structure, and during the CuO reduction, it collapses and diffuses to the center. This behavior can be observed in a light displacement of the peak $2\theta = 45$ °. In our case, the peak position for Cu_{fcc} (111) and Cu_{fcc} (111) ~ $2\theta = 45°$ does not change considerably from its position in each sample. For BE and BET samples, there are also signals associated with the formation of CuO (COD 1011148). In the BET sample, the incorporation of thiophene led to the construction of the Cu_2S structure.

Figure 2.10b shows the deconvolution performed using pseudo-Voight curves over the C (002) peak of graphitic materials [52]. Two signals related to the stacking order of graphitic layers are observed. The π-peak (magenta line) at $2\theta = 26.4$ ° related to a well ordered graphitic structure into A-B-A stacking while the γ-peak (blue line) at $2\theta = 25.8$ related with the turbostratic graphitic structure [53]. For E, the presence of a third signal at $2\theta = 23.7°$could be linked to an expanded graphitic structure due to a deficient oxidation process. Jeong et al. [54] described that after a controlled oxidation process in graphitic networks, diffraction patterns between $2\theta = 15.1°$ and $2\theta = 26.6°$ could be obtained due to high and poor oxidation process.

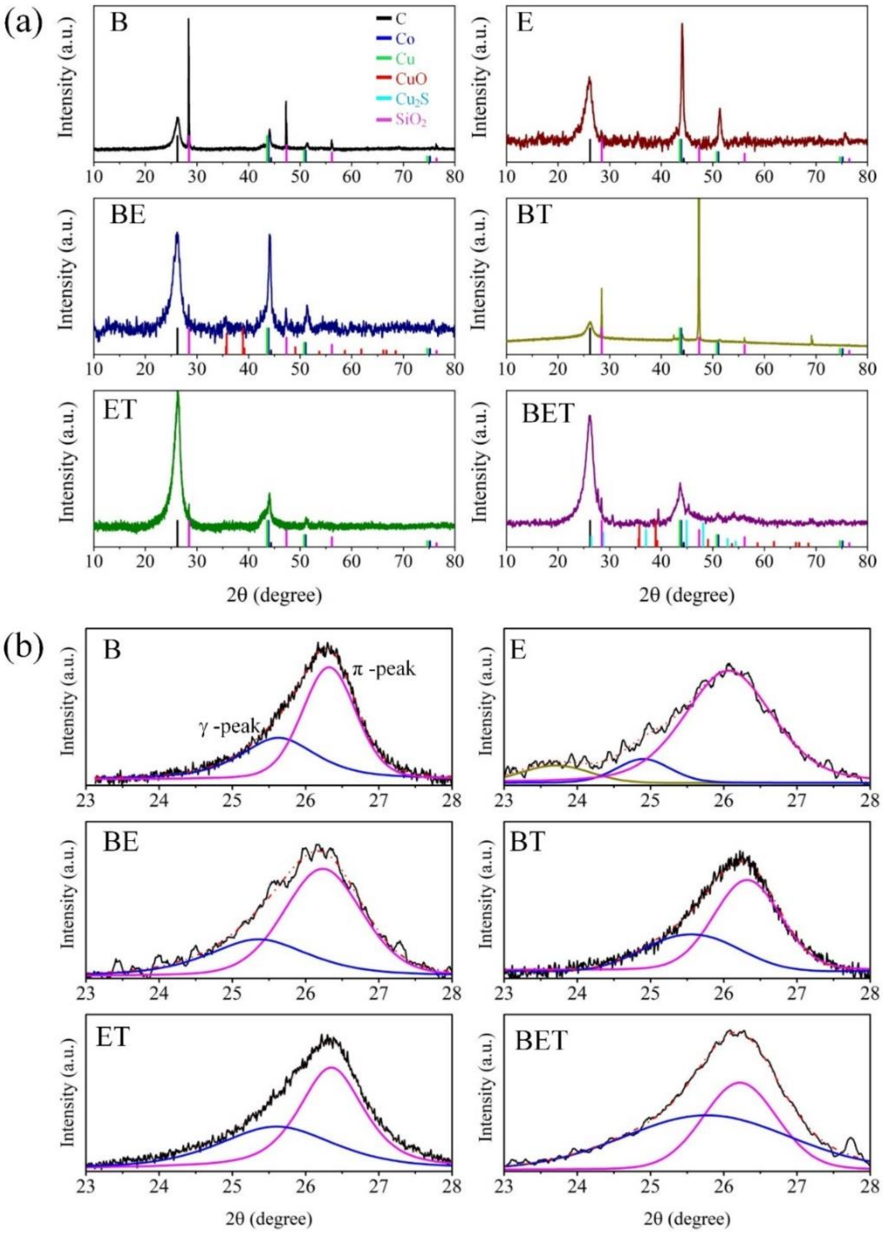

Figure 2.10: (a) XRD diffractograms from 2θ = 10° to 90° where mainly crystallographic phases due to C, Cu, Co, CuO, Cu_2S, and SiO_2 are observed. (b) 2θ = 23° to 28° over the C(002) peak where, through Pseudo-Voight deconvolution, it is possible to differentiate between π-peak (highly-ordered) and γ-peak (turbostratic).

Figure 2.11a illustrates the 2θ position variation of the g-peak and p-peak related for all samples. It is possible to observe that for the π-peak (related to well ordered graphitic structure), there is not a significant variation over the six samples. At the same time, for g-peak (turbostratic graphite), there is a higher variation for E sample that could be correlated to the incorporation of oxygen in the graphitic structure leading to an expansion of the graphitic layers. By the measurement of the area obtained by the deconvolution process can be associated with a relative concentration of a turbostratic and well-ordered graphitic structure (Figure 2.11b). While the BET sample has a higher concentration of turbostratic structure (58%) is associated with an increase of structural defects and the change of tubular structure into sharped and corrugated graphitic fibers. A similar effect can also be appreciated in the ET sample, where the defective structure could be associated with the high value of γ-peak. The lower concentration of turbostratic structure is found in the E sample (10 %) that also shows a third signal related to an expanded graphitic structure, which has a significant contribution of 9%.

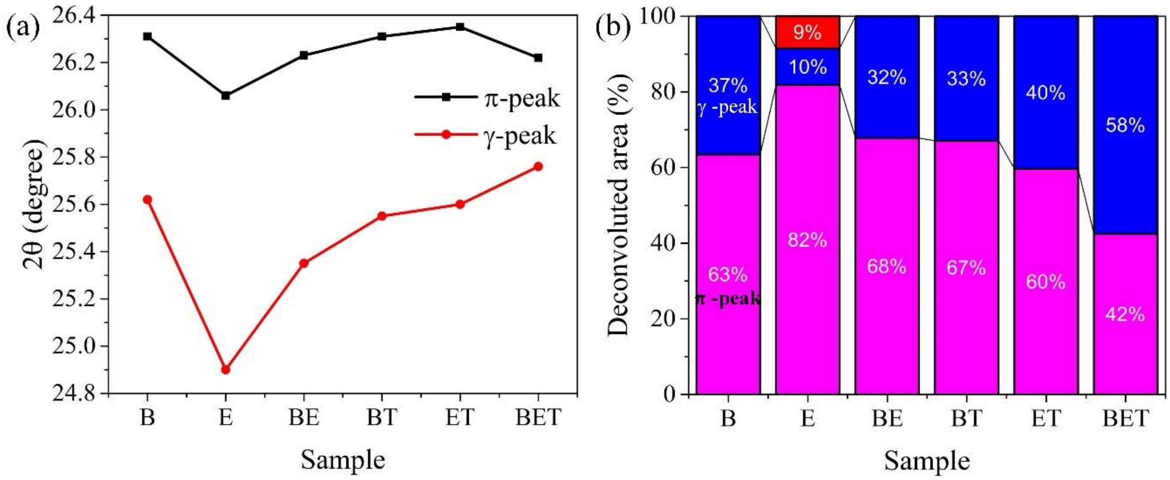

Figure 2.11: (a) 2θ degree variation over the π-peak and γ-peak from the pseudo-Voight deconvolution on C(002) crystal direction through samples. (b) Deconvoluted area of the p-peak, g-peak, and third peak (E sample) observed over the C(002) cristal direction in samples.

2.4 Influence of time in the growth of carbon nanostructures

After all results, the BET sample seems to be very interesting in order to observe significant structural changes at the first 30 min of synthesis. Also, the type of structure found in the

BET sample has a higher degree of defects, and somehow, the corrugated carbon nanofibers tend to intertwine, which probably after long time treatments will promote a three-dimensional carbon structure.

Figure 2.12 depicts the type of carbon nanostructures that grow using the BET solution over the Co-Cu substrate. Figure 2.12a illustrates the type of structures found at 0 min of synthesis. In this case, no trace of graphitic materials and semi-spherical metallic nanoparticles with a diameter of 49.4 nm ± 23 nm and higher value at 158 nm are observed. These nanoparticles are the result of the thermal treatment of the nanostructured thin films of Co and Cu and probably are also structured by a phase mixed with Co atoms and Cu atoms. Nafria et al. [51] describe that during the thermal reduction of $CuO-Co_2O_3$, there is a rearrangement over the crystal structure of nanoparticles depended on the metal concentration the formation of Cu@Co (high Cu concentration) or Co@Cu (high cobalt concentration) is observed without the formation of any allow. In our case, it is probable that the particles where growth in a Co@Cu core-shell structure.

Figure 2.12b shows the carbon nanofibers after 30 min of treatment. This type of morphologies consists of corrugated carbon nanofibers that intertwine to create a macroscopic CNF with wrinkled edges. The size of these carbon nanofibers falls over 469 nm ± 120 nm and above the 10 μm length. Also, a metallic particle can be observed at the tip of one corrugated CNF (red arrow). Figure 2.12c depicts the type of carbon nanostructures found after 120 min of treatment. There is an increase in length, size, and diameter of the wrinkled carbon nanofibers and turns into thick-long wrinkled nanostructured belts (CNB). This CBS shows the dimension of approximately 300 nm thickness, 1.5 μm with and above 15 μm length. Flat particles are observed at the tip of these structures (red arrow).

Figure 2.12d illustrates the type of morphologies found after 4 hours of treatment. In this case, the CBS with similar dimensions but wider (about 2.5 μm) and thicker (about 400 um) are observed. Also, some short wrinkled CNF are identified. An interesting effect is observed over the surface of the CBS, where short and thin tubular carbon nanotubes grew, probably associated with small metallic nanoparticles anchored to the surface of the CBS that catalyzes the short CNT with diameters of 42.0 nm ± 7.2 nm. With the previous information, time synthesis has a high impact on the type of carbon nanostructure obtained. From CNF going by three-dimensional carbon nanostructures and finally, after long time treatments, the formation of a hybrid graphitic structure of CNT over CBS can be observed.

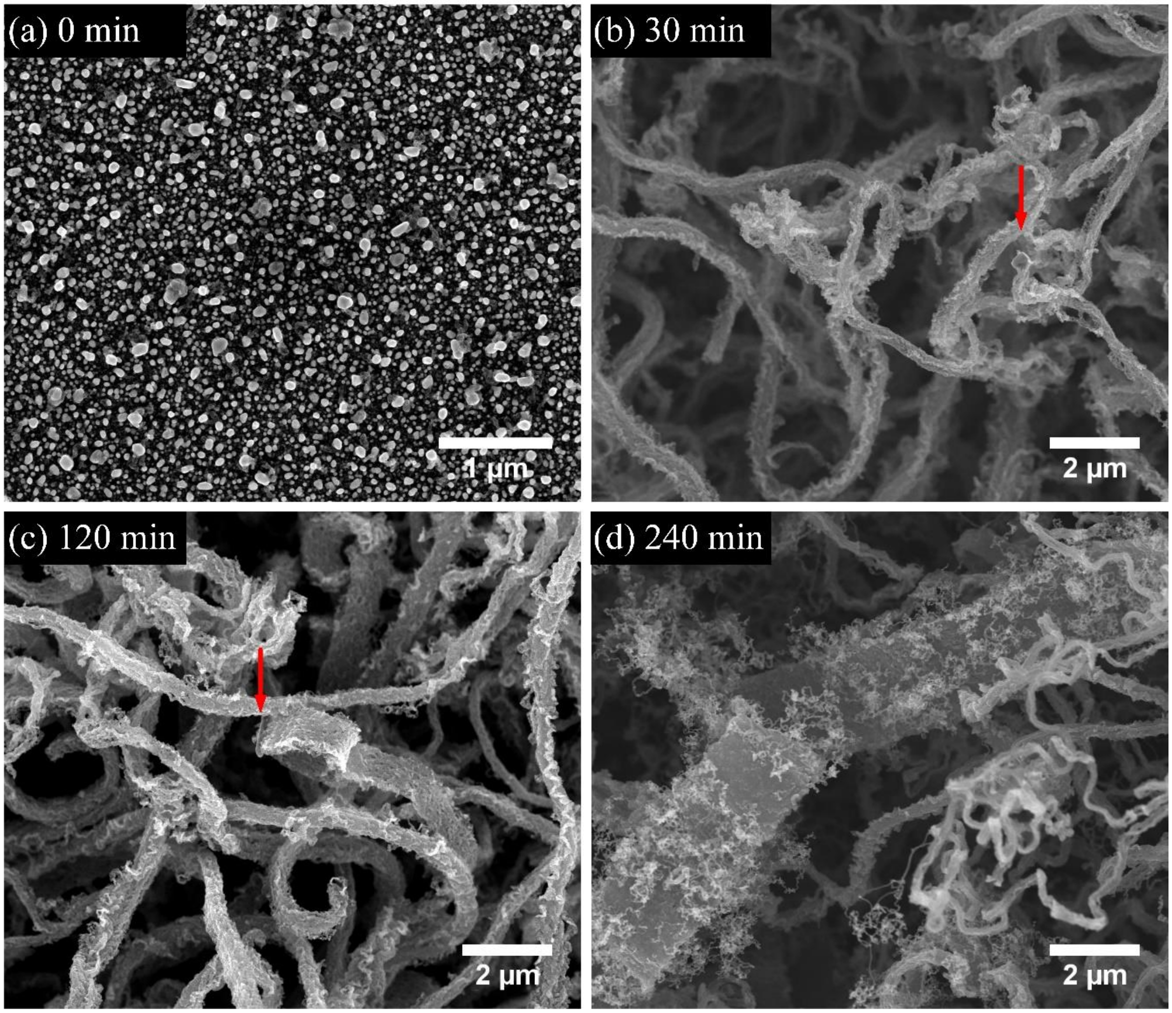

Figure 2.12: Time comparative of the type of structure that grows over the Co-Cu substrate using BET solution at (a) Synthesis at 0 min, where mainly nanoparticles are observed, (b) Synthesis at 30 min where corrugated intertwined nanofibers are observed. (c) Wrinkled carbon belt nanostructures growth at 120 min. (d) Growth of complex CNT-Wrinkled carbon belt structure at 240 min.

In order to compare the variation of their graphitic structure with time, Raman spectroscopy was used. Figure 2.13a shows the normalized Raman D-G region (from 1000 cm^{-1} to 1800 cm^{-1}) for samples at 30 min (blue line), 120 min (green line), and 240 min (red line). No significant differences are observed. However, light variations over the intensity and positions are detected. Figure 2.13b shows the variation over the position of the D and G band. In all cases, the variation over the position is very similar. However, a slight shift to the right was observed for the 120 min. This shift observed previously indicates, in the case of G band, a relatively higher nitrogen doping or electron doping. In contrast, shift to the left could be related to an increase of the sp^2 amorphous carbon [45,48]. For D band, in 120 min sample, displacement of the D band to higher values could be linked to an increase of defects randomness in the CBS. The I_D/I_G ratio indicates that the 30 min sample of the corrugated CNF has a higher defective ratio compared with the formation of the CBS (120 min) and CNT over CNB (240 min). Figure 2.13c illustrates the 2D region (from 2100 cm^{-1} to 3300 cm^{-1}) of the Raman spectra. In all three cases, the 2D section is very similar; however, there are variations over the position of the 2D-band. For 30 min and 240 min, the 2D band is shifted to lower values promoted by hole-doping (figure 2.13c). The shift observed in 120 min sample in accordance with the displacement of the G-band is associated with electron-doping [28]. The I_{2D}/I_G ratio indicates that the 30 min sample had graphitic sections with a lower number of graphene layers, probably correlated with the defective graphitic border sections in the corrugated CNF.

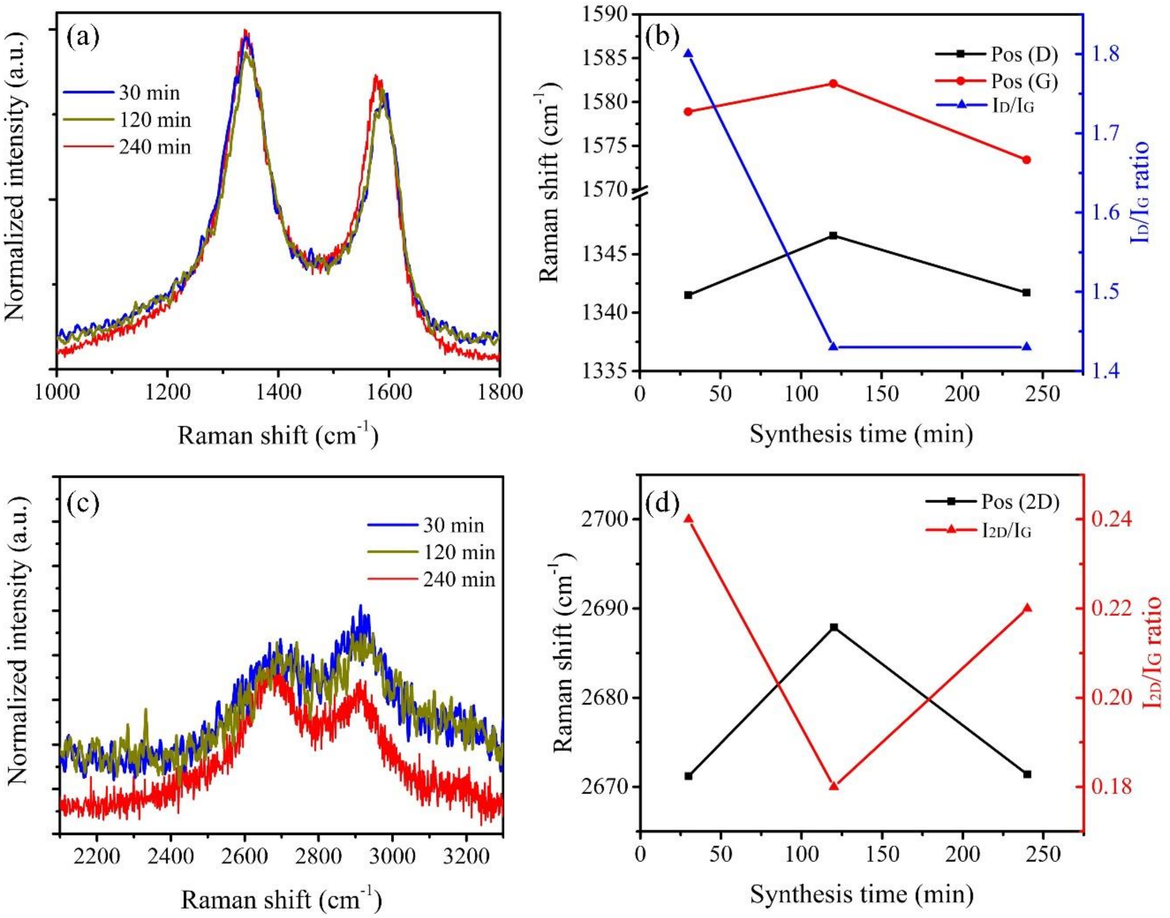

Figure 2.13: (a) D-G region for 30 min (blue line), 120 min (green line), and 240 min (red line) samples. (b) Displacement of the D-band and G-band compared with I_D/I_G ratio. (c) 2D region Raman spectra for three samples. (d) Displacement of 2D-band compared with I_{2D}/I_G ratio.

2.5 Conclusions

Different types of morphologies from CNT, CNF to 3D carbon nanostructure were growth by the use of a Co-Cu thin film as a catalyst in an AACVD system. The mixture of precursors like benzylamine, ethanol, and thiophene promotes the growth of a variety of carbon nanostructures due to the incorporation of oxygen, nitrogen, and sulfur. Corrugated CNT associated with high oxygen concentration, curved CNT related to high nitrogen content, and highly corrugated and defective CNF related to the incorporation of sulfur atoms is observed.

It is also observed how oxygen incorporation through the use of ethanol increases the number of defects. However, the effect of sulfur from thiophene is more aggressive, promotes high I_D/I_G ratios around 1.7 in Raman spectra, and modifies abruptly the types of graphitic structure that grows over Co-Cu films. The use of thiophene and the incorporation of sulfur combined with B and BE solutions change the growth mechanism from a growth-based mechanism to a tip-based mechanism where Co-Cu nanoparticles encourage the formation of wrinkled and corrugated highly defected carbon nanofibers. Also, the use of different precursors leads to electronic modification on the graphitic surface. The use of B promotes a hole doping, probably associated with nitrogen incorporation, the use of E promotes an electron doping associated with oxygen functional structures in graphitic network and BET mixture relays over the hole doping.

Interaction of sulfur and oxygen with Co and Cu leads to the formation of Cu_xO and CuS in a core-shell structure with Co following Co@Cu_xO-CuS, which works as a catalyst for the wrinkled and corrugated carbon nanofibers using the BET solution over 30 min of synthesis. However, after 240 min of synthesis time, these wrinkled carbon nanofiber grows to create a 3D graphitic carbon nanostructure. This methodology could lead to the growth of a new type of graphitic morphologies over thin-film substrates.

Contrary to expectations, the use of multiple precursors in manufacturing allows the growth of well-defined graphitic structures that can be obtained in one step CVD system procedure. Despite all the possible variables associated with the experiment like temperature variation, bimetallic catalyst and mixture of precursors, each of them plays a crucial role to synthesize a variety of morphologies with a high degree of functionalization, doped with nitrogen or with a high degree of defects that can be used in various applications. In nanoscience the specific interaction and nucleation of nanoparticles (Co and Cu) combined with an specific interaction with pyrolized productions from precursors allow us to have complex but well stablished morphologies.

2.6 References

[1] A. Bianco, Y. Chen, Y. Chen, D. Ghoshal, R.H. Hurt, Y.A. Kim, N. Koratkar, V. Meunier, M. Terrones, A carbon science perspective in 2018: Current achievements

and future challenges, Carbon. 132 (2018) 785–801. https://doi.org/10.1016/j.carbon.2018.02.058.

[2] A. Bianco, Y. Chen, E. Frackowiak, M. Holzinger, N. Koratkar, V. Meunier, S. Mikhailovsky, M. Strano, J.M.D. Tascon, M. Terrones, Carbon science perspective in 2020: Current research and future challenges, Carbon. 161 (2020) 373–391. https://doi.org/10.1016/j.carbon.2020.01.055.

[3] M. Baro, S. Ramaprabhu, Multi-edged wrinkled graphene-like carbon-wrapped carbon nanotubes and highly conductive Pt-free counter electrode for dye-sensitized solar cells, Journal of Nanoparticle Research. 16 (2014). https://doi.org/10.1007/s11051-014-2711-9.

[4] L. Zhang, F. Zhang, X. Yang, G. Long, Y. Wu, T. Zhang, K. Leng, Y. Huang, Y. Ma, A. Yu, Y. Chen, Porous 3D graphene-based bulk materials with exceptional high surface area and excellent conductivity for supercapacitors, Sci Rep. 3 (2013) 1408. https://doi.org/10.1038/srep01408.

[5] Y. Li, Y. Liu, M. Wang, X. Xu, T. Lu, C.Q. Sun, L. Pan, Phosphorus-doped 3D carbon nanofiber aerogels derived from bacterial-cellulose for highly-efficient capacitive deionization, Carbon. 130 (2018) 377–383. https://doi.org/10.1016/j.carbon.2018.01.035.

[6] C. Pham-Huu, N. Keller, V. V. Roddatis, G. Mestl, R. Schlögl, M.J. Ledoux, Large scale synthesis of carbon nanofibers by catalytic decomposition of ethane on nickel nanoclusters decorating carbon nanotubes, Physical Chemistry Chemical Physics. 4 (2002) 514–521. https://doi.org/10.1039/b106512m.

[7] Z. Lin, Z. Zeng, X. Gui, Z. Tang, M. Zou, A. Cao, Carbon Nanotube Sponges, Aerogels, and Hierarchical Composites: Synthesis, Properties, and Energy Applications, Advanced Energy Materials. 6 (2016). https://doi.org/10.1002/aenm.201600554.

[8] X. Xie, K. Kretschmer, J. Zhang, B. Sun, D. Su, G. Wang, Sn@CNT nanopillars grown perpendicularly on carbon paper: A novel free-standing anode for sodium ion batteries, Nano Energy. 13 (2015) 208–217. https://doi.org/10.1016/j.nanoen.2015.02.022.

[9] Y. Li, W. Liao, Z. Li, T. Feng, L. Sun, C. Guo, J. Zhang, J. Li, Building three-dimensional porous nano-network for the improvement of iron and nitrogen-doped carbon oxygen reduction electrocatalyst, Carbon. 125 (2017) 640–648. https://doi.org/10.1016/j.carbon.2017.09.106.

[10] X. Gui, J. Wei, K. Wang, A. Cao, H. Zhu, Y. Jia, Q. Shu, D. Wu, Carbon nanotube sponges, Advanced Materials. 22 (2010) 617–621. https://doi.org/10.1002/adma.200902986.

[11] J.C. Li, P.X. Hou, S.Y. Zhao, C. Liu, D.M. Tang, M. Cheng, F. Zhang, H.M. Cheng, A 3D bi-functional porous N-doped carbon microtube sponge electrocatalyst for oxygen reduction and oxygen evolution reactions, Energy and Environmental Science. 9 (2016) 3079–3084. https://doi.org/10.1039/c6ee02169g.

[12] C. Shan, W. Zhao, X.L. Lu, D.J. O'Brien, Y. Li, Z. Cao, A.L. Elias, R. Cruz-Silva, M. Terrones, B. Wei, J. Suhr, Three-dimensional nitrogen-doped multiwall carbon nanotube sponges with tunable properties, Nano Letters. 13 (2013) 5514–5520. https://doi.org/10.1021/nl403109g.

[13] A. Gohier, C.P. Ewels, T.M. Minea, M.A. Djouadi, S. Huang, M. Woodson, R. Smalley, J. Liu, J. Dijon, P.D. Szkutnik, A. Fournier, T. Goislard De Monsabert, H. Okuno, E. Quesnel, V. Muffato, E. De Vito, N. Bendiab, A. Bogner, N. Bernier, I.K. Song, Y.S. Cho, G.S. Choi, J.B. Park, D.J. Kim, P. Ayala, R. Arenal, M. Rümmeli, A. Rubio, T. Pichler, E. Gracia-espino, B. Rebollo-plata, H. Martínez-gutiérrez, E. Muñoz-sandoval, F. López-urías, M. Endo, H. Terrones, M. Terrones, L. Huang, B. White, M.Y. Sfeir, M. Huang, H.X. Huang, S. Wind, J. Hone, S. O'Brien, S. Li, H. Li, X. Wang, Y. Song, Y. Liu, L. Jiang, D. Zhu, R. Lv, M. Terrones, J. Zhang, M. Terrones, C.R. Park, R. Mukherjee, M. Monthioux, N. Koratkar, Y.S. Kim, R. Hurt, E. Frackowiak, T. Enoki, Y.Y. Chen, Y.Y. Chen, A. Bianco, How to switch from a tip to base growth mechanism in carbon nanotube growth by catalytic chemical vapour deposition, Carbon. 48 (2004) 1210–1213. https://doi.org/10.1021/nl049691d.

[14] E. Muñoz-Sandoval, A.J. Cortes-López, B. Flores-Gómez, J.L. Fajardo-Díaz, R. Sánchez-Salas, F. López-Urías, Carbon sponge-type nanostructures based on coaxial nitrogen-doped multiwalled carbon nanotubes grown by CVD using benzylamine as precursor, Carbon. 115 (2017). https://doi.org/10.1016/j.carbon.2017.01.010.

[15] X. Qi, C. Qin, W. Zhong, C. Au, X. Ye, Y. Du, Large-scale synthesis of carbon nanomaterials by catalytic chemical vapor deposition: A review of the effects of synthesis parameters and magnetic properties, Materials. 3 (2010) 4142–4174. https://doi.org/10.3390/ma3084142.

[16] A. Chambers, N.M. Rodriguez, R.T.K. Baker, Modification of the Catalytic Behavior of Cobalt by the Addition of Copper, Society. (1995) 10581–10589.

[17] L. Guevara, C. Wanner, R. Welsh, M.A. Atwater, Using Mechanical Alloying to Create Bimetallic Catalysts for Vapor-Phase Carbon Nanofiber Synthesis, Fibers2. 3 (2015) 394–410. https://doi.org/10.3390/fib3040394.

[18] O.C. Carneiro, N.M. Rodriguez, R.T.K. Baker, Growth of carbon nanofibers from the iron-copper catalyzed decomposition of CO/C2H4/H2 mixtures, Carbon. 43 (2005) 2389–2396. https://doi.org/10.1016/j.carbon.2005.04.022.

[19] E. Munoz-Sandoval, N. Perea-Lopez, R. Lima-Juarez, G.J. Labrada-Delgado, B.A. Rivera-Escoto, A. Zamudio, H.G. Silva-Pereyra, E. Robles-Avila, M. Terrones, Synthesis, characterization and magnetic properties of Co@Au core-shell nanoparticles encapsulated by nitrogen-doped multiwall carbon nanotubes, Carbon. 77 (2014) 722–737. https://doi.org/10.1016/j.carbon.2014.05.077.

[20] B.W. Mwakikunga, Progress in ultrasonic spray pyrolysis for condensed matter sciences developed from ultrasonic nebulization theories since michael faraday, Critical Reviews in Solid State and Materials Sciences. 39 (2014) 46–80. https://doi.org/10.1080/10408436.2012.687359.

[21] B.G. Sumpter, V. Meunier, J.M. Romo-Herrera, E. Cruz-Silva, D.A. Cullen, H. Terrones, D.J. Smith, M. Terrones, Nitrogen-mediated carbon nanotube growth: Diameter reduction, metallicity, bundle dispersability, and bamboo-like structure formation, ACS Nano. 1 (2007) 369–375. https://doi.org/10.1021/nn700143q.

[22] V. V. Shinkarev, A.M. Glushenkov, D.G. Kuvshinov, G.G. Kuvshinov, Nanofibrous carbon with herringbone structure as an effective catalyst of the H2S selective oxidation, Carbon. 48 (2010) 2004–2012. https://doi.org/10.1016/j.carbon.2010.02.008.

[23] N.M. Rodriguez, A. Chambers, R.T.K. Baker, Catalytic Engineering of Carbon Nanostructures, Langmuir. 11 (1995) 3862–3866. https://doi.org/10.1021/la00010a042.

[24] K. Bogdanov, A. Fedorov, V. Osipov, T. Enoki, K. Takai, T. Hayashi, V. Ermakov, S. Moshkalev, A. Baranov, Annealing-induced structural changes of carbon onions: High-resolution transmission electron microscopy and Raman studies, Carbon. 73 (2014) 78–86. https://doi.org/10.1016/j.carbon.2014.02.041.

[25] M. Klinger, A. Jäger, Crystallographic Tool Box (CrysTBox): Automated tools for transmission electron microscopists and crystallographers, Journal of Applied Crystallography. 48 (2015) 2012–2018. https://doi.org/10.1107/S1600576715017252.

[26] M.S. Dresselhaus, G. Dresselhaus, R. Saito, A. Jorio, Raman spectroscopy of carbon nanotubes, Physics Reports. 409 (2005) 47–99. https://doi.org/10.1016/j.physrep.2004.10.006.

[27] A. Das, A.K. Sood, A. Govindaraj, A.M. Saitta, M. Lazzeri, F. Mauri, C.N.R. Rao, Doping in Carbon Nanotubes Probed by Raman and Transport Measurements, 136803 (2007) 1–4. https://doi.org/10.1103/PhysRevLett.99.136803.

[28] A. Das, S. Pisana, B. Chakraborty, S. Piscanec, S.K. Saha, U. V Waghmare, K.S. Novoselov, H.R. Krishnamurthy, A.K. Geim, A.C. Ferrari, A.K. Sood, Monitoring dopants by Raman scattering in an electrochemically top-gated graphene transistor, 3 (2008) 1–6. https://doi.org/10.1038/nnano.2008.67.

[29] M. Kalbac, A. Reina-Cecco, H. Farhat, J. Kong, L. Kavan, M.S. Dresselhaus, The influence of strong electron and hole doping on the Raman intensity of chemical vapor-deposition graphene, ACS Nano. 4 (2010) 6055–6063. https://doi.org/10.1021/nn1010914.

[30] A.C. Ferrari, D.M. Basko, Raman spectroscopy as a versatile tool for studying the properties of graphene, Nat Nanotechnol. (2013) 1–13. https://doi.org/10.1038/nnano.2013.46.

[31] M.S. Dresselhaus, A. Jorio, M. Hofmann, G. Dresselhaus, R. Saito, Perspectives on carbon nanotubes and graphene Raman spectroscopy, Nano Letters. 10 (2010) 751–758. https://doi.org/10.1021/nl904286r.

[32] L. Zuccaro, K. Kern, K. Balasubramanian, Identifying chemical functionalization on individual carbon nanotubes and graphene by local vibrational fingerprinting, ACS

Nano. 9 (2015) 3314–3323. https://doi.org/10.1021/acsnano.5b00479.

[33] K. Kudin, B. Ozbas, H.C. Schniepp, R.K. Prud'homme, I.A. Aksay, R. Car, Raman Spectra of Graphite Oxide and Functionalized Graphene Sheets, Nano Lett. 8 (2008) 36.

[34] P. Vecera, J.C. Chacón-Torres, T. Pichler, S. Reich, H.R. Soni, A. Görling, K. Edelthalhammer, H. Peterlik, F. Hauke, A. Hirsch, Precise determination of graphene functionalization by in situ Raman spectroscopy, Nature Communications. 8 (2017). https://doi.org/10.1038/ncomms15192.

[35] F. Shariatmadar Tehrani, Transformation from amorphous to nano-crystalline SiC thin films prepared by HWCVD technique without hydrogen dilution, Bulletin of Materials Science. 38 (2015) 1333–1338.

[36] Y. Deng, A.D. Handoko, Y. Du, S. Xi, B.S. Yeo, In Situ Raman Spectroscopy of Copper and Copper Oxide Surfaces during Electrochemical Oxygen Evolution Reaction: Identification of CuIII Oxides as Catalytically Active Species, ACS Catalysis. 6 (2016) 2473–2481. https://doi.org/10.1021/acscatal.6b00205.

[37] C. Domingo, G. Santoro, Raman spectroscopy of carbon nanotubes, Optica Pura y Aplicada. 1136 (2005) 175–186. https://doi.org/10.1016/j.physrep.2004.10.006.

[38] J. Bin Wu, M.L. Lin, X. Cong, H.N. Liu, P.H. Tan, Raman spectroscopy of graphene-based materials and its applications in related devices, Chemical Society Reviews. 47 (2018) 1822–1873. https://doi.org/10.1039/c6cs00915h.

[39] P. Tan, S. Dimovski, Y. Gogotsi, Raman scattering of non-planar graphite : arched edges , polyhedral crystals , whiskers and cones, Phil. Trans. R. Soc. Lond. A. 362 (2004) 2289–2310.

[40] J. Campos-Delgado, Y.A. Kim, T. Hayashi, A. Morelos-Gómez, M. Hofmann, H. Muramatsu, M. Endo, H. Terrones, R.D. Shull, M.S. Dresselhaus, M. Terrones, Thermal stability studies of CVD-grown graphene nanoribbons: Defect annealing and loop formation, Chemical Physics Letters. 469 (2009) 177–182. https://doi.org/10.1016/j.cplett.2008.12.082.

[41] C. Vallés, M. Pérez-Mendoza, P. Castell, M.T. Martínez, W.K. Maser, A.M. Benito, Towards helical and Y-shaped carbon nanotubes: The role of sulfur in CVD processes, Nanotechnology. 17 (2006) 4292–4299. https://doi.org/10.1088/0957-4484/17/17/002.

[42] M. Miyasaka, A. Rajca, M. Pink, S. Rajca, Cross-conjugated oligothiophenes derived from the (C2S) n helix: Asymmetric synthesis and structure of carbon-sulfur [11]helicene, Journal of the American Chemical Society. 127 (2005) 13806–13807. https://doi.org/10.1021/ja055414c.

[43] M.I. Ionescu, Y. Zhang, R. Li, H. Abou-Rachid, X. Sun, Nitrogen-doping effects on the growth, structure and electrical performance of carbon nanotubes obtained by spray pyrolysis method, Applied Surface Science. 258 (2012) 4563–4568. https://doi.org/10.1016/j.apsusc.2012.01.028.

[44] A. Kaniyoor, S. Ramaprabhu, A Raman spectroscopic investigation of graphite oxide derived graphene A Raman spectroscopic investigation of graphite oxide derived graphene, 032183 (2014) 0–13. https://doi.org/10.1063/1.4756995.

[45] C. Casiraghi, A. Hartschuh, H. Qian, S. Pliscanec, C. Georgia, A. Fasoli, K.S. Novoselov, D.M. Basko, A.C. Ferrari, Raman spectroscopy of graphene edges, Nano Letters. 9 (2009) 1433–1441. https://doi.org/10.1021/nl8032697.

[46] J. Mao, Y. Wang, J. Zhu, J. Yu, Z. Hu, Thiol functionalized carbon nanotubes: Synthesis by sulfur chemistry and their multi-purpose applications, Applied Surface Science. 447 (2018) 235–243. https://doi.org/10.1016/j.apsusc.2018.03.188.

[47] F. Hassani, H. Tavakol, Synthesis of sulfur-doped carbon nanotubes from sulfur powder using chemical vapor deposition, Fullerenes Nanotubes and Carbon Nanostructures. 26 (2018) 479–486. https://doi.org/10.1080/1536383X.2018.1448793.

[48] A.C. Ferrari, Raman spectroscopy of graphene and graphite: Disorder, electron-phonon coupling, doping and nonadiabatic effects, Solid State Communications. 143 (2007) 47–57. https://doi.org/10.1016/j.ssc.2007.03.052.

[49] A.K. Gupta, T.J. Russin, H.R. Gutiérrez, P.C. Eklund, Probing Graphene Edges via Raman scattering, ACS Nano. 3 (2009) 45–52.

[50] F. López-Urías, J.L. Fajardo-Díaz, A.J. Cortés-López, C.L. Rodríguez-Corvera, L.E. Jiménez-Ramírez, E. Muñoz-Sandoval, Understanding the electrochemistry of armchair graphene nanoribbons containing nitrogen and oxygen functional groups: DFT calculations, Physical Chemistry Chemical Physics. 22 (2020) 4533–4543. https://doi.org/10.1039/c9cp05857e.

[51] R. Nafria, A. Genç, M. Ibáñez, J. Arbiol, P. Ramírez de la Piscina, N. Homs, A. Cabot, Co–Cu Nanoparticles: Synthesis by Galvanic Replacement and Phase Rearrangement during Catalytic Activation, Langmuir. (2016) acs.langmuir.5b04622. https://doi.org/10.1021/acs.langmuir.5b04622.

[52] D.K. Singh, P.K. Iyer, P.K. Giri, Diameter dependence of interwall separation and strain in multiwalled carbon nanotubes probed by X-ray diffraction and Raman scattering studies, Diamond and Related Materials. 19 (2010) 1281–1288. https://doi.org/10.1016/j.diamond.2010.06.003.

[53] A.J. Cortés-López, E. Muñoz-Sandoval, F. López-Urías, Efficient carbon nanotube sponges production boosted by acetone in CVD-Synthesis, Carbon. 135 (2018) 145–156. https://doi.org/10.1016/j.carbon.2018.04.046.

[54] H.K. Jeong, M.H. Jin, K.P. So, S.C. Lim, Y.H. Lee, Tailoring the characteristics of graphite oxides by different oxidation times, Journal of Physics D: Applied Physics. 42 (2009). https://doi.org/10.1088/0022-3727/42/6/065418.

CHAPTER THREE:

GROWTH OF N-DOPED WRINKLED CARBON NANOBELT (N-CBS) AS 3D CARBON NANOSTRUCTURES

3.1 Introduction

The creation of new 2D carbon allotropes [1,2], or 3D macroscopic architectures [3,4] is changing the perspective of carbon nanomaterials research. Instead of investigating individual or groups of carbon nanomaterials, now the hybrid or complex 2D or 3D structures are the focus of many research groups. Carbon nanotube networks [5], wrinkled graphene sheets [6], nanofibers [7] serve as building blocks for such exotic new 3D carbon nanomaterials. Supercapacitors, superhydrophobic, exceptional electrodes for lithium batteries, and other breakthrough applications have derived from such complex constructions [8–10]. The possibility of building arrangements, such as multiwalled carbon nanotubes (MWCNTs) networks, graphene-MWCNT hybrids, MWCNT sponges by different methods like CVD synthesis, template method, CNT suspension or hydrothermal reduction is a frequent topic of several theoretical and experimental investigations [11–16].

Numerous techniques have been used to create such nanomaterials [3]. For example, nano-building blocks of single-walled carbon nanotubes (SWCNTs) and MWCNTs were used as a construction unity to create macrostructures in a sol-gel solution [17,18]. 3D carbon nanostructures were fabricated using an inorganic or polymeric matrix as a template [19,20]. It has been demonstrated that the structure and physical-chemical properties of such carbon nanomaterials depend preeminently on the synthesis conditions, precursors, and catalyst [21–23]. However, the use of bimetallic catalysts to grow 3D carbon architectures is far to be understood [24]. Chambers et al. [25] reported a multi-growth arrangement of carbon nanotubes on specific crystallographic planes of cobalt nanoparticles as a consequence of adding copper during the synthesis. Other mixtures such as Ag-Co, Fe-Co, and Ni-Cu catalysts favored carbon nanostructures with unusual morphologies [26,27]. Doping is another important issue to be considered to produce carbon 3D frameworks. The presence of large amounts of sp^3 hybridization, can be obtained by different dopants such as oxygen [28,29], boron [30,31], phosphorous [32,33], nitrogen [34] and sulfur [35,36]. In general, sulfur acts as an anchoring point for the incorporation of other species producing the formation of branches or the formation of negative curvatures over carbon nanotubes. Sulfur also promotes changes in the electrical properties of the complicated 3D MWCNTs frameworks [20,35–38]. Interesting is that carbon morphologies like wrinkled graphene and wrinkled N-CNTs can be used to fabricate complex 3D architectures without the participation of foreign atoms [39]. Chen et al. [40] modified the structure of graphene layers by mechanical processes, achieving the formation of wrinkled graphene with super-hydrophobicity properties. In the present investigation, assembled wrinkled carbon fibers forming belts were produced using aerosol-assisted chemical vapor deposition (AACVD)-based template synthesis.

In this chapter, based on different characterization techniques, we provide evidence related to the formation of wrinkled nitrogen-doped carbon nanobelt structure (N-CBS) as a 3D-carbon nanostructure by the use of a Co-Cu thin film deposition as a catalyst. We also provide a schematic description associated with the growth mechanism, the influence of time in size-growth of Co-Cu nanoparticles, and the variation of morphology attributed to a change of Cu for Au and Ag. Also, to recreate the N-CBS, a growth mechanism was developed by the use of Co-Cu thin-films, a comparative description linked to the use of a Co-Cu granular mixture was included.

3.2 Methodology

A 20 nm - 2 nm cobalt-copper thin films were prepared following the methodology described in chapter 2 by a plasma deposition in an Intercovamex V3 sputtering system and by the described by Muñoz-Sandoval et al. [41]. Co-Cu substrates of around 1cm x 1cm are introduced to a quartz tube of 1.1 m length and one inch of internal diameter. The system is connected following the schema described in chapter 2, figure 2.2a. The furnace temperature near to the sprayer was set at 750 °C (Furnace 1), and the temperature of the subsequent oven (Furnace 2) was set at 850 °C. A flow of 2.5 l/min of an H_2-Ar (5%-95%) works as a carrier gas.

To determinate the influence of a reduction process into the nucleation of the Co-Cu nanoparticles, substrates were taken to the temperature described above and maintained over 0 min, 4 min, 8 min, and 12 min without turning on the sprayer then were cooled for its analysis. For the N-CBS growth, the reduction time was set at 4 min, the sprayer is then turn on, and the synthesis is carried by two hours. An important aspect to consider is that all samples described in this chapter correspond to the sample positioned between both furnaces at a temperature of 800 °C.

The samples were characterized by scanning electron microscopy (SEM) and backscattered electrons scanning electron microscopy (BSE-SEM) using a Helios Nanolab 600 Dual Beam (FIB/SEM) and a Quanta 250 (eSEM). High-resolution transmission electron microscopy (HRTEM), Z-contrast and energy dispersive X-ray spectroscopy (EDX) images were acquired using a TEM JEOL 200CX (200 keV), microscope. X-ray diffraction patterns were gotten by an RX Advance equipment with a copper tube and λ = 1.54 Å. The Raman spectroscopy studies were performed by a Renishaw Micro-Raman equipment with a 532 cm^{-1} laser wavelength, and the X-ray photoelectrons spectroscopy (XPS) PHI 5000 Versaprobe II equipment with an Al-Ka (1486.7 eV) source was employed to get the concentration of C, N, O, Co, Cu and S at 23.9 eV of pass energy. The magnetic properties were measure using a physical property measurement system (PPMS) with a Dynacool Quantum Design at 300 K. For the electrochemical properties, a Calomel electrode in a KCl saturated solution was used as a reference electrode. The N-CBS were pulverized using a silica ball mill over 5 min and mixed in a 10 % w/w solution with Nafion ® (10% w/w on ethanol - Sigma), the suspension was deposited over a 2.2 mm diameter graphite electrode to be used as work electrode. The cyclic voltammetry was developed using a KCl 0.5 M solution as an electrolyte, with a potential window from -1.5 V to 1.7 V at a scan rate of 100 mV/s.

3.3 Reduction time effect over the size of the catalytic particle

Figure 3.1 illustrates the nanoparticle nucleation of the Co-Cu thin film after a thermal reduction process during a pre-treatment before the growth of the N-CBS. Four different reduction times of 0 min, 4 min, 8 min, and 12 min were tested in order to observe the changes in the size and shape of the Co-Cu nanoparticles. Figure 3.1a depicts the effect of submitting the Co-Cu thin films at a reduction time of 0 min. From the first moment, it is observed the formation of semi-spherical Co-Cu nanoparticles and the nucleation of graphitic material from the Co-Cu nanoparticles (yellow arrow). The nanoparticles observed had a size between 50 nm and 250 nm were the highest concentration had a size around 50 nm. After 4 min reduction time (Figure 3.1b), the overall size of the Co-Cu nanoparticle decreases as a higher concentration of particles was between 20 nm to 40 nm. The higher size observed was around 160 nm. The main concentration of particles had a size of 50 nm, very similar to the 0 min reduction time. Also, an increase in graphitic carbon was observed as the catalytic growth of graphitic material is carried out (yellow arrow). Figure 3.1c illustrates the changes observed after 8 min of reduction pre-treatment. Evidence of the formation of elongated particles (red arrow) surrounded by small Co-Cu particles of around 80 nm (yellow arrow) and graphitic material was observed. The nanoparticles maintain a size between 20 nm to 100 nm. Figure 3.1d shows that after 12 min of the reduction process, a bimodal size distribution it was observed with main sizes at 55 nm and 110 nm. Faceted nanoparticles (red arrow) and highly defective graphitic structure coming from Co-Cu particles (yellow arrow) were also detected.

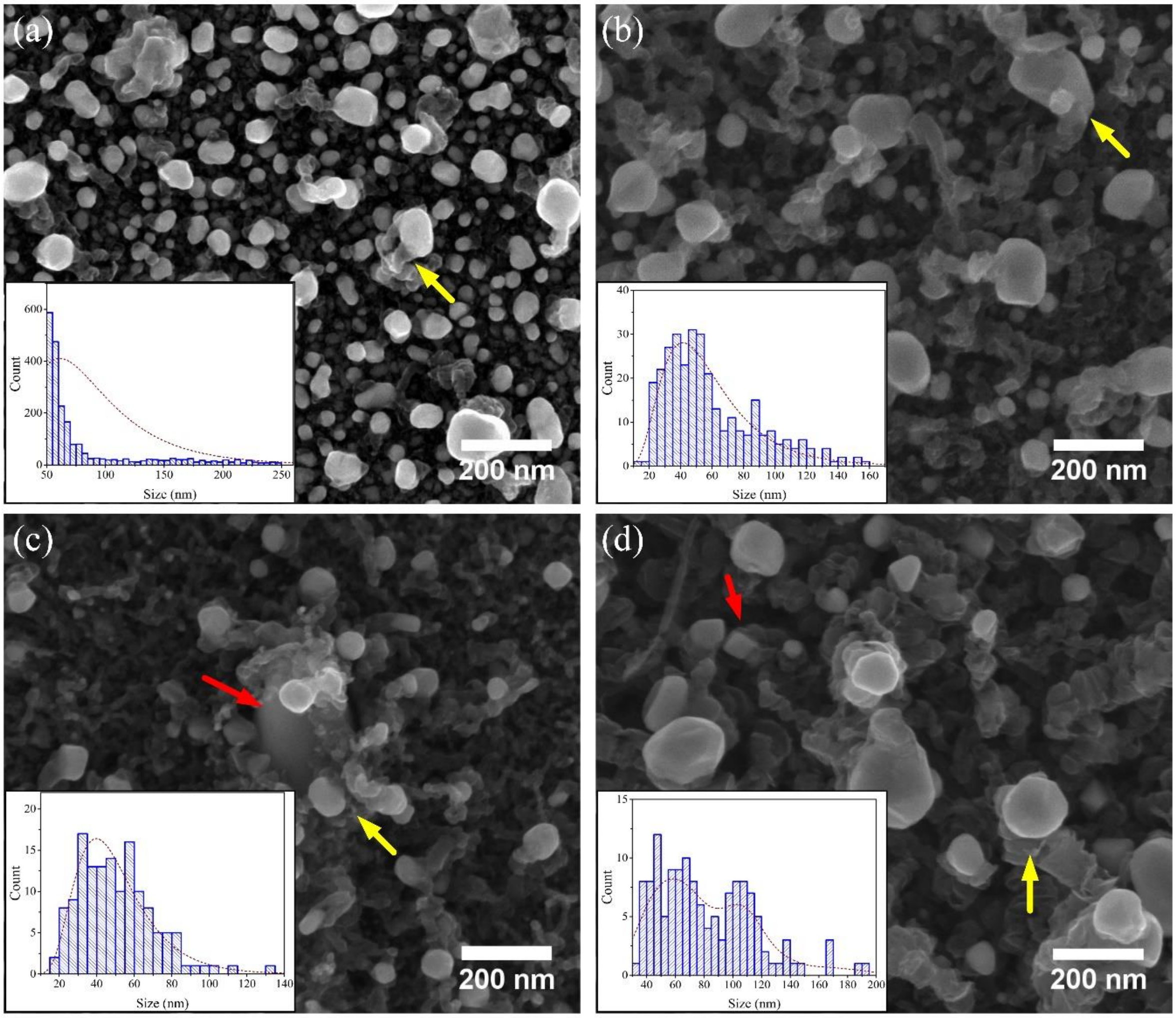

Figure 3.1: Nanoparticle nucleation of the Co-Cu thin film after a reduction pre-treatment in the CVD system at the time of (a) 0 min, (b) 4 min (c) 8 min and (d) 12 min.

In summary, the growth of Co-Cu nanoparticles from the thin film is carried out from the first minutes with the main size of about 50 nm. As time increases, two effects occur: 1) A particle size diminution with particles around 40 nm; 2) The nucleation of nanoparticles leading to a size increase. This effect was well observed at 12 min of reduction time. Also, the presence of elongated nanoparticles surrounded by small Co-Cu nanoparticles (~100 nm) at the 8 min is significant.

3.4 Synthesis of the 3D wrinkled carbon belt structure

Figure 3.2a depicts a low magnification SEM image of the N-CBS sample obtained after submitting the Co-Cu thin film substrate to the CVD process (see figure 2.2 S2-position chapter 2). The sample was structured by the N-CBS, where the main dimensions are 2.3 μm ± 1.2 μm width, 0.38 μm ± 0.16 μm thickness, and 13.2 μm ± 8.8 μm lengths reaching lengths of above 50 μm (inset). Figure 3.2b shows some N-CBS with widths of 3.9 μm and 2.2 μm that illustrates fibers at the edges and highly curved sections (yellow arrow). High magnification SEM image (figure 3.2c) clearly shows a frontal view of one N-CBS that exhibits a porous texture and corrugated surface. The main structure seems to be structured by highly intertwined CNF. Also, the N-CBS appears to have periodic growth. An FFT analysis over the surface (inset) and a 3D surface plot developed using the contrast differences (inset) reveal curvature probably associated with a growth process influenced by the flow variations generated by the nebulizer.

Three types of nanoparticles were observed in the W-CBS. Figure 3.2d illustrates an agglomerate of irregular Co-Cu nanoparticles, which leads to the formation of smaller and irregular N-CBS with no particular growth direction. Figure 3.2e shows an elongated particle (~ 1.1 μm length) that some other Co-Cu particle agglomerates. This particle presumably is responsible for the growth of the N-CBS. A particular characteristic of this nanoparticle is that the N-CBS grows in one direction (red arrow) what probably was associated with a tip growth mechanism. Figure 3.2f shows an individual Co-Cu nanoparticle (yellow arrow) that promotes the growth of intertwined and irregular CNF agglomerates that seems to be an intermediate part or unities of the CBS. These intertwined CNF agglomerates had widths around 0.5 μm (figure 3.2g), shows individual CNF at the borders (yellow arrow figure 3.2h) and seem to have a continuous growth leading a porous and irregular structure (figure 3.2i).

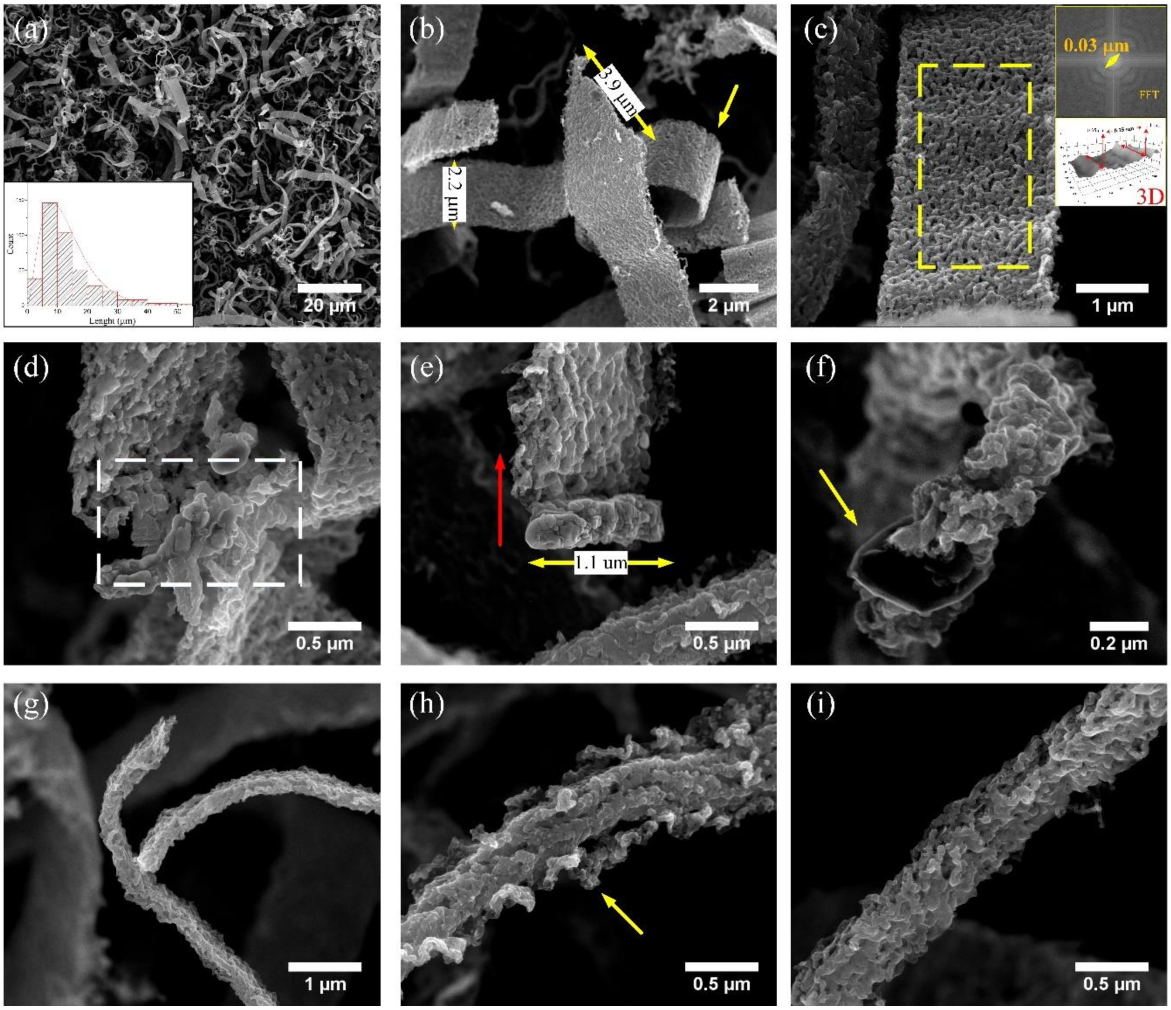

Figure 3.2: SEM images of the synthesized N-CBS. **(a)** Low magnification image revealing the N-CBS grown over Co:Cu thin film. (b) N-CBS of ~2.2 μm and 3.9 μm width and showing highly curved sections (yellow arrow). (c) Front view of N-CBS reveling periodic growth every 0.3 μm by FFT and surface 3D plot (inset). (d) Nanoparticle agglomerate leading to irregular N-CBS growth. (e) Elongated Co-Cu nanoparticle that catalyzes the N-CBS. (f) An intermediate N-CBS structure by an individual Co-Cu particle. (g) Intertwined intermediate N-CBS. (h) Intermediate N-CBS revealing individual CNF at the edges (yellow arrow). (i) Porous intermediate N-CBS.

Figure 3.3 illustrates the backscattered electron (BSE) SEM images associated with the metallic particles contained in the N-CBS sample. Figure 3.3a depicts a low magnification BSE-SEM image where the brightest spots are associated with metallic particles. These elongated nanoparticles seem to be distributed in all samples and apparently at the tip of one N-CBS (figure 3.3b). A high-magnification BSE-SEM image over the face of one N-CBS (figure 3.3c) shows that the main also contains small nanoparticles distributed all over the belt structure. The nanoparticles have a size between 2 nm to 5 nm. Figure 3.3d depicts an agglomerate of Co-Cu nanoparticles that lead to the formation of intertwined CNF. Figure 3.3e illustrates an individual Co-Cu nanoparticle responsible for the formation of defective intertwined CNF. By BSE-SEM (Figure 3.3f), it is possible to observe that also these small structures are fully covered by nanometric Co-Cu nanoparticles (~ 2 nm) embedded in the main body.

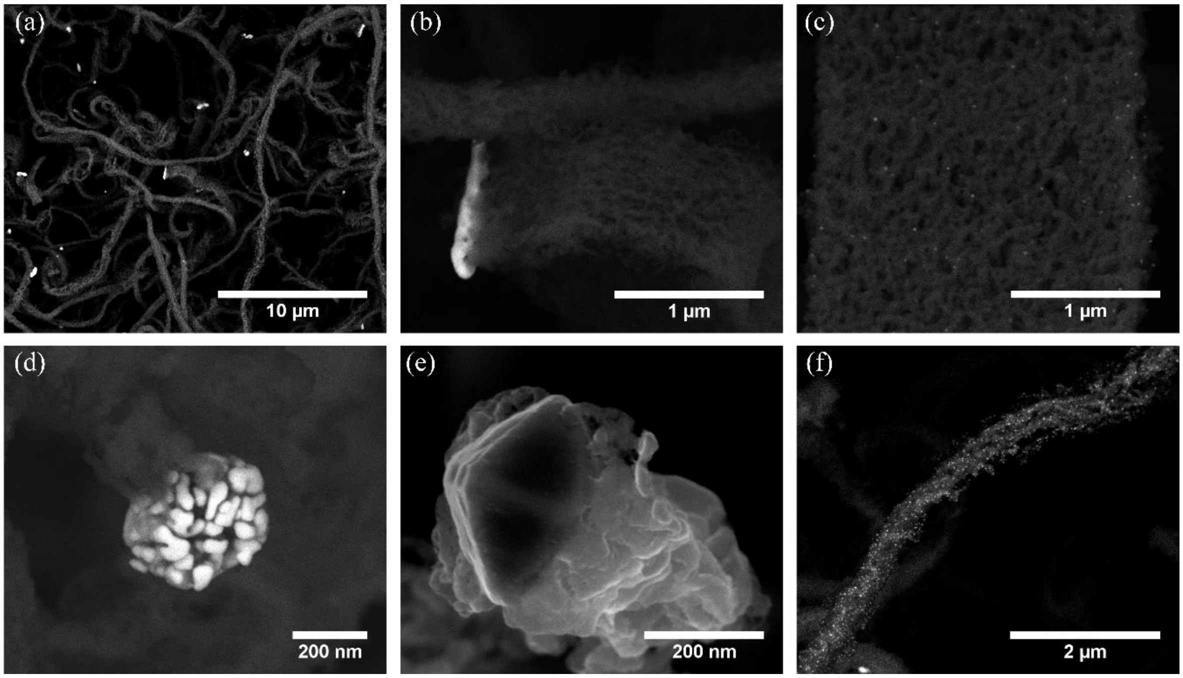

Figure 3.3: (a) BSE-SEM image at a low magnification where N-CBS are observed. (b) Elongated nanoparticle at the tip of one N-CBS. (c) The face view of one N-CBS that reveals nanoparticles (~ 2 nm) distributed all the body. (d) Co-Cu nanoparticle agglomerate. (e) Presumably, a Co-Cu nanoparticle. (f) Intertwined CNF intermediate structure fully decorated with nanoparticles.

Figure 3.4 depicts TEM and HR-TEM images of the N-CBS structure and the wrinkled carbon nanofibers. Figure 3.4a illustrates a single N-CBS with an 800 nm width, irregular edges, and wrinkled morphology. Evidence on the internal structure of N-CBS can be observed in figure 3.4b, showing clearly that the N-CBS were formed by assembled wrinkled carbon fibers. Due to the irregular junctions between carbon fibers, some holes were created (yellow arrows). Figure 3.4c shows an individual wrinkled carbon fiber, presumably the building block that leads to the formation of the N-CBS. This carbon fiber was highly corrugated and revealed a high wall defective structure. An HRTEM image of the wrinkled carbon fiber reveals that the structure consists of curved graphite material with an estimated interlayer distance of ~3.5 Å (figure 3.4d). Defective graphitic layers promoting the hole formation in the graphitic network (holey graphene) were also observed (figure 3.4e). Another exciting aspect is the presence of small metal nanoparticles presumably Cu, with diameters around 5 nm anchored on the surface of the carbon fiber can be appreciated in figure 3.4f.

Figure 3.4(g-h) illustrates a TEM comparative image of the wall-graphitic layers in an N-doped CNT like the observed in B-Sample-Chapter 2 and the wrinkled carbon nanofibers that build the N-CBS. Figure 3.4g shows the wall in an N-doped MWCNT with well-aligned graphite layers (see yellow square), the corresponding FFT analysis (black) and refinement (green) are also shown. However, in the case of the wrinkled carbon nanofiber (figure 3.3h), the wall structure is so curved that it shows the multidirectional growth of graphitic layers, respectively (inset).

A TEM image depicted in figure 3.5a, it is possible to observe a catalytic particle responsible for the growth of the wrinkled carbon fiber. EDS analysis (figure 3.5b) demonstrated that the nanoparticle is mainly structured by Co, Cu, and O. Notice that the carbon fiber preferentially grows one of the faces of the cobalt particle (figure 3.5a). Furthermore, the Co nanoparticle is surrounded by a thin layer of ~3.5 nm. Chambers et al. [25] reported that carbon fibers grow preferentially perpendicular to the face defined by the plane (111) of Co nanoparticles. HRTEM allows us to better identify the structure of the thin layer (figure 3.5c). By a fast Fourier transform (FFT) refinement over the green square reveals an interlayer distance of ~2.63 Å (figure 3.5d), which corresponds to the (012) crystallography plane of CuO. Figure 3.5e shows a Z-contrast TEM image of a Co nanoparticle with a ~20 nm diameter. Figure

3.5f depicts an elemental line-scan along the nanoparticle, revealing the presence of Co, Cu, O, and S. Notice that the main contribution comes from Co, followed by Cu and O with traces of S. TEM observations suggest that the wrinkled carbon nanofibers grew from Co@CuO-CuS nanoparticles. Likely sulfur and copper-oxide hinder the growth of carbon nanotubes, forming defected carbon fibers. Assembled defected carbon fiber formation occurs when many cobalt nanoparticles described above come together.

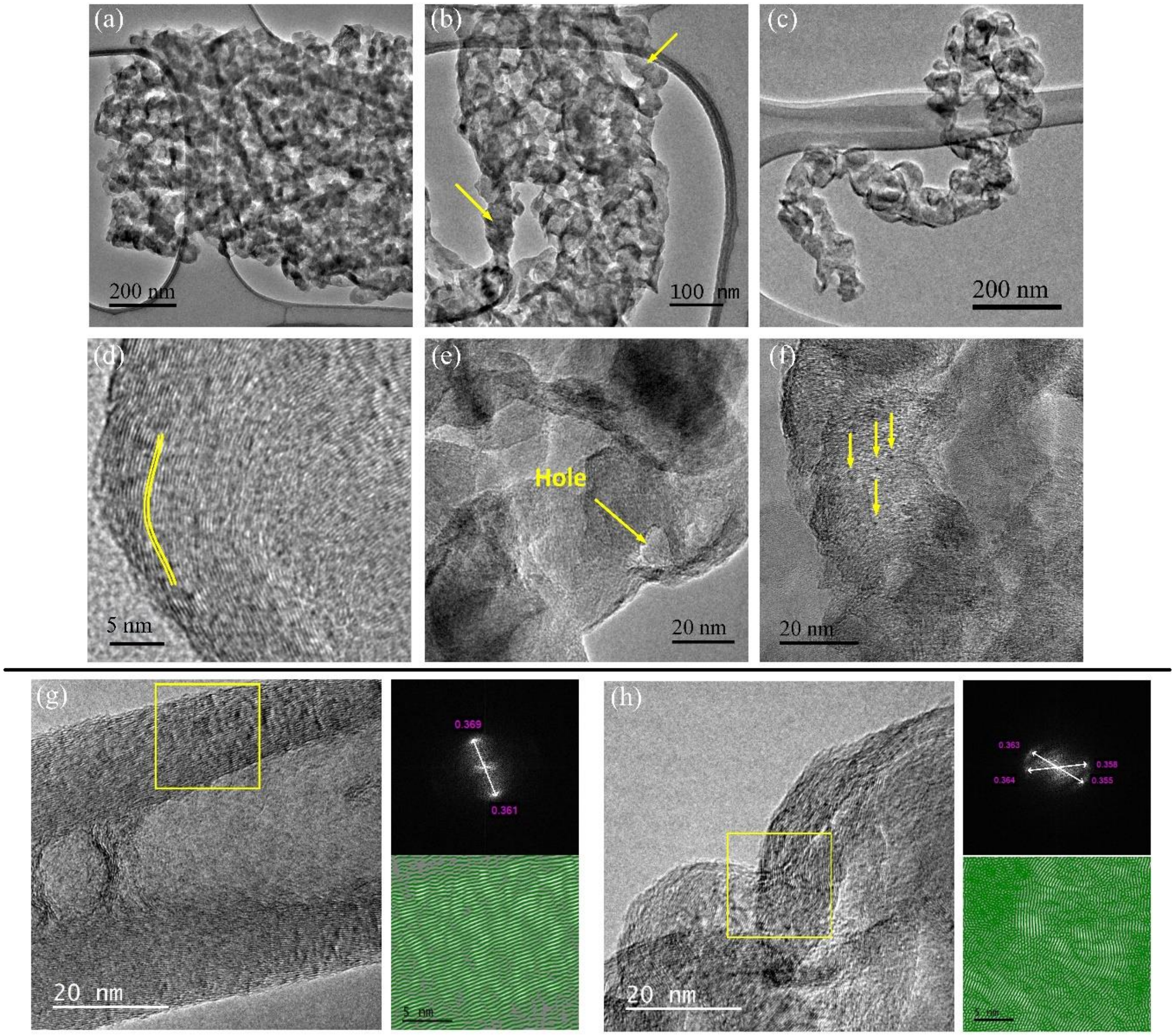

Nitrogen doped CNT (B-sample cap2)

N-CBS structure

Figure 3.4: TEM and HRTEM images of N-CBS structure. (a)-(b) Top views of N-CBS. The arrows in (b) indicate the wrinkled carbon fibers. (c) High magnification image of wrinkled carbon fiber. (d)-(f) HRTEM images of wrinkled carbon fibers. (d) Curved graphite layers with an interlayer distance of ~3.5 Å, (e) holed wrinkled graphitic section, and (f) Cu-

nanoparticles of ~2 nm diameter anchored on the surface of wrinkled carbon fiber. (g)-(h) Illustrates a comparative refinement over a HRTEM image of the N-CNT (B-sample Chapter 2) and wrinkled carbon nanofiber of the N-CBS.

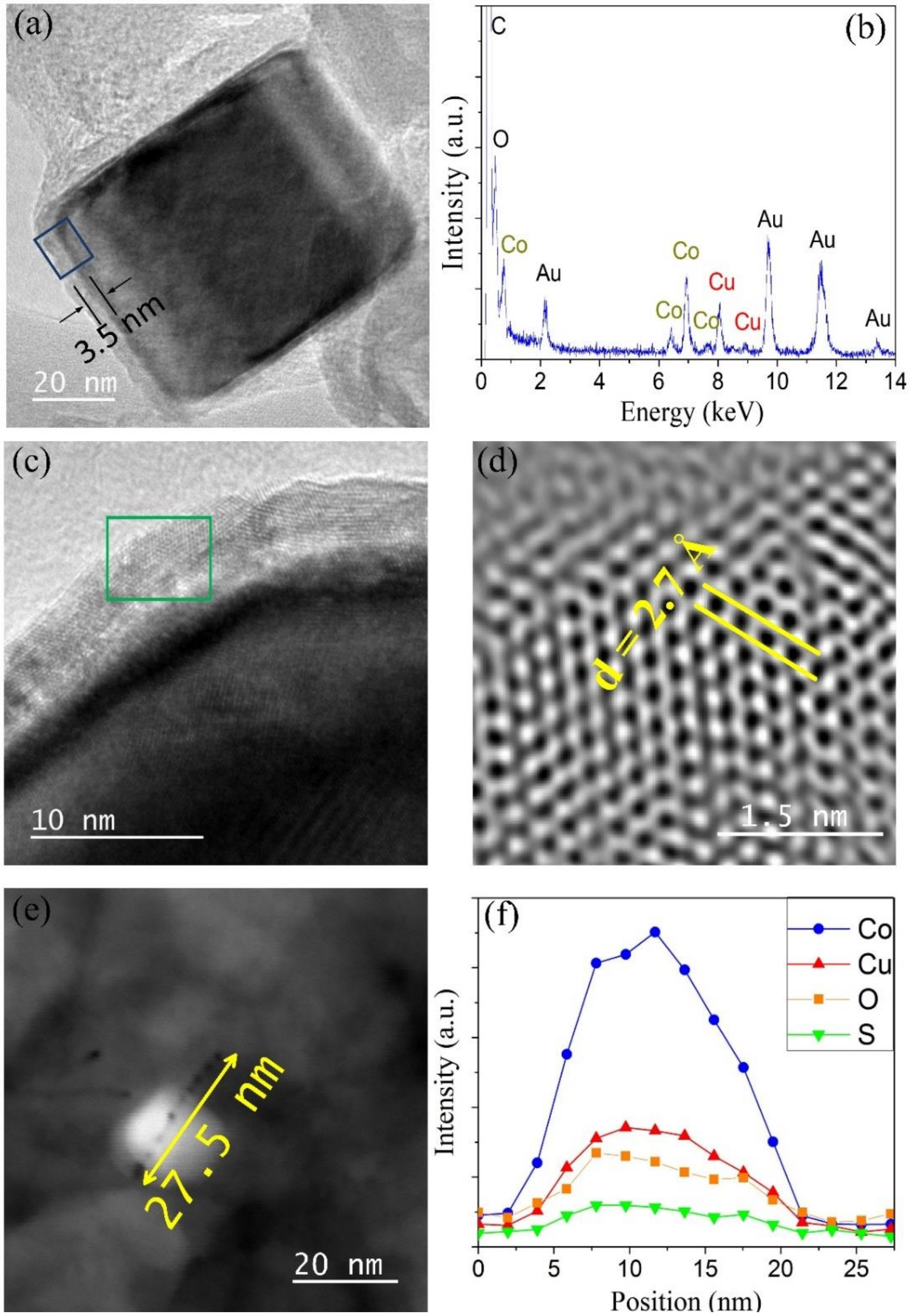

Figure 3.5: **(a)** HRTEM images of a catalytic Co-Cu nanoparticle. **(b)** EDS analysis revealing the presence of Co, Cu, and O in the catalytic particle. **(c)** Few layers of copper oxide surrounding the Co nanoparticle. **(d)** The FFT analysis on the region enclosed in **(c)**

yielded an interlayer distance of 2.63 Å, which corresponds to the (012) crystallographic plane of cobalt-copper oxide. **(e)** Z-contrast TEM image on a Co nanoparticle of ~20 nm diameter and the corresponding elemental line-scan along the nanoparticle **(f)**, revealing Co, Cu, O, and S.

The assembled wrinkled carbon nanofibers adopt a belt morphology when cobalt nanoparticles are hosted on the surface of the copper-oxide bar-shaped structures. Figure 3.6a exhibit a macroscopic view of a Co-Cu thin film exposed to heat treatment for 2 hours in the absence of precursors under Ar-H_2 flow. There are two types of nanostructures obtained after this procedure: mainly cobalt-copper semi-spherical nanoparticles with size around 136.7 nm ± 68.2 nm and bar-shaped Co-Cu particles (yellow arrows) distributed along with the sample. Figure 3.6b shows an elongated Co-Cu particle observed in figure 3.6a white rectangle. This particle with a length of around 1.1 µm is surrounded by semi-spherical nanoparticles of around ~80 nm and some extremely small of around 20 nm. An EDS analysis over the particle reveals a high concentration of Cu (40.2 wt%), followed by Co (14.7 wt%) and O (9.7 wt%). The bar shape Cu particles are very similar to those observed at the tip of the N-CBS structures (figure 3.2e) and those observed in early reduction time, as described in figure 3.1c.

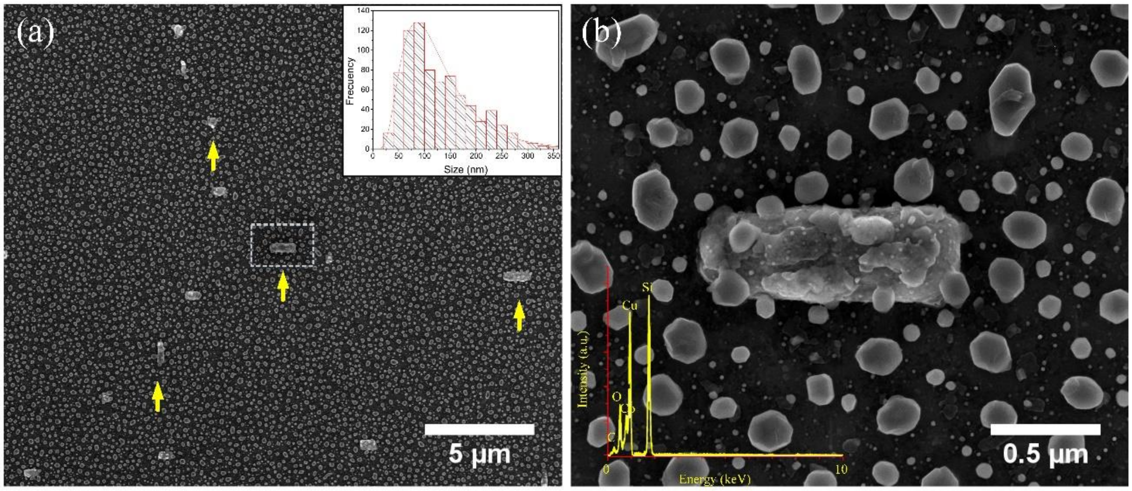

Figure 3.6: (a) Macroscopic SEM view of a Co-Cu substrate after 2h of the reduction process at 800 °C where the yellow arrow indicates the formation of bar-shaped structures. **(b)** Zoom developed over the white rectangle in **(a)** over a bar shape particle. Inset reveals a high concentration of Cu over the elongated particle (40.2 wt%).

Figure 3.7a displays an EDS-mapping analysis over a bar-shaped Co-Cu particle, as described above. The EDS analysis reveals that the semi-spherical Co-Cu particles are mainly structured by Co and O, while the bar shape particle is structured primarily by Cu and O. The XRD characterizations of N-CBS revealed the presence of different crystalline phases (figure 3.7b). The peak at 26.4° corresponds to the (002) crystallographic plane of graphite materials with an interlayer distance of ~3.4 Å. Signals of Co and Cu in a face-centered cubic structure were identified with crystallographic open database COD 4313211 and COD 9011619, respectively, and preferentially oriented in the (111) crystallographic plane. Copper oxide (II), copper sulfide (I), and copper peroxide (II) (COD 1011148, COD 9005550, and COD 1521320) were also identified. The presence of Si comes from the Si/SiO_2 substrate.

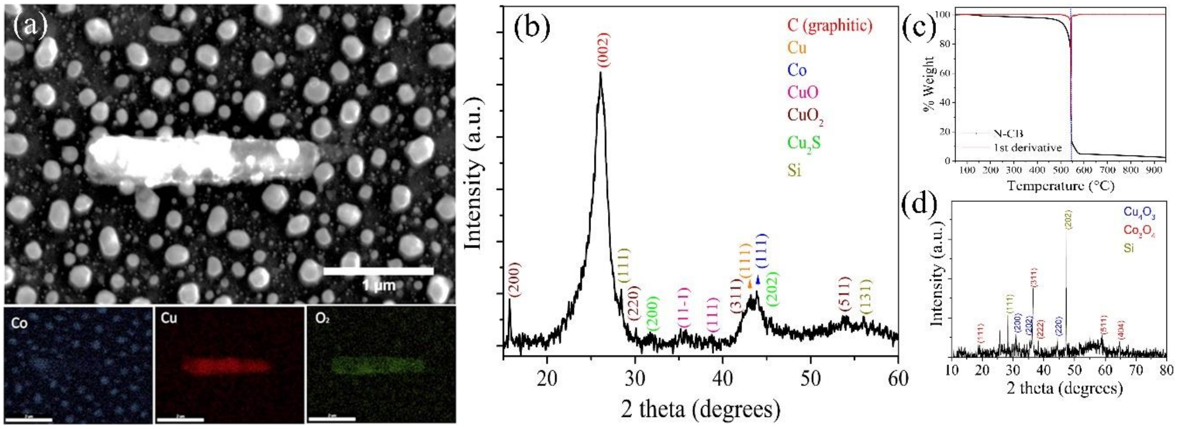

Figure 3.7: **(a)** EDS-mapping analysis of cobalt (blue), copper (red), and oxygen (green) obtained from nanoparticles exhibited in figure 3.3b. Note that the bar-shaped particle is formed by copper-oxide, and the spherical nanoparticles are structured mainly by Co. **(b)** XRD pattern of N-CBS showing the presence graphite material, Co (FCC), Cu (FCC), CuO, CuO_2, Cu_2S, and Si. **(c)** TGA with an oxidation temperature of 546 °C and a remaining weight of 2.5% at 950 °C. **(d)** XRD patterns of the TGA remaining material, revealing the presence of Co_3O_4, Cu_2O, and Si.

TGA results for N-CBS are shown in figure 3.7c. The sample lost 1% of its weight at 150 °C, likely due to the removal of oxygen functional groups or water evaporation. At 500 °C, a lost weight of ~2% was reached. This behavior is related to the oxidation of amorphous carbon. Finally, 97.5% of its weight is lost at 545 °C. This fact indicates that the N-CBS are thermally stable. The sharp oxidation showed in the TGA curve could be related to the fact that N-CBS are graphitic structures with several edges and defects. N-CBS are thermally stable with an oxidation temperature higher than that obtained for nitrogen-doped carbon nanotube, which is 430 °C [33]. The residual or remaining material at 950 °C was 2.5% of the initial total weight of the sample, revealing the presence of Cu_4O_3, Co_3O_4, and Si by XRD (figure 3.7d).

Raman spectroscopy characterization is depicted in figure 3.8a. The typical peaks of graphite materials were identified as the D-band peak located at 1345 cm^{-1} which is related to defects (vacancies, edges, corrugation), the G-band peak observed at 1580 cm^{-1} associated with the C-C stretching mode in graphite materials, the presence of the overtone 2D-band peak at 2677 cm^{-1} and the D+G peak at 2916 cm^{-1} are related to the formation of few-layer graphite and irregular surfaces respectively. Deconvolution analysis of the G-band peak (figure 3.8b) revealed the presence of two peaks G1 and G2 centered at 1577 cm^{-1} and 1597 cm^{-1}, respectively. The G1-band peak is attributed to in-plane vibration of the C-C bonds, whereas the G2 peak is due to the influence of doping or defective structure in the type of electron doping, commonly associated with a p-doped surface [42–44]. G-band splitting has also been observed in multiwalled carbon nanotubes and few-layer graphene. In multiwalled carbon nanotubes, the two-peak decomposition of the G-band Raman peak was related to the innermost and outermost layers [45], where the displacement to the right could be affected by functionalities or doping on the outermost layer in MWCNTs. In few-layer graphene, the G-band splitting was attributed to *p*-type doping [46]. The I_D/I_G ratio is commonly associated with a graphitization degree and is a defective structure estimate. In this case, the estimated ratio of the intensity of the D-band and G-band peaks (I_D/I_G) is 1.1, indicating the formation of a highly defective structure.

XPS measurements were carried out for the surface elemental analysis of N-CBS samples. The presence of carbon (93.5%), nitrogen (1.9%), and oxygen (4.6%) was identified over the surface spectra figure 3.8c. A deconvolution analysis allows us to identify the binding energies of bonds, doping structures, and chemical functional groups attached to the surface of the N-CBS. The full width half maximum (FWHM), the peak gravity center, and the integrated area under each curve are indicated in table 3.1, 3.2, and 3.3. Figure 3.7(d-f) depicts the expanded XPS spectra for C1s, O1s, and N1s regions, respectively. For C1s peak, it was found sp^2 and sp^3 hybridized carbon and oxidized carbon species such as C-O, C=O, and COO^- which could be attributed to the presence of phenolic, carbonyl, carboxyl, epoxy groups (Table 3.1). These carbon-oxygen bonds could also be part of more complex systems such as ethoxy, ether, and ester groups attached to the N-CBS surface. Also, in the case of the C-C sp^3 hybridization can be associated with the formation of amorphous carbon, diamond-like carbon structures, or the formation of combined sp^2-sp^3 carbon structures. The expanded O1s peak (Table 3.3) revealed the presence of C-O, C=O, COO^-, being the C-O (40.8%), the more representative (figure 3.8e). The C-O bonds could be associated with phenolic groups on the surface or the incorporation of oxygen in an ester chemical group. The O-C=O species could be attributed to the presence of ester or carboxyl groups. A low concentration of copper oxide species is detected. However, due to the limited atomic concentration detection of XPS equipment (~0.1 At %), it is possible that phases like CuO were surface traces while a higher concentration of Cu_2O was detected (~0.4 %).

The expanded N1s peak (figure 3.8f) revealed the presence of N-pyrrolic, N-pyridinic, N-quaternary doping, and N-O bonds of nitrogen functionalization. A quantitative estimation from the deconvolution analysis yielded that N-pyrrolic and N-pyridinic doping dominate in the sample with a 33.7% and 32.6% respectively (Table 3.2). These types of doping are in graphite layers in the presence of defects, such as vacancies and edges. The N-pyrrolic doping in N-CBS is relevant for chemical reaction applications. Previous investigations demonstrated that wrinkled graphene sheet doped with N-pyrrolic are highly efficient for oxygen-reduction reaction (ORR) catalyst activity [47,48]. Furthermore, N-pyridinic or N-substitutional doping does not produce a considerable alteration of the structure and introduce electrons into the systems. Both features are essential for electronic device applications [49,50].

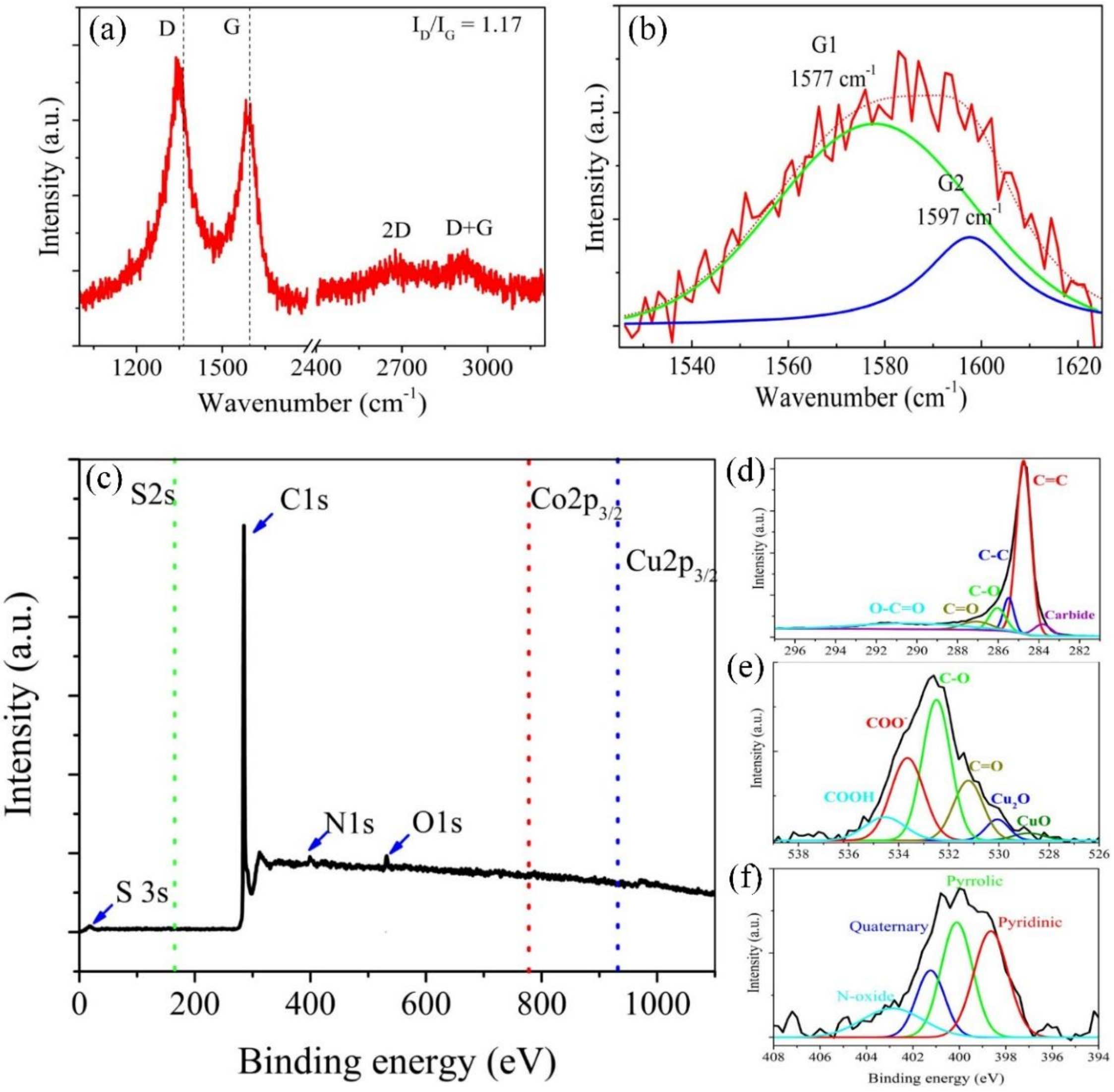

Figure 3.8: **(a)** Raman shift of N-CBS. The ratio of the intensity of the D-Raman peak and G-Raman peak (I_D/I_G) is indicated. **(b)** Deconvolution analysis of the G-Raman peak showing the presence of two peaks (G1 peak placed at 1577 cm^{-1} and G2 peak at 1597 cm^{-1}). **(c)** XPS survey scans revealing N, C, O, and S. **(d-f)** Deconvoluted XPS spectra. **(d)** C1s spectra indicating sp^2 hybridized carbons (C=C), sp^3 hybridized carbons (C-C), and C=O, C-O, COO$^-$, and metal carbide compounds. **(e)** O1s spectra show Cu(II), Cu(I) oxide, COO$^-$, C=O, and C-O bonds. **(f)** N1s spectra present the N-pyridinic, N-pyrrolic, N-quaternary, and pyridine-oxide. Binding energies are indicated in table 3.2.

Table 3.1: Deconvolution results of C1s XPS spectra N-CBS. The gravity center in eV, full width at half maximum (FWHM), and the area under the curve of the different chemical species (%) are shown.

Bond type in C1s	Binding energy center (eV)	FWHM (eV)	Relative %	Total %
Carbide	283.8	1.0	2.8	2.6
C=C	284.7	0.8	59.7	55.8
C-C	285.4	0.6	11.9	11.1
C-O	286.0	0.9	9.5	8.8
C=O	287.0	1.7	7.2	6.7
COO-	288.3	3.7	5.5	5.1
π–π	291.6	3.5	3.4	3.1

Table 3.2: Deconvolution results of N1s XPS spectra of N-CBS. The gravity center in eV, full width at half maximum (FWHM), and the area under the curve of the different chemical species (%) are shown.

Bond type in N1s	Binding energy center (eV)	FWHM (eV)	Relative %	Total %
Pyridinic	398.6	1.8	32.6	0.6
Pyrrolic	400.1	1.6	33.7	0.6
Quaternary	401.2	1.5	17.4	0.3
N-O	402.8	3.0	16.2	0.3

Table 3.3: Deconvolution results for O1s XPS spectra in N-CBS. The gravity center in eV, full width at half maximum (FWHM), and the area under the curve of the different chemical species (%) are shown. Red color indicates data values below At% limit detection.

Bond type in O1s	Binding energy center (eV)	FWHM (eV)	Relative %	Total %
CuO	528.9	0.7	1.6	0.0
Cu_2O	530.3	1.3	9.0	0.4
C=O	531.3	1.3	14.0	0.6
C-O	532.5	1.4	40.8	1.8

COO-	533.8	1.5	26.9	1.2
COOH	534.5	1.8	7.7	0.3

3.5 Growth mechanism approach

The formation of N-CBS structures is far to be clear; however, based on the characterizations presented above, some ideas on how these structures grow could be suggested. Figure 3.9a displays a possible growth mechanism of N-CBS. Before turning on the sprayer, the Co-Cu film is transformed into Co@Cu semi-spherical nanoparticles and CuO bar-shaped particles like “monoliths” that are randomly dispersed over the substrate like the observed in Figure 3.9b. During the first moments when a vaporized precursor reaches the substrate. Figure 3.9c depicts how the dispersed semi-spherical particles begin to grow wrinkled carbon nanostructures, and the CuO bar-shaped particle tent to be surrounded by Co@Cu particles.

Figure 3.9(d-h) illustrates the growth process after the two-hour synthesis treatment of the Co-Cu film. Figure 3.9d schematizes that when the sprayer is turned on, vapor containing carbon, oxygen, and sulfur interact with Co@Cu nanoparticles. We believe that S and O promote the formation of CuO and Cu_2S islands surrounding the Co nanoparticle (black square). These islands limit the growth of carbon structures, and the uncovered cobalt promotes the formation of complex graphitic structures like the wrinkled carbon nanofibers. Doung et al. [51] described how CuO structures work as a grain boundary limiting the growth of graphitic sections. Figure 3.9f shows that an individual Co@Cu nanoparticle tent to grow interlinked wrinkled carbon nanofibers that grow at different spots in the metallic particle. When the sulfured and oxygenated Co@Cu nanoparticles come together to form agglomerates, these promote the growth of thinner N-CBS, as shown in figure 3.9g. The N-CBS morphologies emerged due to the formation of CuO bar-shaped nanoparticles covered by sulfured and oxygenated Co@Cu nanoparticles (figure 3.9h). However, more experimental studies are needed to understand how the N-CBS grow fully.

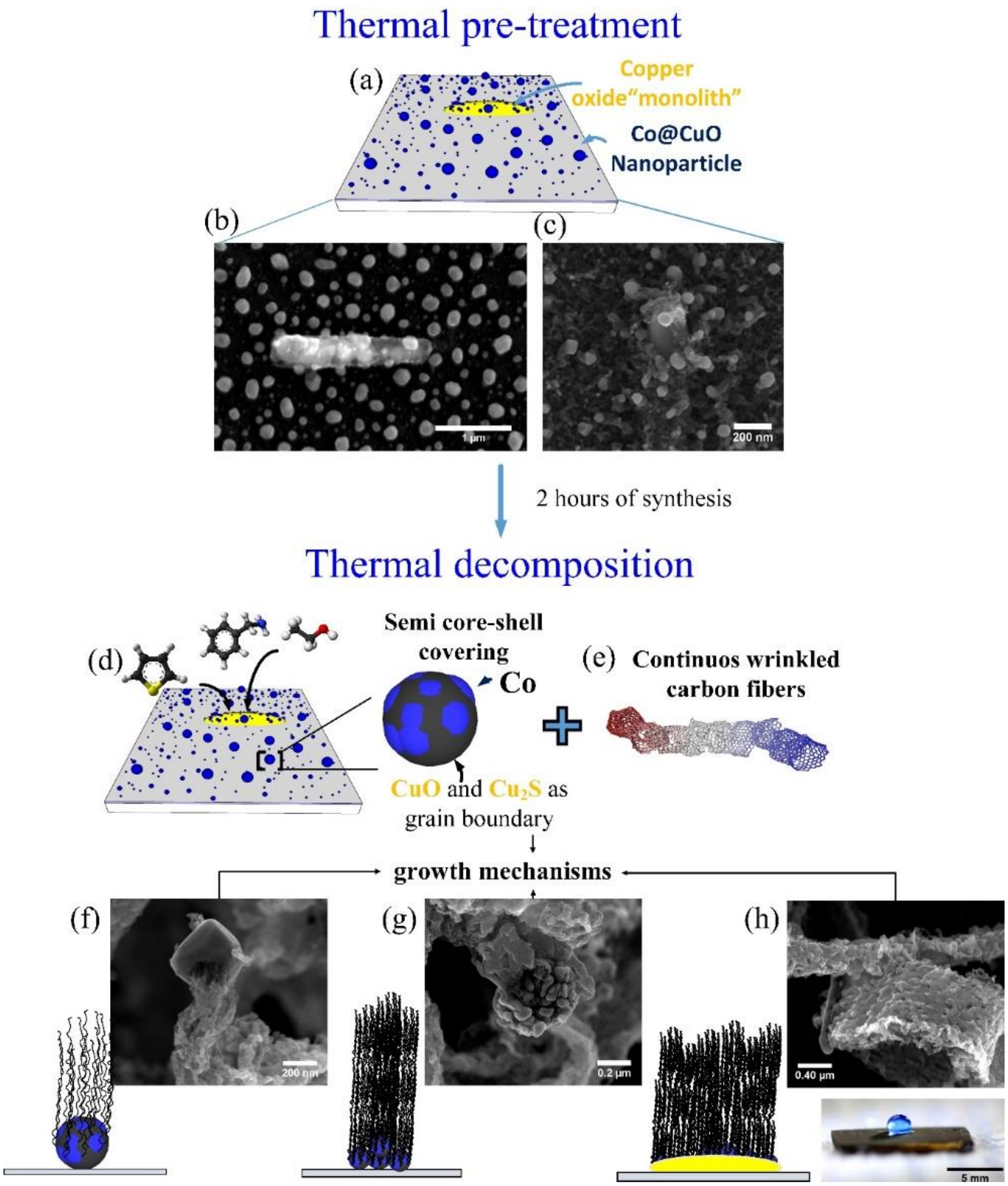

Figure 3.9: Schematic representation of the growth mechanism followed two steps. **(a-c)** pre-treatment of the Co-Cu substrate provokes the formation of copper oxide monoliths and semi-spherical nanoparticles. **(d-h)** After synthesis, the formation of the semi-spherical particles leads to the formation of wrinkled carbon nanofibers, and the Co-Cu monoliths the formation of the N-CBS.

3.6 Effect of other metals (Co-Ag and Co-Au) in the growth of 3D carbon nanostructures

3.6.1 Methodology

Following the same methodology described in chapter 2 and previously in this chapter, a 20 nm – 2 nm cobalt-silver and cobalt-gold thin films were prepared by a sputtering plasma deposition in Intercovamex V3 equipment. The deposition rate of silver was established with a pulsed power supply, Ar pressure of 1.9 x10^{-2} torr and deposition time of 37 seconds. In the case of the 2 nm of gold deposition, pulsed power supply was used following the energy of 15 W, a 1.9x10^{-2} torr of Ar pressure, and 13 seconds of deposition.

To evaluate the influence of the Ag and Au metals in the N-CBS growth same procedure depicted in chapter 2 was employed. Thin films of 20nm (Co) and 2 nm (Ag, Au) where deposited on Si/SiO_2 substrates of 1cm x 1cm are used as a catalyst in a two furnace CVD system. Furnace 1 was set at 750 °C, and the subsequent Furnace 2 was set at 850 °C. A flow of 2.5 l/min of an H_2-Ar (5%-95%) works as a carrier gas. The synthesis time was set at 2h.

3.6.2 Results

Figure 3.10 illustrates a corresponding SEM image associated with the influence of other metals like Ag and Au over the growth of the N-CBS. The samples obtained at 750 °C, 800 °C, and 850 °C were described as S1, S2, and S3, respectively (see figure 2.2, chapter 2). Figure 3.10a-c develops the effect of Ag in the growth of N-CNB. The S1-Ag (figure 3.10a) shows the main production of defective CNF and CNT. However, there is no visual evidence associated with the formation of orientated carbon structures. The S2-Ag sample (figure 3.10b) illustrates the formation of structures with homogeneous thickness. These structures are very similar to the intertwined CNF structure observed in figure 3.2h and figure 3.2i when Cu has used; however, no signal of N-CBS structures are observed. These structures have diameters of 223 nm ± 45 nm, smaller for those reported for Cu that had a diameter of around 500 nm. Also, the length of these intertwined CNF is smaller (~1.06 µm ± 0.38 µm). Some semi-spherical particles are also observed at the tip of these structures (yellow arrow). Figure 3.10c shows the structures obtained at 850 °C. The growth mechanism changes completely, and only traces of CNF or CNT formation are observed while the main structure seems to be welded in an amorphous carbon structure. This effect could be a consequence of the Ag melting coating the substrate surface and limiting the growth of tubular structures.

Figure 3.10d-f illustrates the effect of Au nanoparticles over the growth of N-CBS. The type of structures observed at 750 °C (S1-Au Figure 3.10d) are highly similar to the observed using Ag however, a high ratio of CNT over defective CNF were observed. Also, nanoparticles (~ 40 nm) are observed at the tip of some defective CNF (yellow arrow). Figure 3.10e depicts the S2-Au sample (800 °C). Here the formation of long, curved, and intertwined CNF and small CNF are observed. Still, no formation of N-CBS structures is detected. The thickness of these structures oscillates between 300 and 600 nm. Figure 3.10f shows the S3-Au sample (850 °C), where no more trace of intertwined CNF is observed. The growth mechanism changes, and the formation of highly curved and defective CNF are observed.

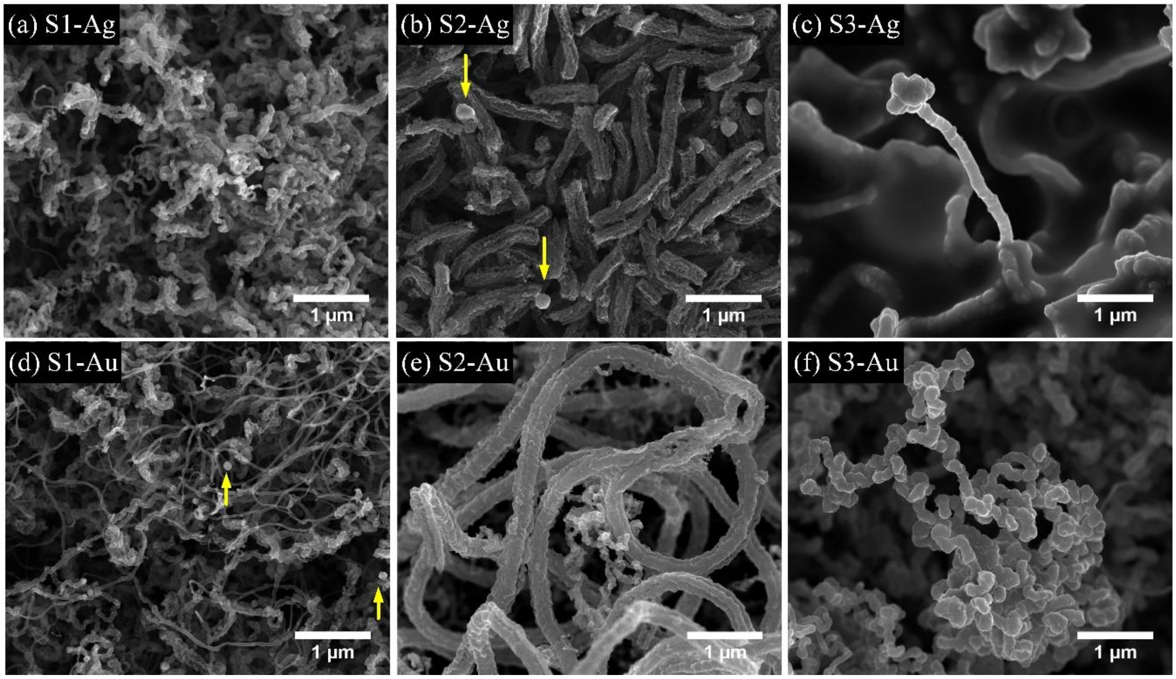

Figure 3.10: Synthesis with Co-Ag substrate: **(a)** Formation of defective CNF and CNT at 750 °C; **(b)** Intertwined CNF and presence of semi-spherical nanoparticles (yellow arrow) at 800°C; **(c)** Graphitic carbon sections welded at 850 °C. Synthesis with Co-Au substrate: **(d)** Defective CNF and CNT with semi-spherical nanoparticles (yellow arrow) at 750 °C; **(e)** Intertwined CNF at 800 °C; **(f)** Curved and defective CNF.

In order to observe if there exist graphitic structural differences between the S2-Cu sample where the N-CBS grew and the same sections using Ag and Au (S2-Ag and S2-Au respectively), Raman spectroscopy was employed. Figure 3.11a shows a comparative between S2-Cu, S2-Ag, and S2-Au samples. The D-band associated with the "breathing mode" process and the G-band related to the in-plane vibration of graphitic structures [52,53] are highly noticeable in all cases. Also, the presence of the second-order vibration modes like 2D and D+D´ are well observed in all samples. However, the G* and the 2D´ associated with curvature and high surface irregularities [54,55] are better observed in S2-Au and S2-Ag probably associated with the curvature and surface irregularities of the observed defective CNF. The I_D/I_G ratio associated with the degree of a defective structure as goes over the unity [56] indicates a high defective structure for all samples.

Figure 3.11b illustrates the displacement of the D-band and G-band. The changes in D-band are commonly associated with the edge concentration and space distribution [57], while the variations in G-band are generally associated with electronic changes in the graphitic network [58]. In this case, the S2-Cu and S2-Au are very similar, where D band had values of 1340 cm^{-1} and 1344 $cm^{-1,}$ respectively, which could be indicative of an increase due to border effect. However, for the S2-Ag sample, the D-band displaces to a higher value, probably indicating an increase of borders randomness. In the case of G-band, S2-Cu and S2-Au had similar values of 1588 cm^{-1} and 1586 $cm^{-1,}$ while S2-Ag increases to 1596 cm^{-1} (~10 cm^{-1}). The shift of the G-band to higher values from 1584 cm^{-1} (reported for CNT) is associated with a N-doping effect [59] and to a p- or n- doping i.e. increasing or decreasing electrons in the system. In this case, it could be related to electron-doping. Figure 3.11c depicts the relative area obtained after a deconvolution process developed from 1000 cm^{-1} to 1900 cm^{-1} using a Lorentz fitting. No significant changes are observed for the contribution of the G-band and D2 band related to a hydrogenated surface. However, for the S2-Cu sample where N-CBS structure was observed, D1-band increases its relative area indicating a higher concentration of sp3 structures connected to the intertwined effect of CNF and the formation of the N-CBS structure. For S2-Au and S2-Ag, this value is lower and could be associated with the formation of thinner defective CNF and the limitation of the growth of N-CBS structure.

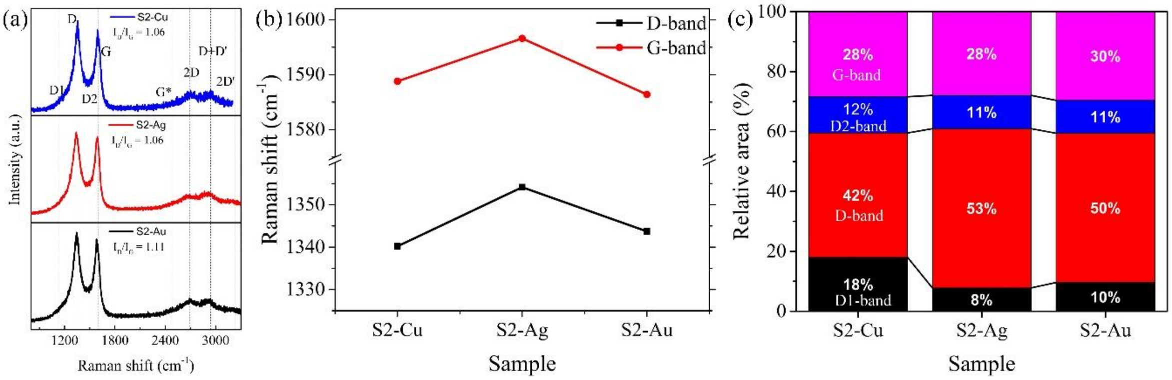

Figure 3.11: (a) Raman spectroscopy comparative between S2-Cu, S2-Ag, and S2-Au. **(b)** Displacement of D-band and G-band. **(c)** Relative area percentage associated with the D1, D, D2, and G bands obtained by the deconvolution process using Lorentz fitting.

3.7 Conclusions

In conclusion, we have proposed a novel method to synthesize amazing sp^2 carbon material with fascinating structural irregularities. This material consists of nitrogen-doped carbon nanobelts structures (N-CBS), which were synthesized using the template-based chemical vapor deposition method. Cu-Co films fabricated using magnetron sputtering were used as a template. N-CBS grew when a nebulized solution containing ethanol-benzylamine-thiophene was pyrolyzed and passed through the reactor for 2 hours. The N-CBS grew in the zone where both tubular furnaces are joined at 800 °C (S2). A closer examination of the N-CBS revealed that these are formed by assembled wrinkled carbon fibers laterally joined. By TEM characterizations, we demonstrated that the corrugated carbon fibers have highly defected sp^2 carbon materials. Our finding provides a novel carbon material with several structural irregularities (holes, edges, corrugation, doping), which could serve as an excellent ORR catalyst. Furthermore, this material could use as a high capacity electrode for supercapacitors and lithium-ion batteries in nano-devices. Other templates formed by noble metals like Au and Ag were tested for the synthesis of these exotic carbon structures. However, no signs of N-CBS formation other than the formation of defective intertwined CNF that are the base of the N-CBS structures. The findings here found demonstrate that the development of very thin films under special conditions of temperature, pressure and catalyst could be arranged to fabricate exotic carbon nanomaterials.

The construction of three dimensional carbon nanomaterials under this conditions presents not only highly defective morphology in a unique way, but promotes the nitrogen doping, oxygen functionalization and Cu NPS that could improve their chemical or physical properties.

3.8 References

[1] J.M. Romo-Herrera, M. Terrones, H. Terrones, S. Dag, V. Meunier, Covalent 2D and 3D networks from 1D nanostructures: Designing new materials, Nano Letters. 7 (2007) 570–576. https://doi.org/10.1021/nl0622202.

[2] J. Zhang, M. Terrones, C.R. Park, R. Mukherjee, M. Monthioux, N. Koratkar, Y.S. Kim, R. Hurt, E. Frackowiak, T. Enoki, Y. Chen, Y. Chen, A. Bianco, Carbon science in 2016: Status, challenges and perspectives, Carbon. 98 (2016) 708–732. https://doi.org/10.1016/j.carbon.2015.11.060.

[3] R. Du, Q. Zhao, N. Zhang, J. Zhang, Macroscopic Carbon Nanotube-based 3D Monoliths, Small. 11 (2015) 3263–3289. https://doi.org/10.1002/smll.201403170.

[4] Z. Dai, L. Liu, X. Qi, J. Kuang, Y. Wei, H. Zhu, Z. Zhang, Three-dimensional Sponges with Super Mechanical Stability: Harnessing True Elasticity of Individual Carbon Nanotubes in Macroscopic Architectures., Scientific Reports. 6 (2016) 18930. https://doi.org/10.1038/srep18930.

[5] S. Ozden, T. Tsafack, P.S. Owuor, Y. Li, A.S. Jalilov, R. Vajtai, C.S. Tiwary, J. Lou, J.M. Tour, A.D. Mohite, P.M. Ajayan, Chemically interconnected light-weight 3D-carbon nanotube solid network, Carbon. 119 (2017) 142–149. https://doi.org/10.1016/j.carbon.2017.03.086.

[6] W. Liu, T. Dang, Z. Xiao, X. Li, C. Zhu, X. Wang, Carbon nanosheets with catalyst-induced wrinkles formed by plasma-enhanced chemical-vapor deposition, Carbon. 49 (2011) 884–889. https://doi.org/10.1016/j.carbon.2010.10.049.

[7] M.E.M. Buan, N. Muthuswamy, J.C. Walmsley, D. Chen, M. Rønning, Nitrogen-doped carbon nanofibers on expanded graphite as oxygen reduction electrocatalysts, Carbon. 101 (2016) 191–202. https://doi.org/10.1016/j.carbon.2016.01.081.

[8] Y. Xu, C. Chen, Z. Zhao, Z. Lin, C. Lee, X. Xu, C. Wang, Y. Huang, M.I. Shakir, X. Duan, Solution Processable Holey Graphene Oxide and Its Derived Macrostructures for High-Performance Supercapacitors, (2015). https://doi.org/10.1021/acs.nanolett.5b01212.

[9] S. Li, H. Li, X. Wang, Y. Song, Y. Liu, L. Jiang, D. Zhu, Super-hydrophobicity of large-area honeycomb-like aligned carbon nanotubes, Journal of Physical Chemistry B. 106 (2002) 9274–9276. https://doi.org/10.1021/jp0209401.

[10] S. Huang, J. Wang, Z. Pan, J. Zhu, P.K. Shen, Ultrahigh capacity and superior stability of three- dimensional porous graphene networks containing in situ grown carbon nanotube clusters as an anode, Journal of Materials Chemistry A: Materials for Energy and Sustainability. 5 (2017) 7595–7602. https://doi.org/10.1039/C6TA11191B.

[11] A. Dasgupta, L. Pulickal, C. Rotella, Y. Lei, M. Terrones, Covalent three-dimensional networks of graphene and carbon nanotubes : synthesis and environmental applications, Nano Today. 12 (2017) 116–135. https://doi.org/10.1016/j.nantod.2016.12.011.

[12] X. Gui, J. Wei, K. Wang, A. Cao, H. Zhu, Y. Jia, Q. Shu, D. Wu, Carbon nanotube sponges, Advanced Materials. 22 (2010) 617–621. https://doi.org/10.1002/adma.200902986.

[13] J. Niu, M. Li, W. Choi, L. Dai, Z. Xia, Growth of junctions in 3D carbon A quantum mechanical molecular dynamic study, Carbon. 67 (2013) 627–634. https://doi.org/10.1016/j.carbon.2013.10.036.

[14] S. Jin, S. Xin, L. Wang, Z. Du, L. Cao, J. Chen, X. Kong, M. Gong, J. Lu, Y. Zhu, H. Ji, R.S. Ruoff, Covalently Connected Carbon Nanostructures for Current Collectors in Both the Cathode and Anode of Li – S Batteries, (2016) 9094–9102. https://doi.org/10.1002/adma.201602704.

[15] S. Luo, Y. Luo, H. Wu, M. Li, L. Yan, K. Jiang, L. Liu, Q. Li, S. Fan, J. Wang, Self-assembly of 3D Carbon Nanotube Sponges: A Simple and Controllable Way to Build Macroscopic and Ultralight Porous Architectures, Advanced Materials. (2016) 1–8. https://doi.org/10.1002/adma.201603549.

[16] Y. Yang, N.D. Kim, V. Varshney, S. Sihn, Y. Li, A.K. Roy, J.M. Tour, J. Lou, In situ mechanical investigation of carbon nanotube–graphene junction in three-dimensional carbon nanostructures, Nanoscale. (2017) 2916–2924. https://doi.org/10.1039/C6NR09897E.

[17] C. Jiang, A. Saha, C.C. Young, D.P. Hashim, C.E. Ramirez, P.M. Ajayan, M. Pasquali, A.A. Martí, Macroscopic Nanotube Fibers Spun from Single-Walled Carbon Nanotube Polyelectrolytes, ACS Nano. 8 (2014) 9107–9112. https://doi.org/10.1021/nn502552q.

[18] H. Sun, Z. Xu, C. Gao, Multifunctional , Ultra-Flyweight , Synergistically Assembled Carbon Aerogels, (2013) 2554–2560. https://doi.org/10.1002/adma.201204576.

[19] J. Niu, Z. Xia, Template-directed growth and mechanical properties of carbon nanotube-graphene junctions with nano-fillets: Molecular dynamic simulation, RSC Advances. 6 (2016) 56077–56082. https://doi.org/10.1039/c6ra11844e.

[20] L. Wang, Y. Zhao, M.L. Thomas, H.R. Byon, In Situ Synthesis of Bipyramidal Sulfur with 3D Carbon Nanotube Framework for Lithium – Sulfur Batteries, (2014) 2248–

2252. https://doi.org/10.1002/adfm.201302915.

[21] C. Shan, W. Zhao, X.L. Lu, D.J. O'Brien, Y. Li, Z. Cao, A.L. Elias, R. Cruz-Silva, M. Terrones, B. Wei, J. Suhr, Three-dimensional nitrogen-doped multiwall carbon nanotube sponges with tunable properties, Nano Letters. 13 (2013) 5514–5520. https://doi.org/10.1021/nl403109g.

[22] J. Dijon, P.D. Szkutnik, A. Fournier, T.G. De Monsabert, H. Okuno, E. Quesnel, V. Muffato, E. De Vito, N. Bendiab, A. Bogner, N. Bernier, How to switch from a tip to base growth mechanism in carbon nanotube growth by catalytic chemical vapour deposition, Carbon. 48 (2010) 1210–1213. https://doi.org/10.1016/j.carbon.2010.06.064.

[23] E. Muñoz-Sandoval, A.J. Cortes-López, B. Flores-Gómez, J.L. Fajardo-Díaz, R. Sánchez-Salas, F. López-Urías, Carbon sponge-type nanostructures based on coaxial nitrogen-doped multiwalled carbon nanotubes grown by CVD using benzylamine as precursor, Carbon. 115 (2017). https://doi.org/10.1016/j.carbon.2017.01.010.

[24] X. Qi, C. Qin, W. Zhong, C. Au, X. Ye, Y. Du, Large-scale synthesis of carbon nanomaterials by catalytic chemical vapor deposition: A review of the effects of synthesis parameters and magnetic properties, Materials. 3 (2010) 4142–4174. https://doi.org/10.3390/ma3084142.

[25] A. Chambers, N.M. Rodriguez, R.T.K. Baker, Modification of the Catalytic Behavior of Cobalt by the Addition of Copper, Society. (1995) 10581–10589.

[26] L. Guevara, C. Wanner, R. Welsh, M.A. Atwater, Using Mechanical Alloying to Create Bimetallic Catalysts for Vapor-Phase Carbon Nanofiber Synthesis, Fibers2. 3 (2015) 394–410. https://doi.org/10.3390/fib3040394.

[27] O.C. Carneiro, N.M. Rodriguez, R.T.K. Baker, Growth of carbon nanofibers from the iron-copper catalyzed decomposition of CO/C2H4/H2 mixtures, Carbon. 43 (2005) 2389–2396. https://doi.org/10.1016/j.carbon.2005.04.022.

[28] J.H. Zhou, Z.J. Sui, J. Zhu, P. Li, D. Chen, Y.C. Dai, W.K. Yuan, Characterization of surface oxygen complexes on carbon nanofibers by TPD, XPS and FT-IR, Carbon. 45 (2007) 785–796. https://doi.org/10.1016/j.carbon.2006.11.019.

[29] U. Narayan-Maiti, Chemically modified/doped carbon nanotubes & graphene for optimized nanostructures & nanodevices, Advanced Materials. 26 (2014) 40–67.

[30] D. Golberg, Y. Bando, W. Han, K. Kurashima, T. Sato, Single-walled B-doped carbon, B/N-doped carbon and BN nanotubes synthesized from single-walled carbon nanotubes through a substitution reaction, Chemical Physics Letters. 308 (1999) 337–342. https://doi.org/10.1016/S0009-2614(99)00591-6.

[31] L. Yang, S. Jiang, Y. Zhao, L. Zhu, S. Chen, X. Wang, Q. Wu, J. Ma, Y. Ma, Z. Hu, Boron-doped carbon nanotubes as metal-free electrocatalysts for the oxygen reduction reaction, Angewandte Chemie - International Edition. 50 (2011) 7132–7135. https://doi.org/10.1002/anie.201101287.

[32] Z. Liu, F. Peng, H. Wang, H. Yu, J. Tan, L. Zhu, Novel phosphorus-doped multiwalled

nanotubes with high electrocatalytic activity for O2 reduction in alkaline medium, Catalysis Communications. 16 (2011) 35–38. https://doi.org/10.1016/j.catcom.2011.08.038.

[33] E. Cruz-silva, D.A. Cullen, L. Gu, J.M. Romo-herrera, E. Muñoz-sandoval, F. López-urías, B.G. Sumpter, V. Meunier, J. Charlier, Ḱ.D.J. Smith, H. Terrones, M. Terrones, Heterodoped nanotubes: theory, synthesis, and characterization of phosphorus-nitrogen doped Multiwalled Carbon Nanotubes, ACS Nano. 2 (2008) 441–448.

[34] P. Ayala, R. Arenal, M. Rümmeli, A. Rubio, T. Pichler, The doping of carbon nanotubes with nitrogen and their potential applications, Carbon. 48 (2010) 575–586. https://doi.org/10.1016/j.carbon.2009.10.009.

[35] J.M. Romo-Herrera, B.G. Sumpter, D.A. Cullen, H. Terrones, E. Cruz-Silva, D.J. Smith, V. Meunier, M. Terrones, An atomistic branching mechanism for carbon nanotubes: Sulfur as the triggering agent, Angewandte Chemie - International Edition. 47 (2008) 2948–2953. https://doi.org/10.1002/anie.200705053.

[36] a Chuvilin, E. Bichoutskaia, M.C. Gimenez-Lopez, T.W. Chamberlain, G. a Rance, N. Kuganathan, J. Biskupek, U. Kaiser, a N. Khlobystov, Self-assembly of a sulphur-terminated graphene nanoribbon within a single-walled carbon nanotube., Nature Materials. 10 (2011) 687–692. https://doi.org/10.1038/nmat3082.

[37] J. Guo, Y. Xu, C. Wang, Sulfur-Impregnated Disordered Carbon Nanotubes Cathode for Lithium Sulfur Batteries.pdf, Nano Letters. 11 (2011) 4288–4294.

[38] P.A. Denis, R. Faccio, A.W. Mombru, Is it possible to dope single-walled carbon nanotubes and graphene with sulfur?, ChemPhysChem. 10 (2009) 715–722. https://doi.org/10.1002/cphc.200800592.

[39] M. Baro, S. Ramaprabhu, Multi-edged wrinkled graphene-like carbon-wrapped carbon nanotubes and highly conductive Pt-free counter electrode for dye-sensitized solar cells, Journal of Nanoparticle Research. 16 (2014). https://doi.org/10.1007/s11051-014-2711-9.

[40] P.Y. Chen, J. Sodhi, Y. Qiu, T.M. Valentin, R.S. Steinberg, Z. Wang, R.H. Hurt, I.Y. Wong, Multiscale Graphene Topographies Programmed by Sequential Mechanical Deformation, Advanced Materials. 28 (2016) 3564–3571. https://doi.org/10.1002/adma.201506194.

[41] E. Munoz-Sandoval, N. Perea-Lopez, R. Lima-Juarez, G.J. Labrada-Delgado, B.A. Rivera-Escoto, A. Zamudio, H.G. Silva-Pereyra, E. Robles-Avila, M. Terrones, Synthesis, characterization and magnetic properties of Co@Au core-shell nanoparticles encapsulated by nitrogen-doped multiwall carbon nanotubes, Carbon. 77 (2014) 722–737. https://doi.org/10.1016/j.carbon.2014.05.077.

[42] A.C. Ferrari, J. Robertson, Resonant Raman spectroscopy of disordered, amorphous, and diamondlike carbon, Physical Review B. 64 (2001) 075414. https://doi.org/10.1103/PhysRevB.64.075414.

[43] F. Cervantes-Sodi, G. Csányi, S. Piscanec, A.C. Ferrari, Edge-functionalized and

substitutionally doped graphene nanoribbons: Electronic and spin properties, Physical Review B - Condensed Matter and Materials Physics. 77 (2008). https://doi.org/10.1103/PhysRevB.77.165427.

[44] V. Georgakilas, M. Otyepka, A.B. Bourlinos, V. Chandra, N. Kim, K.C. Kemp, P. Hobza, R. Zboril, K.S. Kim, V. Georgakilas, M. Otyepka, A.B. Bourlinos, V. Chandra, N. Kim, K.C. Kemp, P. Hobza, R. Zboril, K.S. Kim, Functionalization of Graphene : Covalent and Non- Covalent Approaches , Derivatives and Applications Functionalization of Graphene : Covalent and Non-Covalent Approaches , Derivatives and Applications, Chemical Reviews. 112 (2012) 6156–6214. https://doi.org/10.1021/cr3000412.

[45] X. Zhao, Y. Ando, L.C. Qin, H. Kataura, Y. Maniwa, R. Saito, Multiple splitting of G-band modes from individual multiwalled carbon nanotubes, Applied Physics Letters. 81 (2002) 2550–2552. https://doi.org/10.1063/1.1502196.

[46] M. Bruna, S. Borini, Observation of Raman G -band splitting in top-doped few-layer graphene, Physical Review B - Condensed Matter and Materials Physics. 81 (2010) 1–7. https://doi.org/10.1103/PhysRevB.81.125421.

[47] Z. Luo, S. Lim, Z. Tian, J. Shang, L. Lai, B. MacDonald, C. Fu, Z. Shen, T. Yu, J. Lin, Pyridinic N doped graphene: synthesis, electronic structure, and electrocatalytic property, Journal of Materials Chemistry. 21 (2011) 8038. https://doi.org/10.1039/c1jm10845j.

[48] G. Huang, L. Yang, X. Ma, J. Jiang, S.H. Yu, H.L. Jiang, Metal-Organic Framework-Templated Porous Carbon for Highly Efficient Catalysis: The Critical Role of Pyrrolic Nitrogen Species, Chemistry - A European Journal. 22 (2016) 3470–3477. https://doi.org/10.1002/chem.201504867.

[49] D. Guo, R. Shibuya, C. Akiba, S. Saji, T. Kondo, J. Nakamura, Active sites of nitrogen-doped carbon materials for oxygen reduction reaction clarified using model catalysts, 351 (2016) 361–365.

[50] T. Sharifi, G. Hu, X. Jia, T. Wagberg, Formation of active sites for oxygen reduction reactions by transformation of nitrogen functionalities in nitrogen-doped carbon nanotubes., Preprints - American Chemical Society, Division of Energy & Fuels. 58 (2013) 1203–1204. https://doi.org/10.1021/nn302906r.

[51] D.L. Duong, G.H. Han, S.M. Lee, F. Gunes, E.S. Kim, S.T. Kim, H. Kim, Q.H. Ta, K.P. So, S.J. Yoon, S.J. Chae, Y.W. Jo, M.H. Park, S.H. Chae, S.C. Lim, J.Y. Choi, Y.H. Lee, Probing graphene grain boundaries with optical microscopy, Nature. 490 (2012) 235–239. https://doi.org/10.1038/nature11562.

[52] M.S. Dresselhaus, A. Jorio, M. Hofmann, G. Dresselhaus, R. Saito, Perspectives on carbon nanotubes and graphene Raman spectroscopy, Nano Letters. 10 (2010) 751–758. https://doi.org/10.1021/nl904286r.

[53] A.C. Ferrari, D.M. Basko, Raman spectroscopy as a versatile tool for studying the properties of graphene, Nat Nanotechnol. (2013) 1–13. https://doi.org/10.1038/nnano.2013.46.

[54] P. Tan, S. Dimovski, Y. Gogotsi, Raman scattering of non-planar graphite : arched edges , polyhedral crystals , whiskers and cones, Phil. Trans. R. Soc. Lond. A. 362 (2004) 2289–2310.

[55] J. Bin Wu, M.L. Lin, X. Cong, H.N. Liu, P.H. Tan, Raman spectroscopy of graphene-based materials and its applications in related devices, Chemical Society Reviews. 47 (2018) 1822–1873. https://doi.org/10.1039/c6cs00915h.

[56] M.S. Dresselhaus, G. Dresselhaus, R. Saito, A. Jorio, Raman spectroscopy of carbon nanotubes, Physics Reports. 409 (2005) 47–99. https://doi.org/10.1016/j.physrep.2004.10.006.

[57] C. Casiraghi, A. Hartschuh, H. Qian, S. Pliscanec, C. Georgia, A. Fasoli, K.S. Novoselov, D.M. Basko, A.C. Ferrari, Raman spectroscopy of graphene edges, Nano Letters. 9 (2009) 1433–1441. https://doi.org/10.1021/nl8032697.

[58] A. Das, S. Pisana, B. Chakraborty, S. Piscanec, S.K. Saha, U. V Waghmare, K.S. Novoselov, H.R. Krishnamurthy, A.K. Geim, A.C. Ferrari, A.K. Sood, Monitoring dopants by Raman scattering in an electrochemically top-gated graphene transistor, 3 (2008) 1–6. https://doi.org/10.1038/nnano.2008.67.

[59] M.I. Ionescu, Y. Zhang, R. Li, H. Abou-Rachid, X. Sun, Nitrogen-doping effects on the growth, structure and electrical performance of carbon nanotubes obtained by spray pyrolysis method, Applied Surface Science. 258 (2012) 4563–4568. https://doi.org/10.1016/j.apsusc.2012.01.028.

CHAPTER FOUR:

INFLUENCE OF CU IN THE GROWTH OF HELICAL CARBON NANOSTRUCTURES AND STACKED GRAPHENE CARBON NANOFIBERS

4.1 Introduction

In the last three decades, carbon nanotubes and graphene have attracted the attention due to their outstanding physical-chemical properties [1–5] and their potential application in electronics systems [6–8], sensors [9,10], energy devices [11–13], and biomaterials [14]. While for the production of carbon nanotubes has been led by different version of chemical vapor deposition (CVD) [15–20], the production of graphene has been performed using different techniques such as CVD [21–23], silicon carbide sublimation [24,25], molecular monomer coupling [26,27], liquid-phase exfoliation [28–30], and also mechanical exfoliation [31]. Nevertheless, the low cost, large mass production, good reproducibility, and easily in the process control make the CVD a viable method to produce and modify carbon nanostructures.

Three of the most used catalysts for the synthesis of carbon nanostructures are cobalt [32,33], nickel [34,35], and iron [36,37]. Cu is mostly used for the synthesis of graphene due to low carbon solubility values (<0.0001 % at.), low cost and easy manipulation [38]. Li *et al.* [39] improved the synthesis of large-area graphene using copper foils (25 μm thickness) as a catalyst in a CVD system at 1000 °C. They found that the graphene growth is self-limited to the Cu surface foil and it grows mainly by a surface-catalyzed reaction rather than by a precipitation process. They also found that during the cooling process the precipitation of carbon atoms increases the number of graphene layers. Cu foils have been used as a substrate for the growth of another type of carbon nanostructures [40,41]. For instance, Atthipalli *et al.* [42] reported the use Ni and Inconel films deposited on Cu-foil substrate to be used in a CVD system to fabricate multiwalled carbon nanotubes (MWCNTs) with a mixture of xylene and ferrocene as precursors. They showed that Inconel substrate interacts directly with the copper substrate and influence the growth of dense bundles of MWCNTs leading to high capacitive behavior ideal for supercapacitor applications. Lahiri *et al* [43]. used Cu-foils to deposit Ti and Ni layers to grow well-aligned MWCNTs by CVD method. The obtained MWCNT material was used into an emission field equipment. They found that the MWCNT-Cu material has a high resistance to structural damage and good emission stability. Nevertheless, the engineering of growing carbon tubular nanostructures over copper substrates to be utilized as a catalyst is open to research and developing [44]. For example, Zhu *et al.* [45] described the formation of bamboo-like CNTs over Cu-foil (without any modification) at different temperatures using a CVD system and ethanol as a precursor. They concluded that the formation of Cu nanoparticles (NPs) migrated from the Cu substrate was responsible for the formation of the carbon tubular structure.

Following the above investigations, in this work, we analyze the different carbon nanomaterials grown on Cu-foils placed alongside the reactor in a CVD experiment. We have found that a diverse carbon nanostructure can grow depending on the position where the Cu-foil was located at the reactor. In particular, herringbone-like stacking and helical structures were fabricated for the first time in Cu-foils using ethanol as only carbon source. Also, pre-treatments such as sonication and reduction of Cu-foils play a crucial role in the growth of carbon materials. In the following, the experimental setup, the characterization techniques, result discussion, and conclusions will be addressed.

4.2 Methodology for the use of Cu films in a CVD system

Cu foils of 0.25 mm thickness (Aldrich, 99.99%) were used as a substrate to grow carbon nanomaterials. Rectangular pieces of 4cm × 1 cm of Cu-foil were cleaned in an ultrasonic bath by using sequentially ethanol (96.5% - CTR Scientific), isopropanol (96 % - CTR Scientific) and acetone (99.97 % - CTR Scientific) for 1 hour each. The use of ethanol and isopropanol is for The Cu-foil pieces were dried for 5 min at 65 °C inside a convection oven. To prevent any trace of copper oxide on the surface of cleaned Cu-foils, they were reduced inside a quartz tube of 1.1 m long by using a mixture of 5 % w/w H_2/Ar flow at 0.1 l/min. After that, six Cu-foils were placed along the quartz tube with a separation distance of 5 cm and classified as S1 to S6 being S1 the closest to the gas inlet. During the vapor-catalytic chemical vapor deposition (VC-CVD) experiment, the ethanol vapor was transported by a gas mixture of H_2/Ar with a flow rate of 1.0 l/min. The synthesis process is maintained at 980 °C for 1 hour. All samples were characterized using a Helios Nanolab 600 Dual Beam with a backscattered electron detector (BSE-SEM) and secondary electron detector for scanning electron microscopy (SEM), a Tecnai F30 for high-resolution transmission electron microscopy (HRTEM). To study the quality of samples a Renishaw micro Raman spectrometer with 532 nm excitation laser wavelength was employed. To determinate the surface chemistry Fourier transformed Infrared Spectroscopy (FTIR) was developed in a Thermo-Scientific Nicolet 6700 equipment at a scan of 128 with an ATR tip. The crystalline phases were determined using an X-ray diffractometer Bruker D8 Advance in a wide-angle X-ray scattering (WAXS) and small-angle X-ray scattering (SAXS) configurations. The furnace temperature profile was measured every two centimeters inside the furnace employing a K-type thermocouple with a stainless steel probe of 50 cm length and 3 mm diameter. For the electrochemical measurements, a saturated Calomel electrode (E = 0.241 NHE) was used as a reference electrode and the Cu-foils with carbon materials grown on their surface were used as a working electrode. A Pt gauze was used as contra electrode. The cyclic voltammetry measurements were performed by using a KCl 0.5 M solution as support electrolyte, in a potential window from -0.7 V to 0.7 V at a scan rate of 20 mV/s.

4.3 Position influence in the growth of helical carbon nanostructures

Figure 4.1a displays the position of the Cu foils (S1 to S6). Notice that S5 is partially inside the furnace, whereas S6 is completely out of the furnace. From temperature profile alongside the reactor (figure 4.1b) we found that the temperature at the zone where S6 was placed (317 °C) is really smaller than at zone where S3 was 949 °C.

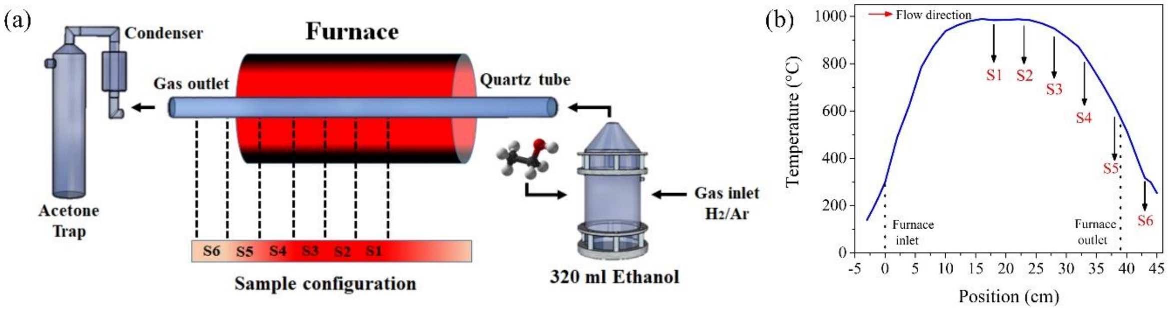

Figure 4.1: (a) Schematic representation of the vapor-catalytic chemical vapor deposition system (VC-CVD). Six Cu-foils were located alongside the quartz tube (reactor), which were labeled by S1, S2, S3, S4, S5, and S6. The ethanol vapor was transported by a gas composed by H_2/Ar (5% / 95% wt/wt). **(b)**The furnace temperature was kept at 960 ºC and the temperature profile alongside the furnace can be seen in.

Figure 4.2 shows the carbon material grown alongside the reactor. In S1 (figure 4.2a), it is observed the presence of carbon nanotubes with diameters of ~50 nm, carbon nanowalls, and multilayer graphene-wrapped Cu-NPs (see figure 4.2a). In S2 to S4 (figure 4.2b-4.2d), Cu-NPs coalesced, making large Cu aggregates that were surrounded by small Cu-NPs and partially covered by possibly carbon material. Few carbon nanotubes are also found. We believe that ethanol thermal decomposition in ethylene and water played a crucial role in the state of these small Cu-NPs [46]. Ethanol is probably decomposed at the beginning of furnace and ethylene and water vapor travel to S1 and S2, forming carbon-like films (Figure 4.2a, and 4.2b). Apparently, in this zone, there is no reaction because the temperature is stable (Figure 4.1b). However, at S3 the temperature starts to diminish, and in S4 the change is abrupt. S3 micrograph apparently shows 200 nm diameter carbon formations at the surface (Figure 4.2c). In the case S4, the carbon-like structures are more disordered and it is possible to observe agglomerates of small nanoparticles (~18 nm) immerse in that carbon-like formations (Figure 4.2d). In this site, the reduction of temperature possibly provokes the formation of nanoparticles at the surface whose size (~15 nm) is ideal for the growth of CNTs at such temperature [47] (figure 4.2e-4.2f). At S5 and S6 this situation is more important than at S3 and S4. The water vapor and ethylene are cooling and could react with the small Cu nanoparticles forming the nanostructures observed. It can be noted that such nanostructures present similar diameter than the nanoparticles.

Similar structures were also found by Verissimo *et al.*[48] reported the growth of carbon helical structure or nanocoils on partially oxidized Ni films. Also, Cui *et al.*[49] fabricate long single-walled CNT over Cu nanoparticles over Si/SiO_2 substrate and found that the carbon nanostructures obtained are due the nucleation of small copper nanoparticles over the edge of a silicon substrate. Qin *et al.* [50] grew CNFs with helical morphology, but they used acetylene as carbon source and copper tartrate for the nucleation of the copper catalyst. It seems that the sizes and configuration of Cu-NPs strongly depend on the position of SN (N = 1-6) that were placed (see Figure 4.3). For example, in S1 at 960 °C can be observed Cu NPs agglomerates surrounded by graphitic materials and apparently over carbon films (figure 4.3a). In S3 (figure 4.3b), decreases the formation of Cu-NPS agglomerates over carbon layers. For S4 (figure 4.3c), the continuity of carbon film is lost and Cu-NPs can be observed with less carbon coating. S6 (figure 4.3d) is where Cu-NPs are distributed with a bimodal size distribution of ~15 nm and ~ 150 nm. They are also covered partially with carbon materials. Zhu *et al.* [45] explained that the formation of Cu-NPs could be due to the diffusion through the graphite carbon layers. This situation was studied by Jackson *et al.* [51] where they concluded that migration of Cu could be due to a high interaction with graphite and through porous carbon layers.

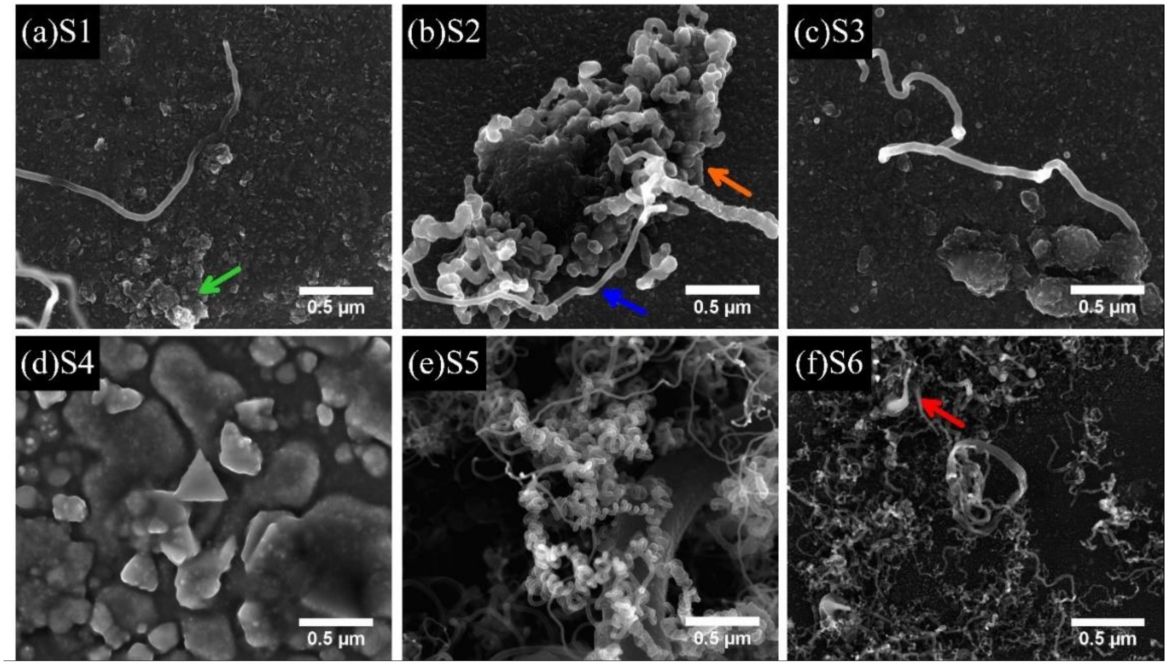

Figure 4.2: Different carbon nanostructures were grown alongside the reactor (S1-S6). **(a)** S1: Cu-NPs surrounded by graphite and graphite oxide, as confirmed by XRD. **(b)** S2: short carbon nanofibers. **(c)** S3: showing the presence of Cu-NPs covered by graphite material and tubular carbon nanostructures. **(d)** S4: large Cu-NPs surrounded by carbon films materials. **(e)** S5 showing the presence of helical carbon nanotubes and ultra-thin carbon nanotubes. **(d)** S6 exhibiting thin carbon nanotubes and defective Cu-NPs.

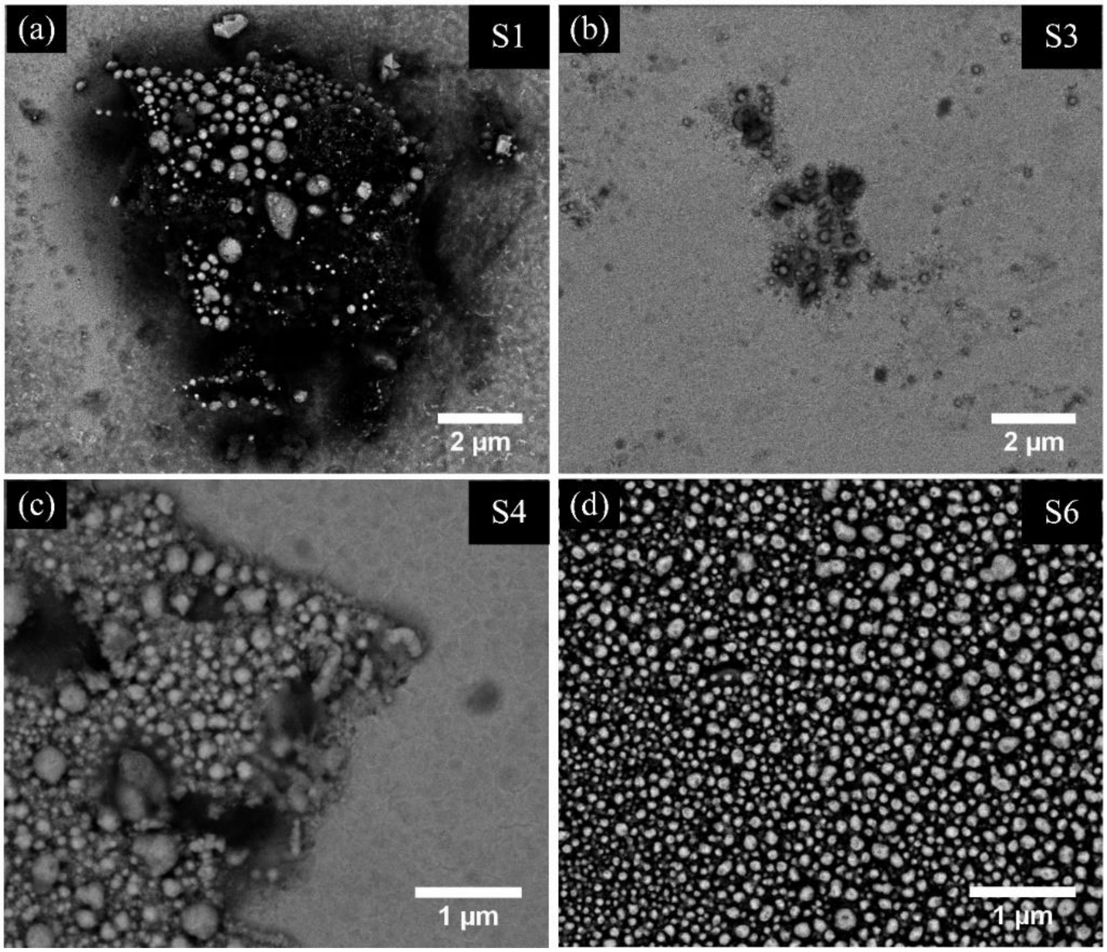

Figure 4.3: SEM images in the backscattered mode for (a) S1, (b) S3, (c) S4, and (d) S6, revealing the presence of Cu-NPs (the brightest regions).

Figure 4.4a depicts the XRD patterns for S1-S6, exhibiting mainly three peaks attributed to Cu-FCC crystal (PDF card 00-004-0836) with the (111) preferential crystallographic plane. The intensities corresponding to the Cu (200) peak were also measured. In this case, the intensity increases for S2 but then linearly decreases for S3, S4, S5, and S6 (figure 4.4b). This plane has been critical to growth continuous polycrystalline graphene structure [52], but Cu (111) is used to obtain oriented graphene growth. The theoretical ratio between Cu(111) and Cu(200) is approximately 2.21. In our case, only in S1 is observed such value (figure 4.4c). In other cases, there is a preferential growth of the Cu(111) crystal size (obtained by Shcherrer equation) as the temperature decreases (figure 4.4d). Figure 4.4e illustrates a considerable intensity reduction of the Cu (220) peak intensity for S5 (Table 4.1), increasing the Cu(111)/Cu(220) ratio. Ogawa *et al.* [53] reported the growth of graphene on Cu-films. They found that the multidomain graphitic structure is grown on the Cu(100) face.

Furthermore, the intensity reduction of the Cu(200) for samples collected near the furnace outlet (S5 and S6) could be attributed to the growth of Cu-NPs that derive in faceted nanoparticles with well-determined planes over the Cu(111). For S5 and S6, lattice planes of (111), (200), and (220) correspond to Cu_2O in an FCC crystal (PDF 01-077-7719). Probably, the decomposition process of the ethanol and the formation of copper oxide over the surface play an important role in the process of the helical nanostructure and carbon nanofibers growth [54,55]. Inspection on the XRD patterns at low angles revealed the presence the (002) crystal plane, typical of graphite materials (PDF-03-065-6512), see Figure 4.4f. This C(002) peak was clearly identified for S1 and probably S6. Interestingly, presence in S1 of expanded graphite materials was also identified at $2\theta=14.13°$, which corresponds to an interlayer distance of 6.24 Å. This is clear evidence of the presence of graphite oxide [56]. Additionally, another signal at $2\theta=16.8°$ correspond to an interlayer distance of 5.27 Å could be associated with poor oxidized graphite [57].

Table 4.1: S1 to S6 XRD Intensities of crystal planes for the Cu–FCC structure (PDF card 00-004-0836).

Sample	**Normalized Intensity (111)**	**Normalized Intensity (200)**	**Normalized Intensity (220)**
S1	1.00	0.44	0.11
S2	1.00	0.82	0.44
S3	1.00	0.66	0.16
S4	1.00	0.37	0.10
S5	1.00	0.27	0.04
S6	0.95	0.18	1.00

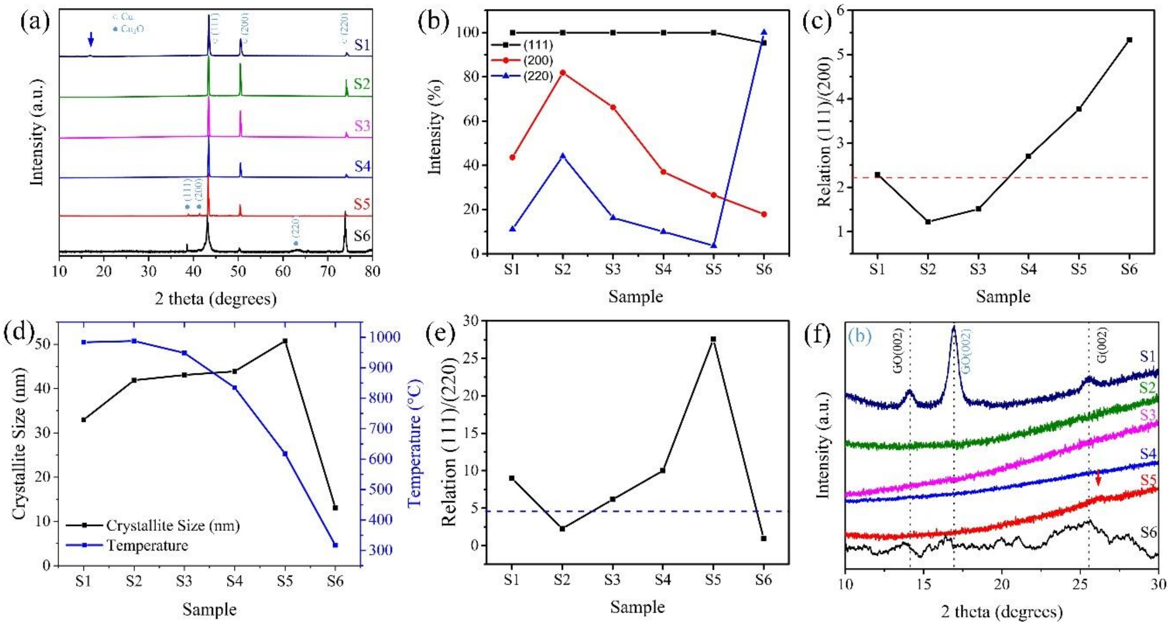

Figure 4.4: (a) XRD patterns for S1-S6 with mainly a Cu-FCC phase (PDF 00-004-0836). **(b-e)** Normalized intensities of the different crystallographic planes obtained from the XRD patterns. Cu(111) plane (square symbols), Cu(200) crystallographic plane (circle symbols) and Cu(220) crystallographic plane (triangle symbols). Notice that the intensity of Cu(200) and Cu(220) crystallographic planes for samples S5 and S6 the dotted line indicates the theoretical ratio for reference Cu-FCC phase material (PDF 00-004-0836). Also, the measurement of crystallite size using the Scherrer equation and temperature versus position. **(f)** Close up inspection in the 10-30 degrees range revealed the presence of three peaks in S1, these signals correspond to the (002) crystallographic plane, typical of graphitic material (25.8 °), the (002) crystallographic plane attributed to graphite oxide (14.1 °) and graphite poorly oxidized (16.8 °).

A Raman spectrum is a fingerprint of the different graphite material grown on the Cu-foils. We have identified different features of the Raman spectra according to the Cu-foil position in the furnace (see figure 4.5a). The samples exhibited the typical bands of graphite materials revealing exciting trends. The D-band that is attributed to defected graphite materials revealed changes in intensity and width in the different samples. In the cases of S2, S3, S4, and S5, the intensity increases with a narrow shape related to the formation of nanocrystalline graphite[58]. For S1 and S6, D bands with low intensities and wide bands were observed. However, the G band for all cases is relatively wide, being more appreciable in S4, S5, and S6. The ratio between the D band intensity (I_D) and G band intensity (I_G) provides a quantification of the defects in graphitic materials. Therefore, large values of I_D/I_G mean that defects dominate. Notice that S1 and S6 exhibited the lowest values of I_D/I_G revealing the presence of well-ordered graphite material (S1) and low sp^3 amorphous or turbostratic carbon (S6) [59]. S5 showed the most significant value of $I_D/I_{G,}$ indicating a high degree of defects (table 4.2). This increase could be due likely to the inter-walls interaction and lattice distortion on the helical nanostructures [60]. Figure 4.5b depicts the FTIR analysis developed on the Cu foils at different positions. For S1 the presence of C-O from ether configuration (~1050 cm^{-1}) is observed. For S2 to S6 the C=C bond (~1510 cm^{-1}) is well appreciated. This C=C bond is related to the formation of the graphitic structure. A magnification of the stretching vibrations due C-H bond (doublet at ~2900 cm^{-1}) and the C-H rock vibration (780 cm^{-1}) could be related to a continuous hydrogenation process of edges and sp^3 carbon hybridization. Also, the presence of C-O bonds at 2200 cm^{-1}, 1250 cm^{-1}, and 1050 cm^{-1} are related to the formation of carbon monoxide and ether structures, respectively. These compounds can be associated with water formation and interaction with C [17].

A detailed analysis of D- and G-bands is shown in figure 4.6, where both peaks were deconvoluted using Lorentz curves. In almost all cases, five Lorentz curves were necessary to adjust the Raman spectra, except to S1 where only four were used. The interpretation of the different Lorentz curves has been widely discussed in the literature[61–64]. D1-band is related to the influence of C-sp^3 hybridization, D-band, which correspond to the defects, D2-band attributed to C-H bonds, D3-band associated with C-OH bonds at the surface, G band represent the C=C bonds into graphite material, and D´-band is associated to the dispersive vibration mode. It is clear from figure 4.6 that the width and intensity of the Lorentz curves change in each sample. The area under each Lorentz curve provides an estimation of the different carbon material involved in the sample. For S6, absence of the D´-band and the appearance of the D3-band could be associated with phenolic functionalization on the graphitic layer [65]. However, the deconvoluted bands are not enough to differentiate between tubular or laminar growing along the reactor. It is necessary for a more in-depth study of the role of Cu-foil and its effect on the growth of carbon samples.

Table 4.2: Peak position and intensity of the D, G, and 2D-bands and the ratio of intensities I_D/I_G and I_{2D}/I_G for S1 to S6. All data were derived from the Raman spectra deconvolution analysis using Lorentz distribution curves.

	D-band		***G-band***		***2D-band***		***Ratio***	
Sample	Pos	I (a.u.)	Pos	I (a.u.)	Pos	I (a.u.)	I_D/I_G	I_{2D}/I_G
S1	1351	3270	1602	3790	2713	470	0.8	0.1
S2	1357	4460	1591	2843	2706	2110	1.5	0.6
S3	1356	5308	1590	3237	2701	1260	1.6	0.2
S4	1357	3889	1589	2376	2704	835	1.6	0.2
S5	1357	7562	1594	4195	2705	1064	1.8	0.2
S6	1349	3056	1606	3169	2754	278	0.9	0.1

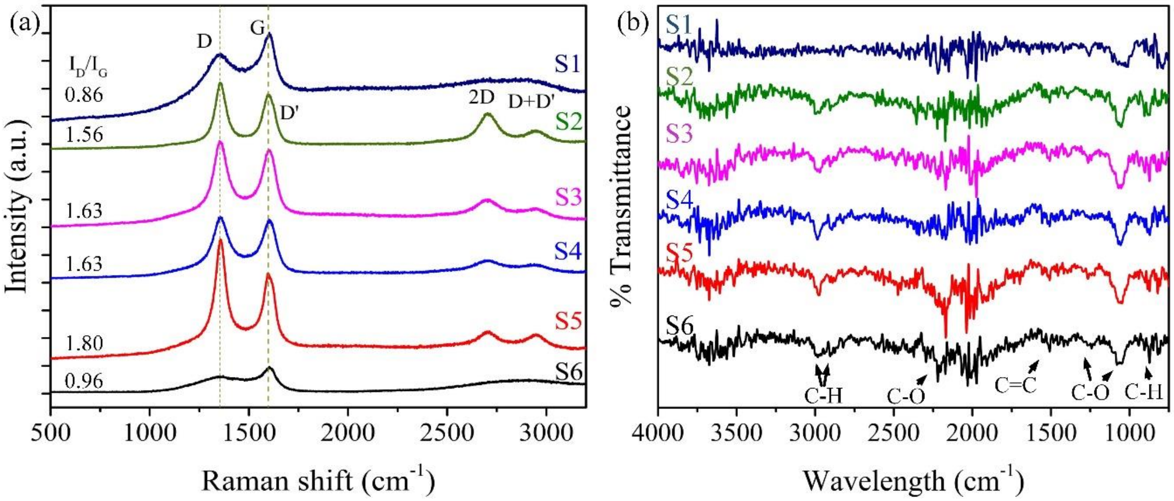

Figure 4.5: (a) Raman spectra depict structural variations through S1 to S6 where intensities I_D/I_G are indicated. (b) FTIR analysis developed through S1 to S6, where signals related to C-H, C-O, and C=C are observed.

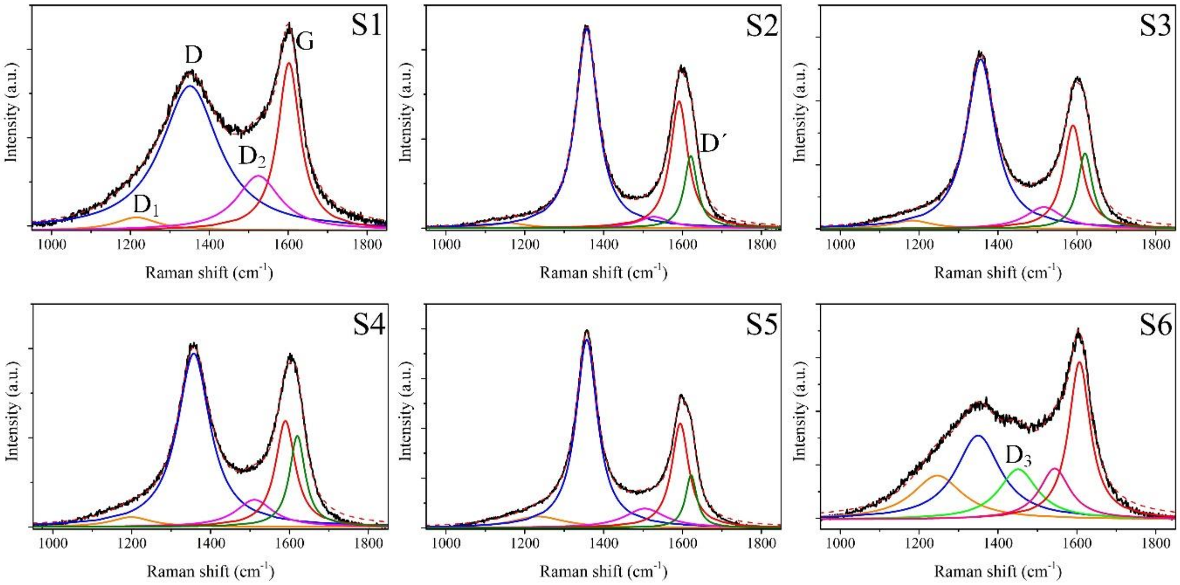

Figure 4.6: Deconvoluted Raman spectra from S1 to S6 in the range of 1000 cm^{-1} to 1850 cm^{-1}: D1-band (~1200 cm^{-1}) related to the influence of C-sp^3 hybridization, D band (~1350 cm^{-1}) which correspond to the defect formation, D2-band (~1510 cm^{-1}) linked with the C-H bonds, D3-band (~1450 cm^{-1}) linked with the C-OH bonds effect over the surface, G band (~1590 cm^{-1}) represent the C=C bonds in-plane vibration and the dispersive vibration mode D´-band (~1620 cm^{-1}).

The 2D region of the Raman spectra could help to understand more details of the graphitic nature over the samples. Figure 4.7 displays the deconvoluted 2D-band fitted using Lorentzian curves. The intensity of 2D-band decreases from S2 to S6 while the D+D´-band intensity remains the same. This D+D´-band is related to the high dispersive effect due to defects in the carbon structure [66]. This behavior is probably related to the growth of edges formation in the multiwalled helical nanostructure, nanocoil and nanotube graphitic structures (S5 and S6). In the case of the G*-band which is linked to surface roughness [67] , the area under the curve varies from S1 to S6, where S6 showed a higher relation value. This tendency is possibly associated with the Cu-NPs-graphite shell structure and strain effects observed in S6 [68,69]. The 2D´ band is regularly associated with the roughness surface aspects and corrugated morphology that were observed in S1 and S6 (table 4.3).

Table 4.3: Peak position and maximum high intensity (I) for the D1, D2, D3, and D´, G*. D+D´, 2D´-bands for S1 to S6. All data were derived from the Raman spectra deconvolution analysis using Lorentz distribution curves.

	D1		***D2***		***D3***		***D´***	
Sample	Pos	I (a.u.)	Pos	I (a.u.)	Pos	I (a.u.)	Pos	I (a.u.)
S1	1215	292	1524	1234	N.D.	N.D.	N.D.	N.D.
S2	1160	114	1527	254	N.D.	N.D.	1620	1619
S3	1182	257	1516	679	N.D.	N.D.	1620	2359
S4	1198	220	1511	608	N.D.	N.D.	1620	2042
S5	1234	457	1504	776	N.D.	N.D.	1621	2123
S6	1246	533	1543	1644	1451	1039	N.D	N.D.

	G*		***D+D'***		***2D'***	
Sample	Pos	I (a.u.)	Pos	I (a.u.)	Pos	I (a.u.)
S1	2583	135	2888	499	2986	240
S2	2477	121	2948	796	N.D.	-
S3	2466	102	2941	632	N.D.	-
S4	2478	117	2940	512	N.D.	-
S5	2523	94	2945	956	N.D.	-
S6	2625	142	2885	290	2998	180

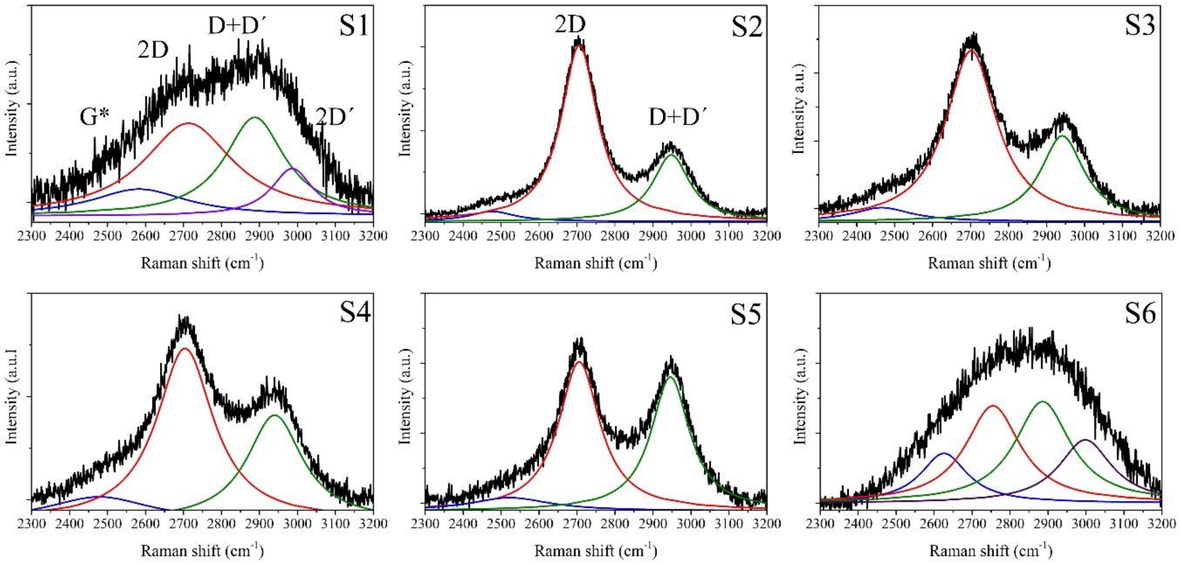

Figure 4.7: Deconvoluted Raman spectra for S1-S6 from 2300 cm^{-1} to 3200 cm^{-1} using Lorentz curves. Four vibration modes were identified G*-band at ~2500 cm^{-1}, 2D-band at ~2700 cm^{-1}, D+D´ band at ~2950 cm$^{-1,}$ and 2D´-band at ~3050 cm^{-1}.

Figure 4.8 shows SEM images revealing a diversity of carbon nanostructures grown in zone S5. Figure 4.8a shows a wide Y-shape carbon fiber with diameters of ~480 nm (red arrow), carbon tubular structures (blue arrow), and helical structures (green arrow) were also detected. Figure 4.8b displays a higher magnification of Figure 4.8a, showing clearly the helical nanostructure (green arrow) and very small ~17 nm diameter tubular nanostructures (blue arrow). Figure 4.8c displays 25 nm diameter curling CNTs from S5, where some of them are forming junctions (red arrows). The inset in this figure depicts the diameter distribution where CNTs with 15 nm to 40 nm were found. Figure 4.8d shows the helical structure with a continuous coil pitch of ~27 nm diameter and a coil diameter of ~ 50 nm. This type of structure was also observed by Yudasaka *et al.* [70] where they attributed this coil morphology to a strain effect due to the incorporation of aromatic nitrogen. In our case, without the presence of nitrogen in the structure, the coil effect could be attributed to diffusion variation over irregularly shaped nanoparticles leading to non-uniform extrusion promoting curvature on CNF and CNT.

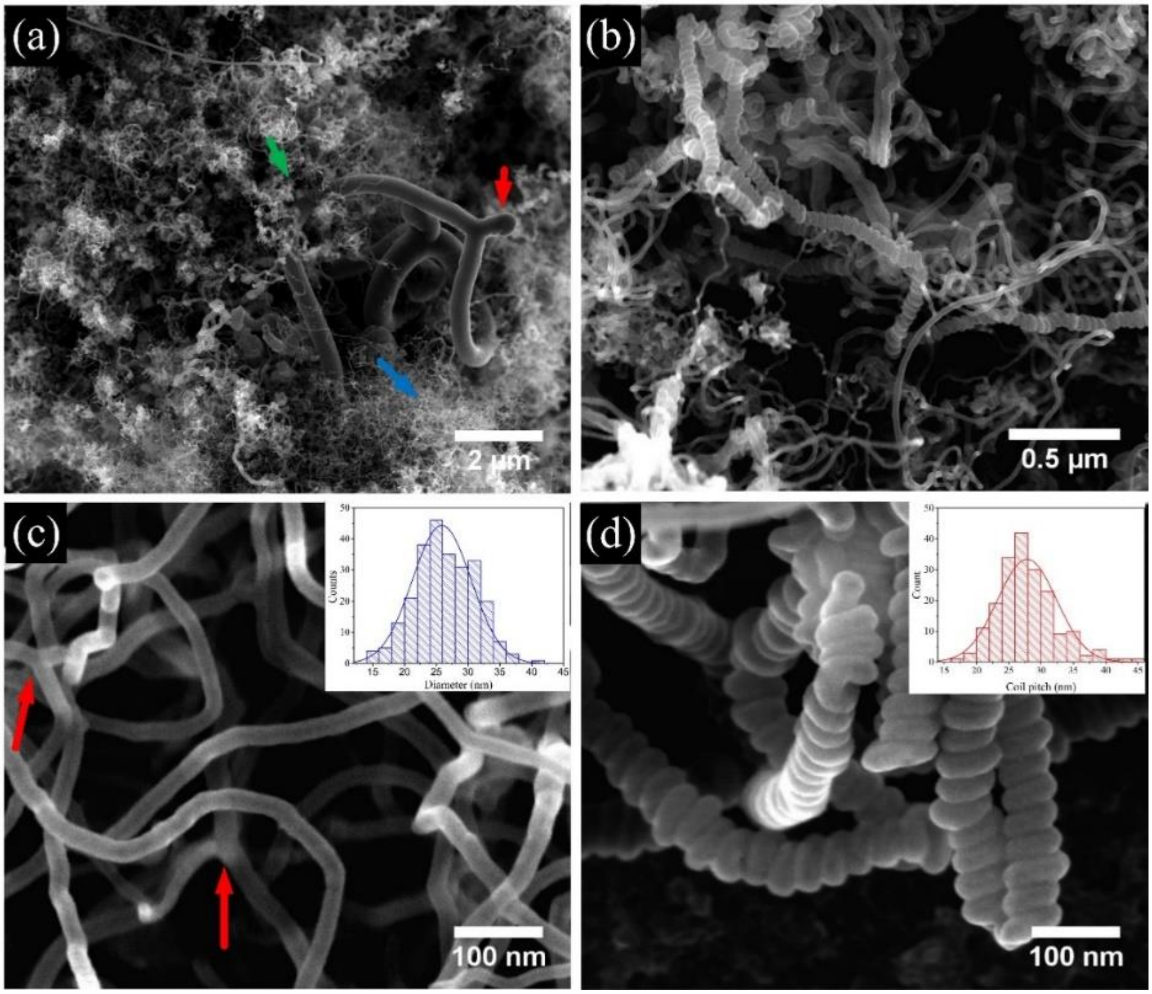

Figure 4.8: SEM images from S5. **(a)** Low magnification image showing carbon nano- and micro-materials. **(b)** Small diameter carbon nanotubes and helical carbon nanostructures. **(c)** High magnification images of multiwalled carbon nanotubes **(c)** and helical carbon structures **(d)**. The insets in **(b)** and **(c)** show the diameter and the coin pitch distributions, respectively.

Figure 4.9a depicts a TEM image of a helical nanostructure found in S5. This helical structure has a ~70 nm average coil irregular diameter and coil pitch of 19 nm; The inset is a representation of a continuous tubular coil structure with a helix angle of ~82°. Figure 4.9b micrograph corresponds to a smaller helical structure (~50 nm) were the helix angle (~73°) is slightly different as the showed in the inset. Figure 4.9c shows the cross-section of the helical structure, revealing the carbon layers. The inset in this figure demonstrates the presence of the layered carbon material (19 carbon layers). Figure 4.9d shows CNTs with a bamboo shape structure with surface irregularities corresponding to S5. Peng *et al.* [71] reported similar bamboo-like carbon nanotubes with diameters around ~100 nm, when Cu-foils was used as catalyst and ethanol was employed as the carbon feedstock in a CVD experiment. Our carbon nanotubes of around 30 nm (figure 4.9e) showed a defective bamboo-like and also curved structures. The inset shows the bamboo shape structure with tip termination of the CNT. The growth of curved graphitic layers could be promoted by the irregular shaped Cu-NPs with pointed shape [72,73]. Figure 4.9f illustrates the tip of a bamboo shape CNT where graphitic layers (3.64 Å) goes outside the tubular structure (yellow arrows), leading to border formation.

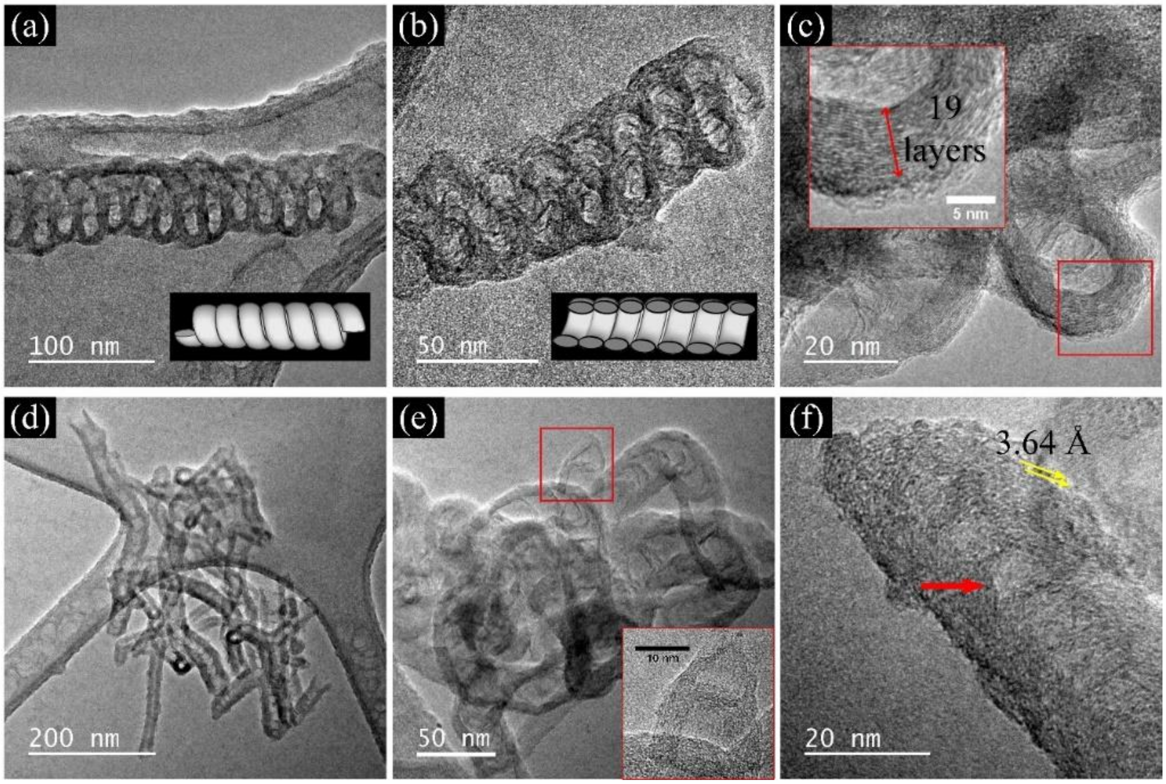

Figure 4.9: TEM and HRTEM images from S5. **(a-b)** Helical-tubular carbon nanostructure **(c)** Cross-section of the helical structure revealing ~19 graphitic layers. **(d-e)** Carbon nanotube with a deformed bamboo shape structure. **(f)** HRTEM image showing the graphitic layers of carbon nanotubes and deformed bamboo shape structures (red arrow).

Figure 4.10 displays HRTEM images of other carbon nanostructure found in S5. Figure 4.10a shows a carbon fiber-like built by a carbon layer arrangement adopting a herringbone-like stacking [74,75]. The carbon layers were stacked along with the axis carbon fiber (figure 4.10b). This peculiar stacking was possibly formed by spherical or semi-spherical with pointed edges Cu-NPs [76]. Figure 4.10c displays two encountered carbon nanotubes with a bamboo shape. It seems like they coalesced but with different orientations (see inset). These nanostructures have not been observed before, probably two almost coalesced Cu nanoparticles were oriented at different directions when catalyst this twin CNTs.

Figure 4.10d depicts carbon nanotubes with layer stacking very similar to those found in Figure 4.10a but they seem also attached to forming a double CNT. Cervantes-Sodi *et al.* [77] reported the synthesis of nanospring (helical structure) using SiO_2-iron nanoparticles as a catalyst and attributing the coil morphology anisotropy of micro catalyst surface and the different rates of carbon dissolution that causes a gradient in the fiber extrusion velocity. In our case, Cu-NPs shape and orientation could be responsible for the growth of carbon nanotubes and helical nanostructures. Also, Qin *et al.* [50] describe a reconstruction of Cu NPs can be reached at a temperature above 220 °C, (underwater and ethylene atmosphere preferable), leading to the lower surface energy formation following the crystallographic planes $\gamma\{111\} < \gamma\{100\} < \gamma\{110\}$ orientations. In our case, probably the decomposition of ethanol and the formation of water and ethylene increases the high oriented reconstructed Cu NPs (111) having its maxima over S5 and S6 (figure 4.4e). This situation led to the formation of highly oriented crystalline Cu-NPs. Water interaction with these amorphous C that coats and contaminates the Cu-NPS helps to its oxidation and removal, which increases its catalytic potential [78].

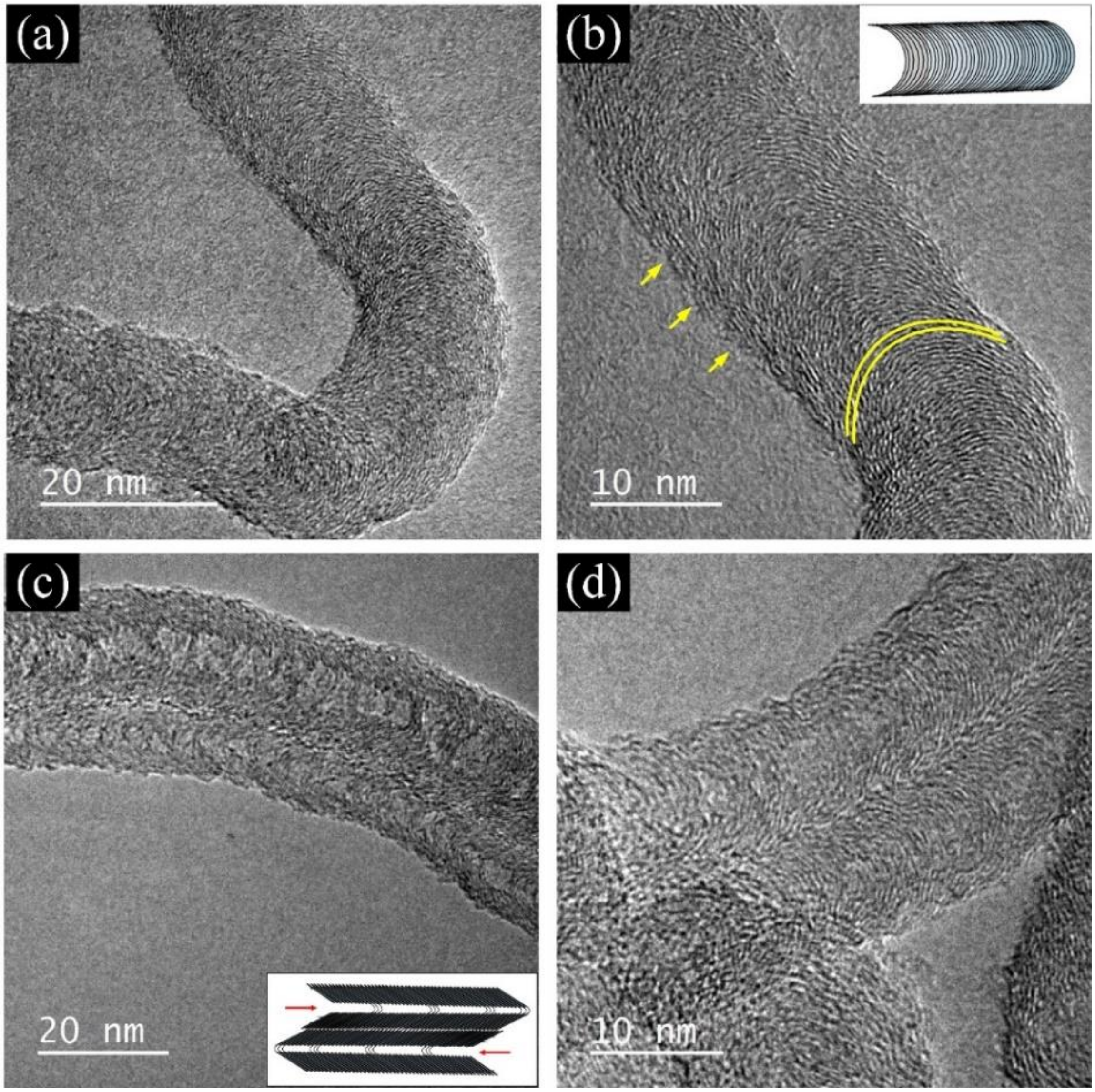

Figure 4.10: HRTEM images of carbon nanofibers from S5. **(a)** A continue stacking of short graphitic layers grown in one direction. Curved short graphitic layers were stacking, leading to high border formation (yellow arrow) **(b)**. **(c-d)** Graphitic layers with a bamboo shaped-herringbone stacking

Figure 4.11a shows a carbon layer covered spherical Cu-NP (100 nm diameter). Also very small Cu-NPs (~6 nm diameter, yellow arrows). It seems these small NPs are distributed in the body of CNTs and over the graphitic layers that cover the Cu-foil. Figure 4.11b depicts an HRTEM image of such Cu-NP of 5.9 nm diameter, and a detailed analysis of this particle is described in figure 4.11c, here the FFT analysis revealed the well-defined crystallographic directions. An inverse FFT analysis showed an interlayer distance of 2.65 Å, which corresponds to Cu (110) spacing of the FCC structure [79].

Figure 4.11d shows a TEM image of a ~60 nm Cu-NP inside at the tip of a helical nanostructure from S5. This Cu-NP presents an irregular shape with a thin film of CuO on the surface top. Notice that few graphite layers surround this Cu-NP. An interesting elongated conic-shape Cu-NP (60 nm base 200 nm long) inside carbon fiber is shown in figure 4.11e. This kind of morphology (conical-shaped nanoparticle) usually is characteristic of bamboo-like multiwall carbon nanotubes, and CNF fabricated with Fe and Fe_3C [80]. Figure 4.11d displays a Cu-NP with an irregular truncated large conical shape (500 nm high 200 nm base) nanoparticle associated with the formation of irregular "bamboo-shaped" curved carbon nanotubes. Considering the size and shape of the Cu-NPs, several authors have discussed the optimal size where diffusion of C atoms diffused over the Cu matrix. It has been found that semi-spherical ~10 nm diameter Cu-NPs nanoparticles lead to the CNT formation and particles of 100 nm ~ with preferred crystalline orientation over the Cu(111) plane with a pointed shape lead to herringbone fiber formation. Also, truncated conical particles are found to promote the bamboo-shaped CNT structure. This could be a consequence of a tip growth mechanism due to Cu special geometry[72,81]. These results are concomitant with our case. The smaller Cu-NPs lead to the formation of defective CNT followed by nanocoiled CNT and bigger shaped particles (> 40 nm) lead to the formation of herringbone fibers and herringbone CNTs. Figure 4.12 depicts a gallery of TEM images where nanoparticles of ~ 5 nm are diffused over the graphitic netwkork and attached over the walls of CNT and CNF.

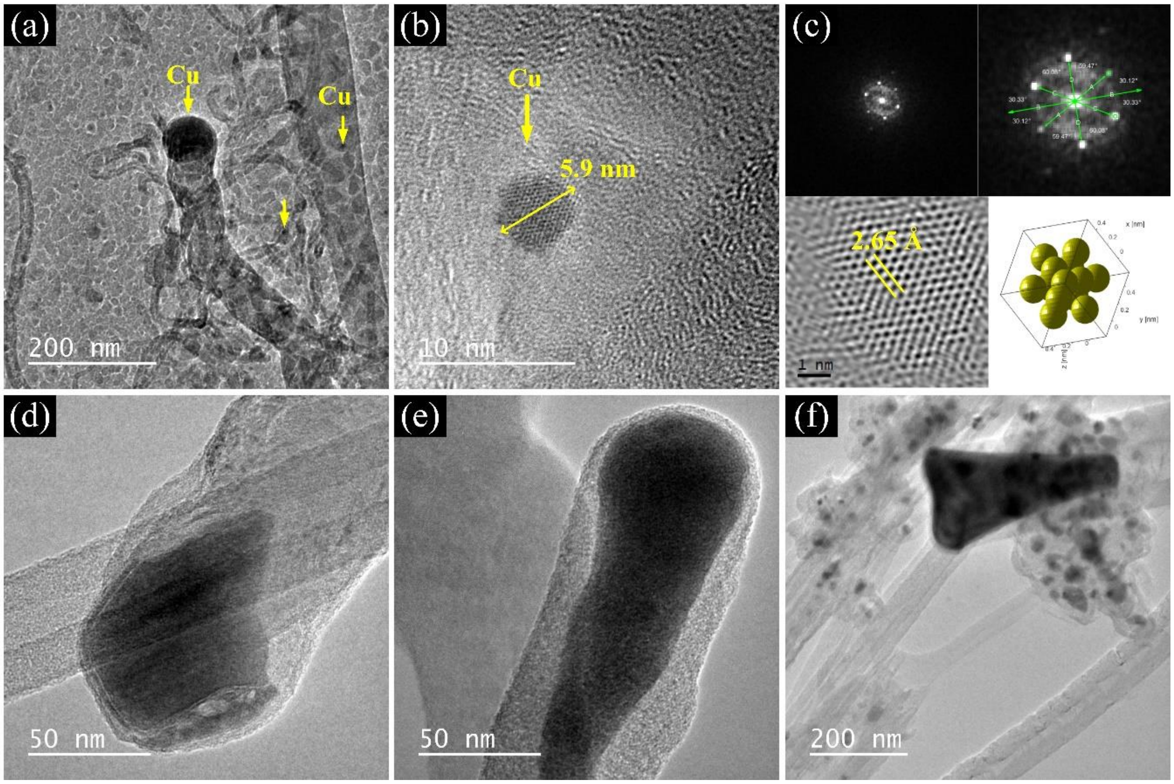

Figure 4.11: TEM and HRTEM images from S5. **(a)** Cu-NPs embedded into graphitic layers. **(b)** Cu-NP showing a single-crystal pattern and its corresponding FFT and I-FFT analysis are shown in **(c)**. **(d)** Cu-NP with irregular morphology. **(d)** Cu-NP with a conical shape. **(e)** Cu-NP with a truncated conical shape.

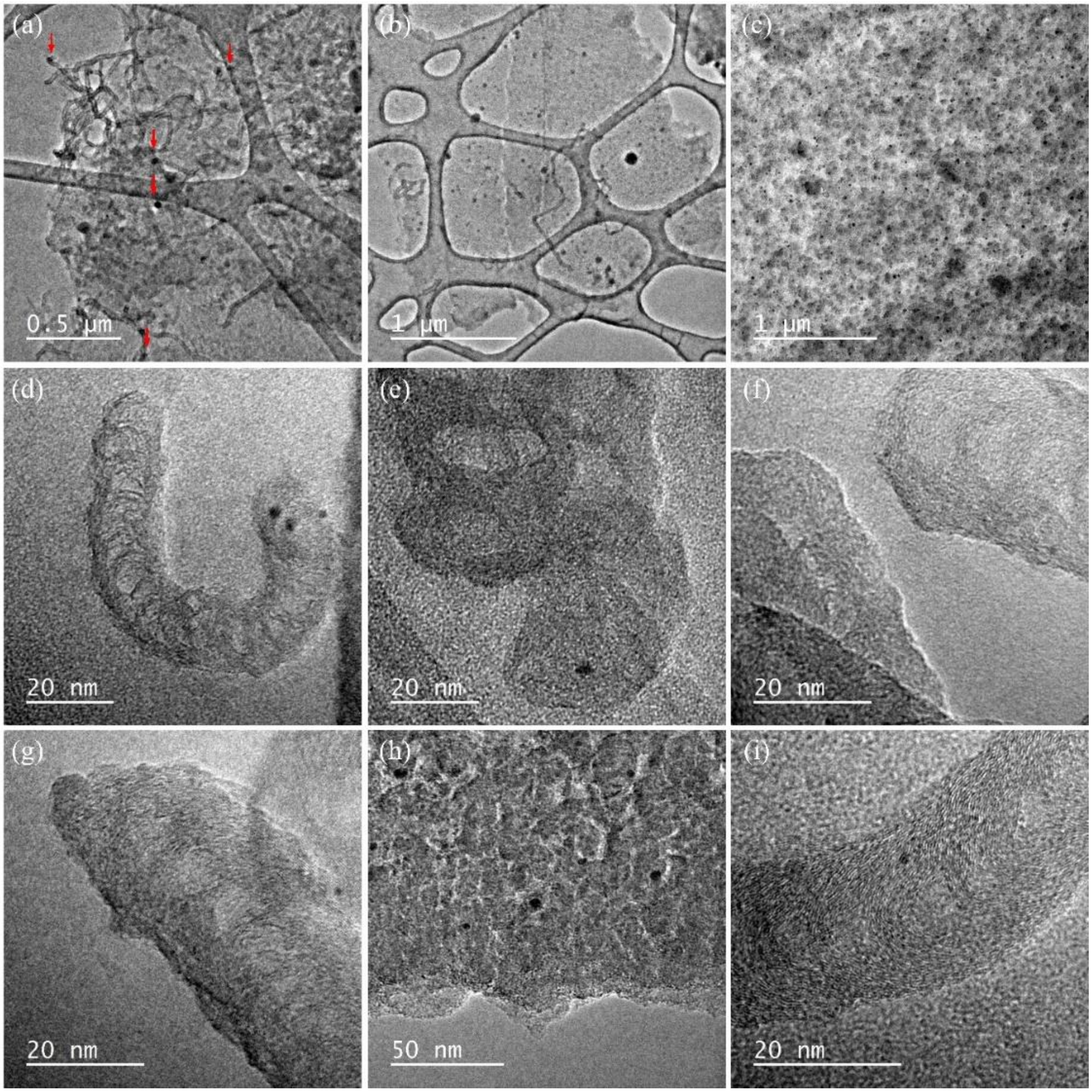

Figure 4.12: (a)-(c), (h) Cu NPs dispersed over the graphitic matrix, (d)-(g), (i) small nanoparticles diffused inside the carbon nanotubes.

4.4 Surface modification by a pretreatment over Cu films

In order to study their surface morphology, atomic force microscopy (AFM) characterization was performed on Cu-foils prepared and used to grow the carbon nanomaterial. Figure 4.13a shows atomic force microscopy images, revealing the surface relief with valleys and heights of the pristine Cu-foil (Cu-Ref). After the Cu-foils were sonicated using ethanol (Cu-Et) and isopropanol (Cu-Iso), no relative surface variation was observed as roughness average (Ra) did not change considerably (figure 4.13b and figure 4.13c respectively) which could be indicative of low surface interaction. Figure 4.13d shows the last sonication process using acetone. The sonication using acetone (Cu-Ace) exhibits damaged on their surface with irregular regions leading to a high surface roughness of 113 nm. However, after a reduction process (Cu-Red) at 700 °C, the Cu-foils surface showed a less rugged surface (figure 4.13e). The FTIR analysis (figure 4.13f) was developed in order to observe chemical damage over each cleaning process. For ethanol and isopropanol, O-H stretch vibration (~3100 cm^{-1}) are observed indicative of traces of alcohols over the surface. Nevertheless, no signals of copper oxide formation were observed. After the use of acetone, no more traces of alcohol were observed, but instead low hydrogenated and C-O interaction with the surface was observed probably due to the exfoliation and light reduction effect on the surface. The surface changes can be observed by SEM images in figure 4.14.

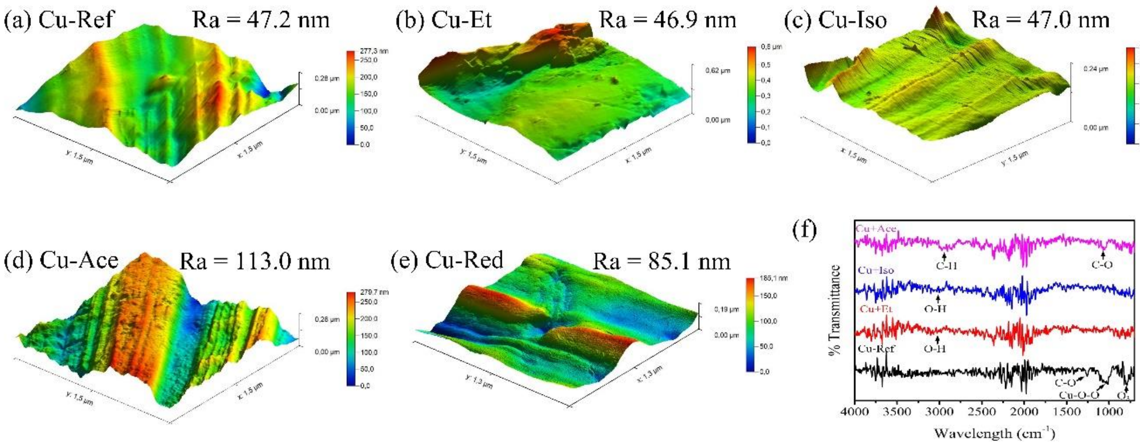

Figure 4.13: Atomic force microscopy images showing the roughness of the surface and surface roughness average (Ra). **(a)** Pristine Cu-foils. **(b)** Cu-foil after ethanol sonication treatment, (c) Cu foil after second cleaning step using isopropanol and after sonication. (d) Last cleaning process using acetone and after sonication **(e)** Cleaned Cu-foils after a reduction process. (f) FTIR analysis developed in each step of the Cu-foils cleaning process.

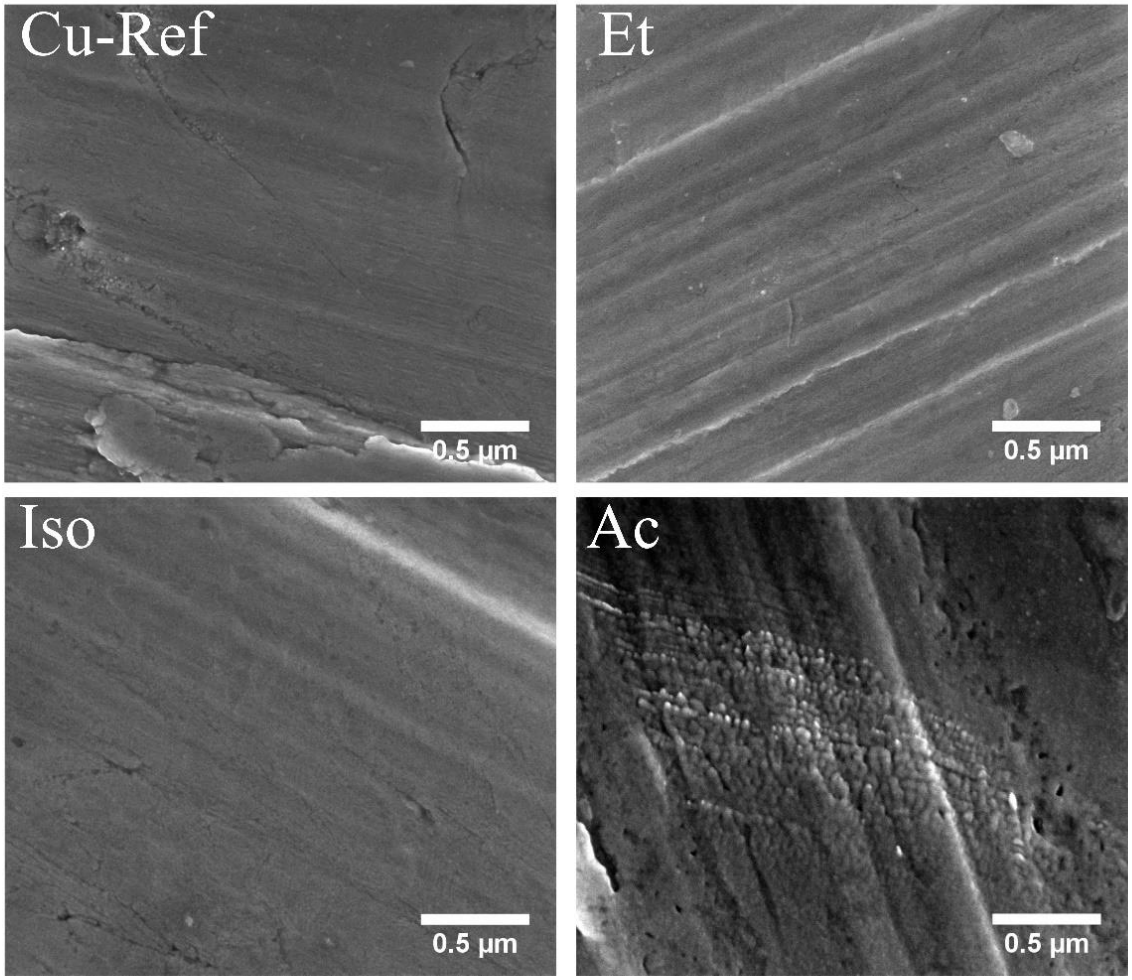

Figure 4.14: SEM micrograph of the Cu-foil after the cleaning and sonication procedure in each step using ethanol (Et), isopropanol (Iso) and Acetone (Ac).

Figure 4.15a displays the resistivity of Cu-foils with SN (N=1-6) measured by a four-probe arrangement. No meaningful changes were appreciated as the resistivity maintains values around the pristine Cu-foil value of 8.02×10^{-5} ohm-cm^{-2}, nevertheless the S2 showed higher resistivity (8.94×10^{-5} ohm-cm^{-2}). This could indicate a higher C/O ratio leading to a high resistance effect [82]. It can be noticed that in S5 with a high presence of helical nanostructure and the "bamboo-shaped" carbon nanotubes, the resistivity is less than that showed by pristine Cu-foil. Lau *et al.* [83] described that this type of coiled CNT structure could be considered as superconductors. Nevertheless, in this case, only a lightly enhanced conductivity was obtained. This can be associated with the coil carbon nanostructure and Cu-NPs formation. Figure 4.15b shows the results obtained from the cyclic voltammetry measurements, for pristine Cu-foil (ref) two anodic peaks were obtained near to 0.41 V and 0.59 V (black dotted line), these signals are related respectively to the oxidation reactions: $Cu \rightarrow Cu^{+1}$ and $Cu^{+1} \rightarrow Cu^{+2} + e^{-}$. Also, a cathodic signal was obtained at -0.16 V. For S5 containing helical nanostructures can be observed an increase in the voltamperogram width that can be related to an increase in surface capacitance of this material, that results in a displacement of the anodic/cathodic peaks towards higher values (blue dotted line). Figure 4.15c displays the oxidation potential (corrected to NHE) of $Cu° \rightarrow Cu^{+1} + e^{-}$ reaction for S1 to S6. Regarding the pristine Cu-foil, the potential is ~0.55 V, which is around the standard electrode oxidation potential for Cu° (0.52 V). S5 and S6, also exhibit values of the oxidation potential very close to the 0.52 V value. This effect could be attributed to the low ionic diffusion through the interface diffusion layer in graphite nanostructures [84]. The higher values of oxidation potentials for S1 to S4 could be attributed to the deposition of graphitic material. The charge capacity (figure 4.15d) of materials can be related to the anodic (I_{pa}) and cathodic (I_{ca}) peak potential intensities [85]. The S5 shows the higher charge capacity, corresponding to a quasi-reversible process ($I_{ca}/I_{pa} \sim 1$), this effect could be a consequence of the formation of the helical nanostructures but also to the formation of copper oxide [86]. For S6, with the lower values of I_{pa} and I_{ca}, the charge capacity was reduced considerably, due to the enhanced formation of amorphous carbon [87].

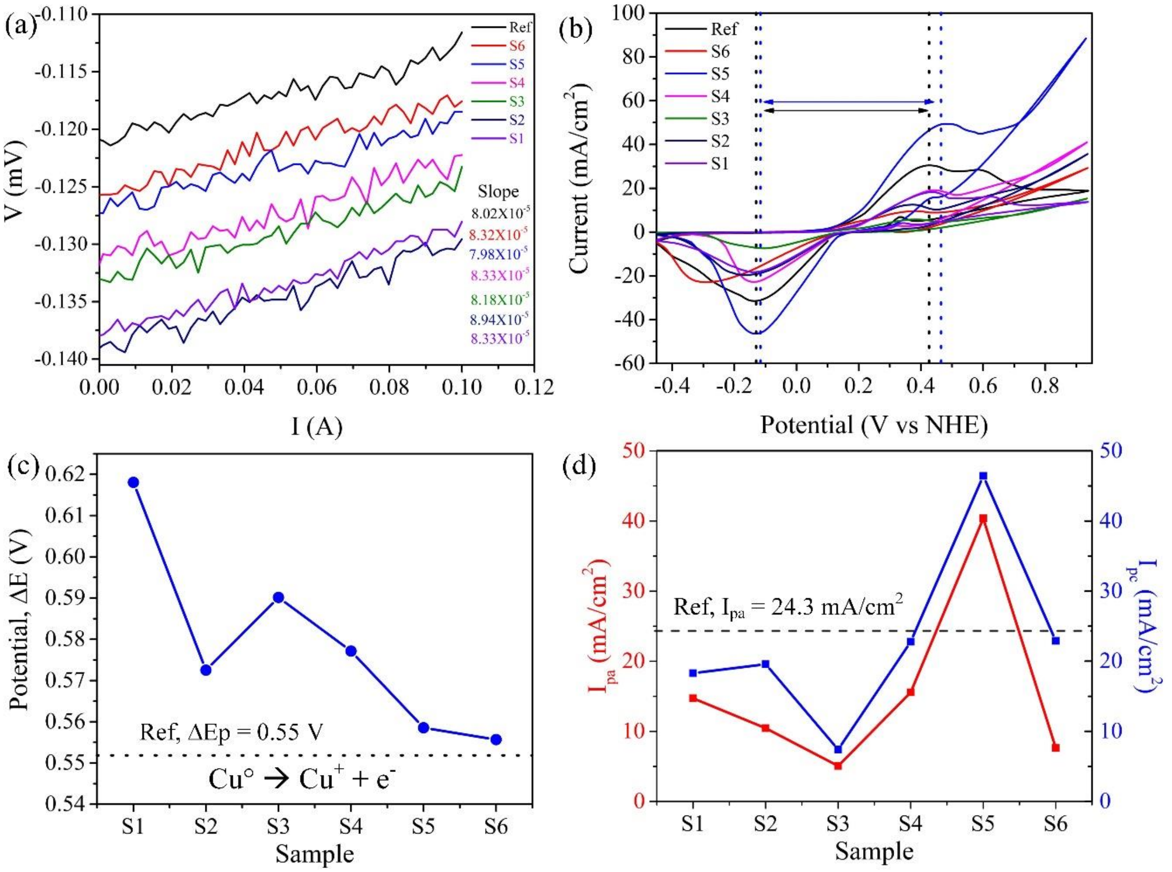

Figure 4.15: (a) V vs I plot (four-probe measurements), the values of the slope (Ω/cm^2) represent the resistivity and are given in the inset. **(b)** Cyclic voltammetry measurements in the range of -0.7 V to 0.7 V with a scan rate of 20 mV/s. **(c)** Oxidation potential and **(d)** anodic and cathodic currents of S1 to S6.

Oxide metal surfaces are regularly hydrophilic; however, some metal surfaces have a hydrophobic surface, Cu has a lower hydrophobic character compared with other metals like Au, Ag or Hg [88]. After the cleaned and reducing treatment, the oxygen-related molecules are removed from the Cu-foil surface. Figure 4.16a depicts the contact angle of a water droplet set on the surface of Cu-foils. The pristine Cu-foil exhibited a contact angle of 109.3 °. After the cleaning treatment of Cu-foils, the water droplet shown a contact angle of 93.5°, which could be likely due to the decrease of oxygen molecules and an increase of surface roughness [89]. Figure 4.16c shows the contact angle for S1-S6. The lowest contact angle (72.2 º) was obtained for S1. This fact could be related to the presence of oxidized graphite.

The largest contact angle was observed for S5 that is possibly associated with the tubular structures. Notice that the contact angle for S6 is close to that obtained for the pristine reduced Cu-foil. These facts, through S1 to S5 hydrophobicity, could be related to high surface defects variation from the formation of graphene walls and tubular carbon nanostructures. According to the above results (SEM, TEM, Raman, AFM, and Cyclic voltammetry), S5 could be used over diverse applications such as humidity-proof coating for electronic devices, high duration of batteries, and fuel cell devices [90].

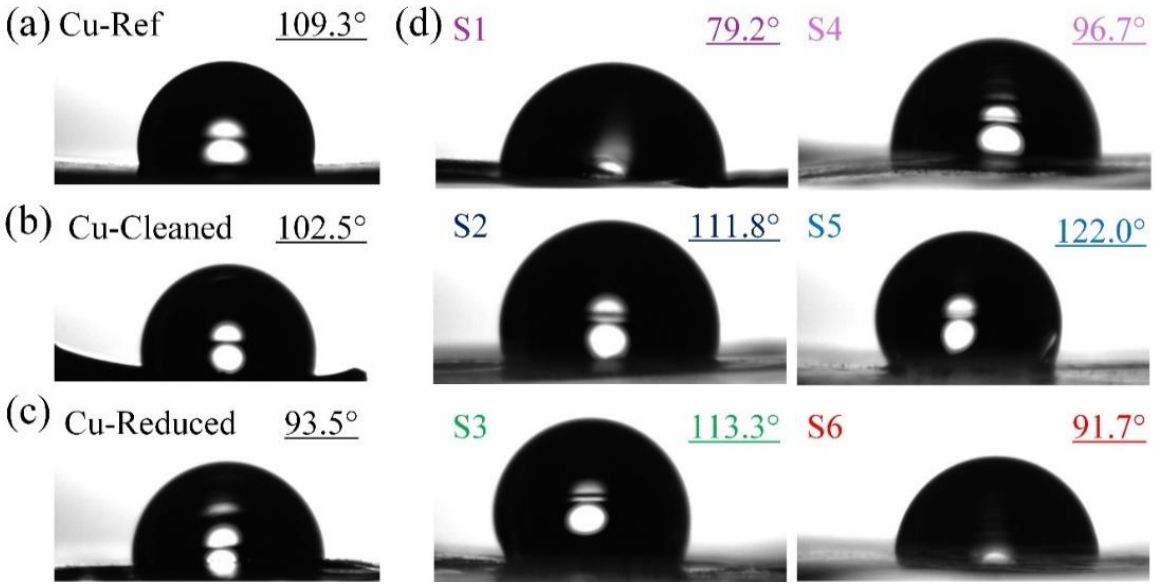

Figure 4.16: Contact angle measurements for **(a-c)** Cu-foils at the pretreatment and before being exposed to vapors and **(c)** Cu-foils after the CVD experiment.

4.5 Growth mechanism approach

In the present study, the modification of Cu-foils previous to the synthesis of carbon nanostructures and the position of the Cu-substrates in the VC-CVD system was significant. Figure 4.17a depicts the variation of the surface roughness obtained through a cleaning procedure and a thermal reduction process, reaching a roughness average of 84 nm. Considering the nature of the VC-CVD system developed at 980 °C in a continuous flow of ethanol, the main decomposition reaction reported for this system considers the formation of water and acetylene[91]. In this case, the acetylene favors the precipitation of C atoms for

CNT growing, and the Cu nanoparticles crystallization over (111) plane [50] and water, works as an intermediary that reacts with the amorphous carbon for the production of CO and CO_2 [17,78]. On our samples, we observed vibrations modes related to the C-O compound by Raman and FTIR spectroscopy (see figure 4.5). Also, the position of the Cu-foils in the reactor plays an important role in the growth of interesting carbon nanomaterials. Figure 4.17c shows the different scenarios considering the position of three Cu-foil inside the furnace. For example, S1 is where a high deposition of carbon material takes place. As the graphitic carbon layer is formed, the copper nanoparticles migrate from the interlayer C-Cu section to the surface with the formation of Cu NPs – Carbon agglomerates. As we get deeper into the furnace, the deposition of carbon due to the decomposition of ethanol is lower. At this stage, shaped Cu-NPs could be found on the surface of the graphitic layer covered by graphitic material, in some cases, it is considered that the water formed by the decomposition of ethanol could lead to the removal of a-C and activation of the Cu-NPs to the formation of short CNT. In the case of the substrate where the temperature drops it is considered that a high interaction of water with Cu-NPs lead to the formation of highly crystalline tip shaped Cu-NPs over the Cu (111) plane with size between 15 nm to 200 nm, what increases the potential of Cu-NPs to synthesis tubular carbon nanostructures. Depending on the shape of the Cu-NPs the diffusion of carbon into the Cu-NPs can lead to the formation of Helical-CNT, CNT, Herringbone-CNT, and Herringbone-CNF.

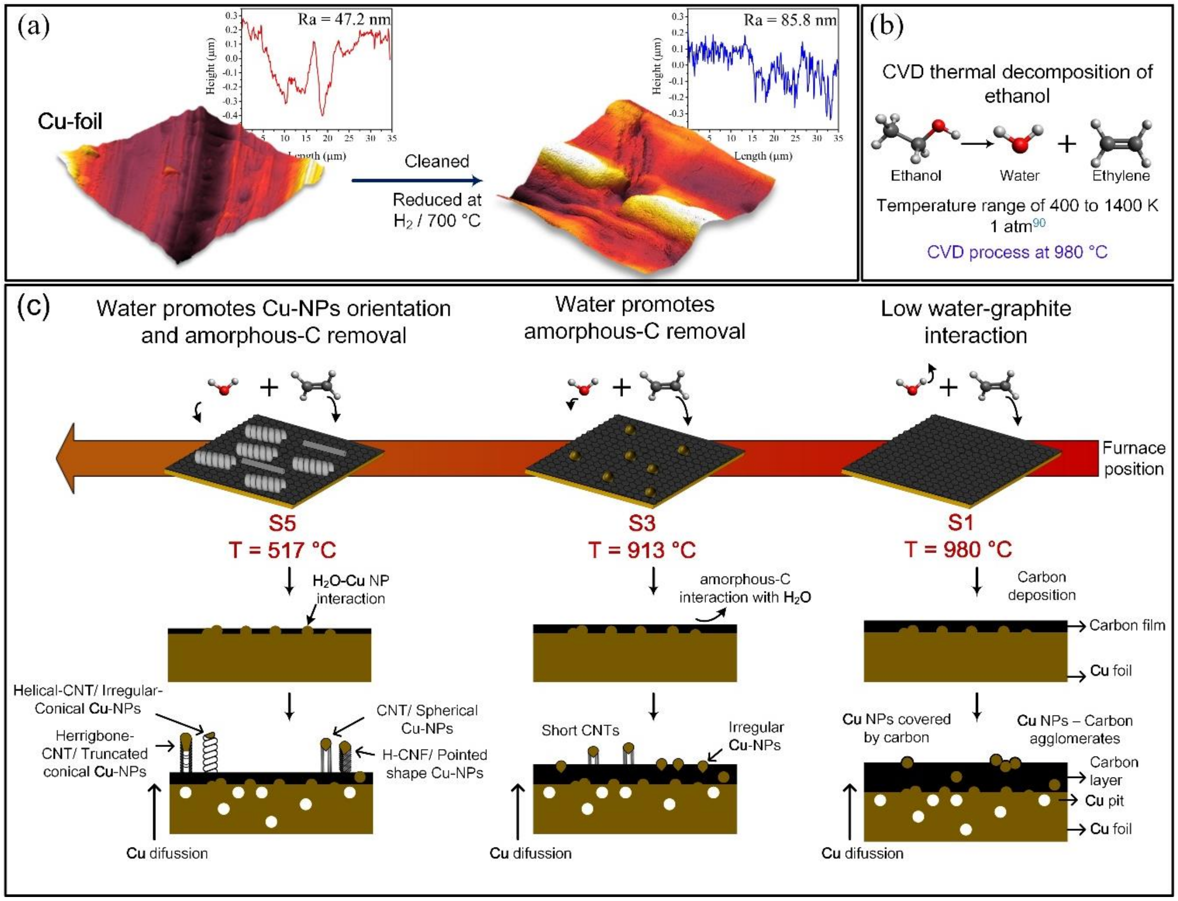

Figure 4.17: Growing mechanism explained in three stages: (a) Modification of roughness of copper foil due to a cleaning and reduction process. (b) Ethanol decomposition mechanism in a CVD process. (c) Growing stages inside the quartz furnace where water interaction with Cu substrate and graphite plays a role in the growth of different carbon nanostructures.

4.6 Conclusions

We demonstrated that Cu-foils is an effective substrate for the production of a helical shape, herringbone tubular graphitic structures and graphite carbon materials using only ethanol as carbon source. At the center of the reactor (S1), graphitic material was grown over the Cu-foil, leading to an increase over the oxide-reduction potential of Cu species in the Cu-substrate. However, at the end of the furnace (S5) where the temperature decreases the interaction of the formed water by the decomposition of ethanol, and the Cu-foils promote the growth of helical CNT combined with herringbone-CNT and CNF as the formation of CNT. The temperature profile alongside the furnace and the position inside the furnace are determinant parameters that provoke the growth of well-oriented and shaped Cu-NPs that influence the formation of a variety of tubular carbon nanostructures. The formation of graphite is mostly produced over other sections. Cu NPs shape and size play a significant role in the determination of the type of tubular structure synthesized. As far as we know, it is the first time that hydrogen-reduced copper substrates are used to grow helical-tubular carbon nanostructures and herringbone type nanotubes with small graphene pieces as building blocks over the copper substrate in a simple one-step synthesis method.

4.7 References

[1] A. Bianco, Y. Chen, Y. Chen, D. Ghoshal, R.H. Hurt, Y.A. Kim, N. Koratkar, V. Meunier, M. Terrones, A carbon science perspective in 2018: Current achievements and future challenges, Carbon. 132 (2018) 785–801. https://doi.org/10.1016/j.carbon.2018.02.058.

[2] Q. Xu, W. Li, L. Ding, W. Yang, H. Xiao, W.J. Ong, Function-driven engineering of 1D carbon nanotubes and 0D carbon dots: Mechanism, properties and applications, Nanoscale. 11 (2019) 1475–1504. https://doi.org/10.1039/c8nr08738e.

[3] A.C. Ferrari, F. Bonaccorso, V. Fal'ko, K.S. Novoselov, S. Roche, P. Bøggild, S. Borini, F.H.L. Koppens, V. Palermo, N. Pugno, J.A. Garrido, R. Sordan, A. Bianco, L. Ballerini, M. Prato, E. Lidorikis, J. Kivioja, C. Marinelli, T. Ryhänen, A. Morpurgo, J.N. Coleman, V. Nicolosi, L. Colombo, A. Fert, M. Garcia-Hernandez, A. Bachtold, G.F. Schneider, F. Guinea, C. Dekker, M. Barbone, Z. Sun, C. Galiotis, A.N. Grigorenko, G. Konstantatos, A. Kis, M. Katsnelson, L. Vandersypen, A. Loiseau, V. Morandi, D. Neumaier, E. Treossi, V. Pellegrini, M. Polini, A. Tredicucci, G.M. Williams, B. Hee Hong, J.H. Ahn, J. Min Kim, H. Zirath, B.J. Van Wees, H. Van Der Zant, L. Occhipinti, A. Di Matteo, I.A. Kinloch, T. Seyller, E. Quesnel, X. Feng, K. Teo, N. Rupesinghe, P. Hakonen, S.R.T. Neil, Q. Tannock, T. Löfwander, J. Kinaret, Science and technology roadmap for graphene, related two-dimensional crystals, and hybrid systems, Nanoscale. 7 (2015) 4598–4810. https://doi.org/10.1039/c4nr01600a.

[4] R. Lv, M. Terrones, Towards new graphene materials: Doped graphene sheets and nanoribbons, Materials Letters. 78 (2012) 209–218. https://doi.org/10.1016/j.matlet.2012.04.033.

[5] Z. Lin, Z. Zeng, X. Gui, Z. Tang, M. Zou, A. Cao, Carbon Nanotube Sponges, Aerogels, and Hierarchical Composites: Synthesis, Properties, and Energy Applications, Advanced Energy Materials. 6 (2016). https://doi.org/10.1002/aenm.201600554.

[6] V. Schroeder, S. Savagatrup, M. He, S. Lin, T.M. Swager, Carbon nanotube chemical sensors, Chemical Reviews. 119 (2019) 599–663. https://doi.org/10.1021/acs.chemrev.8b00340.

[7] M.B. Gholivand, L. Mohammadi-Behzad, H. Hosseinkhani, Application of a Cu-chitosan/multiwalled carbon nanotube film-modified electrode for the sensitive determination of rutin, Analytical Biochemistry. 493 (2016) 35–43. https://doi.org/10.1016/j.ab.2015.08.033.

[8] X. Li, L. Tao, Z. Chen, H. Fang, X. Li, X. Wang, J. Bin Xu, H. Zhu, Graphene and related two-dimensional materials: Structure-property relationships for electronics and optoelectronics, Applied Physics Reviews. 4 (2017). https://doi.org/10.1063/1.4983646.

[9] D. Zhang, C. Jiang, J. Liu, Y. Cao, Carbon monoxide gas sensing at room temperature using copper oxide-decorated graphene hybrid nanocomposite prepared by layer-by-layer self-assembly, Sensors and Actuators, B: Chemical. 247 (2017) 875–882. https://doi.org/10.1016/j.snb.2017.03.108.

[10] E.W. Hill, A. Vijayaragahvan, K. Novoselov, Graphene sensors, IEEE Sensors Journal. 11 (2011) 3161–3170. https://doi.org/10.1109/JSEN.2011.2167608.

[11] A. Borenstein, O. Hanna, R. Attias, S. Luski, T. Brousse, D. Aurbach, Carbon-based composite materials for supercapacitor electrodes: A review, Journal of Materials Chemistry A. 5 (2017) 12653–12672. https://doi.org/10.1039/c7ta00863e.

[12] X. Zhong, B. Papandrea, Y. Xu, Z. Lin, H. Zhang, Y. Liu, Y. Huang, X. Duan, Three-dimensional graphene membrane cathode for high energy density rechargeable lithium-air batteries in ambient conditions, Nano Research. 10 (2017) 472–482. https://doi.org/10.1007/s12274-016-1306-4.

[13] M. Sheng, F. Zhang, B. Ji, X. Tong, Y. Tang, A Novel Tin-Graphite Dual-Ion Battery Based on Sodium-Ion Electrolyte with High Energy Density, Advanced Energy Materials. 7 (2017). https://doi.org/10.1002/aenm.201601963.

[14] E. Abbasi, A. Akbarzadeh, M. Kouhi, M. Milani, Graphene: Synthesis, bio-applications, and properties, Artificial Cells, Nanomedicine and Biotechnology. 44 (2016) 150–156. https://doi.org/10.3109/21691401.2014.927880.

[15] K.A. Shah, B.A. Tali, Synthesis of carbon nanotubes by catalytic chemical vapour deposition: A review on carbon sources, catalysts and substrates, Materials Science in Semiconductor Processing. 41 (2016) 67–82. https://doi.org/10.1016/j.mssp.2015.08.013.

[16] B. Hu, H. Ago, Y. Ito, K. Kawahara, M. Tsuji, E. Magome, K. Sumitani, N. Mizuta, K.I. Ikeda, S. Mizuno, Epitaxial growth of large-area single-layer graphene over Cu(1 1 1)/sapphire by atmospheric pressure CVD, Carbon. 50 (2012) 57–65. https://doi.org/10.1016/j.carbon.2011.08.002.

[17] S.D. Shandakov, A. V. Kosobutsky, M.S. Rybakov, O.G. Sevostyanov, D.M. Russakov, M. V. Lomakin, A.I. Vershinina, I.M. Chirkova, Effect of gaseous and

condensate products of ethanol decomposition on aerosol CVD synthesis of single-walled carbon nanotubes, Carbon. 126 (2018) 522–531. https://doi.org/10.1016/j.carbon.2017.10.064.

[18] R. Kar, N.N. Patel, N. Chand, R.K. Shilpa, R.O. Dusane, D.S. Patil, S. Sinha, Detailed investigation on the mechanism of co-deposition of different carbon nanostructures by microwave plasma CVD, Carbon. 106 (2016) 233–242. https://doi.org/10.1016/j.carbon.2016.05.027.

[19] F. Yu, M. Yang, F. Li, C. Su, B. Ma, Z. Yuan, J. Chen, J. Ma, The growth mechanism of single-walled carbon nanotubes with a controlled diameter, Physica E: Low-Dimensional Systems and Nanostructures. 44 (2012) 2032–2040. https://doi.org/10.1016/j.physe.2012.06.007.

[20] O. Guellati, D. Bégin, F. Antoni, S. Moldovan, M. Guerioune, C. Pham-Huu, I. Janowska, CNTs' array growth using the floating catalyst-CVD method over different substrates and varying hydrogen supply, Materials Science and Engineering B: Solid-State Materials for Advanced Technology. 231 (2018) 11–17. https://doi.org/10.1016/j.mseb.2018.03.001.

[21] S.-J. Chang, M.S. Hyun, S. Myung, M.-A. Kang, J.H. Yoo, K.G. Lee, B.G. Choi, Y. Cho, G. Lee, T.J. Park, Graphene growth from reduced graphene oxide by chemical vapour deposition: seeded growth accompanied by restoration, Scientific Reports. 6 (2016) 22653. https://doi.org/10.1038/srep22653.

[22] K.S. Novoselov, V.I. Fal, L. Colombo, P.R. Gellert, M.G. Schwab, K. Kim, V.I.F. ko, L. Colombo, P.R. Gellert, M.G. Schwab, K. Kim, A roadmap for graphene, Nature. 490 (2013) 192–200. https://doi.org/10.1038/nature11458.

[23] X. Chen, L. Zhang, S. Chen, Large area CVD growth of graphene, Synthetic Metals. 210 (2015) 95–108. https://doi.org/10.1016/j.synthmet.2015.07.005.

[24] W.A. de Heer, C. Berger, M. Ruan, M. Sprinkle, X. Li, Y. Hu, B. Zhang, J. Hankinson, E. Conrad, Large area and structured epitaxial graphene produced by confinement controlled sublimation of silicon carbide, Proceedings of the National Academy of Sciences. 108 (2011) 16900–16905. https://doi.org/10.1073/pnas.1105113108.

[25] P.R. Whelan, V. Panchal, D.H. Petersen, D.M.A. Mackenzie, C. Melios, I. Pasternak, J. Gallop, F.W. Østerberg, P.U. Jepsen, W. Strupinski, O. Kazakova, P. Bøggild, Electrical Homogeneity Mapping of Epitaxial Graphene on Silicon Carbide, ACS Applied Materials and Interfaces. 10 (2018) 31641–31647. https://doi.org/10.1021/acsami.8b11428.

[26] P. Ruffieux, S. Wang, B. Yang, C. Sanchez, J. Liu, T. Dienel, L. Talirz, P. Shinde, C.A. Pignedoli, D. Passerone, T. Dumslaff, X. Feng, K. Müllen, R. Fasel, On-surface synthesis of graphene nanoribbons with zigzag edge topology, Nature. (2016) 531–489.

[27] L. Kan, Z. Xu, C. Gao, General avenue to individually dispersed graphene oxide-based two-dimensional molecular brushes by free radical polymerization, Macromolecules. 44 (2011) 444–452. https://doi.org/10.1021/ma102371d.

[28] Y. Hernandez, V. Nicolosi, M. Lotya, F.M. Blighe, Z. Sun, S. De, S. Krishnamurti, R. Goodhue, J. Hutchison, V. Scardaci, C. Andrea, High yield production of graphene by liquid phase exfoliation of graphite, Nature Nanotechnology. 3 (2008) 563–568. https://doi.org/10.1038/nnano.2008.215.

[29] A. Ciesielski, P. Samorì, Graphene via sonication assisted liquid-phase exfoliation, Chemical Society Reviews. 43 (2014) 381–398. https://doi.org/10.1039/c3cs60217f.

[30] X. Cui, C. Zhang, R. Hao, Y. Hou, Liquid-phase exfoliation, functionalization and applications of graphene, Nanoscale. 3 (2011) 2118–2126. https://doi.org/10.1039/c1nr10127g.

[31] M. Yi, Z. Shen, A review on mechanical exfoliation for the scalable production of graphene, Journal of Materials Chemistry A. 3 (2015) 11700–11715. https://doi.org/10.1039/c5ta00252d.

[32] L. Huang, B. White, M.Y. Sfeir, M. Huang, H.X. Huang, S. Wind, J. Hone, S. O'Brien, Cobalt ultrathin film catalyzed ethanol chemical vapor deposition of single-walled carbon nanotubes, Journal of Physical Chemistry B. 110 (2006) 11103–11109. https://doi.org/10.1021/jp060693r.

[33] C. Bower, O. Zhou, W. Zhu, D.J. Werder, S. Jin, Nucleation and growth of carbon nanotubes by microwave plasma chemical vapor deposition, Applied Physics Letters. 77 (2000) 2767–2769. https://doi.org/10.1063/1.1319529.

[34] Z. Chen, W. Ren, L. Gao, B. Liu, S. Pei, H. Cheng, Three-dimensional flexible and conductive interconnected graphene networks grown by chemical vapour deposition, Nature Materials. 10 (2011) 424–428. https://doi.org/10.1038/nmat3001.

[35] T.O.M. Samuels, A.W. Robertson, H. Kim, M. Pasta, H. Jamie, Three Dimensional Multi-layered Graphene and Multi- layer Graphene-CNT Hybrid Materials via Rapid Thermal Annealing of Nickel Acetate as a Pt Nanoparticle Support, Journal of Materials Chemistry A. 5 (2017) 10457.

[36] A. Botello-Méndez, J. Campos-Delgado, A. Morelos-Gómez, J.M. Romo-Herrera, Á.G. Rodríguez, H. Navarro, M.A. Vidal, H. Terrones, M. Terrones, Controlling the dimensions, reactivity and crystallinity of multiwalled carbon nanotubes using low ethanol concentrations, Chemical Physics Letters. 453 (2008) 55–61. https://doi.org/10.1016/j.cplett.2007.12.073.

[37] T. Yamada, T. Namai, K. Hata, D.O.N.N. Futaba, K. Mizuno, J. Fan, M. Yudasaka, M. Yumura, S. Iijima, Size-selective growth of double-walled carbon nanotube forests from engineered iron catalysts, (2006) 131–136. https://doi.org/10.1038/nnano.2006.95.

[38] S. Bhaviripudi, X. Jia, M.S. Dresselhaus, J. Kong, Role of kinetic factors in chemical vapor deposition synthesis of uniform large area graphene using copper catalyst, Nano Letters. 10 (2010) 4128–4133. https://doi.org/10.1021/nl102355e.

[39] X. Li, W. Cai, J. An, S. Kim, J. Nah, D. Yang, R. Piner, A. Velamakanni, I. Jung, E. Tutuc, S.K. Banerjee, L. Colombo, R.S. Ruoff, Large area synthesis of high quality

and uniform graphene films on copper foils, Science. 324 (2009) 1312–1314. https://doi.org/10.1126/science.1171245.

[40] G. Li, Y. Li, H. Liu, Y. Guo, Y. Li, D. Zhu, Architecture of graphdiyne nanoscale films, Chemical Communications. 46 (2010) 3256–3258. https://doi.org/10.1039/b922733d.

[41] J.L. Fajardo-Díaz, F. López-Urías, E. Muñoz-Sandoval, Wrinkled Nitrogen-doped Carbon Belts, Scientific Reports. 8 (2018). https://doi.org/10.1038/s41598-018-21898-6.

[42] G. Atthipalli, Y. Tang, A. Star, J.L. Gray, Electrochemical characterization of carbon nanotube forests grown on copper foil using transition metal catalysts, Thin Solid Films. 520 (2011) 1651–1655. https://doi.org/10.1016/j.tsf.2011.08.105.

[43] I. Lahiri, R. Seelaboyina, J.Y. Hwang, R. Banerjee, W. Choi, Enhanced field emission from multi-walled carbon nanotubes grown on pure copper substrate, Carbon. 48 (2010) 1531–1538. https://doi.org/10.1016/j.carbon.2009.11.064.

[44] J.H. Xia, X. Jiang, C.L. Jia, The size effect of catalyst on the growth of helical carbon nanofibers, Applied Physics Letters. 95 (2009) 1–4. https://doi.org/10.1063/1.3271031.

[45] J. Zhu, J. Jia, F.L. Kwong, D.H.L. Ng, Synthesis of bamboo-like carbon nanotubes on a copper foil by catalytic chemical vapor deposition from ethanol, Carbon. 50 (2012) 2504–2512. https://doi.org/10.1016/j.carbon.2012.01.073.

[46] J. Li, A. Kazakov, F.L. Dryer, Experimental and numerical studies of ethanol decomposition reactions, Journal of Physical Chemistry A. 108 (2004) 7671–7680. https://doi.org/10.1021/jp0480302.

[47] W. Zhou, Z. Han, J. Wang, Y. Zhang, Z. Jin, X. Sun, Y. Zhang, C. Yan, Y. Li, Copper catalyzing growth of single-walled carbon nanotubes on substrates, Nano Letters. 6 (2006) 2987–2990. https://doi.org/10.1021/nl061871v.

[48] C. Veríssimo, S.A. Moshkalyov, A.C.S. Ramos, J.L. Gonçalves, O.L. Alves, J.W. Swart, Different carbon nanostructured materials obtained in catalytic chemical vapor deposition, Journal of the Brazilian Chemical Society. 17 (2006) 1124–1132. https://doi.org/10.1590/S0103-50532006000600009.

[49] R. Cui, Y. Zhang, J. Wang, W. Zhou, Y. Li, Comparison between copper and iron as catalyst for chemical vapor deposition of horizontally aligned ultralong single-walled carbon nanotubes on silicon substrates, Journal of Physical Chemistry C. 114 (2010) 15547–15552. https://doi.org/10.1021/jp100286c.

[50] Y. Qin, Z. Zhang, Z. Cui, Helical carbon nanofibers with a symmetric growth mode, Carbon. 42 (2004) 1917–1922. https://doi.org/10.1016/j.carbon.2004.03.020.

[51] J.G. Jackson, R.W. Fonseca, J.A. Holcombe, Migration of Ag, Cd and Cu into highly oriented pyrolytic graphite and pyrolytic coated graphite, Spectrochimica Acta Part B: Atomic Spectroscopy. 50 (1995) 1837–1846. https://doi.org/10.1016/0584-8547(95)01377-6.

[52] H.I. Rasool, E.B. Song, M. Mecklenburg, B.C. Regan, K.L. Wang, B.H. Weiller, J.K. Gimzewski, Atomic-scale characterization of graphene grown on copper (100) Single Crystals, Journal of the American Chemical Society. 133 (2011) 12536–12543. https://doi.org/10.1021/ja200245p.

[53] Y. Ogawa, B. Hu, C.M. Orofeo, M. Tsuji, K.I. Ikeda, S. Mizuno, H. Hibino, H. Ago, Domain structure and boundary in single-layer graphene grown on Cu(111) and Cu(100) films, Journal of Physical Chemistry Letters. 3 (2012) 219–226. https://doi.org/10.1021/jz2015555.

[54] F. Du, J. Liu, Z. Guo, Shape controlled synthesis of Cu2O and its catalytic application to synthesize amorphous carbon nanofibers, Materials Research Bulletin. 44 (2009) 25–29. https://doi.org/10.1016/j.materresbull.2008.04.011.

[55] H. Zhang, X. Ren, Z. Cui, Shape-controlled synthesis of Cu2O nanocrystals assisted by PVP and application as catalyst for synthesis of carbon nanofibers, Journal of Crystal Growth. 304 (2007) 206–210. https://doi.org/10.1016/j.jcrysgro.2007.01.043.

[56] K. Zhang, Y. Zhang, S. Wang, Enhancing thermoelectric properties of organic composites through hierarchical nanostructures, Scientific Reports. 3 (2013) 1–7. https://doi.org/10.1038/srep03448.

[57] H.K. Jeong, M.H. Jin, K.P. So, S.C. Lim, Y.H. Lee, Tailoring the characteristics of graphite oxides by different oxidation times, Journal of Physics D: Applied Physics. 42 (2009). https://doi.org/10.1088/0022-3727/42/6/065418.

[58] A.C. Ferrari, D.M. Basko, Raman spectroscopy as a versatile tool for studying the properties of graphene, Nat Nanotechnol. (2013) 1–13. https://doi.org/10.1038/nnano.2013.46.

[59] A.C. Ferrari, Raman spectroscopy of graphene and graphite: Disorder, electron-phonon coupling, doping and nonadiabatic effects, Solid State Communications. 143 (2007) 47–57. https://doi.org/10.1016/j.ssc.2007.03.052.

[60] T. Luo, J. Liu, L. Chen, S. Zeng, Y. Qian, Synthesis of helically coiled carbon nanotubes by reducing ethyl ether with metallic zinc, Carbon. 43 (2005) 755–759. https://doi.org/10.1016/j.carbon.2004.10.048.

[61] P. Vecera, J.C. Chacón-Torres, T. Pichler, S. Reich, H.R. Soni, A. Görling, K. Edelthalhammer, H. Peterlik, F. Hauke, A. Hirsch, Precise determination of graphene functionalization by in situ Raman spectroscopy, Nature Communications. 8 (2017). https://doi.org/10.1038/ncomms15192.

[62] A. Kaniyoor, S. Ramaprabhu, A Raman spectroscopic investigation of graphite oxide derived graphene A Raman spectroscopic investigation of graphite oxide derived graphene, 032183 (2014) 0–13. https://doi.org/10.1063/1.4756995.

[63] J. Bin Wu, M.L. Lin, X. Cong, H.N. Liu, P.H. Tan, Raman spectroscopy of graphene-based materials and its applications in related devices, Chemical Society Reviews. 47 (2018) 1822–1873. https://doi.org/10.1039/c6cs00915h.

[64] A.K. Gupta, T.J. Russin, H.R. Gutiérrez, P.C. Eklund, Probing Graphene Edges via

Raman scattering, ACS Nano. 3 (2009) 45–52.

[65] K. Kudin, B. Ozbas, H.C. Schniepp, R.K. Prud'homme, I.A. Aksay, R. Car, Raman Spectra of Graphite Oxide and Functionalized Graphene Sheets, Nano Lett. 8 (2008) 36.

[66] M.S. Dresselhaus, A. Jorio, M. Hofmann, G. Dresselhaus, R. Saito, Perspectives on carbon nanotubes and graphene Raman spectroscopy, Nano Letters. 10 (2010) 751–758. https://doi.org/10.1021/nl904286r.

[67] P. Tan, S. Dimovski, Y. Gogotsi, Raman scattering of non-planar graphite : arched edges , polyhedral crystals , whiskers and cones, Phil. Trans. R. Soc. Lond. A. 362 (2004) 2289–2310.

[68] D. Yoon, Y.W. Son, H. Cheong, Strain-dependent splitting of the double-resonance raman scattering band in graphene, Physical Review Letters. 106 (2011) 1–4. https://doi.org/10.1103/PhysRevLett.106.155502.

[69] K. Bogdanov, A. Fedorov, V. Osipov, T. Enoki, K. Takai, T. Hayashi, V. Ermakov, S. Moshkalev, A. Baranov, Annealing-induced structural changes of carbon onions: High-resolution transmission electron microscopy and Raman studies, Carbon. 73 (2014) 78–86. https://doi.org/10.1016/j.carbon.2014.02.041.

[70] V. Thirumal, A. Pandurangan, R. Jayavel, S.R. Krishnamoorthi, R. Ilangovan, Synthesis of nitrogen doped coiled double walled carbon nanotubes by chemical vapor deposition method for supercapacitor applications, Current Applied Physics. 16 (2016) 816–825. https://doi.org/10.1016/j.cap.2016.04.018.

[71] X. Peng, K. Koczkur, A. Chen, Synthesis of well-aligned bamboo-like carbon nanotube arrays from ethanol and acetone, Journal of Physics D: Applied Physics. 41 (2008) 095409. https://doi.org/10.1088/0022-3727/41/9/095409.

[72] M. Lin, J.P.Y. Tan, C. Boothroyd, K.P. Loh, E.S. Tok, Y.L. Foo, Dynamical observation of bamboo-like carbon nanotube growth, Nano Letters. 7 (2007) 2234–2238. https://doi.org/10.1021/nl070681x.

[73] Z. Ren, P.-X. Gao, A review of helical nanostructures: growth theories, synthesis strategies and properties, Nanoscale. 6 (2014) 9366–9400. https://doi.org/10.1039/C4NR00330F.

[74] A. Shaikjee, N.J. Coville, The synthesis, properties and uses of carbon materials with helical morphology, Journal of Advanced Research. 3 (2012) 195–223. https://doi.org/10.1016/j.jare.2011.05.007.

[75] V. V. Shinkarev, A.M. Glushenkov, D.G. Kuvshinov, G.G. Kuvshinov, Nanofibrous carbon with herringbone structure as an effective catalyst of the H2S selective oxidation, Carbon. 48 (2010) 2004–2012. https://doi.org/10.1016/j.carbon.2010.02.008.

[76] N.M. Rodriguez, A. Chambers, R.T.K. Baker, Catalytic Engineering of Carbon Nanostructures, Langmuir. 11 (1995) 3862–3866. https://doi.org/10.1021/la00010a042.

[77] F. Cervantes-Sodi, J.J. Vilatela, J.A. Jiménez-Rodríguez, L.G. Reyes-Gutiérrez, S. Rosas-Meléndez, A. Íñiguez-Rábago, M. Ballesteros-Villarreal, E. Palacios, G. Reiband, M. Terrones, Carbon nanotube bundles self-assembled in double helix microstructures, Carbon. 50 (2012) 3688–3693. https://doi.org/10.1016/j.carbon.2012.03.042.

[78] B. Kruszka, A.P. Terzyk, M. Wiśniewski, P.A. Gauden, M. Szybowicz, Synthesis of carbon nanotubes and nanotube forests on copper catalyst, Materials Research Express. 1 (2014) 035040. https://doi.org/10.1088/2053-1591/1/3/035040.

[79] M. Klinger, A. Jäger, Crystallographic Tool Box (CrysTBox): Automated tools for transmission electron microscopists and crystallographers, Journal of Applied Crystallography. 48 (2015) 2012–2018. https://doi.org/10.1107/S1600576715017252.

[80] Z. He, J.L. Maurice, A. Gohier, C.S. Lee, D. Pribat, C.S. Cojocaru, Iron catalysts for the growth of carbon nanofibers: Fe, Fe3C or both?, Chemistry of Materials. 23 (2011) 5379–5387. https://doi.org/10.1021/cm202315j.

[81] S.Y. Lee, M. Yamada, M. Miyake, Synthesis of carbon nanotubes over gold nanoparticle supported catalysts, Carbon. 43 (2005) 2654–2663. https://doi.org/10.1016/j.carbon.2005.05.045.

[82] C. Punckt, F. Muckel, S. Wolff, I.A. Aksay, C.A. Chavarin, G. Bacher, W. Mertin, The effect of degree of reduction on the electrical properties of functionalized graphene sheets, Applied Physics Letters. 102 (2013) 1–6. https://doi.org/10.1063/1.4775582.

[83] K.T. Lau, M. Lu, D. Hui, Coiled carbon nanotubes: Synthesis and their potential applications in advanced composite structures, Composites Part B: Engineering. 37 (2006) 437–448. https://doi.org/10.1016/j.compositesb.2006.02.008.

[84] C.E. Banks, T.J. Davies, G.G. Wildgoose, R.G. Compton, Electrocatalysis at graphite and carbon nanotube modified electrodes: Edge-plane sites and tube ends are the reactive sites, Chemical Communications. (2005) 829–841. https://doi.org/10.1039/b413177k.

[85] H. Zhang, M. Zhang, Synthesis of CuO nanocrystalline and their application as electrode materials for capacitors, Materials Chemistry and Physics2. 108 (2008) 184–187.

[86] W.Z. Le, Y.Q. Liu, Preparation of nano-copper oxide modified glassy carbon electrode by a novel film plating/potential cycling method and its characterization, Sensors and Actuators, B: Chemical. 141 (2009) 147–153. https://doi.org/10.1016/j.snb.2009.05.037.

[87] F. Rohman, U. Azizah, B. Prihandoko, Study of electrochemical performance of amorphous carbon-coated graphite for Li-ion battery, AIP Conference Proceedings. 1823 (2017). https://doi.org/10.1063/1.4978113.

[88] G. Valette, Hydrophilicity of metal surfaces. Silver, gold and copper electrodes, Journal of Electroanalytical Chemistry. 139 (1982) 285–301.

https://doi.org/10.1016/0022-0728(82)85127-9.

[89] Z. Yoshimitsu, A. Nakajima, T. Watanabe, K. Hashimoto, Effects of surface structure on the hydrophobicity and sliding behavior of water droplets, Langmuir. 18 (2002) 5818–5822. https://doi.org/10.1021/la020088p.

[90] X. Zhang, F. Shi, J. Niu, Y. Jiang, Z. Wang, Superhydrophobic surfaces: from structural control to functional application, Journal of Materials Chemistry. 18 (2008) 621–633.

[91] A. Li, S. Zhang, B. Reznik, S. Lichtenberg, G. Schoch, O. Deutschmann, Chemistry and kinetics of chemical vapor deposition of pyrolytic carbon from ethanol, Proceedings of the Combustion Institute. 33 (2011) 1843–1850. https://doi.org/10.1016/j.proci.2010.06.037.

CHAPTER FIVE:

GROWTH OF OTHER 3D CARBON NANOSTRUCTURES

5.1. Introduction
5.2 Growth of carbon nanotube sponge using pyridine mixture
    5.2.1 Experimental details
    5.2.2 Results and discussion
    5.2.3 Theoretical procedure
    5.2.4 Conclusions
5.3 Growth of a carbon nanotube sponge using 1,2-dichlorobenzene
    5.3.1 Experimental details
    5.3.2 Results and discussion
    5.3.3 Growth mechanism approach
    5.3.4 Theoreticla procedure
    5.3.5 Conclusions
5.4 References

5.1 Introduction

A way to maintain the material properties of carbon nanostructures at the bulk level is using carbon allotropes as "building blocks" to create 3D carbon frameworks [1–3]. For example, using the single wall and multiwall carbon nanotubes [4,5], graphene intercalation [6,7], and other combinations, several nanostructured architectures have been fabricated [8,9]. Dai et al. [10] created a carbon nanotube sponge using a pumped chemical vapor deposition (CVD) device and 1, 2-dichlorobenzene, ferrocene on a piece of quartz glass. They found that junctions between carbon nanostructures provide mechanical stability, elasticity, and excellent fatigue resistance. Luo et al. [11] synthesized well-aligned carbon nanotubes (CNT) by a two-step process. First, they produced the CNT by CVD, and subsequently they mixed them with sodium dodecyl sulfate (SDS) in aqueous solution over sonication to create a CNT-SDS sponge via van der Waals interactions, this material exhibited a low density (< 50 mg/cm^{-3}), high porosity (>99.9 %) and high conductivity (~1.25 S/cm). He et al. [9] combined a melamine foam matrix impregnated with cobalt and iron solution in a CVD carbonization process to grow a hierarchical porous structure foam of nitrogen-doped CNT with a high capacitance performance. Regarding applications, three-dimensional carbon structures have been used in energy, medicine, material, and environmental sciences [12,13]. For example, Lu et al. [14] synthesized a hybrid sulfur/graphene carbon sponge with a high specific capacitance of 6.0 mAh/cm^2 at the first 11 cycles and stable capacity of 4.53 mAh/cm^2 after 300 cycles. Gui, et al. [15] developed a CNT-sponge with oil absorption capacities of 100 times its weight with the possibility of being used several times after a burning process without losing its absorption capacities.

Another issue for fabricating carbon-bulk nanostructures with exceptional electrical and chemical properties is the introduction of foreign atoms in the carbon network [16,17]. It is known that the incorporation of heteroatoms on the graphitic network induces structural and electronic transport changes. For example, phosphorous over the carbon network increase the surface area and the electrical density with potential application as a supercapacitor electrode [18]. Boron is used to inducing elbows, knees, and corrugated walls into carbon nanotubes and else increases the yield of high-oleophilic carbon nanotube sponges [19,20]. On the other hand, sulfur is used to create Y junctions has been reported that a carbon electrode sulfur and nitrogen co-doped increases the dynamic reaction and the cycling performance of LiS_2 batteries [21,22]. Furthermore, a high concentration of nitrogen promotes bends inwards the graphite layers and the formation of the "bamboo shape" structure [16,23]. Svintsiskiy et al. [24] reported that the nitrogen in carbon nanotubes was at the internal arches as in the external surface of the graphitic wall while for the nitrogen in platelet carbon nanofibers tend to be at the edges bending the graphitic layers. Additionally, nitrogen pyridinic and pyrrolic doping and amine functionalization on three-dimensional carbon nanostructures is used for the development of metal-free catalyst [25–27]. However, over the edge of non-saturated carbon atoms, nitrogen can be incorporated directly in a C-N bond or C-N-O bond. For example, the nitrogen can be found at the edges of carbon nanostructures built-in amines, amides, lactam, nitrogen oxides, pyridine-N-oxide, pyridinium, and hydrazone functional groups [28–30].

Furthermore, one of the main issues of using different precursors to fabricate carbon nanostructures relays over the idea of functionalization and doping with nitrogen, oxygen, phosphorus, sulfur, boron [31–34], and other non-common atoms like silicon, aluminum, and chloride [35–37]. This process modifies the electronic structure and chemical surface reactivity of carbon graphitic structures [35]. In the case of three-dimensional carbon nanostructures, different precursors have been addressed to create a tunable structure for different applications. Gui et al. reported the growth of a carbon nanotube sponge (CNS) with extraordinary absorption capacities of 140 times its weight. They used 1,2-dichlorobenzene as a precursor mixed with ferrocene and incorporated into a syringe-aerosol assisted chemical vapor deposition (AACVD) system to grow the CNS over a quartz sheet [12]. Muñoz-Sandoval et al. reported the synthesis of a nitrogen-doped carbon nanotube sponge using a mixture of ferrocene, thiophene, benzylamine, and ethanol [38]. Erbay et al. synthesize an interconnected carbon nanotube structure in a sponge configuration using a mixture of acetylene and ferrocene with an extraordinary energy power density (2150 W/m^3) compared with commercial carbon felts [39]. Shinde et al. depict the use of a mixture of aminoguanidine hydrochloride, phosphoric acid, methane sulfonic acid, and ammonium persulfate to create a phosphorous-sulfur co-doped carbon nitride sponge to be used as an electrode for Zn-Air batteries [26]. Zhao et al. synthesize CNT using 1,2-dichlorobenzene by syringe pump-CVD method and were incorporated into a polydimethylsiloxane (PDMS) matrix to increase the mechanical strength and viscoelastic behavior [40]. The growth mechanism of carbon nanotube sponges is still under debate, whereas the doping or functionalize effect over the structure is also a topic to take into account [1,41,42].

5.2 Growth of carbon nanotube sponge using pyridine mixture

5.2.1 Experimental details

Nitrogen-doped and functionalized carbon nanofiber sponges (N-CFS) were synthesized by the AACVD technique. Figure 5.1 shows the approach which involves the pyrolysis using two different sprayers: i) sprayer A with an ethanol (C_2H_5OH), thiophene (C_4H_4S, 0.124 wt.%) and ferrocene ($Fe(C_5H_5)_2$ 1.252 wt.%) solution; ii) sprayer B with a 1:1 volume ratio of benzylamine ($C_6H_5CH_2NH_2$) and pyridine (C_5H_5N) solution mixed with thiophene (C_4H_4S, 0.5 wt.%) and ferrocene ($Fe(C_5H_5)_2$, 2.5 wt.%). The AACVD experiments were carried out at 1020 °C for 4 hours. In the case of the sprayer-A, an Ar gas with a flow of 0.8 l/min transported the cloud, and in the case of sprayer B, the gas carrier was a mixture of Ar-H_2 (95%-5%) with a flow of 1.0 l/min. The resulting material was collected from the reaction quartz tube by scraping and classified according to different zones in the quartz tube. Scanning and transmission electron microscopy characterizations (SEM and TEM) were used for morphological studies of the samples via a Helios Nanolab 600 Dual Beam and an FEI Tecnai F30, respectively. A Renishaw micro Raman spectrometer with a 532 nm excitation laser wavelength was used to evaluate the crystalline structure. The carbon, nitrogen, and oxygen content in the carbon N-CSTNs were measured by XPS (PHI 5000 VersaProbeII). Thermogravimetric analysis was performed using an STA 6000 Perkin-Elmer equipment in a temperature range of 50-950 °C with a heating speed of 10 °C /min under the dynamic flow of oxygen (20 ml/min). The magnetization saturation was measured by Dynacool equipment (Quantum Design) at 300 K. For the electrochemical properties, an Ag/AgCl electrode (0.197 V vs. NHE) was used as a reference electrode, and the N-CFS was used supported over a 916 stainless steel mesh to be as work electrode. The cyclic voltammetry was developed using an HCl 0.5 M solution as an electrolyte, with a potential window from -0.6 V to 1 V with variation in the scan rate from 10 mV/s to 400 mV/s.

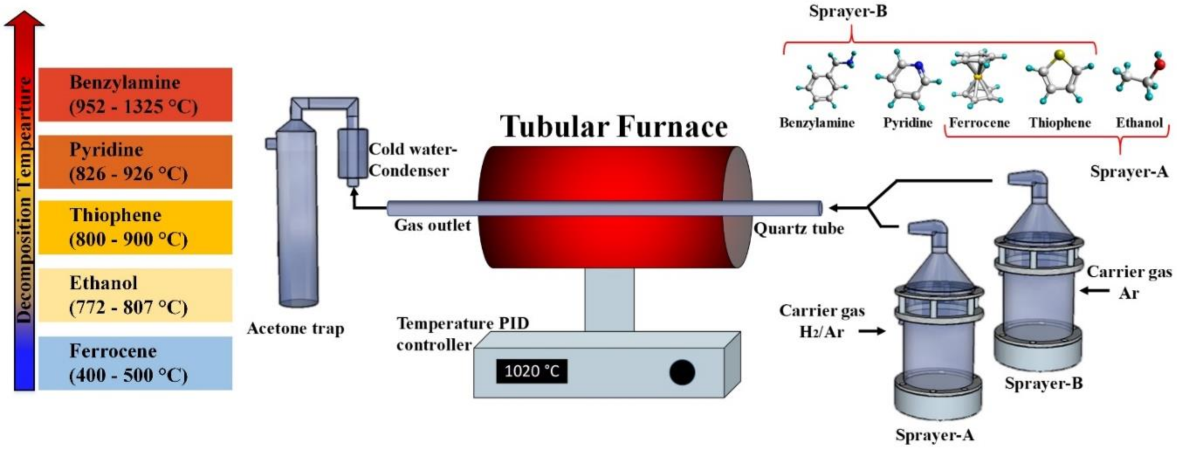

Figure 5.1: Schematic representation of a modified aerosol assisted chemical vapor deposition (AACVD) method used to synthesize the N-CFS materials. The AACVD arrangement consists of two independent sprayers feeding the reactor. The samples were synthesized at 1020 °C. The decomposition temperature ranges for the different precursors involved in the synthesis are also shown.

5.2.2 Results and discussion

Figure 5.2 depicts the SEM images of the synthesized N-CFS material, where the overall construction is constructed by entangled and interconnections of curved and robust carbon nanofibers. The junctions and knots are observed in figure 5.2a. Three types of morphologies were identified: i) branched and curved tubular carbon nanostructures with diameter of ~250 nm, where the entangled effect promotes in some cases the formation of junctions (red arrow); ii) thinner carbon fibers with diameter of ~120 nm producing complex knots (green arrow) and iii) the formation of spherical agglomerates of graphitic material (yellow arrow). Figure 5.2b depicts a magnification over one section of branched carbon fibers. Here is observed a cross-linked effect of carbon fiber with the formation “Y” and “+” junctions (red arrows). High magnification images reveal a rough appearance of the carbon nanofiber surface, see figures 5.2(c-d). The cross-section of two carbon fibers is shown in figure 5.2c, where flat-type termination (blue arrow) and elliptical termination (red arrow) are observed. Also, Figure 5.2d shows the surface profile along the dashed line on the carbon fiber, revealing the valleys and elevations with a distance of ~85 nm between them (see the inset plot).

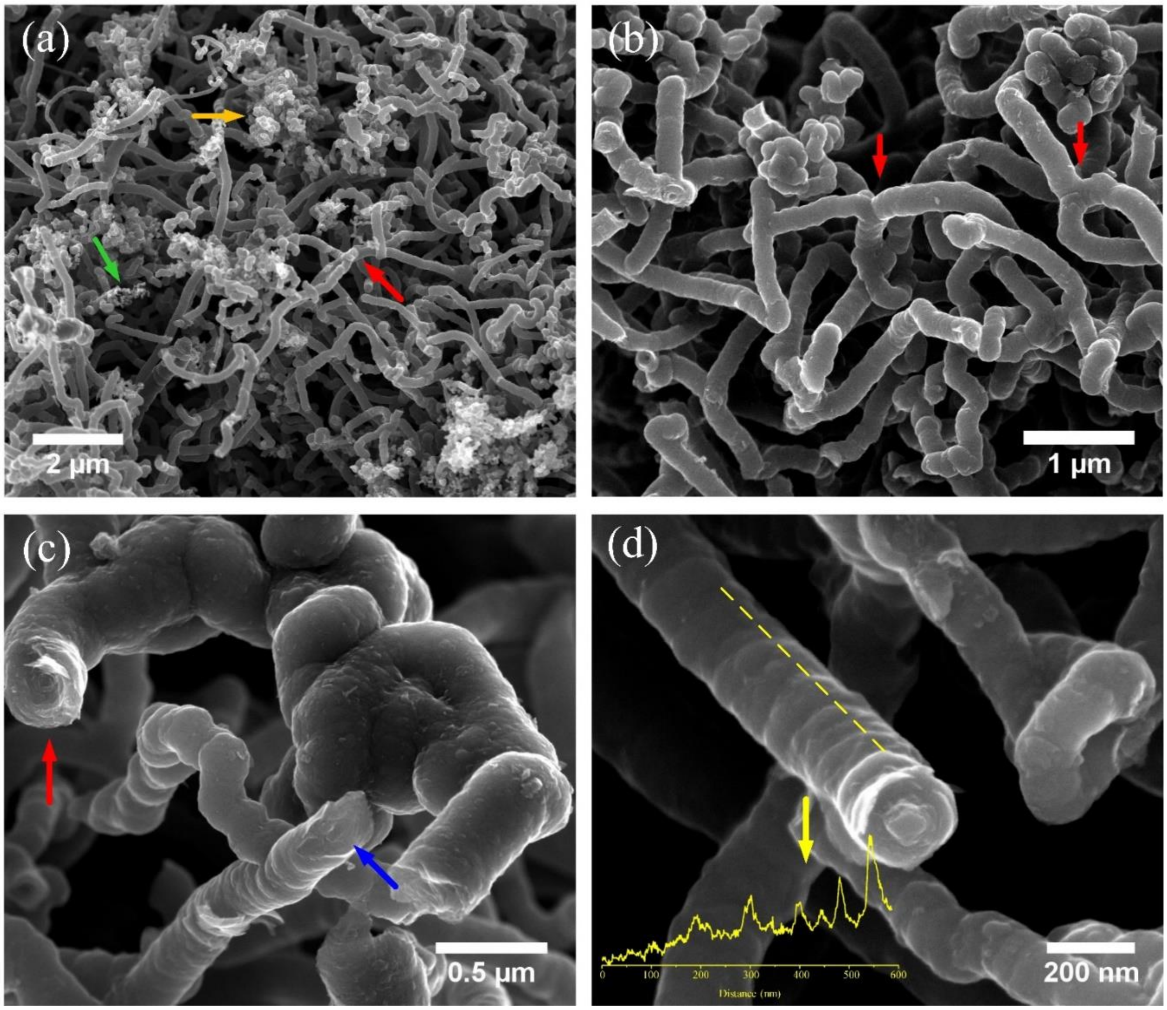

Figure 5.2: SEM images of carbon sponge material. **(a)** General view of the N-CFS where three morphologies are visible: curved tubular carbon nanostructures, curly carbon nanotubes, semi-spherical carbon aggregates. **(b)** Junctions between the carbon nanofibers (red arrow). **(c)** Cross-sections of the N-CFS with cylindrical geometry and unfolded graphitic structure (red arrow) and elliptical geometry (blue arrow). (**d**) Line-profile along the carbon fiber showing the surface reliefs.

The TEM image of carbon fibers showed a zigzagging behavior with a corrugated aspect, see blue and red arrows (figure 5.3a). Figure 5.3b displays the N-CFS with a highly deformed structure where protuberances are exhibited over the walls leading to bulky-smooth curves (red arrow) of sharp graphitic edges (blue arrow). Over the tip end of the N-CFS (Figure 5.3c), an unfolding effect is observed where the graphitic layers seem to be surrounding the structure similar to a graphite whisker structure [43]. The inset in figure 5.3c depicts a defined crystalline section embedded in the graphitic layer with an interlayer distance of 3.34 Å, presumably SiO_2 material as a consequence of interaction with the quartz tube. Figure 5.3d depicts two carbon fibers with irregular diameter, and high-stress sections are observed (red and green squares). Figure 5.3(e-h) illustrates the HRTEM images of the red and green squares. In figure 5.3d, the red box shows how the growing direction of the carbon fiber goes transversal to its axis, which indicates a "platelet-like" structure of carbon fiber [44]. In the case of the red box (figure 5.3e), homogeneous graphitic layers are observable; after an FFT treatment of the section, an interlayer distance of 3.6 Å was determined (figure 5.3f). Over the green box in figure 5.3g, the carbon fiber illustrates the transversal direction of the graphitic layers with an interlayer distance of 3.7 Å, lightly expanded considering the 3.45 Å interlayer distances for multiwalled carbon nanotubes containing nitrogen [45]. Figure 5.3i shows a section of carbon fiber where two directions of the graphitic layers where observed. At the center, the graphitic layers go transversal to the growing axis while at the border, curved graphitic layers resembling a wrapping effect are observed (blue arrow). Figure 5.3j illustrates presumably iron-base catalytic nanoparticle of ~65 nm surrounded by ~8 nm of graphitic material. A smaller Fe-base nanoparticle (13 nm) seems to interrupt the longitudinal growth of graphitic layers (red arrow). By Z-contrast-TEM analysis over one carbon fiber (figure 3k), it is possible to observe that material with high atomic density is concentrated at the center of the carbon fiber. Nevertheless, the material is dispersed like elongated clusters embedded in graphitic layers (figure 5.3l). Energy-dispersive X-ray spectroscopy developed at the center of a carbon fiber reveals a high concentration of Si (figure 5.4).

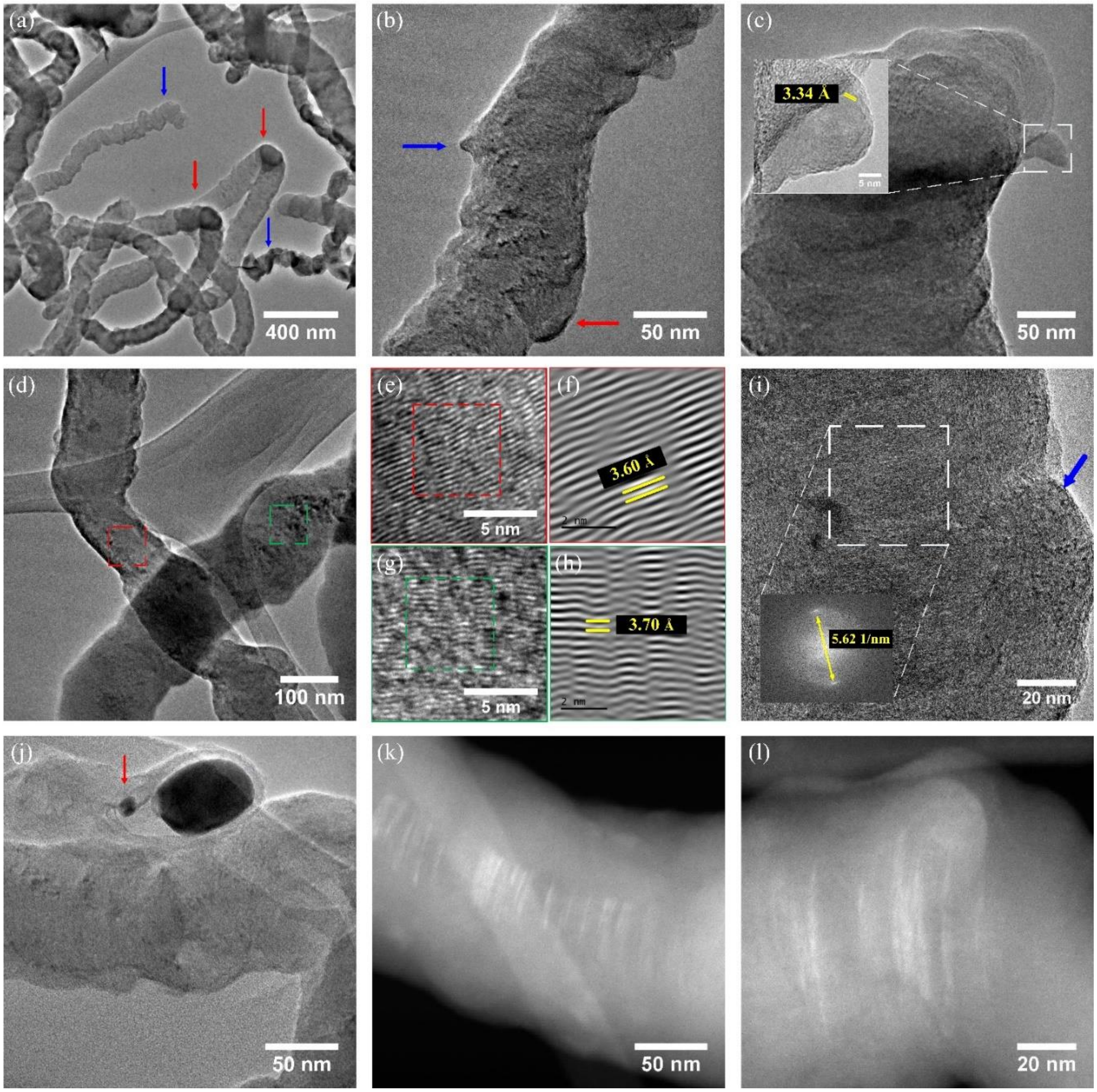

Figure 5.3: TEM and HRTEM images showing the different materials contained in the sample. **(a)** Typical carbon fiber structure part of the N-CFS structure. (b) Bulky CNF with surface irregularities. **(c)** Tip of a carbon fiber showing unfolded graphitic layers are observed; the inset shows a section of the graphitic material with an interlayer distance of 3.34 Å. **(d)** Carbon fiber, the red and green enclosed areas are analyzed in **(e-h)** by FFT refinement. **(i)** Borders and layered carbon fibers. **(j)** Iron nanoparticle (~65 nm) partially surrounded by graphitic material. **(k)** Z-contrast-TEM image over the main body of the CNF where the bright spots indicate higher density material (Si). **(l)** An HR-Zeta contrast-TEM image where the material concentrates at the center of the CNF.

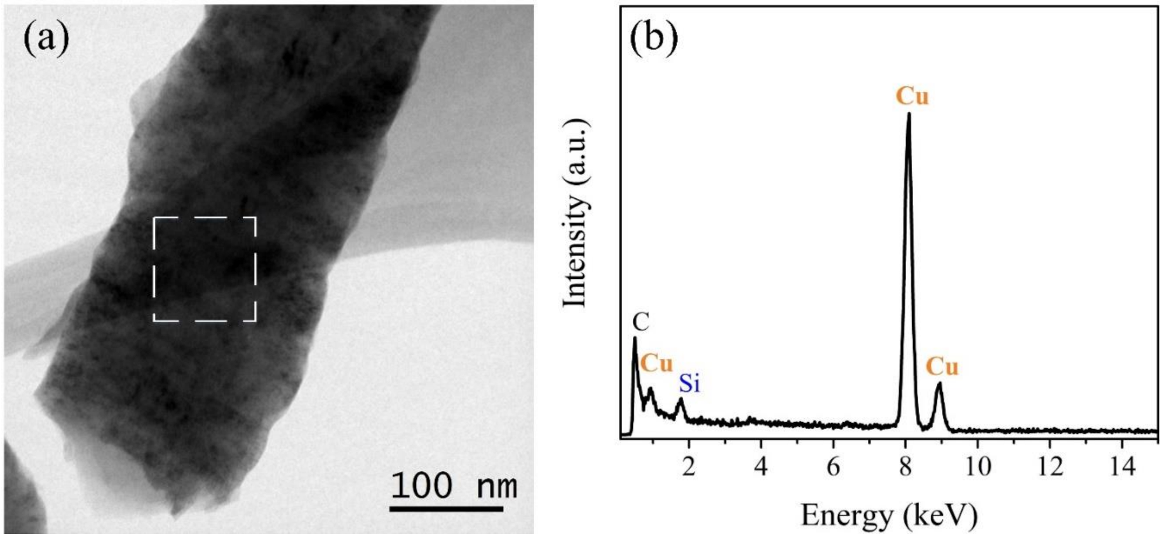

Figure 5.4: **(a)** HR-TEM image of typical carbon fiber that forming the N-CFS. **(b)** Elemental analysis over the white square in section **(a)**.

Figure 5.5a illustrates the X-ray diffraction pattern of the N-CFS material. A high-intensity peak identified at 26 degrees corresponds to the C (002) plane attributed to the graphitic structure. Also, a broad signal from 43 to 46 degrees was identified as iron compounds due to the formation of iron carbide (PDF 00-035-0772) and α-Fe (PDF 00-006-0696). A deconvolution analysis was developed over the C (002) plane using two pseudo-Voight curves [46] (figure 5.5b). Two signals were identified as π-peak related to well-ordered graphitic layers at 26.1 degrees (3.41 Å), and γ-peak related to the formation of turbostratic carbon at 25.4 degrees (3.48 Å), see table 5.1. It is clear from XRD characterization that the N-CFS is principally formed by a high oriented graphitic material (52.9 %) and a high concentration of turbostratic carbon (47.0 %). Nevertheless, to understand the nature of the graphitic structure, Raman spectroscopy was employed.

Figure 5.5c shows the identified D-band and G-band related to the breathing mode of the sp^2 C-C vibration due to structural defects and vacancies (1354 cm^{-1}) and the in-plane sp^2 C-C vibration mode (1584 cm^{-1}) respectively [47]. Also, second-order vibration modes were identified at 2667 cm^{-1} like 2D band related to a number of graphitic layers and the electronic configuration over the structure [47,48], in this case, the position of the 2D band shifted to the left could be related to a high electron concentration at the surface [48]. The D+D' band at 2896 cm^{-1} is related to a dispersion effect due to high defects formation [49]. A signal in 2133 cm^{-1} lightly visible could be related to the formation of graphynes type structures or alternated carbon-nitrogen lineal chains with C≡N bonds [50,51], possibly formed as a consequence due to the decomposition mechanism of pyridine. A deconvolution using Lorentz curves was developed over the D and G section using four peaks (figure 5.5d) where the formation of a D* and a D** bands are related to the influence of sp^3 C-C of amorphous carbon (1224 cm^{-1}) and the C-H influence over the edge of graphitic layers (1496 cm^{-1}) [52,53] (table 5.2). Additionally, the D** band can also be related to the effect of C-O functionalization over the C=C sp^2 bond on the graphitic structure [54]. The position of the D band and G band decreases (~15 cm^{-1}) to lower wavelengths compared with carbon nanotube sponge synthesized using benzylamine [41], this could be due to the presence of edges (D band) and high defects by bond disorder or owing to functionalization effects (G band) [55–57]. The I_D/I_G relation of 0.85 indicates a low defective graphitic carbon structure [47].

Table 5.1: Deconvolution data over the C(002) plane using pseudo-voight adjustment.

Center/ 2θ	**Peak**	**FWHM / 2θ**	**% Relative**	**Interlayer distance / Å**
25.62	γ	2.4	47.0	3.5
26.03	π	1.1	52.9	3.4

Table 5.2: Deconvolution data using Lorentz curves for Raman spectra over the D and G band.

Band	**Center / cm^{-1}**	**FWHM / cm^{-1}**	**Intensity (a.u.)**	**Relative Area (%)**
D*	1224.5	181.2	56.2	8.3
D	1354.7	158.2	364.3	49.2
D**	1496.8	122.2	111.6	11.8
G	1584.7	80.6	425.9	30.4

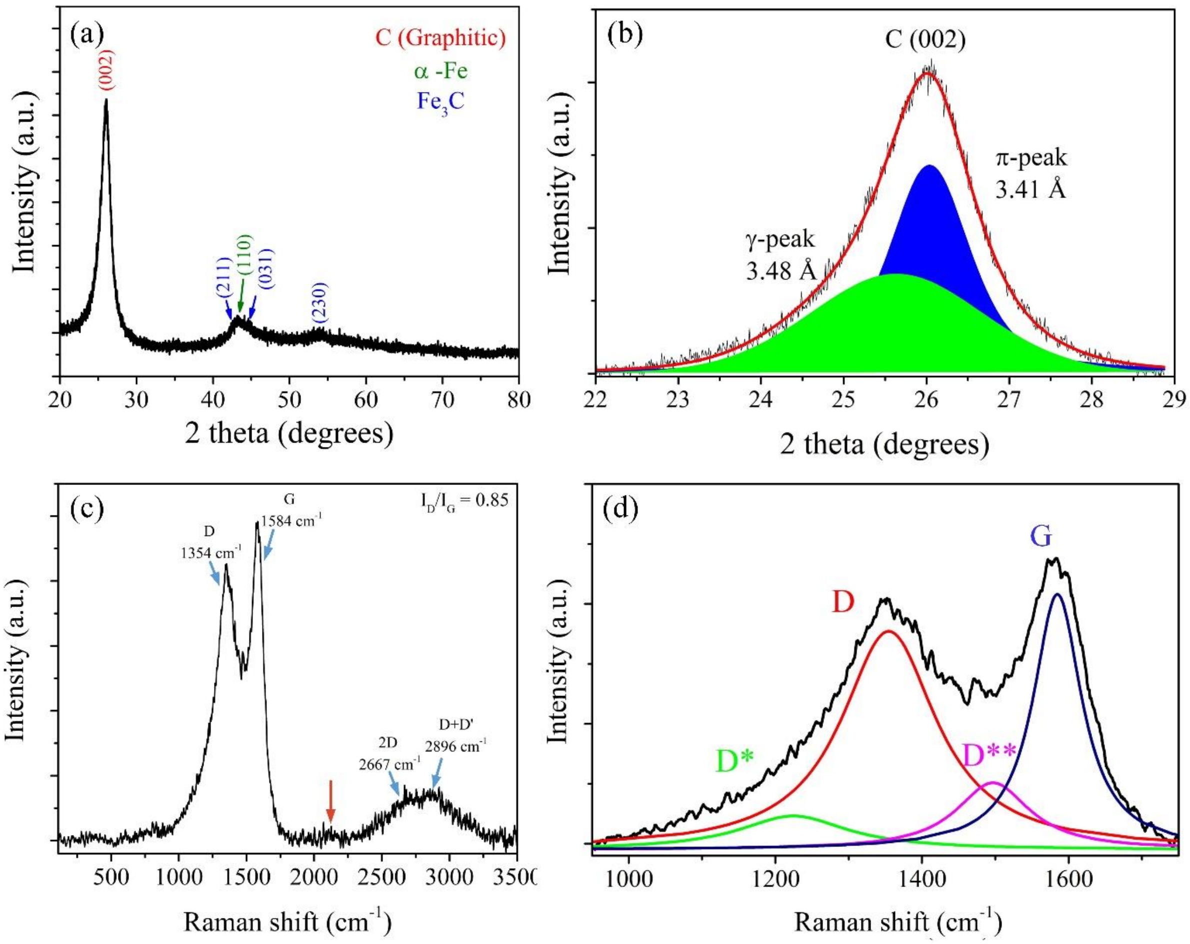

Figure 5.5: **(a)** XRD diffraction pattern showing the C(002) peak attributed to graphitic material and signals associated with α-Fe (green), and Fe_3C (blue). **(b)** Deconvolution over the C (002) signal into two peaks: π-peak at 2θ = 26.1° related with the formation of well-aligned carbon nanostructure and the γ-peak at 2θ = 25.2° related with the formation of turbostratic graphene sheets and amorphous carbon. **(c)** Raman spectra from different synthesized samples using an excitation source of 533 nm (1.958 eV) laser. The D- band, and G-band for N-CFS at 1348 cm^{-1} and 1582 cm^{-1}, respectively. The I_D/I_G ratio (0.87) indicates a less defective structure. **(d)** Deconvolution of Raman spectra using Lorentz fitting. Two more peaks are visible, the formation of D**-peak (1496 cm^{-1}) and D*-peak (1224 cm^{-1}) related to the influence in the sp^2 vibration modes by $-sp^3$ C-H bonding, C-O bonding, and amorphous carbon.

Chemical surface features of the carbon fibers using XPS are shown in figure 5.6. The XPS survey revealed a high concentration of oxygen and nitrogen at the surface, reaching 9.2 wt./wt. % and 2.9 wt./wt. %, respectively (figure 5.6a). Also, non-common incorporation of Si over the surface is observed (1.3 wt./wt. %). Figure 5.6b depicts the expanded high-resolution C1s peak. The C=C attributed to the graphitic structure, and the C-C due to the sp^3 aliphatic structures were deconvoluted. Besides, a considerable amount of the C at the surface related to the carbide formation (36 wt./wt. %) was detected. This fact could be related to the bond energies of Fe_3C formation (283.6 eV). Also, the interaction of carbon atoms with the Si (282.7 eV) is observables [58]. The formation of oxygen functionalities was identified with the energy formation of C-O (285.7 eV), C=O (286.5 eV), and COOH (287.4 eV) [59]. In the case of the C-N bond energy, this overlaps with the C-O energy vibration [60]. Figure 5.6c illustrates the deconvolution for the N1s region. A large amount of formation of the N-pyrrolic doping (N-5) is observed compared with N-pyridinic (N-6) and N-quaternary (N-Q). Furthermore, nitrogen functionalization is distinguished with energies corresponding to the amide, imine, and amide configuration (N3) [61,62], the pyridine-N-oxide (P-NOx), and the nitro (NOx) [63,64]. A signal below 398 eV is detected as N-Si binding energy possible due to the formation of C-Si interconnected graphitic materials [65]. In the case of the O1s section (figure 5.6d), the main contribution is observed over the C-O/COO- binding energies a part of hydroxyls, esters, amides, and anhydrides functionalities (532.1 eV) [66]. The presence of the FeO(OH) (530 eV) could be a consequence of the partial oxidation of external iron particles and Si-O bonds (533 eV) possible as part of a Si-O-CNT reaction [67]. More oxygen species were recognized as carbonyl functionalities (530.9 eV) and carboxylic functional groups (533.8 eV).

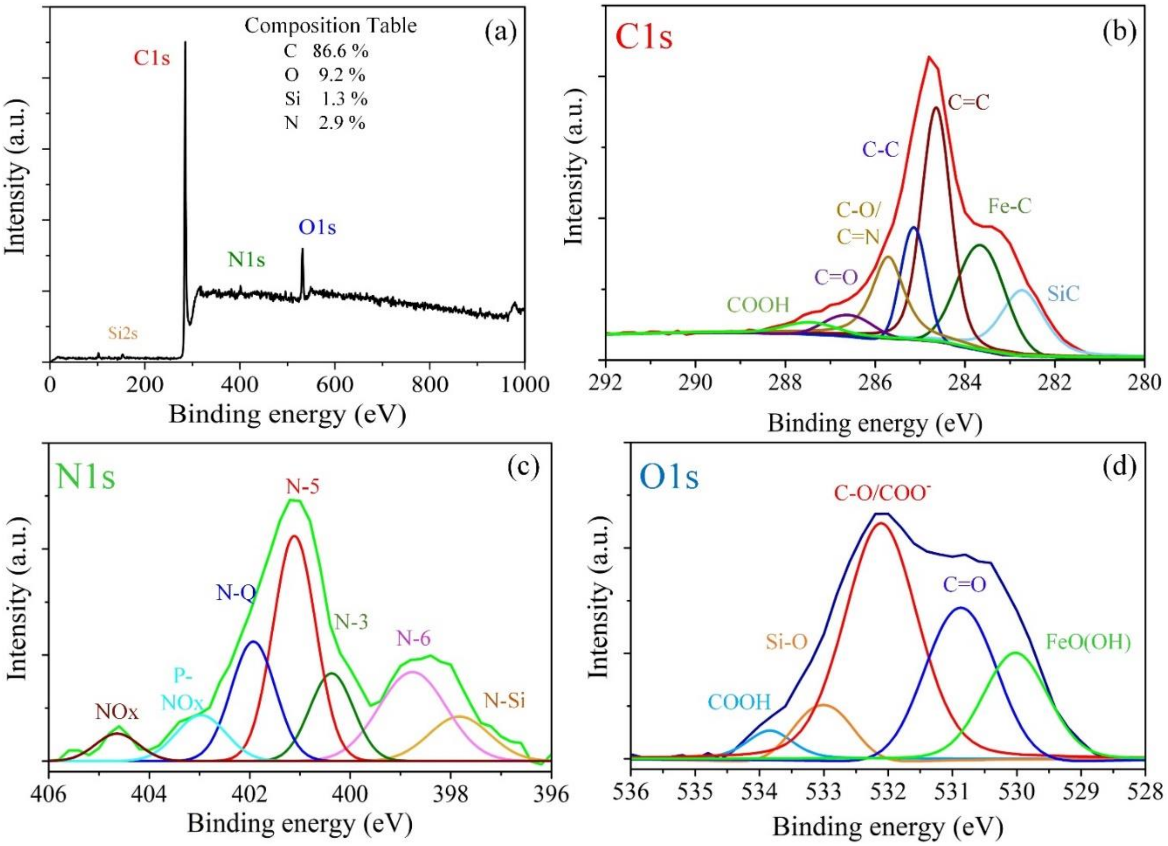

Figure 5.6: (a) XPS survey scans revealing the presence of N, C, O, and Si. **(b-d)** Deconvoluted of the high-resolution XPS spectra. **(b)** C1s spectra showing the presence sp^2 hybridized carbons (C=C bonds), sp^3 hybridized carbons (C-C bond), and carbonyl C=O, and metal carbide compounds **(c)** O1s spectra showing the presence C=O, C-O, and Si-O bonds. **(d)** N1s spectrum revealing the presence of N-pyridinic (N-6), N-pyrrolic (N-5), N-quaternary (N-Q), and pyridine-oxide (P-NOx), and nitro structures over the surface (NOx), also the observation of nitrogen functionalities (N3) and N-Si bond. Deconvolution data such as binding energies, type of bond, FWHM, and integrated area can be seen in table 5.3.

Table 5.3: Deconvolution data of the high-resolution XPS spectra. Results for C1s, O1s, and N1s peaks.

Region	***Group***	***Binding energy (BE) , eV***	***FWMH eV***	***% Relative***	***% Total***
C 1s	SiC	282.7	1.1	11.7	10.1

	Fe_3C	283.6	1.2	24.3	21.0
	C=C	284.6	0.8	32.2	27.9
	C-C	285.1	0.7	13.6	11.8
	C-OH / C - N	285.7	0.9	10.6	9.2
	C=O	286.5	1.2	4.9	4.2
	COOH	287.4	1.3	2.5	2.2
O 1s	FeO(OH)	530.0	1.2	17.2	1.6
	C=O	530.9	1.3	28.3	2.6
	COO- / C-O	532.1	1.3	42.7	3.9
	SiO_2	533.0	1.0	8.3	0.8
	COOH	533.8	0.8	3.5	0.3
N 1s	N-Si	397.8	1.4	8.9	0.2
	N-6	398.8	1.6	19.2	0.6
	N-3	400.4	1.0	13.4	0.4
	N-5	401.1	1.0	30.6	0.9
	N-Q	401.9	1.0	18.2	0.5
	P-NOx	403.0	1.2	6.6	0.2
	NOx	404.6	1.0	3.1	0.1

Figure 5.7a displays the FTIR spectra of N-CFS material. Signals were associated with the formation of the C-H_x aliphatic structure, probably as part of an amine, ester, and ether functionalities by the doublet over ~2900 cm $^{-1}$. The complement of the oxygen functional groups can be observed between 1650 cm^{-1} and 1850 cm^{-1}, where stretching vibrations due C=O configurations overlap and are related to the formation of carbonyl, carboxylic acid, quinone, pyrone, ester, and amides functionalities [60]. The C-O vibration at ~1250 cm^{-1} is related to the formation of ester and ether chemical compounds, probably part of the structure as furans or pyrans and anchored to the graphitic structure on the surface. In the case of nitrogen vibration modes related to nitrogen species, those associated with the formation of amide and amine functionalities are appreciated near the ~3500 cm^{-1}. The identification of a signal around 1645 cm^{-1} could be related to the formation of the amide structure. Geo et al. [57] indicate three significant peaks for amide structure anchored to MWCNT placed at 1639 cm^{-1} (O=C-N), 3320 cm^{-1} (N-H), and 2930/2852 cm^{-1} ($-CH_2$-/-CH_3) and a overshadow peak at 1565 cm^{-1} due to the C=C vibration mode associated with the incorporation of amide

groups. Vibration modes related to the formation of nitrile structure and sp C ≡ C vibration mode nitriles and carbides were identified at ~2180 $cm^{-1,}$ possibly associated with the light formation of graphyne structure [51]. Figure 5.7b schematize the different configuration that the oxygen and nitrogen atoms acquire for doping or functionalization. For oxygen, the functionalization of the graphitic structure can be achieved by the incorporation of amines, amides, imines, and the formation of the nitro group and Pyridine-N-oxide being these two, the more common [68]. TGA characterizations demonstrated that the sample is thermally stable (figure 5.8a), with a negligible loss of weight for DT< 570 °C and DT < 686 °C probably associated to a two types of graphitic structures. At the end of the oxidation process at ~710 ºC can be observed that almost all the carbon structures were destroyed (figure 5.8b-c). The residual material contains sharped carbon edges and agglomerated pieces of the carbon materials (figure 5.8e).

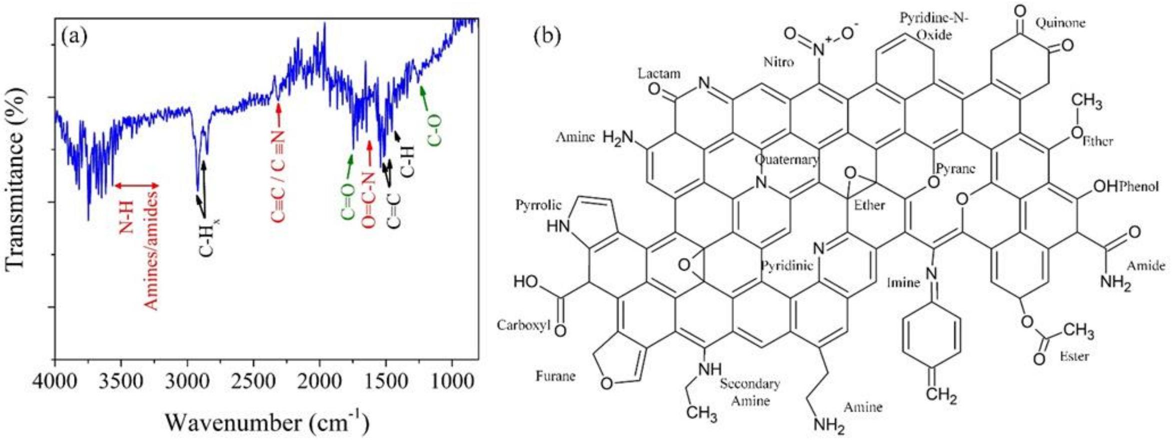

Figure 5.7: (a) FTIR spectra revealed the presence of C-O and C=O (ketone, aldehyde, carboxylic acid, ester, and ether functionalities) and nitrogen bond related to the amine/amide functionalization, also a weak signal of cyanide bond vibration. **(b)** Schematic representation of oxygen and nitrogen functionalities in a graphene sheet, notice that most of the functional groups are at the edges.

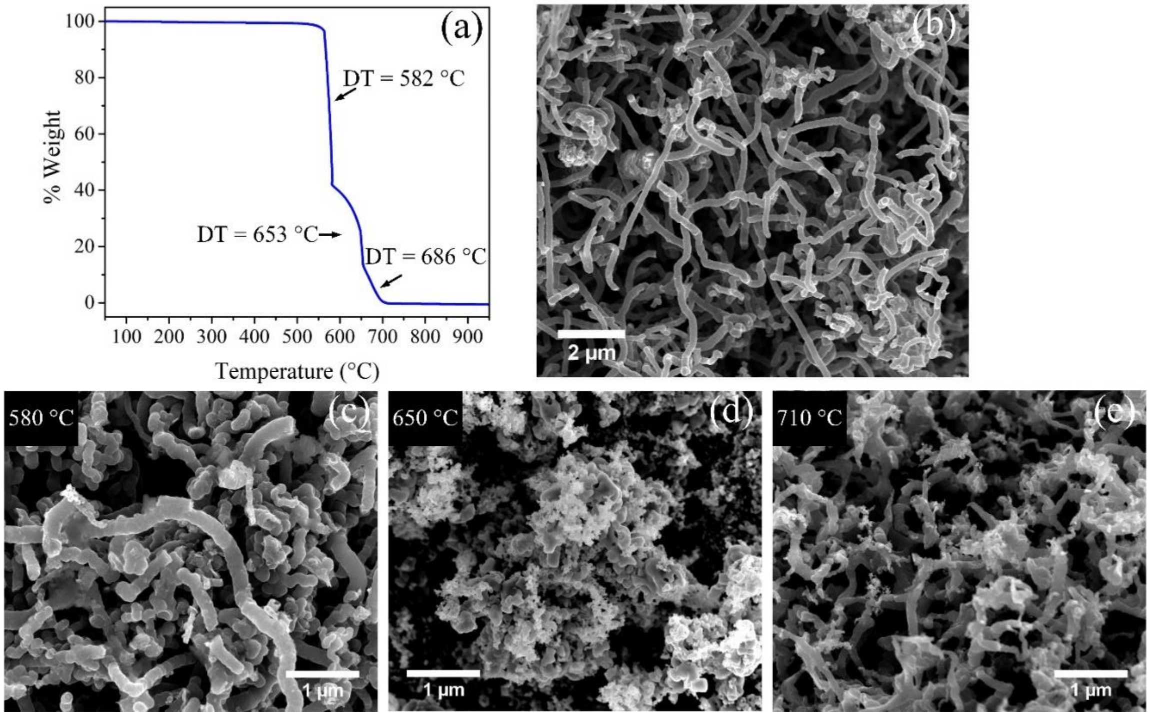

Figure 5.8: (a) Weight loss vs. temperature plot from TGA measurements. **(b)** SEM image of the pristine carbon nanotube sponge. **(c-e)** SEM images, revealing the sample evolution at different temperatures. The images in **(c-e)** were obtained by performing three independent TGA measurements with a final temperature indicated in each image. These temperatures are just less than those obtained in the TGA curve.

Figure 5.9a illustrates the cyclic voltammetry curve at a rate of 10 mV/s. It is notable for the absence of the quinone oxide-reduction process due to the high surface oxygen content. This situation could be indicative that the main of the oxygen groups lay in the formation of ethers and ester functionalities. A light protuberance is observed over the -0.1V that can be related to the influence of nitrogen species like nitrogen doping and N-H functionalities like amines and amides in the oxidation process [69–71]. Figure 5.9b depicts the increase of the discharge rate (10 mV/s to 600 mV/s), showing a growth of capacity growth almost linear to the potential rate (not showed). Figure 5.9c illustrates the magnetization curve of the N-CFS structure with a coercive field of *Hc* = 245 Oe and saturation magnetization of *Ms* = 1.93 emu/g. This behavior could be compared to the hard ferromagnetic materials (Hc > 125 Oe)

[72,73]. The saturation magnetization presents a value of 1.8 emu/g at ~0.5 T, which is comparable with the reported for pure CNT (Ms < 10 emu/g) [74]. Note that the reverse magnetization is probably by a coherent reversal mechanism, however at M=0, the direction of magnetization changes spontaneously. We did not find another magnetic material different from Fe_3C, but this behavior could be created due to the size of nanoparticles and the lack of magnetic material. Figure 5.9d displays the adsorption and desorption isotherm. Due to the characteristic of the adsorption curve, this can be categorized as type III, where weak interaction of the adsorbate and the surface of the N-CFS structure. Also, the Barrett-Joyner-Halenda (BJH) model (inset) to determine the pore size distribution reveals that the mesoporosity domains over the macroporosity and no signals of microporosity were observed.

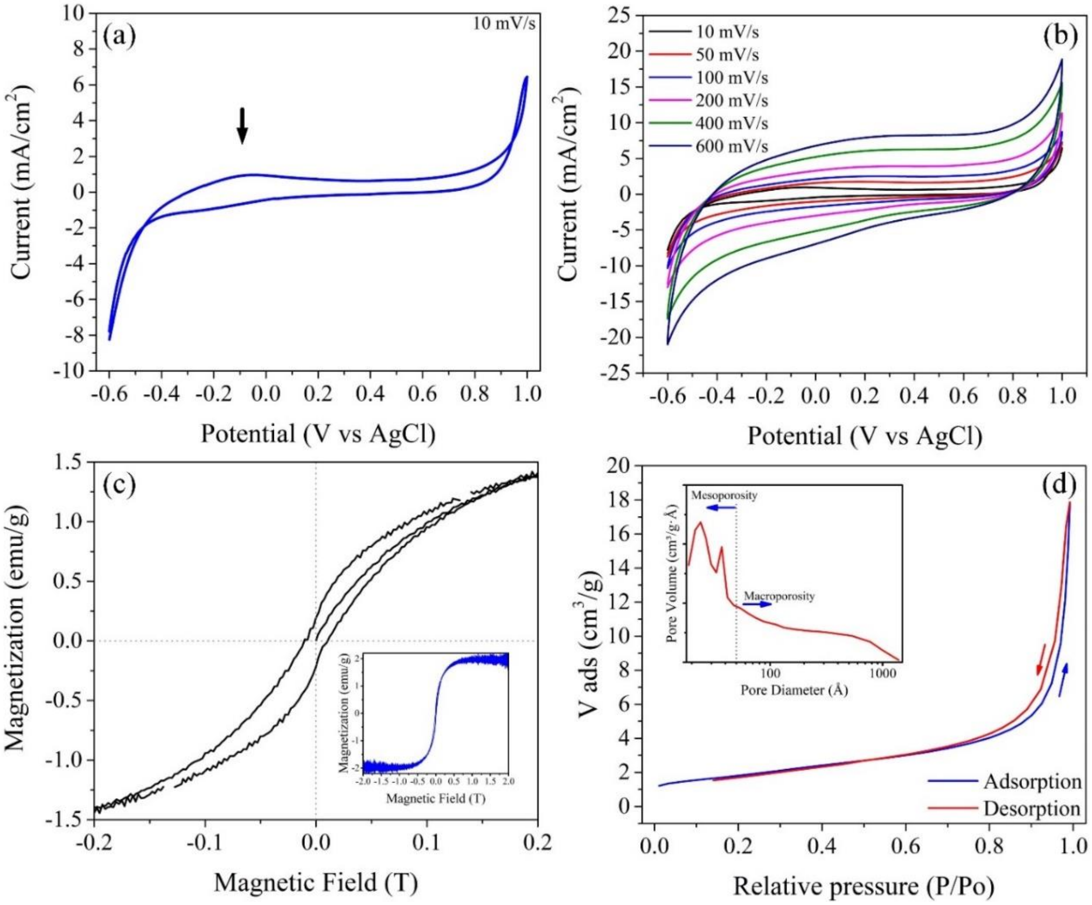

Figure 5.9: (a) Cyclic voltammetry using a scan rate potential of 10 mV/s. **(b)** A charge capacity increase as the potential rate increases. (c) Magnetization curve of the N-CFS

structure where saturation reaches the 2 emu/g and coercive field of 242 Oe. (d) N_2 adsorption-desorption isotherm for the N-CFS structure where the behavior is related to a type III isotherm, and the main macroporosity is observed (inset).

5.2.3 Incorporation of functional groups into the N-CFS

The decomposition temperature of pyridine (~680 °C) [75] and how the nitrogen is delivered from the molecule could be crucial to understand the effect of the different nitrogen-precursors on the structure of the carbon nanotubes. The decomposition mechanism of this precursor should be different since nitrogen in pyridine is found in an aromatic benzene-like ring, while in benzylamine, the nitrogen is found as an amine functional group (CH_2-NH_2) joined to a benzene ring. Ninomiya et al. [75] suggest that for pyridine decomposition, the less energetic state is the formation of cyanovinylacetylene ($^{\cdot}HC{=}CCH{=}CHC{\equiv}N$) radical, leading to the formation of minor fragments like of hydrogen cyanide, acetylene, and acrylonitrile. While, for the benzylamine decomposition, Song et al. [76] described that at high temperatures, the benzylamine leads to the formation of benzyl radical ($C_6H_5CH_2^{\cdot}$) and NH_2. It is expected that the pyridine favors the formation of N-quaternary and N-pyridinic since nitrogen is found in an aromatic benzene-like ring. In contrast, benzylamine should favor the creation of N-pyrrolic or nitrogen functionalities due to the amine functional group (CH_2-NH_2) joined to a benzene ring. In this case, the ethanol decomposition could give rise to the formation of $^{\cdot}CH_2OH$ and $^{\cdot}CH_3$ radicals [77].

5.2.4 Theoretical procedure

Electronic calculations were performed using density functional theory (DFT) [78,79]. The generalized gradient approximation with the Perdew, Burke, and Ernzerhof parametrization was chosen for the exchange-correlation functional [80] as implemented in the SIESTA code [81]. The wave functions for the valence electrons were represented by a linear combination of pseudo-atomic numerical orbitals using a double-ζ polarized basis (DZP) [82], while the core electrons by norm-conserving Troullier-Martins pseudopotentials in the Kleinman-Bylander non-local form [83,84]. The real-space grid used for charge and potential integration is equivalent to a plane wave cut-off energy of 150 Ry. We used a graphene supercell of 6×6 with 140 atoms. In the non-periodic axis, we used a minimum of 30 Å to avoid lateral interactions. A sampling of the 2D Brillouin zones was carried out with 60×60×1 Monkhorst-Pack grids. Density matrix and energy tolerances were both taken as 10^{-5} eV. A variable cell structural relaxation was performed on all systems to include the strain effects introduced by the functional groups. The geometry optimization was performed by conjugate gradient minimization until the maximum force was < 0.04 eV/Å.

From the results above presented, there is an intriguing situation concerning sponge surface composition and its electrochemical activity. On one side, the XPS characterizations showed a high oxygen concentration (9.2 %), while on the other side, the cyclic voltammetry characterizations do not show the redox process related to the quinone (C=O)/hydroquinone(C-OH) electron transfer process. Functional groups containing only C-O-C bonds does not participate in the redox process due to the oxygen atom can only form a maximal two sigma bonds. The high resolution deconvoluted O1s analysis showed that C-O bond concentration is over the other oxygen chemical species, suggesting the presence of ether groups such as furans, pyrans, epoxy, methoxy, and ethoxy, among others. Notice that these groups have a hydrophobic feature, which could also explain the hydrophobic properties of N-CFS. To explain the role of these ether (C-O bonds) functional groups, we performed density-functional calculations considering different oxygen functional groups anchored on the surface of a graphene sheet [85]. The calculation method is described in Supplementary Information. Figure 5.10 displays the optimized structures of furans, pyrans, epoxy, methoxy, ethoxy, and ethyl-ester functional groups. From Mulliken population analysis, the epoxy and furan functional groups pulled out 0.096 and 0.864 electrons, respectively, from the graphitic structure. Conversely, pyrans injected electrons (0.245 electrons). In both cases, electron-donating and withdrawing functional groups could create regions negatively charged, which could be anchoring sites for chemical species positively charged. Figure 5.11 shows the optimized structure of single-walled carbon nanotubes (SWCNT) with furan and pyran functional groups. We observed that the SWCNT(5,5) presents a positive curvature around the functional groups due to the pentagonal defects. From Mulliken population analysis, the furan and pyran functional groups donate electrons to the carbon nanotube. The furans donate 0.546 and 0.305 electrons for SWCNTs (5,5) and (10,0), respectively. The pryans donate 0.170 and 0.217 electrons for SWCNTs (5,5) and (10,0), respectively. The presence of oxygens into the graphite lattice (furans and pyrans) may promote the existence of defects, principally vacancies, and curvature effects. Thus, the vacancies surrounded by oxygens negatively charged could be attractors of cations such as K^+, Na^+, and Li^+, among others.

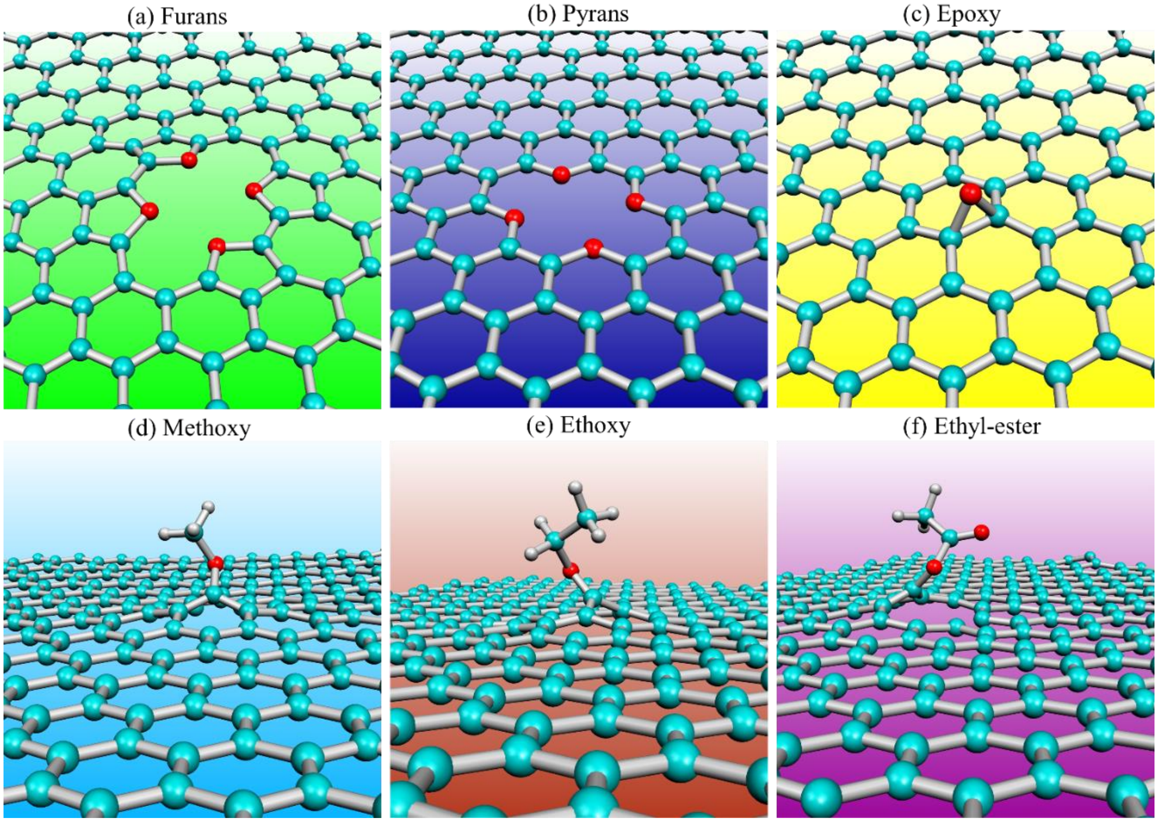

Figure 5.10: Relaxed structure graphene sheet with different oxygen functional groups. **(a)** Furans (oxygen in pentagonal rings), more details on the creation of this defect is reported in Ref. [68]. **(b)** Pyrans (oxygen in hexagonal rings), here vacancies were generated into the graphitic lattice, and carbon doubly coordinated were replaced by oxygens. **(c)** Epoxy (oxygen adatom joined to two carbon atoms). **(d)** Methoxy with C-O bond. **(e)** Ethoxy with C-O bond. **(f)** Ethyl-ester with C-O and C=O bonds. In **(d-f)**, the functional groups were attached to a carbon atom surrounding a vacancy. The oxygen, carbon, and hydrogen atoms are set in red, cyan, and gray colors, respectively.

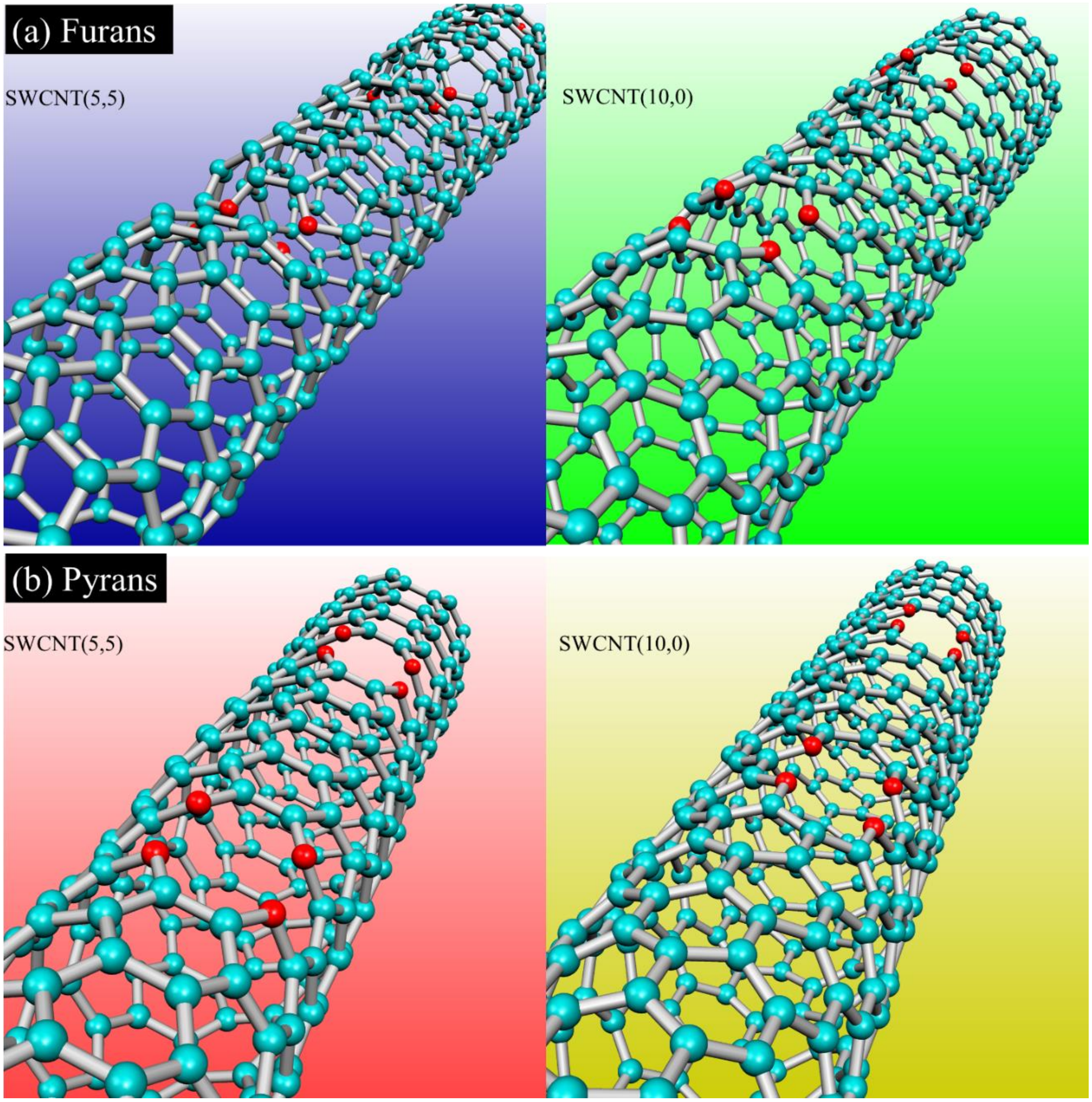

Figure 5.11: Relaxed structure of single-walled carbon nanotubes containing **(a)** furan and **(b)** pyran functional groups. Results for SWCNTs (5,5) and (10,0). Notice that the SWCNT (5,5) with furan functional groups exhibit positive curvature.

5.2.5 Conclusions

We produced entangled nitrogen-doped carbon nanofiber sponges using an aerosol-assisted chemical vapor deposition method. The N-CFS material is formed by carbon fibers of around

200 nm diameter with a rough appearance, making junctions and knots. The main features exhibited by our N-CFS were: exhibited (1) high oxygen concentration, (2) nitrogen-doping and nitrogen-functionalization, (3) transversal graphite layer stacking, (4) Si interaction with CNF, (5) ferromagnetism at room temperature, and (6) electrochemical activity. The N-CFS exhibited a coercive field of 245 Oe, similar to that found in carbon nanotubes. The cyclic voltammetry did not show the quinone peak, suggesting that oxygen functionalities are more related to the ether, ester, and aldehydes structures, as also confirmed by XPS and FTIR characterizations. The magnitude of the oxidation and reduction currents was higher than that found in carbon nanotubes produced by nitrogen precursors. DFT calculations showed that pyran and furans are structurally stable, which incorporates electrons to the graphite structures.

5.3 Growth of a magnetic carbon nanotube sponge using 1,2-dichlorobenzene

5.3.1 Experimental details

The AACVD technique was used to synthesize the CNS. Figure 5.12 shows the approach which involves the pyrolysis using the aerosol assisted chemical vapor deposition system induced by a high-frequency ultrasonic system. The precursors employed were ferrocene ($Fe(C_5H_5)_2$) with 1,2-dichlorobenzene ($C_6H_4Cl_2$) in a saturated mixture with a concentration of 0.06 g/cm^3. Our AACVD consists of the following parts: i) a quartz tube (substrate) of 1.1 m length and 1-inch internal diameter; ii) a nebulizer system (RBI instrumentation) to incorporate the vaporized solution into the quartz tube; iii) a carrier gas mixture of H_2/Ar. The AACVD synthesis was carried out at 860 °C using a tubular furnace and a mixture of H_2/Ar (5%/95%) with a flow of 2.0 l/min for three hours. The resulting material was collected from the quartz tube by internal scraping.

Scanning electron microscopy (Helios Nanolab 600 Dual Beam) and transmission electron microscopy (FEI Tecnai F30) characterization were used for morphological studies of the samples. A Renishaw micro Raman spectrometer with a 532 nm excitation laser wavelength was used to evaluate the crystalline structure. The carbon, nitrogen, and oxygen concentration in the CNS was obtained by XPS (PHI 5000 VersaProbeII). Functional groups by Fourier-transform infrared spectroscopy (FT-IR Nicolet 6700). Thermogravimetric analysis was performed using an STA 4000 Perkin-Elmer equipment in a temperature range of 50-950 °C with a heating rate of 10 °C /min under oxygen atmosphere (20 ml/min). The compression test was developed in a tensometer type W (Monsanto) with load capacities from 600 N to 20 kN. For cyclic voltammetry measurements A CNS suspension was prepared using 10 mg of CNS and 1 ml of isopropanol, then sonicated for 10 min. The suspension is deposited into an ITO glass electrode by a drip process. The solvent is left to evaporation at 110 °C for 2h. A section of 0.66 cm^2 was homogenously covered. A saturated Ag/AgCl electrode (E = 0.197 NHE) was used as a reference electrode. The CNS-ITO electrode run as a working electrode. A Pt wire was used as a counter electrode. The cyclic voltammetry measurements were performed by using an H_2SO_4 0.1 M solution as support electrolyte, in a potential window from – 0.2 V to 1.0 V at a scan rate of 10 mV/s to 400 mV/s.

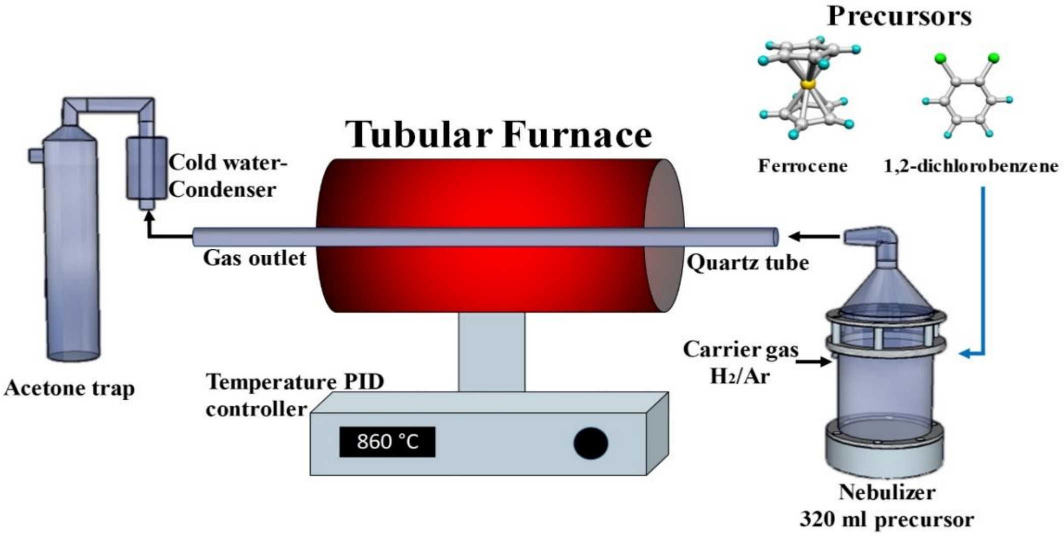

Figure 5.12: Aerosol assisted chemical vapor deposition system (AACVD) to synthesize the chloride functionalized CNS.

5.3.2 Results and discussion

Figure 5.13a illustrates a scanning electron microscopy panoramic view of the carbon tubular structures that conform to the CNS. These tubular structures are randomly ordered, but some of them are attached (red rectangle). Figure 5.13b shows another section where thin tubular carbon nanostructures of ~32 nm diameter can be observed. Their lengths are more than 3 μm, with sections where two or more tubular structures are attached together (red rectangle). Also, they have constricted sections, square tip termination, and are highly folded (blue arrows). By backscattered electrons (BSE-SEM) image (figure 5.13c), it is possible to observe that the carbon tubular structures are filled with metallic nanowires with alterations in its diameter and structure (red arrows). It could be detected the presence of semi-spherical metallic nanoparticles surrounded by carbon material. Figure 5.13d depicts the EDX spectra obtained over a wire nanoparticle inside the tubular structure (white square in figure 5.13c). The EDX revealed the presence of C (68.1 wt. %), Fe (27.5 wt. %), O (3.3 wt. %), Cl (0.6 wt. %) and Si (0.2 wt %). The spherical nanoparticle showed a concentration of Cl (0.7 wt. %) and Fe (26.4 wt. %) (figure 5.14).

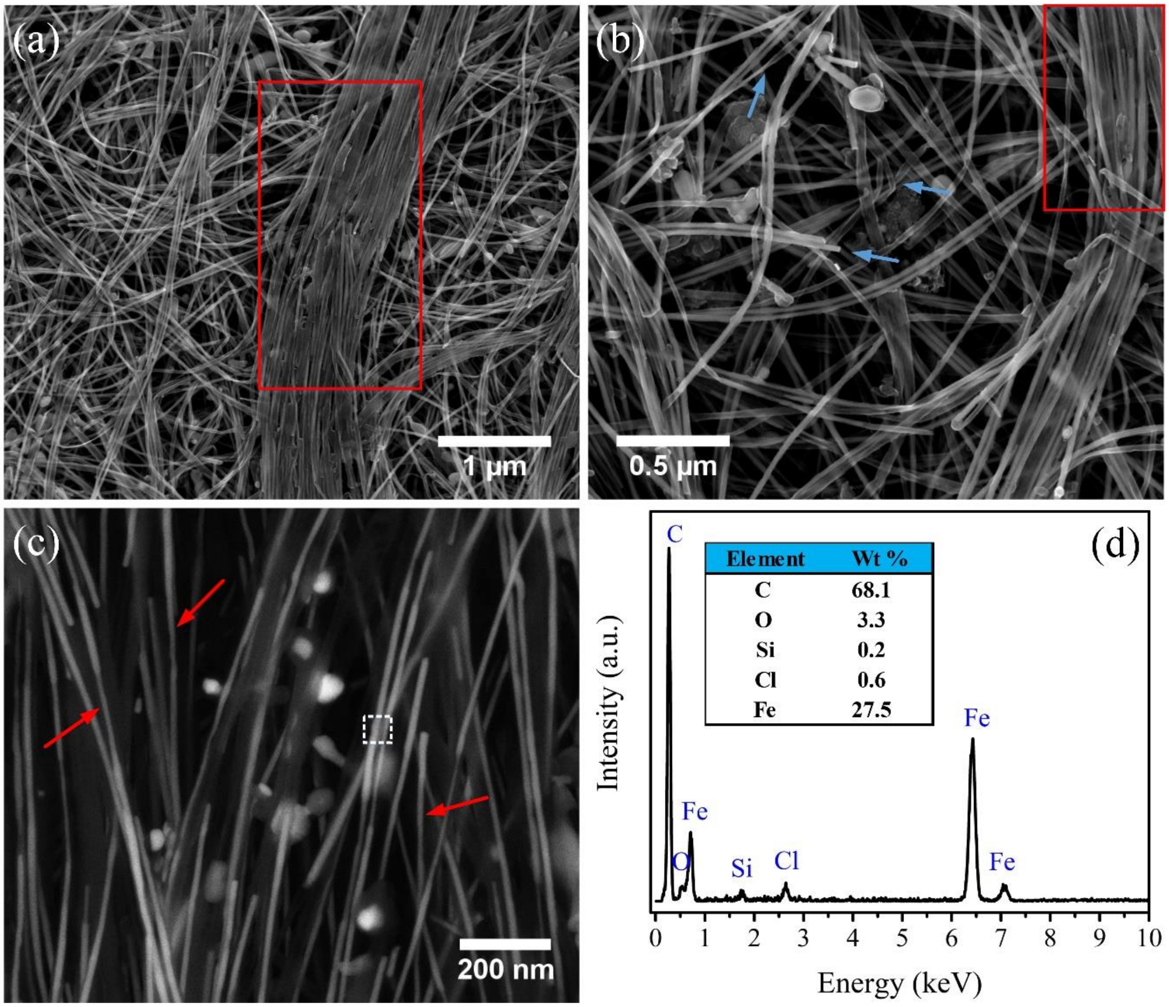

Element	Wt %
C	68.1
O	3.3
Si	0.2
Cl	0.6
Fe	27.5

Figure 5.13: (a-b) SEM images of CNS. **(c)** BSE-SEM image showing metallic wires inside MWCNTs. **(d)** EDX analysis over a metallic nanowire shows the presence of Fe, Cl, and Si.

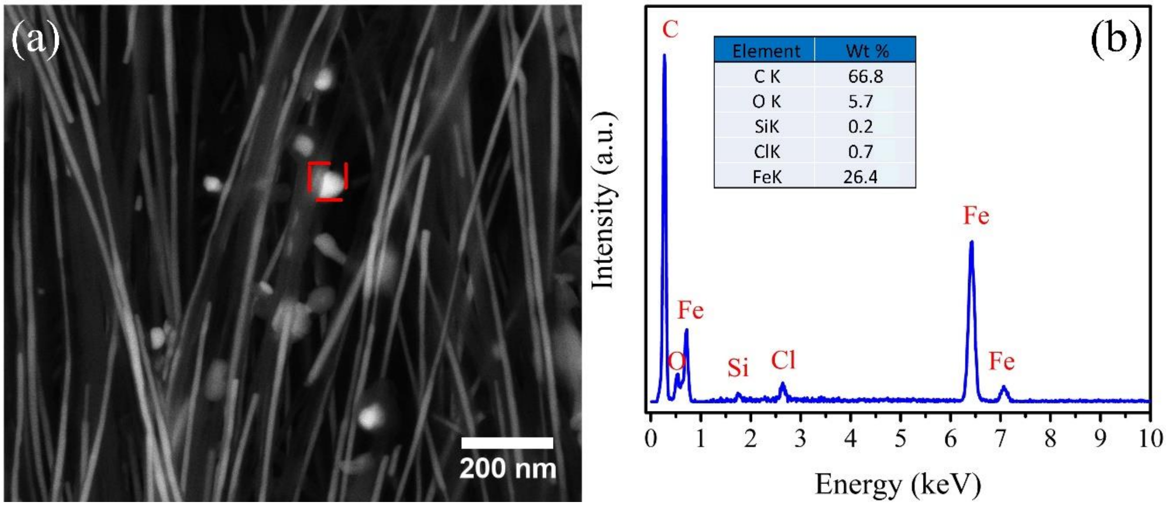

Element	Wt %
C K	66.8
O K	5.7
SiK	0.2
ClK	0.7
FeK	26.4

Figure 5.14: (a) BSE-SEM image where metallic wires are observed inside the tubular nanostructure and spherical metallic particles. **(b)** EDX analysis over one metallic sphere showing the presence of Fe, Cl, and Si.

Figure 5.15a displays a TEM micrograph where morphologies like MWCNTs with internal metallic nanowire (blue arrow), MWCNTs with no particle inside (green arrow), the graphitic structure surrounding a semi-spherical metallic nanoparticle (red arrow), and constricted MWCNTs (black ellipse) were observed. Figure 5.15b depicts a tip termination of MWCNT with a metallic nanoparticle inside. Three spots were analyzed by EDX, where it is possible to observe that the nanoparticle is Fe-based. Oxygen signal in EDX is probably associated with the substrate or due to contamination on the Fe-based nanoparticle surface [86]. Also, traces of Si were located at the nanoparticle center (spot 2) and edge (spot 3). The Si atoms could come from the substrate. Figure 5.15c illustrates a section with four attached MWCNTs, where one of them has an internal nanoparticle. One of these MWCNTs had deformed bamboo shape structures, and some sections of the tubular structure are collapsed (red arrows). A metallic nanowire is observed inside one MWCNT.

The HRTEM image over the white square (figure 5.15d) depicted the iron-based nanowire with a diameter of 21 nm and surrounded by very well-ordered graphitic layers (23 layers). Notice that the carbon nanotube arrangement varies from the showed in figure 5.15b. The Fast Fourier Transform analysis (inset) over the metallic nanoparticle shows the lattice plane and directions associated with the diffraction planes of Fe_3C nanowire. Wepasnick et al. [30] correlated functionalities in TEM images as irregular formations at the CNT surface. They displayed HRTEM images similar to the observed in figure 5.15d, where such irregularities are present in the CNS surface (blue arrow).

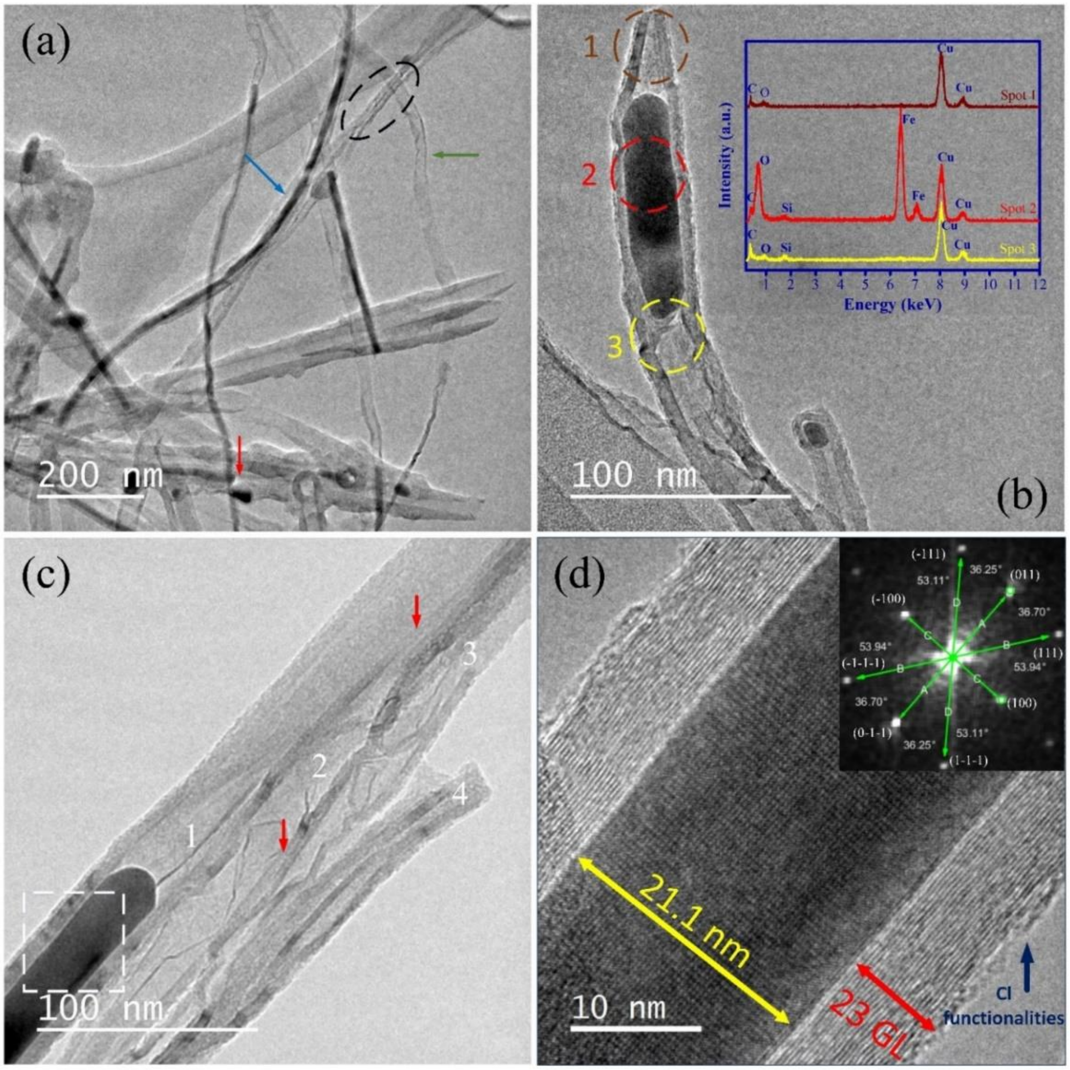

Figure 5.15: (a) Panoramic TEM image where are observed metallic nanowires fill the MWCNTs and semi-spherical metallic particles (red arrows). **(b)** Three EDX analyses over

an isolated Fe-based nanoparticle: spot 1 was over the tip section of the MWCNT; spot 2 at the main body of the Fe-based nanoparticle; and spot 3 at the final section of the Fe-based nanoparticle. **(c)** Section of glued MWCNTs with collapsed structure (red arrows) and filled with Fe-based nanoparticle. **(d)** HR-TEM developed on the white square depicts a 21nm diameter Fe-based nanowire inside MWCNT, inset illustrates the crystallographic directions associated with Fe_3C.

Figure 5.16a illustrates a zone axis of another particle inside MWCNT. Through the FFT (figure 5.16b) and Inverse-FFT (figure 5.16c) analysis, it is possible to observe the particle crystallographic planes. In this case, the distances of 0.381 Å, 0.305 Å, and 0.514 Å corresponding to the (-100) zone axis of orthorhombic Fe_3C nanowire (figure 5.16d) [87]. Wang et al. described that using 1,2-dichlorobenzene to grow carbon nanostructures lead to the formation of γ-Fe and α-Fe particles inside the tubular structures of MWCNTs [88]. Nevertheless, in this case, it promotes the formation of Fe_3C.

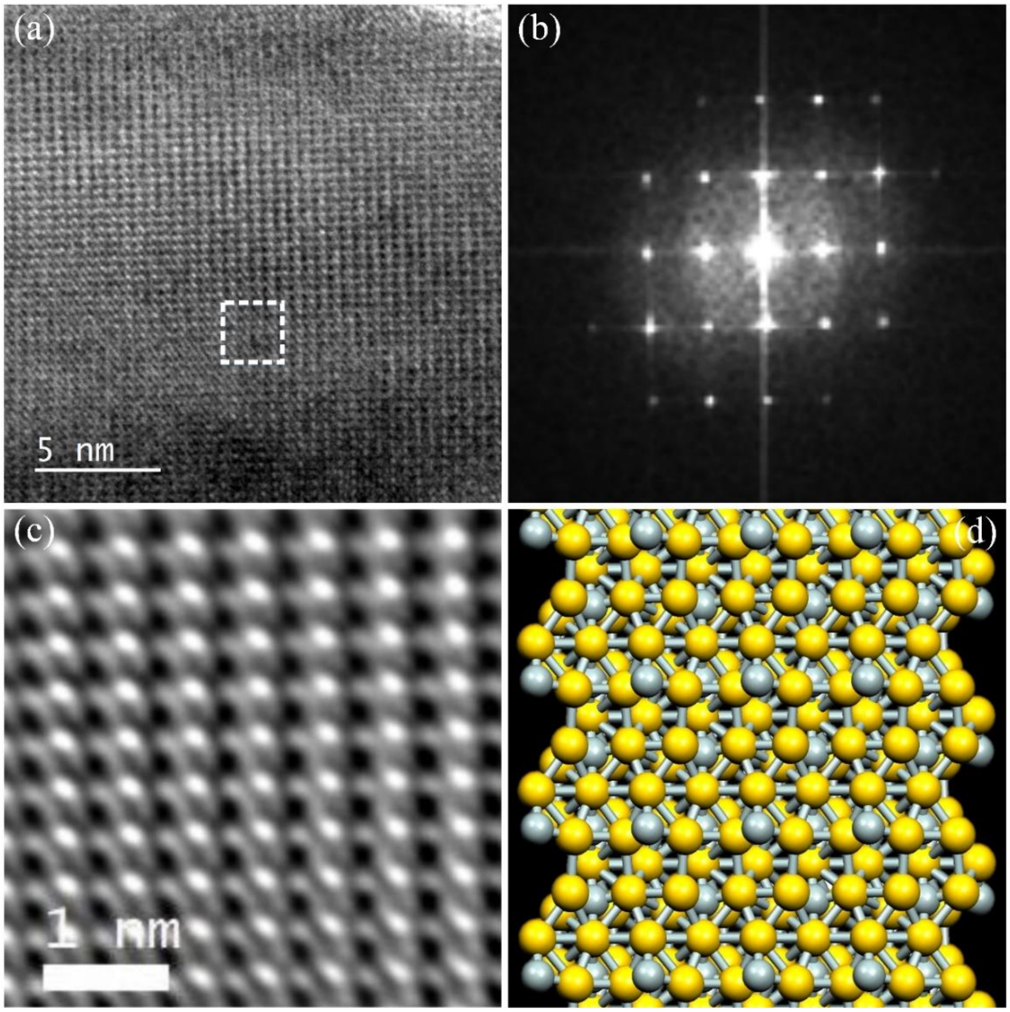

Figure 5.16: (a) HRTEM image of a Fe_3C wire inside the tubular structure. **(b)** FFT analysis developed over the white square in (a). **(c)** Zone-axis HR-TEM image that enhances the crystal structure. **(d)** Cell structure representation of (c) that shows the (100) plane for Fe_3C.

XPS inspection survey spectra (figure 5.17) depicts primarily four elements (Cl, Fe, C, and O). Table 5.4 depicts the binding energies, FWHM, relative percentage (%Rel), and the total percentage (%Total), considering the information observed in survey spectra and associated with the high-resolution regions of C1s, Cl2p, O1s, and Fe2p. Figure 5.18a illustrates the C12p deconvoluted region using Gaussian-Lorentzian (90%-10%) curves. In this case, were observed energies related to the formation of chloride bonds like C-Cl at 200.8 eV, which are correlated to the formation of methyl-chloride functionalities. Also, multiple aromatic chloride functionalities observed at 202.3 eV and 203.2 eV can be associated with the incorporation of Cl atoms at the edges of the graphitic structure and the formation of covalent-chloride functionalities [89]. Besides, it was possible to deconvolute energies linked to the Fe-Cl bond. The total amount of Cl species is 0.8 %, where 0.6 % corresponds to chloride functionalities.

Figure 5.18b depicts the Fe2p3 XPS region where bond energies connected with Fe metallic (0.11 %), Fe-C (0.14 %) can be found. In the case of Fe-O (0.09 %) and Fe-Cl (0.06 %), the low At% concentrations associated with the atomic detection limit of XPS analysis and deconvolution data obtained from the main Fe signal suggests that traces of this elements are observed at the surface (red-colored table 5.4). The deconvoluted area can also estimate the surface chemical species anchored to the graphitic surface. For instance, the C1s region (figure 5.18c) reveals a concentration of C-O total functionalities (C-O, C=O, and COOH) of ~9.1 % that could be a consequence of the interaction of oxygen from the quartz tube and interaction with the atmosphere [60]. The functionalities associated with C-Cl could be overlapped at the C-O functionality position, and the $C-Cl_3$ bond at 291 eV could be overlapped with $\pi-\pi$ interactions (~4.5 %) [37]. The C-C sp^2 hybridization (62.8.0 %) is higher compared with the C-C sp^3 hybridization (11.9 %). The surface total oxygen concentration observed in the XPS survey could contain the contribution of oxygen from SiO_2; however, it overlaps with the position of C-O functionality. Figure 5.18d displays the O1s spectrum where different oxygen species are appreciated like C-O due phenolic (532.0 eV), C=O of carbonyl (531.0 eV), C-O-C related with ether (533.1 eV) and COOH associated to carboxyl acid (534.3 eV) functionalization.

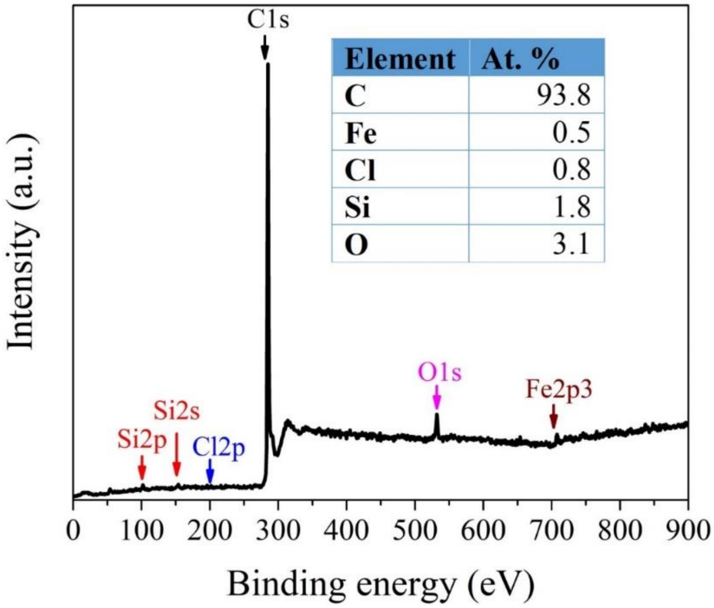

Figure 5.17: Survey XPS spectra where signals related to C, O, Fe, Cl, and Si are observed. The atomic concentration of the involved chemical elements is shown in the inset.

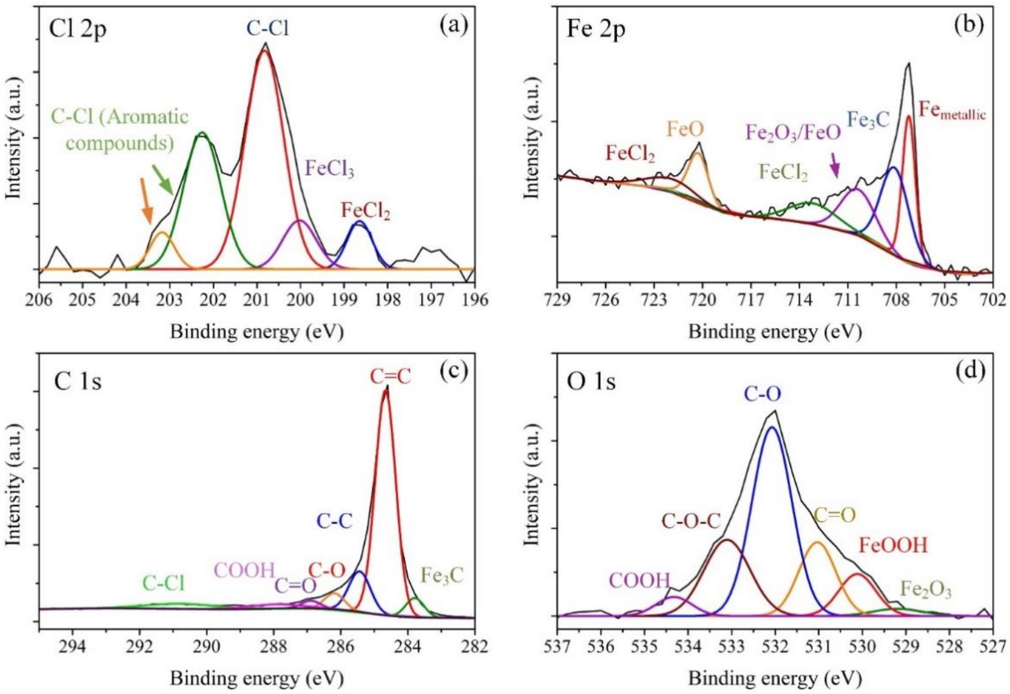

Figure 5.18: High-resolution XPS deconvoluted spectra of the CNS. **(a)** Cl2p spectra show the energies related to the Cl functionalization of the graphitic structure (200.5 eV, 202.2 eV, and 203.2 eV) and the related to the iron interaction (198.5 eV and 200.1 eV). **(b)** Fe2p spectra reveal the bond energies associated with the formation of Fe-O, Fe-Cl species. **(c)**

C1s spectra show the presence of sp^2 hybridized carbons (C=C bonds), sp^3 C-C bond, phenolic (C-O), carbonyl (C=O), and carboxylic (COOH) functionalization and the related to the C-Cl and Fe-Cl interactions. **(d)** O1s spectra where mainly phenolic (C-O) and ether contribution (C-O-C).

Table 5.4: XPS data information obtained from the survey (Figure 5.17) and deconvolution performed over the high-resolution regions of C1s, Cl2p, O1s, Fe2p (figure 5.18). Red-colored indicates bond energy traces associated with low detection limits.

Region	Group	BE (eV)	FWHM (eV)	% Rel	% Total
C1s	Fe_3C	283.7	0.6	5.1	4.7
	C=C	284.6	0.7	67.0	62.8
	C-C	285.4	0.7	12.7	11.9
	C-O	286.1	0.6	4.5	4.2
	C=O	286.8	0.6	2.0	1.8
	COOH	287.9	1.9	3.2	3.0
	C-Cl	290.7	2.5	5.2	4.8
Cl2p	$FeCl_2$	198.6	0.6	6.9	0.0
	$FeCl_3$	200.0	0.9	9.4	0.0
	C-Cl	200.8	1.0	48.9	0.3
	C-Cl (Aromatic)	202.2	1.0	29.4	0.2
	C-Cl (Aromatic)	203.1	0.6	5.1	0.0
O1s	Fe_2O_3	529.1	1.3	2.1	0.0
	FeOOH	530.1	0.9	9.4	0.2
	C=O	531.0	0.9	16.6	0.5
	C-O	532.0	1.0	46.2	1.4
	C-O-C	533.1	1.2	21.3	0.6
	COOH	534.3	0.9	4.16	0.1
Fe2p	Fe metallic	707.2	0.9	22.8	0.1
	Fe_3C	708.0	2.0	28.8	0.1
	Fe_2O_3 / FeO	710.3	2.4	18.2	0.0
	$FeCl_2$	713.1	3.4	11.54	0.0

FeO	720.2	1.4	11.5	0.0
$FeCl_2$	722.0	3.9	6.94	0.0

Figure 5.19a illustrates CNS weight loss versus temperature. In the first stages, the sponge showed at 400 °C, a weight-loss of 2.70 wt. %. This fact is probably due to water vaporization, loss of the oxygen, and decomposition of chloride functionalities [90]. There is a small up of mass weight from 400 °C to 500 °C, probably to oxidation of Si [91]. Two maximum decomposition temperatures T_{D1} at 574.9 °C (71.5 wt.% loss) and T_{D2} at 618.8 °C (8.29 wt.% loss) can be correlated first with the oxidation process of the MWCNTs and second to some graphitic material surrounding the metallic material as was observed in figure 5.15d, respectively. Decomposition temperature for well-ordered MWCNTs is reported to start at 600 °C [92], and for graphitic core-shell materials are between 485°C and 710 °C [93]. Our CNS presents a residual material of 17.5 wt% that could be associated with the formation of iron oxide. In this case, the molar C:Fe ratio is about 31.07:1.

The XRD pattern depicts the crystallographic planes of graphitic carbon (COD 96-101-1061), α-Fe cubic structure (COD 96-110-0109), γ-Fe cubic structure (COD 96-901-507296) and Fe_3C in an orthorhombic structure (COD 96-901-4028) (figure 5.19b). A refinement of the XRD pattern reveals a crystallographic phase of 86.7 % for graphitic carbon, followed by Fe_3C (6.7 %) and γ-Fe (4.1 %) and traces of α-Fe (2.6 %).

Figure 5.19c depicts the Fourier-transform infrared spectroscopy analysis developed over the CNS. Signals linked to the formation with covalent Cl species are observed between 870 cm^{-1} and 737 cm^{-1}. Vibration modes from 869 cm^{-1} and 829 cm^{-1} can be associated with the formation of saturated halogenated species like trichloromethyl radical (CCl_3) or dichloromethyl radical ($CHCl_2$), also identified with multiple-aromatic chloride species [94,95]. The vibration between 759 cm^{-1} and 739 cm^{-1} has a connection with the stretching vibration of C-Cl of chloromethane and single halogenated aromatic surfaces [96]. The C-Cl functionalities are also associated with the capacity of CNT to absorb light in the UV-Vis spectra and could promote amine or amides functionalization in the CNT surface [97,98]. In the case of oxygenated functionalization, the presence of –OH vibration at 3415 cm^{-1}, C=O around 1650 cm$^{-1,}$ and C-O-C at 1000 cm^{-1} reveals the formation of phenolic, ketones, aldehydes, carboxylic acid, ether and ester functionalization [99]. The presence of C=C stretching vibration due to aromatic sp^2 hybridization is marked at 1520 cm^{-1} [100].

Figure 5.19d depicts the Raman spectra of the CNS, where signals at 220 cm^{-1} and 286 cm^{-1} are regarded as the formation of Fe_3C [101]. Moreover, the existence of signals between 390 cm^{-1} and 670 cm^{-1} are attributed to amorphous Si (a-Si), Si-Si, and Si-H phases [102]. For graphitic structure, the D band correlated with the breathing mode of defective structure, and the G band correspond with the in-plane C=C vibration are positioned at 1346 cm^{-1} and 1587 cm^{-1}, respectively. The I_D/I_G ratio indicates the degree of the defective structure as the ratio goes over unity [103]. For the CNS, the I_D/I_G is below the unity (0.8), indicative of a low defective structure [47]. The intensity and shape of the 2D band are associated with the number of graphitic layers [47], and their position changes due to doping over the graphitic structure where higher electron concentration at the surface is found when the 2D band shifts to lower values from 2685 cm^{-1} and contrary [48]. In this case, the CNS structure has an intense signal at the 2D-band placed at 2690 cm^{-1} with an intensity of 0.68 times the G band can be associated to hole doping over few-layered CNT structures. Also, the presence of G*-band can be related to the formation of surface roughness and the D+D´ band with the formation of wrinkled and whisker formation [104,105]. Dimovski et al. reported an increment of the intensities of D+D´ and 2D´ bands for corrugated graphitic structures, effect that can be present also in carbon nanotube tip termination [105].

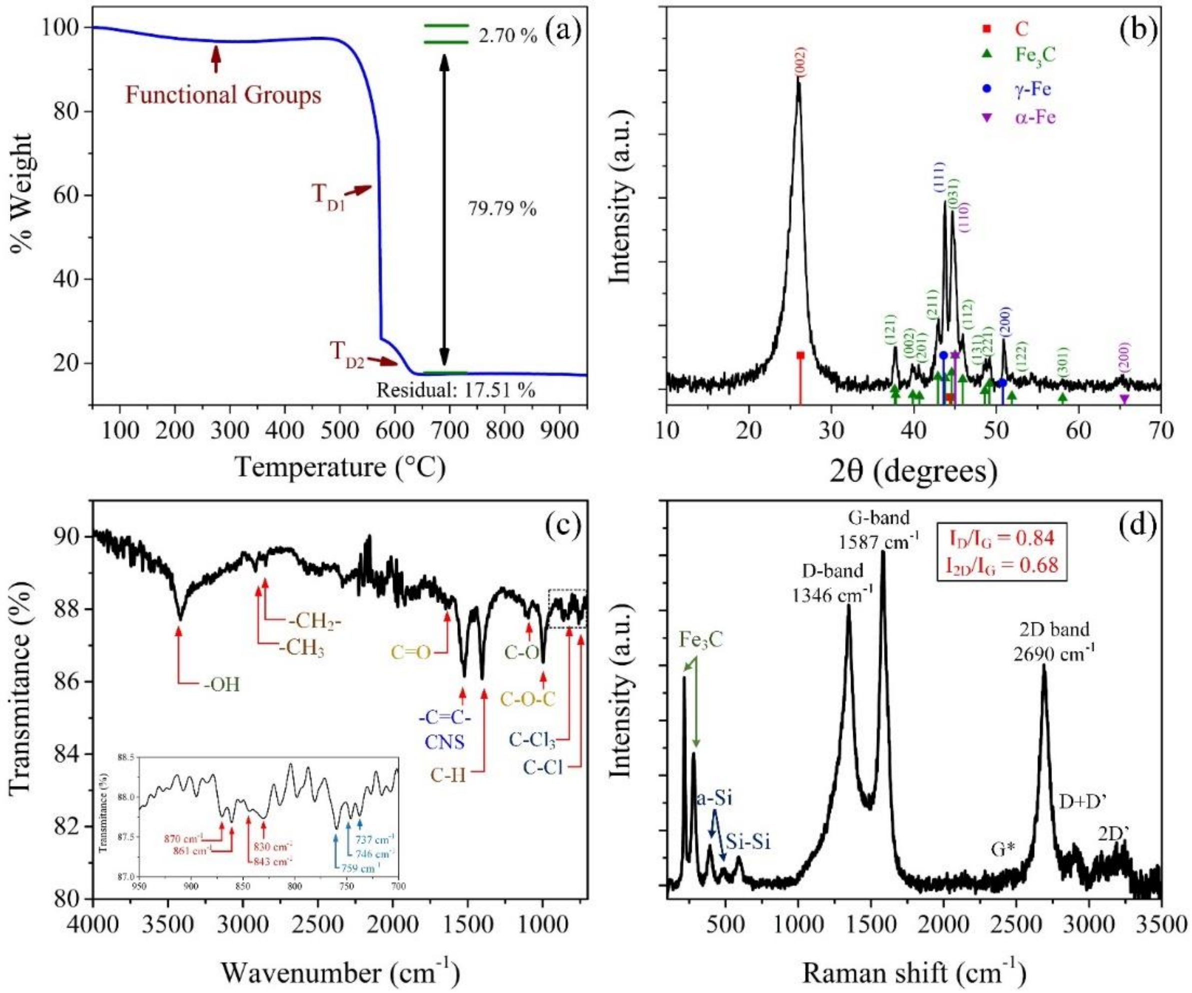

Figure 5.19: (a) TGA plot showing a contribution of 2.7% due likely to functional groups, 79.7% due to graphic structure, and 17.5% due to iron structure. (b) The X-ray diffraction pattern shows the relative diffraction patterns of graphitic carbon, α-Fe, γ-Fe, and Fe_3C. (c) FTIR spectra illustrate the vibration modes of oxygenated species (C-OH, C-O, C-O-C) and the related to chloride species due to the formation of C-Cl3 and C-Cl. (d) Raman spectra illustrate de D-band, G-band, and the 2nd order vibration modes like 2D-band, G*-band, D+D'-band, and 2D´-band.

Figure 5.20a depicts the magnetization curve for the CNS. The saturation magnetization (Ms) is 192.7 emu/g (~1.45×10^6 A/m). This value is similar to the reported by Weissker et al. [106] for iron carbide nanowires inside MWCNTs. The Fe_3C nanowires, in that case, were below 60 nm diameter and hundreds of nanometer lengths. They obtained Ms = 9.8×10^5 A/m [106], being one of the highest values reported until now. The CNS structure as composite has a coercive field strength of 502 Oe at room temperature (figure 5.20b). This value is similar for MWCNTs filled with Fe nanowires that present values from 445 Oe to 660 Oe [107,108], which are higher than Fe bulk (~0.9 Oe) [109] and Fe_3C bulk (100 Oe) [74]. Su et al. [74] reported similar values obtained in complex flower-like carbon nanostructured clusters. Morelos-Gómez et al. [110] demonstrated that the coercive field of Fe_3C nanowires is associated with the length and size of the nanowire inside MWCNTs. For example, they fabricated MWCNTs with diameters of 19.2 nm. The coercive field, in this case, was ~400 Oe at 300 K, while as the diameter of Fe_3C particle decreases, the coercive field increases. In our samples, the coercive value of 502 Oe could come of the mixture of crystallographic phases of α-Fe, γ-Fe, and Fe_3C.

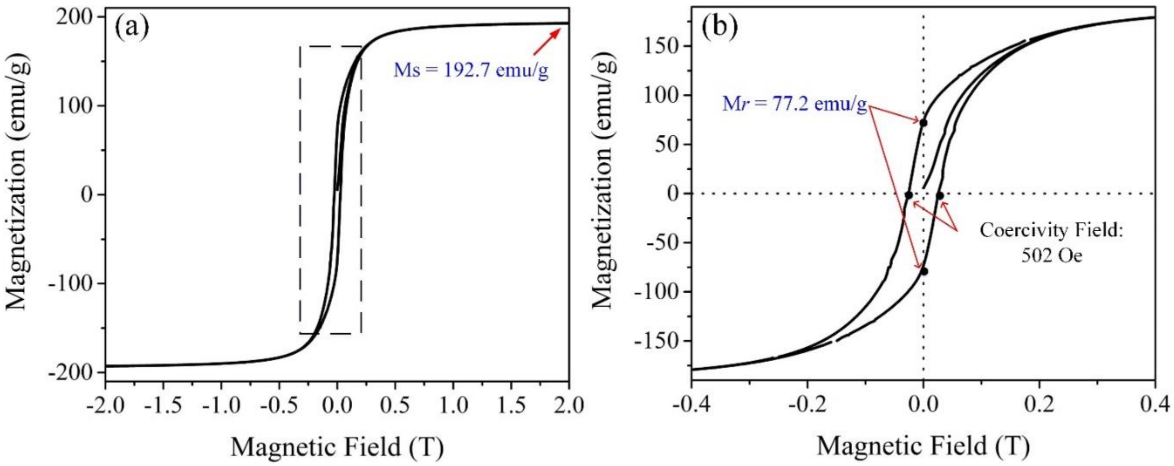

Figure 5.20: (a) Magnetic hysteresis loop for CNS reaching the saturation (M_S) at 197.2 emu/g. **(b)** Close-up over the magnetization curve depicts a coercive field of 502 Oe and a remanence of 77.2 emu/g at 300 K.

Figure 5.21a shows the cyclic voltammetry using the CNS as a working electrode at a scan rate of 10 mV/s in an H_2SO_4 media to increase the wettability and the pseudocapacitance over the oxygen functionalities [111]. An intense anodic signal (A) is observed around 0.476 V with its respective cathodic peak (A´) at 0.389 V. The ΔEp was 0.087 V being in a quasi-reversible redox process [112]. This quasi-reversible redox process could be related to the Fe^{2+}/Fe^{3+} oxide-reduction process [113] of iron species that structures the iron carbide nanowires and exposed iron nanoparticles. Also, a secondary peak-pair B and B´ is observed at 0.641 V and 0.234 V, respectively. This redox process could be connected with the hydroquinone/quinone oxide-reduction process [71]. This fact is in concordance with the XPS and FTIR results, as revealed in the presence of Fe, Fe_3C, Fe_2O_3, $FeCl_2$ metallic structures, and OH and C=O oxygen functionalities. Li et al. obtained a squared voltammetry curve using iron filled MWCNTs in HNO_3 between 0-2 V. The square cyclic voltammetry (CV) curve exhibits high charge capacities [13]. In our case, the deformation of the CV curve and semi-square curve could be a consequence of the increase of electron transport in graphite material due to Cl species [114]. Janas et al. [115] described how the functionalization with Cl increases the electrical conductivity of the CNT due to the influence of the electron density of Cl atoms over the sp^2 C-C electronic density generated by the graphitic structure.

Figure 5.21b depicts the cyclic voltammetry loops for different scan rates. As the scan rate increases, the charge capacity should increase linearly. Figure 5.21c illustrates the linearity of the anodic current (A) as the scan rate increases. Besides, an increase in the scan rate produces an increase over the A/A´ peak and the potential difference between the anodic and cathodic peaks (ΔE_p) following the linearity. Figure 5.21d depicts the galvanostatic charge-discharge cyclic process with a 1.4 V limit potential and over 200 cycles. Figure 5.21e shows the changes in charge capacity after several cycles (0, 50, 100 y 200 cycles). The initial charge-discharge process shows two voltage regions. In the charge curve (0 cycle), a high charge process from 0.2 V to ~1.0 V and slope could be attributed to the oxidation process of Fe to Fe^{+2} and Fe^{+3} species and the slope (from 1.0 V to 1.4 V) to the graphitic doping-functionalities effect. An irreversible capacity loss is observed in the initial cycle. A considerable decrease in the charge capacity in the initial 50 cycles is observed. Several structural factors could impact this behavior like porosity, surface chemistry, thickness, and dimensions of carbon nanostructure. The CNS after 100 cycles reaches its maxima current efficiency (figure 5.21f) after this, after the 200 cycles the CNS decreases and maintains a charge efficiency of 98.8%.

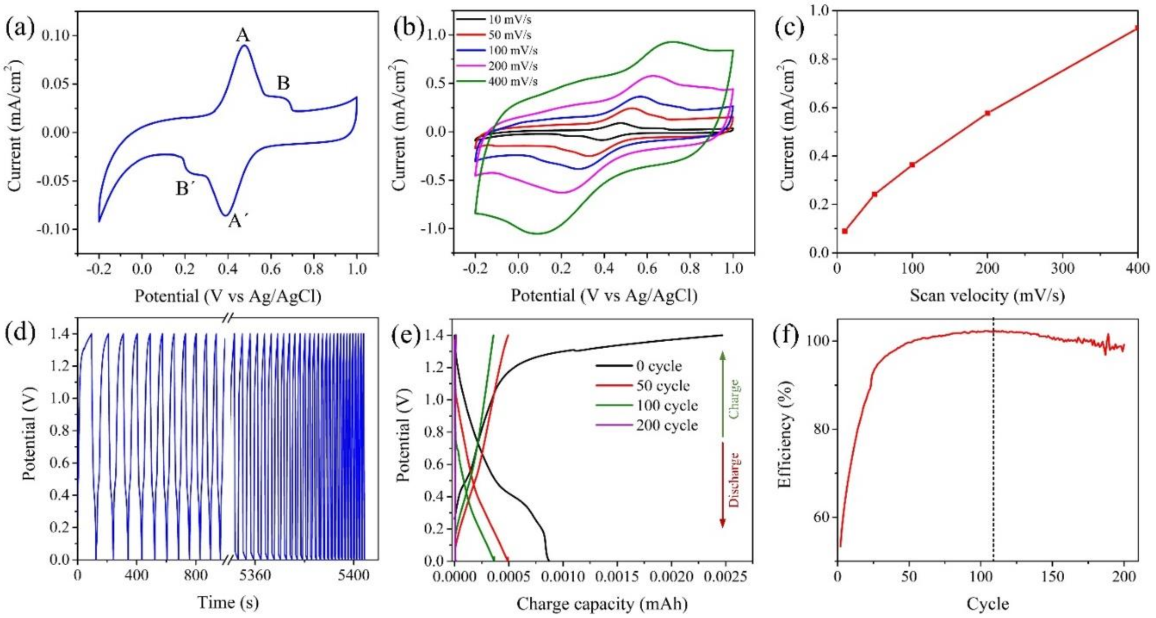

Figure 5.21: (a) Cyclic voltammetry curve of CNS showing a reversible oxidation-reduction peak of the Fe^{2+}/Fe^{3+} redox process (A and A´) and hydroquinone/quinone functionalities (B and B´). **(b)** Current vs. potential plot for different scan rates. **(c)** The relation between scan velocity and anodic current. **(d)** The galvanostatic charge-discharge cyclic process to 1.4V at 200 cycles and constant current density. **(e)** Current charge capacity at different cycles. **(f)** Charge efficiency after 200 cycles.

Figure 5.22a depicts the FTIR spectra of different thermal treated CNS at different temperatures, namely, pristine (black curve), 300 °C (red curve), 400 °C (blue curve), 500 °C (magenta curve), 600 °C (green curve), 700 °C (dark blue curve) and 800 °C (purple curve). Signals at 992 cm^{-1}, 1406 cm$^{-1,}$ and 3413 cm^{-1} are related to the C-O-C, C-H, and C-OH vibration modes, respectively. They are associated with oxygen functional groups (C-O-C and C-OH) and borders (C-H). These three bands disappeared at TT-300 °C. The vibration bands at 1994 cm^{-1} and ~2281 cm^{-1} (blue arrows) are intensified and could be associated with the CO2 formation due to the desorption of oxygen functional groups from 300° to 800 °C [60]. The dotted line at 749 cm^{-1} and 857 cm^{-1} are representative of the position of C-Cl and $C\text{-}Cl_3$ functional groups, respectively. These vibrational modes are observed in pristine, TT-300 °C, and TT-400 °C. At TT-500 °C disappears. Quian et al. [98] reported that chloride functionalities are desorbed between 300 °C to 500 °C. However, the appearance of a signal (yellow arrow) around ~923 cm^{-1} can be related to benzyne ions and ring deformation [116]. Figure 5.22b depicts the cyclic voltammetry results of the thermal treated CNS. Notice that for TT-300°C to 500 °C, the current density intensity is reduced from values around 0.03 mA/cm^2 (CNS-pristine) to around 0.003 mA/cm^2. This behavior could be associated with the loss of Cl functionalities. For TT-700° C, In the case of samples TT-600 °C and TT-800 ° the charge capacity increases for TT-800 °C (~0.25 mA/cm^2) and doubles for TT-600°C (0.05 mA/cm^2). This behavior is probably linked to the signal observed in FTIR connected to the formation of benzyne ions and the ring deformation. The 700-TT case could be associated with morphological changes that are observed in TGA results, as shown in figure 5.19a. Fe-based materials and functional groups (red arrows in figure 5.22b) signals vanish probably due to the detachment of exposed Fe nanoparticles due to sample preparation by sonication and the desorption of functional groups. Interesting is that the cyclic voltammetry curve passes from a pseudocapacitive behavior (CNS-pristine) to a double-layer capacitance behavior [117]. More investigation related to the effect of the thermal treatment in this CNS could give insights over what is happening with the CNT and Fe3C nanowires during voltammetry measurements.

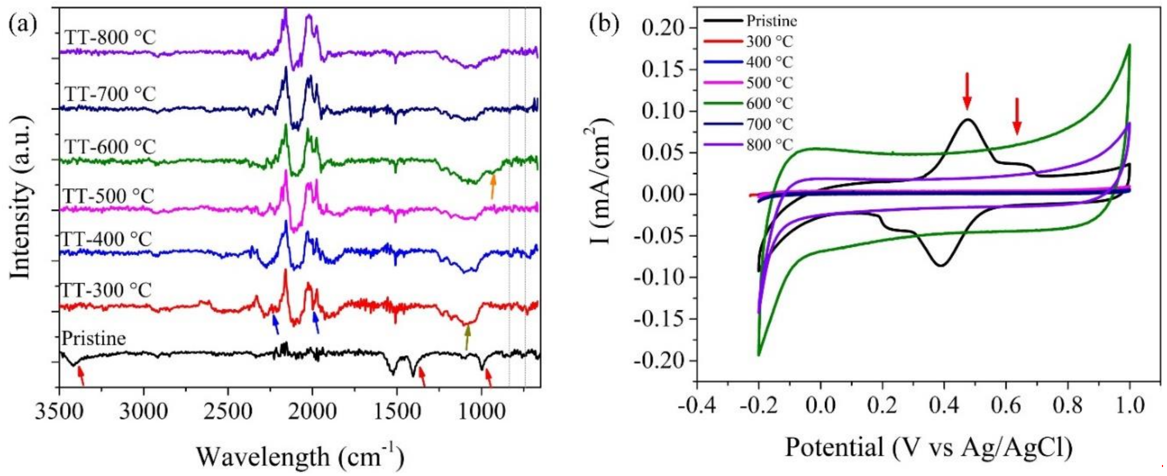

Figure 5.22: (a) FTIR spectra for CNS (pristine) and samples thermally treated (TT-X, being X temperature) from 300 °C to 800 °C in N_2 atmosphere. **(b)** Cyclic voltammetry measurements for CNS and TT-X (X = 300 °C, 400 °C, 500 °C, 600 °C, 700 °C, 800 °C) samples in H_2SO_4 media.

The absorption capacity was tested for the CNS structure. Figure 5.23a depicts a photograph of a piece of 3.38 cm × 0.3 cm × 0.6 cm (volume = 0.60 cm^3) of the CNS. Pieces of approximately 0.5 cm × 0.5 cm × 0.2 cm of the CNS were cut it and used as a sorbent to determine the sorption capacity of polar solvents like methanol and ethylene glycol and non-polar solvents like diesel, vacuum oil and gasoline (figure 5.23b). The CNS absorbs 23.3 times its weight of diesel (highest adsorption) followed by vacuum oil (20.8 wt/wt). The worst adsorption capacity was for methanol (15.2 wt/wt). Figure 5.23c illustrates a comparison of the CNS (red bar) with other sponge-type materials. For example, Gui et al. [12] reported adsorption capacities ~143 times its weight using a CNT-sponge compared with other sponges such as polyurethane sponge, loofah skeleton, polyester, cotton towel, and activated carbon.

Furthermore, it included in the graph is described as an N-doped CNT-sponge with an absorption capacity of 21.3 times its weight by Muñoz-Sandoval et al. [41]. Images in figure 5.23d show the burning process of the sponge after it adsorbs diesel solvent. The burning process starts at 0s when the sponge is initially burned; after 30 seconds, the fire is at its maximum; after 38 seconds, the fire begins to extinguish and ends after 43 seconds. The burned sponge did not show significant structural modifications. A repetitive process of absorption-burning was made for nine times, after the five cycles the CNS loses the 16% of absorption capacity, then it stabilizes. Images in figure 5.23e-h describe the absorption process of oil (cooking-oil mixed with green color) spilled over de-ionized water. This process was monitored through the time that a piece of the CNS was deposited over the oil surface (figure 5.23e) until the moment it reaches saturation (figure 5.23f) after 51 seconds. The sponge can be moved over the water when a magnet is approaching due to the magnetic Fe_3C phase. In figure 5.23g, the magnet was approximated to the glass when the CNS was on the opposite extreme, and then figure 5.23h shows the situation after a few seconds when the CNS is closer to the magnet.

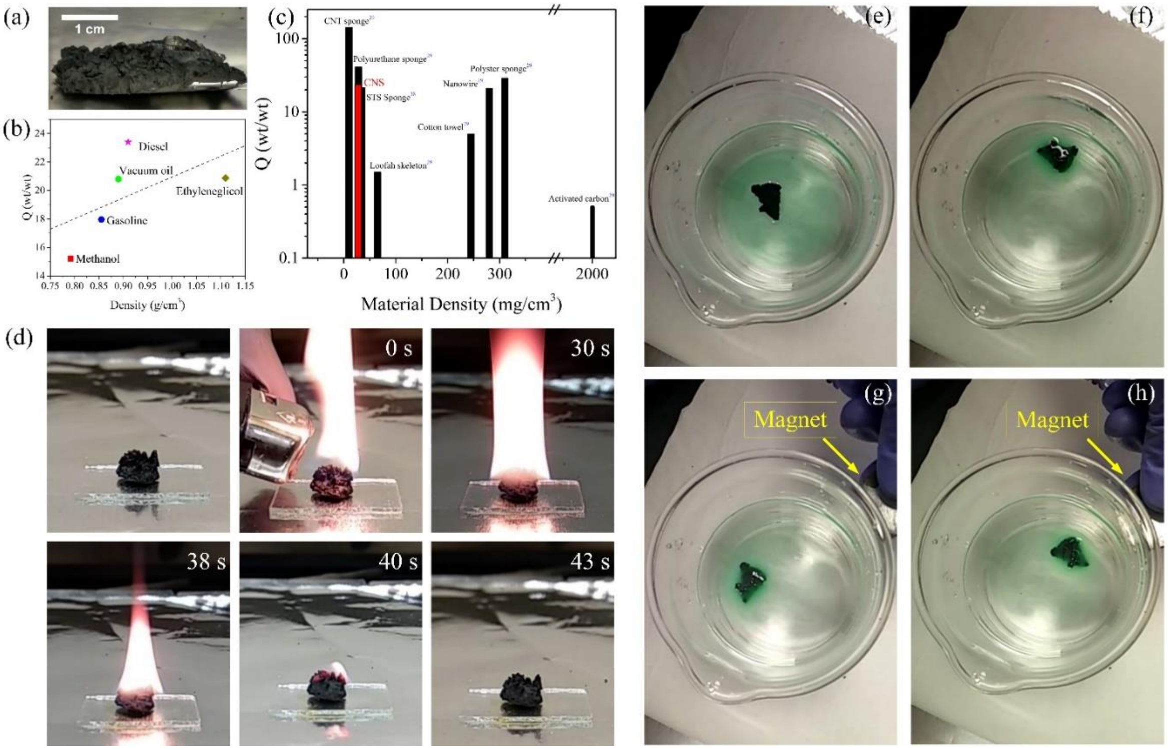

Figure 5.23: (a) A photograph of CNS. **(b)** Absorption capacity using different solvents (polar and non-polar) for the CNS reaching 23 times its weight for Diesel. **(c)** Comparison of absorption capacity for a variety of materials reported by Gui et al. [12] and Muñoz-Sandoval et al. [41] with the CNS (red bar). **(d)** The burning process of the CNS sample at different times. **(e-h)** Oil absorption test over water using the CNS. Note the crystalline formation due to the adsorption and the property of movement over the surface using a magnet.

Figure 5.24a shows a cylinder-shaped CNS with dimensions of 0.6 cm radius and 0.58 cm height. A load is applied in the direction of the red arrow. Figure 5.24b illustrates the compression process. The cylinder broke with a load of 8.4 kN and reached a height of 0.316 mm, i.e., a reduction of the 45.5 % of initial height. After this deformation process, the CNS is fully recovered (figure 5.24c), but some sections collapsed (blue arrow). A rectangular plate-like shaped formed with CNS (figure 5.24d) was also tested. Their dimensions were 0.8 cm x 1.2 cm x 0.5 cm of thickness approximately. Figure 5.24e depicts the load applied to the rectangular plate-like CNS, where a thickness of 0.098 mm is reached after applying a pressure of 2 kN. In this case, a thickness reduction of 80.5% concerning to the original plate was observed. Notice that after the load is released, the rectangular plate-like shape is almost recovered (figure 5.24f). However, some of its parts are detached (blue arrow). Figure 5.24g shows the stress-strain curve (SSC) for the cylinder-like CNS (red line) and the rectangular plate-like CNS (blue line). For the cylinder-like structure, the SSC is similar to the reported for plastic-elastic deformation. A maximum load of 84 MPa with a strain of 36.9 %. The fracture point reaches with a strain of 45.5 %. This behavior could be attributed to the randomness interaction of CNT that builds the CNS. The rectangular plate-like CNS shows only a continuous growth of stress, reaching a tension of 17.1 MPa before breaking. Similar materials demonstrated different loads for breaking. Gui et al. [29] reported maximum compression stress of around 0.05 MPa with a compressive strain of ~ 80 % in their CNS. Li et al. [118] reported a CNT sponge that supports loads of about 2 MPa to 10 MPa with partially breaking. Worsley et al. [119] compared their CNT foam with other materials like carbon or silica and obtained compressive stress for the CNT foam of around 100 MPa.

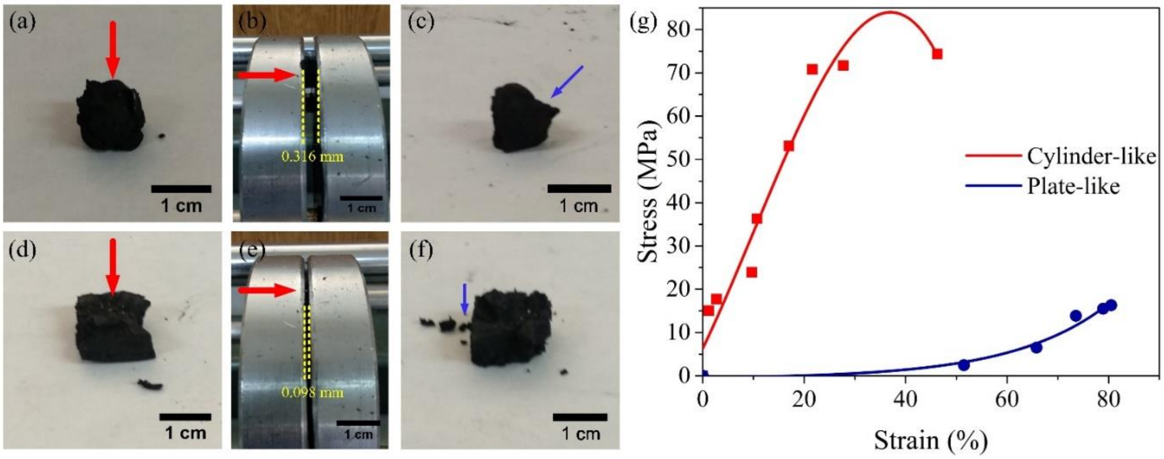

Figure 5.24: (a) Cylinder-like CNS with 0.6 cm radius and 0.58 height, the applied load follows the red arrow. **(b)** Compression stress continues until the CNS is broken; the final strain was 45.5%. **(c)** Cylinder-like CNS after the load is released, a blue arrow depicts a broken section. **(d)** Rectangular plate-like CNS, the red arrow points out the direction of the load is applied. **(e)** The load is applied until the CNS is broken at 0.098mm **(f)** Rectangular plate-like CNS after the load is released, detached parts are observed (blue arrow). **(g)** The

stress-strain curve shows a maximum load of 84 MPa and 17.1 MPa for cylinder-like CNS and rectangular plate-like CNS, respectively.

5.3.3 Growth mechanism approach

Figure 5.25 illustrates a schematic of the growth mechanism of our CNS. Figure 5.25a depicts the decomposition of 1,2-dichlorobenzene. The formation of chlorophenyl radical and chloride radicals is the first step of the decomposition. In a reductive atmosphere, the chloride radical could form hydrochloric acid and chlorine gas. In the case of the chlorophenyl compound, Kern et al. [120] show that the decomposition follows two routes. One is the ring-opening that leads to the production of small aliphatic chains like C_2H_4, C_4H_3, C_4H_2, and halogenated aliphatic structures like CH_3Cl, C_2H_4C. The second route consists of the separation of Cl together with the chain reaction of radicals that probably produce larger species like $C_{12}H_8Cl$, $C_{18}H_{13}Cl$, and others. In both cases, there are HCl and Cl radicals formation [120,121]. Figure 5.25b is a representative proposal of the growth mechanism. In early stages, aliphatic carbon chains are produced by the decomposition of 1,2-dichlorobenzene, and the decomposition of ferrocene promotes the formation of carbon atoms and iron atoms that precipitates over the quartz tube. The Fe atoms coalesce to form a Fe-based nanoparticle (Fe_3C mainly) and the CNT begin to grow. The HCl interacts with amorphous carbon leading to a slower carbon saturation of the Fe-based nanoparticle (figure 5.26c). In this stage also the Cl radicals interacts with the Fe to form $FeCl_2$/$FeCl_3$ that form grain boundaries limiting the typical growth of CNTs. In the following stage (figure 5.26d), the formation of the Fe-based nanowire starts (yellow), provoking a unidirectional growth of the CNT. The CNT extruded the Fe-based nanowire because the Cl-based material prevents the growth of catalyst nanoparticle. After this (figure 5.26e), the Cl reacts with the CNT surface functionalizing it. The CNS is constructed when the Fe_3C nanoparticles precipitate over the CNT and promote a random growth (figure 5.26f).

Figure 5.26(g-j) illustrates SEM images associated with the growth of the CNS through time form 0 min to 3 hours, respectively. At 0 min (figure 5.26g, retro dispersed SEM image), carbon material agglomerates with a high deposition of metallic particles. After 1 hour (figure 5.26h), there is a formation of CNTs (~60 nm diameter) with encapsulated metallic nanowires. Notice that some CNTs are partially oriented, forming thin (white squared). Figure 5.26i shows larger bundles of CNTs (red arrows) approximately ~ 920 nm width and randomly oriented. In this figure, the diameter of the CNT is about 42 nm. The bundle sections are probably associated with the large chloride species anchored to the CNT that works as a semi-polymeric junction structure. At 3 hours (figure 5.26j), the CNT diameters are thinner (~32 nm), and no bundled sections are observed. Unlike what happens in the case of covalent bonds between CNT in some sponges [10,19], or due to van der Waals forces in other types of Self-assembly 3D CNT constructions [11]. In our case, where no curved or very clean CNTs are observed, our CNS maybe is constructed based on covalent unions between defects generated by the chloride functionalization.

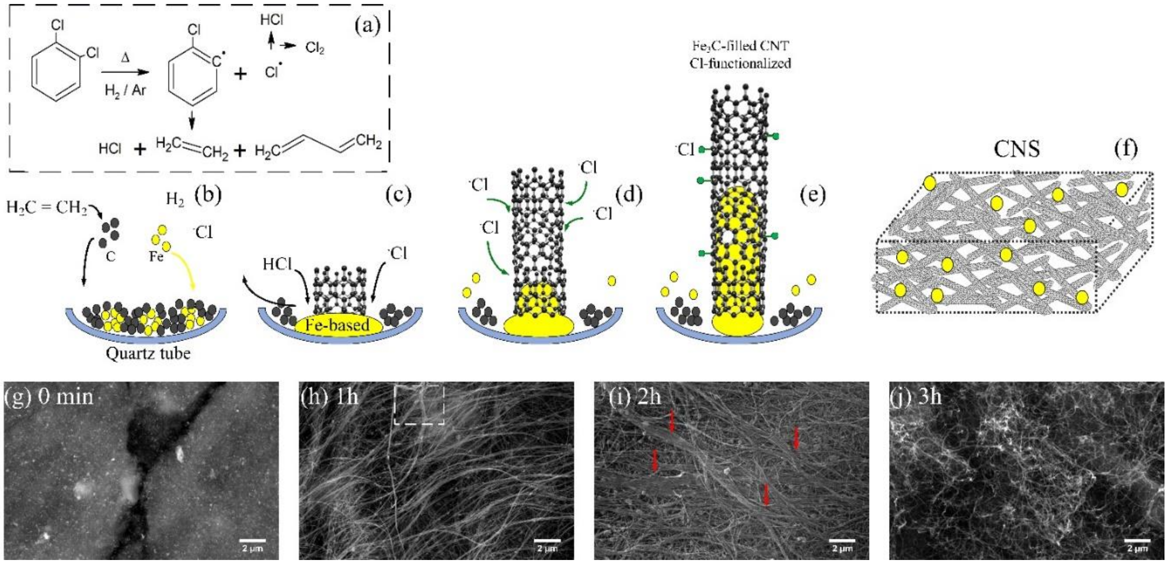

Figure 5.26: (a) Possible decomposition mechanism for 1,2-dichlorobenzene where the formation of chlorophenyl and chloride radicals are observed. **(b-f)** The schematization of the growth mechanism of Fe_3C filled CNT where the interaction of chloride species with amorphous carbon and Fe-based particles promotes the formation of Fe_3C nanowires and chloride functionalization, and finally the CNS. **(g-j)** SEM images associated with the growth of carbon materials through time 0 min (g), 1h (h), 2h (i), and 3h (j). In these last SEM images, the figure (g) is a back-scattering electron SEM image.

5.3.4 Theoretical procedure

Electronic calculations were performed using density functional theory (DFT) [78,79]. The generalized gradient approximation with the Perdew, Burke, and Ernzerhof parametrization was chosen for the exchange-correlation functional [80] as implemented in the SIESTA code [81]. The wave functions for the valence electrons were represented by a linear combination of pseudo-atomic numerical orbitals using a double-ζ polarized basis (DZP) [82], while the core electrons by norm-conserving Troullier-Martins pseudopotentials in the Kleinman-Bylander non-local form [83,84]. The real-space grid used for charge and potential integration is equivalent to a plane wave cut-off energy of 150 Ry. We used a graphene supercell of 6×6 with 140 atoms. In the non-periodic axis, we used a minimum of 30 Å to avoid lateral interactions. A sampling of the 2D Brillouin zones was carried out with 60×60×1 Monkhorst-Pack grids. Density matrix and energy tolerances were both taken as 10^{-5} eV. A variable cell structural relaxation was performed on all systems to include the strain effects introduced by the functional groups. The geometry optimization was performed by conjugate gradient minimization until the maximum force was < 0.04 eV/Å.

Density-functional calculations were performed for the trichloromethyl and chloride functionalization on armchair metallic and zigzag semiconductor carbon nanotubes. Figure 5.27 displays the electronic density of states and the corresponding structural relaxed structures for single-walled carbon nanotubes. In both cases, the starting geometry for the structure optimization was the trichloromethyl on the surface of the carbon nanotubes. After the geometry optimization, in the semiconducting SWCNT(10,0), the trichloromethyl was fragmented into chloride and dichloromethyl (Cl +CCl_2); see figure 5.27a. In the CCl_2, the carbon is joined to two carbon atoms belonging to the carbon nanotube. The electronic density of states showed states just in the Fermi energy level due to the charge transfer. From Mulliken analysis, the CCl_2 and single Cl pulled out from the carbon nanotubes 0.064 and 0.184 electrons, respectively. Results for SWCNT(6,6) are shown in figure 5.27b. The trichloromethyl kept its structure after the optimization treatment, the density of states showed states at the Fermi level. The Mulliken analysis revealed a charge transfer of 0.073 electrons from carbon nanotube to trichloromethyl. The chloride atom pulled out 0.242 and 0.275 electrons for (10,0) and (6,6) SWCNTs, respectively.

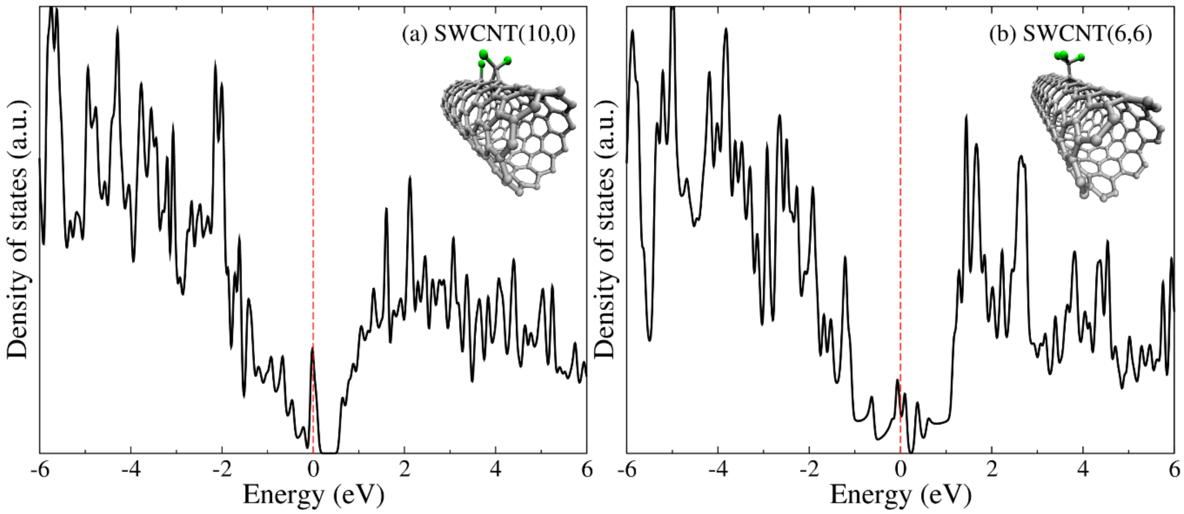

Figure 5.27: Electronic density of states chloride functionalized single-walled carbon nanotubes (SWNT). **(a)** SWCNT (10,0) and **(b)** SWCNT (6,6). The corresponding optimized structures are shown in the inset. In both cases, the starting geometry in the optimization procedure consisted of the SWCNT with a trichloromethyl anchored on its surface. The Fermi energy is set in zero energy (vertical dashed line).

5.3.5 Conclusions

In this work, we report the formation of Fe_3C-nanowire-encapsulated chloride functionalized carbon nanotube forming a CNS. The Fe_3C nanowires present lengths above 3 μm and diameters of ~21 nm, surrounded by well-ordered graphitic layers. Between the most relevant results of our work is the decomposition of the 1,2-dichlorobenzene molecule leading to surface functionalization with chloride, chloromethane, and trichloromethyl radicals. It is one of the first times that chloride functionalization in carbon sponges is reported. Another leads issue is the magnetization saturation obtained mainly due to the Fe_3C nanowires. The value of 192.7 emu/g is one of the most significant values published until now and higher in carbon nanotube sponges. Also, the coercive field is competitive and could be used for the recuperation of oil spills. The cyclic voltammetry measurements demonstrated that the CNS exhibits high charge capacity due to the hydroquinone/quinone process of oxygen functionalities and diffusion of Cl ions. These results are essential to use our CNS as a catalyst in electrochemistry. The CNS depicts oil-sorption capacity with 23 times its weight for diesel. Besides, no structural damage after burning is observed. It is worth mentioning that our CNS can be pressed or burned to recover o eliminate the hydrocarbons without suffering visible deterioration. The CNS is mechanically stable and support high loads (84 MPa). Finally, CNS is a three-dimensional porous carbon nanostructured material with chloride functionalizations and magnetic properties that could be used as an electrode for magnetic Li-ion batteries and magnetic ORR reactions.

5.4 References

[1] A. Dasgupta, L. Pulickal, C. Rotella, Y. Lei, M. Terrones, Covalent three-dimensional networks of graphene and carbon nanotubes : synthesis and environmental applications, Nano Today. 12 (2017) 116–135. https://doi.org/10.1016/j.nantod.2016.12.011.

[2] A.L. Elías, N. Perea-López, L.P. Rajukumar, A. McCreary, F. López-Urías, H. Terrones, M. Terrones, Three-dimensional Nanotube Networks and a New Horizon of Applications, 2013. https://doi.org/10.1016/B978-1-4557-7863-8.00017-7.

[3] J. Zhang, M. Terrones, C.R. Park, R. Mukherjee, M. Monthioux, N. Koratkar, Y.S. Kim, R. Hurt, E. Frackowiak, T. Enoki, Y.Y. Chen, Y.Y. Chen, A. Bianco, Carbon science in 2016: Status, challenges and perspectives, Carbon. 98 (2016) 708–732. https://doi.org/10.1016/j.carbon.2015.11.060.

[4] C. Shan, W. Zhao, X.L. Lu, D.J. O'Brien, Y. Li, Z. Cao, A.L. Elias, R. Cruz-Silva, M. Terrones, B. Wei, J. Suhr, Three-dimensional nitrogen-doped multiwall carbon nanotube sponges with tunable properties, Nano Letters. 13 (2013) 5514–5520. https://doi.org/10.1021/nl403109g.

[5] S. Ozden, T. Tsafack, P.S. Owuor, Y. Li, A.S. Jalilov, R. Vajtai, C.S. Tiwary, J. Lou, J.M. Tour, A.D. Mohite, P.M. Ajayan, Chemically interconnected light-weight 3D-carbon nanotube solid network, Carbon. 119 (2017) 142–149. https://doi.org/10.1016/j.carbon.2017.03.086.

[6] Z. Wu, S. Yang, Y. Sun, K. Parvez, X. Feng, 3D Nitrogen-Doped Graphene Aerogel-Supported Fe 3 O 4 Nanoparticles as Efficient Electrocatalysts for the Oxygen Reduction Reaction, Jacs. 134 (2012) 9082–9085. https://doi.org/10.1021/ja3030565.

[7] L. Zhang, F. Zhang, X. Yang, G. Long, Y. Wu, T. Zhang, K. Leng, Y. Huang, Y. Ma, A. Yu, Y. Chen, Porous 3D graphene-based bulk materials with exceptional high surface area and excellent conductivity for supercapacitors, Sci Rep. 3 (2013) 1408.

https://doi.org/10.1038/srep01408.

[8] S. Vinod, C.S. Tiwary, L.D. Machado, S. Ozden, R. Vajtai, D.S. Galvao, P.M. Ajayan, Synthesis of ultralow density 3D graphene–CNT foams using a two-step method, Nanoscale. 8 (2016) 15857–15863. https://doi.org/10.1039/C6NR04252J.

[9] S. He, H. Hou, W. Chen, 3D porous and ultralight carbon hybrid nanostructure fabricated from carbon foam covered by monolayer of nitrogen-doped carbon nanotubes for high performance supercapacitors, Journal of Power Sources. 280 (2015) 678–685. https://doi.org/10.1016/j.jpowsour.2015.01.159.

[10] Z. Dai, L. Liu, X. Qi, J. Kuang, Y. Wei, H. Zhu, Z. Zhang, Three-dimensional Sponges with Super Mechanical Stability: Harnessing True Elasticity of Individual Carbon Nanotubes in Macroscopic Architectures., Scientific Reports. 6 (2016) 18930. https://doi.org/10.1038/srep18930.

[11] S. Luo, Y. Luo, H. Wu, M. Li, L. Yan, K. Jiang, L. Liu, Q. Li, S. Fan, J. Wang, Self-assembly of 3D Carbon Nanotube Sponges: A Simple and Controllable Way to Build Macroscopic and Ultralight Porous Architectures, Advanced Materials. (2016) 1–8. https://doi.org/10.1002/adma.201603549.

[12] X. Gui, J. Wei, K. Wang, A. Cao, H. Zhu, Y. Jia, Q. Shu, D. Wu, Carbon nanotube sponges, Advanced Materials. 22 (2010) 617–621. https://doi.org/10.1002/adma.200902986.

[13] S. Nardecchia, D. Carriazo, M.L. Ferrer, M.C. Gutiérrez, F. del Monte, Three dimensional macroporous architectures and aerogels built of carbon nanotubes and/or graphene: synthesis and applications., Chemical Society Reviews. 42 (2013) 794–830. https://doi.org/10.1039/c2cs35353a.

[14] S. Lu, Y. Chen, X. Wu, Z. Wang, Y. Li, Three-dimensional sulfur/graphene multifunctional hybrid sponges for lithium-sulfur batteries with large areal mass loading, Scientific Reports. 4 (2014) 4–7. https://doi.org/10.1038/srep04629.

[15] X. Gui, H. Li, K. Wang, J. Wei, Y. Jia, Z. Li, L. Fan, A. Cao, H. Zhu, D. Wu, Recyclable carbon nanotube sponges for oil absorption, Acta Materialia. 59 (2011) 4798–4804. https://doi.org/10.1016/j.actamat.2011.04.022.

[16] P. Ayala, R. Arenal, M. Rümmeli, A. Rubio, T. Pichler, The doping of carbon nanotubes with nitrogen and their potential applications, Carbon. 48 (2010) 575–586. https://doi.org/10.1016/j.carbon.2009.10.009.

[17] J. Park, M. Yan, Covalent functionalization of graphene with reactive intermediates, Accounts of Chemical Research. 46 (2013) 181–189. https://doi.org/10.1021/ar300172h.

[18] J. Patiño, N. López-Salas, M.C. Gutiérrez, D. Carriazo, M.L. Ferrer, F. del Monte, Phosphorus-doped carbon–carbon nanotube hierarchical monoliths as true three-dimensional electrodes in supercapacitor cells, J. Mater. Chem. A. 4 (2016) 1251–1263. https://doi.org/10.1039/C5TA09210H.

[19] D.P. Hashim, N.T. Narayanan, J.M. Romo-Herrera, D.A. Cullen, M.G. Hahm, P. Lezzi, J.R. Suttle, D. Kelkhoff, E. Muñoz-Sandoval, S. Ganguli, A.K. Roy, D.J. Smith, R. Vajtai, B.G. Sumpter, V. Meunier, H. Terrones, M. Terrones, P.M. Ajayan, Covalently bonded three-dimensional carbon nanotube solids via boron induced nanojunctions, Scientific Reports. 2 (2012) 1–8. https://doi.org/10.1038/srep00363.

[20] A.A. Koós, F. Dillon, E.A. Obraztsova, A. Crossley, N. Grobert, Comparison of structural changes in nitrogen and boron-doped multi-walled carbon nanotubes, Carbon. 48 (2010) 3033–3041. https://doi.org/10.1016/j.carbon.2010.04.026.

[21] J.M. Romo-Herrera, B.G. Sumpter, D.A. Cullen, H. Terrones, E. Cruz-Silva, D.J. Smith, V. Meunier, M. Terrones, An atomistic branching mechanism for carbon nanotubes: Sulfur as the triggering agent, Angewandte Chemie - International Edition. 47 (2008) 2948–2953. https://doi.org/10.1002/anie.200705053.

[22] G. Zhou, E. Paek, G.S. Hwang, A. Manthiram, Long-life Li/polysulphide batteries with high sulphur loading enabled by lightweight three-dimensional nitrogen/sulphur-codoped graphene sponge, Nature Communications. 6 (2015) 1–11. https://doi.org/10.1038/ncomms8760.

[23] S.W. Pattinson, V. Ranganathan, H.K. Murakami, K.K.K. Koziol, A.H. Windle, Nitrogen-induced catalyst restructuring for epitaxial growth of multiwalled carbon nanotubes, ACS Nano. 6 (2012) 7723–7730. https://doi.org/10.1021/nn301517g.

[24] D.A. Svintsitskiy, L.S. Kibis, D.A. Smirnov, A.N. Suboch, O.A. Stonkus, O.Y. Podyacheva, A.I. Boronin, Z.R. Ismagilov, Spectroscopic study of nitrogen distribution in N-doped carbon nanotubes and nanofibers synthesized by catalytic ethylene-ammonia decomposition, Applied Surface Science. 435 (2018) 1273–1284. https://doi.org/10.1016/j.apsusc.2017.11.244.

[25] H. Wang, W. Wang, J. Key, S. Ji, Y. Ma, L. Khotseng, W. Lv, R. Wang, Sponge-like carbon containing nitrogen and iron provides a non-precious oxygen reduction catalyst, Journal of Solid State Electrochemistry. 19 (2015) 1181–1186. https://doi.org/10.1007/s10008-014-2719-1.

[26] S.S. Shinde, C.H. Lee, A. Sami, D.H. Kim, S.U. Lee, J.H. Lee, Scalable 3-D Carbon Nitride Sponge as an Efficient Metal-Free Bifunctional Oxygen Electrocatalyst for Rechargeable Zn-Air Batteries, ACS Nano. 11 (2017) 347–357. https://doi.org/10.1021/acsnano.6b05914.

[27] Y. Li, W. Liao, Z. Li, T. Feng, L. Sun, C. Guo, J. Zhang, J. Li, Building three-dimensional porous nano-network for the improvement of iron and nitrogen-doped carbon oxygen reduction electrocatalyst, Carbon. 125 (2017) 640–648. https://doi.org/10.1016/j.carbon.2017.09.106.

[28] C. Zhang, R. Hao, H. Liao, Y. Hou, Synthesis of amino-functionalized graphene as metal-free catalyst and exploration of the roles of various nitrogen states in oxygen reduction reaction, Nano Energy. 2 (2013) 88–97. https://doi.org/10.1016/j.nanoen.2012.07.021.

[29] M. Seredych, D. Hulicova-Jurcakova, G.Q. Lu, T.J. Bandosz, Surface functional groups of carbons and the effects of their chemical character, density and accessibility to ions on electrochemical performance, Carbon. 46 (2008) 1475–1488. https://doi.org/10.1016/j.carbon.2008.06.027.

[30] K.A. Wepasnick, B.A. Smith, K.E. Schrote, H.K. Wilson, S.R. Diegelmann, D.H. Fairbrother, Surface and structural characterization of multi-walled carbon nanotubes following different oxidative treatments, Carbon. 49 (2011) 24–36. https://doi.org/10.1016/j.carbon.2010.08.034.

[31] P.A. Denis, R. Faccio, A.W. Mombru, Is it possible to dope single-walled carbon nanotubes and graphene with sulfur?, ChemPhysChem. 10 (2009) 715–722. https://doi.org/10.1002/cphc.200800592.

[32] M.D. Walle, Z. Zhang, M. Zhang, X. You, Y. Li, Y.N. Liu, Hierarchical 3D nitrogen and phosphorous codoped graphene/carbon nanotubes–sulfur composite with synergistic effect for high performance of lithium–sulfur batteries, Journal of Materials Science. 53 (2018) 2685–2696. https://doi.org/10.1007/s10853-017-1678-1.

[33] A.G. Gonalves, J.L. Figueiredo, J.J.M. Órfão, M.F.R. Pereira, Influence of the surface chemistry of multi-walled carbon nanotubes on their activity as ozonation catalysts, Carbon. 48 (2010) 4369–4381. https://doi.org/10.1016/j.carbon.2010.07.051.

[34] E. Cruz-silva, D. a Cullen, L. Gu, J.M. Romo-herrera, E. Muñoz-sandoval, F. López-urías, B.G. Sumpter, V. Meunier, J. Charlier, Ḱ.D.J. Smith, H. Terrones, M. Terrones, Multiwalled Carbon Nanotubes, ACS Nano. 2 (2008) 441–448. https://doi.org/10.1021/am200933m.

[35] E. Gracia-Espino, F. López-Urías, H. Terrones, M. Terrones, Electron transport study on functionalized armchair graphene nanoribbons: DFT calculations, RSC Advances. 6 (2016) 21954–21960. https://doi.org/10.1039/c5ra25278d.

[36] P.A. Denis, Band gap opening of monolayer and bilayer graphene doped with aluminium, silicon, phosphorus, and sulfur, Chemical Physics Letters. 492 (2010) 251–257. https://doi.org/10.1016/j.cplett.2010.04.038.

[37] D. Bouša, J. Luxa, V. Mazánek, O. Jankovský, D. Sedmidubský, K. Klímová, M. Pumera, Z. Sofer, Toward graphene chloride: Chlorination of graphene and graphene oxide, RSC Advances. 6 (2016) 66884–66892. https://doi.org/10.1039/c6ra14845j.

[38] E. Muñoz-Sandoval, J.L. Fajardo-Díaz, R. Sánchez-Salas, A.J. Cortés-López, F. López-Urías, Two Sprayer CVD Synthesis of Nitrogen-doped Carbon Sponge-type Nanomaterials, Scientific Reports. 8 (2018). https://doi.org/10.1038/s41598-018-20079-9.

[39] C. Erbay, G. Yang, P. De Figueiredo, R. Sadr, C. Yu, A. Han, Three-dimensional porous carbon nanotube sponges for high-performance anodes of microbial fuel cells, Journal of Power Sources. 298 (2015) 177–183. https://doi.org/10.1016/j.jpowsour.2015.08.021.

[40] W. Zhao, T. Li, Y. Li, D.J. O'Brien, M. Terrones, B. Wei, J. Suhr, X. Lucas Lu, Mechanical properties of nanocomposites reinforced by carbon nanotube sponges, Journal of Materiomics. 4 (2018) 157–164. https://doi.org/10.1016/j.jmat.2018.01.006.

[41] E. Muñoz-Sandoval, A.J. Cortes-López, B. Flores-Gómez, J.L. Fajardo-Díaz, R. Sánchez-Salas, F. López-Urías, Carbon sponge-type nanostructures based on coaxial nitrogen-doped multiwalled carbon nanotubes grown by CVD using benzylamine as precursor, Carbon. 115 (2017). https://doi.org/10.1016/j.carbon.2017.01.010.

[42] A. Bianco, Y. Chen, Y. Chen, D. Ghoshal, R.H. Hurt, Y.A. Kim, N. Koratkar, V. Meunier, M. Terrones, A carbon science perspective in 2018: Current achievements and future challenges, Carbon. 132 (2018) 785–801. https://doi.org/10.1016/j.carbon.2018.02.058.

[43] M.S. Kim, Yoong Ahm; Hayashi, Takuya; Endo, Morinobu; Dresselhaus, Carbon Nanofibers, in: R. Vajtai (Ed.), Springer Handbook of Nanomaterials, Springer, Houston, TX, 2013: p. 1234. https://doi.org/10.1007/978-3-642-20595-8.

[44] R. Zheng, Y. Zhao, H. Liu, C. Liang, G. Cheng, Preparation, characterization and growth mechanism of platelet carbon nanofibers, Carbon. 44 (2006) 742–746. https://doi.org/10.1016/j.carbon.2005.09.015.

[45] C. Ducati, K. Koziol, S. Friedrichs, T.J. V Yates, M.S. Shaffer, P.A. Midgley, A.H. Windle, Crystallographic order in multi-walled carbon nanotubes synthesized in the presence of nitrogen, Small. 2 (2006) 774–784. https://doi.org/10.1002/smll.200500513.

[46] D.K. Singh, P.K. Iyer, P.K. Giri, Diameter dependence of interwall separation and strain in multiwalled carbon nanotubes probed by X-ray diffraction and Raman scattering studies, Diamond and Related Materials. 19 (2010) 1281–1288.

https://doi.org/10.1016/j.diamond.2010.06.003.

[47] M.S. Dresselhaus, A. Jorio, M. Hofmann, G. Dresselhaus, R. Saito, Perspectives on carbon nanotubes and graphene Raman spectroscopy, Nano Letters. 10 (2010) 751–758. https://doi.org/10.1021/nl904286r.

[48] A. Das, S. Pisana, B. Chakraborty, S. Piscanec, S.K. Saha, U. V Waghmare, K.S. Novoselov, H.R. Krishnamurthy, A.K. Geim, A.C. Ferrari, A.K. Sood, Monitoring dopants by Raman scattering in an electrochemically top-gated graphene transistor, 3 (2008) 1–6. https://doi.org/10.1038/nnano.2008.67.

[49] A.C. Ferrari, D.M. Basko, Raman spectroscopy as a versatile tool for studying the properties of graphene, Nat Nanotechnol. (2013) 1–13. https://doi.org/10.1038/nnano.2013.46.

[50] S. Zhang, J. Wang, Z. Li, R. Zhao, L. Tong, Z. Liu, Raman Spectra and Corresponding Strain E ff ects in Graphyne and Graphdiyne, (2016). https://doi.org/10.1021/acs.jpcc.5b12388.

[51] M. Inagaki, F. Kang, Graphene derivatives: graphane, fluorographene, graphene oxide, graphyne and graphdiyne, Journal of Materials Chemistry A: Materials for Energy and Sustainability. 2 (2014) 13193–13206. https://doi.org/10.1039/C4TA01183J.

[52] J. Schwan, S. Ulrich, V. Batori, H. Ehrhardt, S.R.P. Silva, Raman spectroscopy on amorphous carbon films, Journal of Applied Physics. 80 (1996) 440–447. https://doi.org/10.1063/1.362745.

[53] A. Kaniyoor, S. Ramaprabhu, A Raman spectroscopic investigation of graphite oxide derived graphene A Raman spectroscopic investigation of graphite oxide derived graphene, 032183 (2014) 0–13. https://doi.org/10.1063/1.4756995.

[54] P. Vecera, J.C. Chacón-Torres, T. Pichler, S. Reich, H.R. Soni, A. Görling, K. Edelthalhammer, H. Peterlik, F. Hauke, A. Hirsch, Precise determination of graphene functionalization by in situ Raman spectroscopy, Nature Communications. 8 (2017). https://doi.org/10.1038/ncomms15192.

[55] A.C. Ferrari, J. Robertson, Interpretation of Raman spectra of disordered and amorphous carbon, Physical Review B. 61 (2000) 14095–14107. https://doi.org/10.1103/PhysRevB.61.14095.

[56] C. Casiraghi, A. Hartschuh, H. Qian, S. Pliscanec, C. Georgia, A. Fasoli, K.S. Novoselov, D.M. Basko, A.C. Ferrari, Raman spectroscopy of graphene edges, Nano Letters. 9 (2009) 1433–1441. https://doi.org/10.1021/nl8032697.

[57] C. Gao, Y.Z. Jin, H. Kong, R.L.D. Whitby, S.F.A. Acquah, G.Y. Chen, H. Qian, A.

Hartschuh, S.R.P. Silva, S. Henley, P. Fearon, H.W. Kroto, D.R.M. Walton, Polyurea-Functionalized Multiwalled Carbon Nanotubes : Synthesis , Morphology , and Raman Spectroscopy, (2005) 11925–11932.

[58] B.P. Swain, The analysis of carbon bonding environment in HWCVD deposited a-SiC:H films by XPS and Raman spectroscopy, Surface and Coatings Technology. 201 (2006) 1589–1593. https://doi.org/10.1016/j.surfcoat.2006.02.029.

[59] H.R. Byon, B.M. Gallant, S.W. Lee, Y. Shao-Horn, Role of oxygen functional groups in carbon nanotube/graphene freestanding electrodes for high performance lithium batteries, Advanced Functional Materials. 23 (2013) 1037–1045. https://doi.org/10.1002/adfm.201200697.

[60] J.L. Figueiredo, M.F.R. Pereira, The role of surface chemistry in catalysis with carbons, Catalysis Today. 150 (2010) 2–7. https://doi.org/10.1016/j.cattod.2009.04.010.

[61] M.I. Ionescu, Y. Zhang, R. Li, H. Abou-Rachid, X. Sun, Nitrogen-doping effects on the growth, structure and electrical performance of carbon nanotubes obtained by spray pyrolysis method, Applied Surface Science. 258 (2012) 4563–4568. https://doi.org/10.1016/j.apsusc.2012.01.028.

[62] K. Ghosh, M. Kumar, T. Maruyama, Y. Ando, Micro-structural, electron-spectroscopic and field-emission studies of carbon nitride nanotubes grown from cage-like and linear carbon sources, Carbon. 47 (2009) 1565–1575. https://doi.org/10.1016/j.carbon.2009.02.007.

[63] R. Arrigo, M. Hävecker, S. Wrabetz, R. Blume, M. Lerch, J. McGregor, E.P.J. Parrott, J.A. Zeitler, L.F. Gladden, A. Knop-Gericke, R. Schlögl, D.S. Su, Tuning the acid/base properties of nanocarbons by functionalization via amination, Journal of the American Chemical Society. 132 (2010) 9616–9630. https://doi.org/10.1021/ja910169v.

[64] R. Pietrzak, XPS study and physico-chemical properties of nitrogen-enriched microporous activated carbon from high volatile bituminous coal, Fuel. 88 (2009) 1871–1877. https://doi.org/10.1016/j.fuel.2009.04.017.

[65] P. Mélinon, B. Masenelli, F. Tournus, A. Perez, Playing with carbon and silicon at the nanoscale, Nature Materials. 6 (2007) 479–490. https://doi.org/10.1038/nmat1914.

[66] Y.C. Chiang, W.H. Lin, Y.C. Chang, The influence of treatment duration on multi-walled carbon nanotubes functionalized by H2SO4/HNO3 oxidation, Applied Surface Science. 257 (2011) 2401–2410. https://doi.org/10.1016/j.apsusc.2010.09.110.

[67] P.C. Ma, J.K. Kim, B.Z. Tang, Functionalization of carbon nanotubes using a silane coupling agent, Carbon. 44 (2006) 3232–3238.

https://doi.org/10.1016/j.carbon.2006.06.032.

[68] R.J.J. Jansen, H. van Bekkum, XPS of nitrogen-containing functional groups on activated carbon, Carbon. 33 (1995) 1021–1027. https://doi.org/10.1016/0008-6223(95)00030-H.

[69] L. Lai, L. Chen, D. Zhan, L. Sun, J. Liu, S.H. Lim, C.K. Poh, Z. Shen, J. Lin, One-step synthesis of NH 2 -graphene from in situ graphene-oxide reduction and its improved electrochemical properties, Carbon. 49 (2011) 3250–3257. https://doi.org/10.1016/j.carbon.2011.03.051.

[70] L. Lai, H. Yang, L. Wang, B.K. Teh, J. Zhong, H. Chou, L. Chen, W. Chen, Z. Shen, R.S. Ruoff, J. Lin, Preparation of supercapacitor electrodes through selection of graphene surface functionalities, ACS Nano. 6 (2012) 5941–5951. https://doi.org/10.1021/nn3008096.

[71] C.L. Rodriguez-Corvera, J.L. Fajardo-Díaz, A.J. Cortés-López, L.E. Jiménez - Ramírez, E. Muñoz-Sandoval, F. López-Urías, Nitrogen-doped carbon fiber sponges by using different nitrogen precursors : synthesis , characterization , and electrochemical activity, Materials Today Chemistry. 14 (2019) 1–13. https://doi.org/10.1016/j.mtchem.2019.100200.

[72] G.E. Fish, Soft Magnetic Materials, 1990. https://doi.org/10.1109/5.56909.

[73] J.M. Silveyra, E. Ferrara, D.L. Huber, T.C. Monson, Soft magnetic materials for a sustainable and electrified world, Science. 362 (2018). https://doi.org/10.1126/science.aao0195.

[74] J. Su, Y. Gao, M. Sun, X. Han, X. Zhang, Q. Zhang, Fe- and Fe 3C-filled carbon nanotube-aligned arrays and flower-like carbon nanostructured clusters with a high coercivity, Micro and Nano Letters. 7 (2012) 271–274. https://doi.org/10.1049/mnl.2011.0597.

[75] Y. Ninomiya, Z. Dong, Y. Suzuki, J. Koketsu, Theoretical study on the thermal decomposition of pyridine, Fuel. 79 (2000) 449–457. https://doi.org/10.1016/S0016-2361(99)00180-5.

[76] S. Song, D.M. Golden, R.K. Hanson, C.T. Bowman, A shock tube study of benzylamine decomposition: Overall rate coefficient and heat of formation of the benzyl radical, Journal of Physical Chemistry A. 106 (2002) 6094–6098. https://doi.org/10.1021/jp020085l.

[77] J. Li, A. Kazakov, F.L. Dryer, Experimental and numerical studies of ethanol decomposition reactions, Journal of Physical Chemistry A. 108 (2004) 7671–7680. https://doi.org/10.1021/jp0480302.

[78] P. Hohenberg, W. Kohn, Inhomogeneous electron gas, Physical Review. 136 (1964) B864.

[79] W. Kohn, L.J. Sham, Self-consistent equations including exchange and correlation effects., Phys. Rev. (1965) A1133.

[80] J.P. Perdew, A. Ruzsinszky, G.I. Csonka, O.A. Vydrov, G.E. Scuseria, L.A. Constantin, X. Zhou, K. Burke, Restoring the density-gradient expansion for exchange in solids and surfaces, 136406 (2007) 1–4. https://doi.org/10.1103/PhysRevLett.100.136406.

[81] Soler J.M., Artacho E., Gale J.D., Garcia A., Junquera J., Ordejon P., Sanchez-Portal D., The SIESTA method for ab initio order-N materials simulation, Journal of Physics - Condensed Matter. 14 (2001) 2745-2779. https://doi.org/10.1088/0953-8984/14/11/302.

[82] J. Junquera, O. Paz, D. Sánchez-Portal, E. Artacho, Numerical atomic orbitals for linear-scaling calculations, Phys. Rev. B. 64 (2001) 235111.

[83] N. Troullier, J.L. Martins, Efficient pseudopotentials for plane-wave calculations, Phys. Rev. B. (1991) 1993.

[84] D.M. Bylander, L. Kleinman, Efficacious Form for Model Pseudopotentials, Physical Review Letters. 48 (1982) 1425–1428.

[85] L.E. Jiménez-Ramírez, D.C. Camacho-Mojica, E. Muñoz-Sandoval, F. López-Urías, First-principles study of transition metal adsorbed on porphyrin-like motifs in pyrrolic nitrogen-doped carbon nanostructures, Carbon. 116 (2017) 381–390. https://doi.org/10.1016/j.carbon.2017.02.018.

[86] F. L??pez-Ur??as, E. Mu??oz-Sandoval, M. Reyes-Reyes, A.H. Romero, M. Terrones, J.L. Mor??n-L??pez, Creation of helical vortices during magnetization of aligned carbon nanotubes filled with Fe: Theory and experiment, Physical Review Letters. 94 (2005) 1–4. https://doi.org/10.1103/PhysRevLett.94.216102.

[87] M. Klinger, A. Jäger, Crystallographic Tool Box (CrysTBox): Automated tools for transmission electron microscopists and crystallographers, Journal of Applied Crystallography. 48 (2015) 2012–2018. https://doi.org/10.1107/S1600576715017252.

[88] W. Wang, K. Wang, R. Lv, J. Wei, X. Zhang, F. Kang, J. Chang, Q. Shu, Y. Wang, D. Wu, Synthesis of Fe-filled thin-walled carbon nanotubes with high filling ratio by using dichlorobenzene as precursor, Carbon. 45 (2007) 2006–2008. https://doi.org/10.1016/j.carbon.2006.12.029.

[89] Y. Wu, X. Lin, X. Shen, X. Sun, X. Liu, Z. Wang, J.K. Kim, Exceptional dielectric properties of chlorine-doped graphene oxide/poly (vinylidene fluoride)

nanocomposites, Carbon. 89 (2015) 102–112. https://doi.org/10.1016/j.carbon.2015.02.074.

[90] M.E. Lipińska, S.L.H. Rebelo, M.F.R. Pereira, J.A.N.F. Gomes, C. Freire, J.L. Figueiredo, New insights into the functionalization of multi-walled carbon nanotubes with aniline derivatives, Carbon. 50 (2012) 3280–3294. https://doi.org/10.1016/j.carbon.2011.12.018.

[91] S. Zhu, C. Zhu, J. Ma, Q. Meng, Z. Guo, Z. Yu, T. Lu, Y. Li, D. Zhang, W.M. Lau, Controlled fabrication of Si nanoparticles on graphene sheets for Li-ion batteries, RSC Advances. 3 (2013) 6141–6146. https://doi.org/10.1039/c3ra22989k.

[92] W. Huang, Y. Wang, G. Luo, F. Wei, High-Temperature Annealing, Carbon. 41 (2003) 2585–2590.

[93] X. Wang, P. Zhang, W. Wang, X. Lei, B. Zou, H. Yang, Synthesis, structure and magnetic properties of graphite carbon encapsulated Fe<inf>3</inf>C nanoparticles for applications as adsorbents, RSC Advances. 5 (2015) 27857–27861. https://doi.org/10.1039/c5ra00624d.

[94] L. Andrews, Infrared detection of trichloromethyl radical in solid argon, The Journal of Physical Chemistry. 71 (2005) 2761–2762. https://doi.org/10.1021/j100867a073.

[95] T.D. Fridgen, X.K. Zhang, J.M. Parnis, R.E. March, Isomerization and Fragmentation Products of CH 2 Cl 2 and Other Dihalomethanes in Rare-Gas Matrices: An Electron Bombardment Matrix-Isolation FTIR Spectroscopic Study † , The Journal of Physical Chemistry A. 104 (2002) 3487–3497. https://doi.org/10.1021/jp993162u.

[96] T. Shimanouchi, H. Matsuura, Y. Ogawa, I. Harada, Tables of molecular vibrational frequencies, J. Phys. Chem. 9 (1980).

[97] E. Unger, A. Graham, F. Kreupl, M. Liebau, W. Hoenlein, Electrochemical functionalization of multi-walled carbon nanotubes for solvation and purification, Current Applied Physics. 2 (2002) 107–111. https://doi.org/10.1016/s1567-1739(01)00072-4.

[98] Z. Qian, J. Ma, J. Zhou, P. Lin, C. Chen, J. Chen, H. Feng, Facile synthesis of halogenated multi-walled carbon nanotubes and their unusual photoluminescence, Journal of Materials Chemistry. 22 (2012) 22113–22119. https://doi.org/10.1039/c2jm34275h.

[99] M.S. Shafeeyan, W.M.A.W. Daud, A. Houshmand, A. Shamiri, A review on surface modification of activated carbon for carbon dioxide adsorption, Journal of Analytical and Applied Pyrolysis. 89 (2010) 143–151. https://doi.org/10.1016/j.jaap.2010.07.006.

[100] V. Ţucureanu, A. Matei, A.M. Avram, FTIR Spectroscopy for Carbon Family Study, Critical Reviews in Analytical Chemistry. 46 (2016) 502–520. https://doi.org/10.1080/10408347.2016.1157013.

[101] H. Wang, G. Li, J. Ma, D. Zhao, The effect of methane decomposition on the formation and magnetic properties of iron carbide prepared from oolitic hematite, RSC Advances. 7 (2017) 3921–3927. https://doi.org/10.1039/c6ra26166c.

[102] F. Shariatmadar Tehrani, Transformation from amorphous to nano-crystalline SiC thin films prepared by HWCVD technique without hydrogen dilution, Bulletin of Materials Science. 38 (2015) 1333–1338.

[103] M.S. Dresselhaus, G. Dresselhaus, R. Saito, A. Jorio, Raman spectroscopy of carbon nanotubes, Physics Reports. 409 (2005) 47–99. https://doi.org/10.1016/j.physrep.2004.10.006.

[104] J. Bin Wu, M.L. Lin, X. Cong, H.N. Liu, P.H. Tan, Raman spectroscopy of graphene-based materials and its applications in related devices, Chemical Society Reviews. 47 (2018) 1822–1873. https://doi.org/10.1039/c6cs00915h.

[105] P. Tan, S. Dimovski, Y. Gogotsi, Raman scattering of non-planar graphite : arched edges , polyhedral crystals , whiskers and cones, Phil. Trans. R. Soc. Lond. A. 362 (2004) 2289–2310.

[106] U. Weissker, M. Löffler, F. Wolny, M.U. Lutz, N. Scheerbaum, R. Klingeler, T. Gemming, T. Mühl, A. Leonhardt, B. Büchner, Perpendicular magnetization of long iron carbide nanowires inside carbon nanotubes due to magnetocrystalline anisotropy, Journal of Applied Physics. 106 (2009). https://doi.org/10.1063/1.3204495.

[107] A.G. Osorio, L.G. Pereira, J.B.M. Da Cunha, C.P. Bergmann, Controlling the magnetic response of carbon nanotubes filled with iron-containing material, Materials Research Bulletin. 48 (2013) 4168–4173. https://doi.org/10.1016/j.materresbull.2013.06.045.

[108] A. Morelos-Gómez, F. López-Urías, E. Muñoz-Sandoval, C.L. Dennis, R.D. Shull, H. Terrones, M. Terrones, Controlling high coercivities of ferromagnetic nanowires encapsulated in carbon nanotubes, Journal of Materials Chemistry. 20 (2010) 5906–5914. https://doi.org/10.1039/c0jm00660b.

[109] F. Geng, H. Cong, Fe-filled carbon nanotube array with high coercivity, Physica B: Condensed Matter. 382 (2006) 300–304. https://doi.org/10.1016/j.physb.2006.03.003.

[110] A. Morelos-Gómez, F. López-Urías, E. Muñoz-Sandoval, C.L. Dennis, R.D. Shull, H. Terrones, M. Terrones, Controlling high coercivities of ferromagnetic nanowires encapsulated in carbon nanotubes, Journal of Materials Chemistry. 20 (2010) 5906–5914. https://doi.org/10.1039/c0jm00660b.

[111] H.A. Andreas, B.E. Conway, Examination of the double-layer capacitance of an high specific-area C-cloth electrode as titrated from acidic to alkaline pHs, Electrochimica Acta. 51 (2006) 6510–6520. https://doi.org/10.1016/j.electacta.2006.04.045.

[112] D.A.C. Brownson, C.E. Banks, The Handbook of Graphene Electrochemistry, 2014. https://doi.org/10.1007/978-1-4471-6428-9.

[113] Z. Ai, T. Mei, J. Liu, J. Li, F. Jia, L. Zhang, J. Qiu, Fe@Fe2O3 core-shell nanowires as an iron reagent. 3. Their combination with CNTs as an effective oxygen-fed gas diffusion electrode in a neutral electro-fenton system, Journal of Physical Chemistry C. 111 (2007) 14799–14803. https://doi.org/10.1021/jp073617c.

[114] D. Ma, Y. Wang, X. Han, S. Xu, J. Wang, Electrode configuration optimization of capacitive deionization cells based on zero charge potential of the electrodes, Separation and Purification Technology. 189 (2017) 467–474. https://doi.org/10.1016/j.seppur.2017.08.025.

[115] D. Janas, S. Boncel, K.K.K. Koziol, Electrothermal halogenation of carbon nanotube films, Carbon. 73 (2014) 259–266. https://doi.org/10.1016/j.carbon.2014.02.062.

[116] P.G. Wenthold, R.R. Squires, W.C. Lineberger, Ultraviolet photoelectron spectroscopy of the o-, m-, and p-benzyne negative ions. Electron affinities and singlet-triplet splittings for o-, m- , and p-benzyne, Journal of the American Chemical Society. 120 (1998) 5279–5290. https://doi.org/10.1021/ja9803355.

[117] E. Frackowiak, F. Béguin, Carbon materials for the electrochemical storage of energy in capacitors, Carbon. (2001) 937–950. https://doi.org/https://doi.org/10.1016/S0008-6223(00)00183-4.

[118] P. Li, C. Kong, Y. Shang, E. Shi, Y. Yu, W. Qian, F. Wei, J. Wei, K. Wang, H. Zhu, A. Cao, D. Wu, Highly deformation-tolerant carbon nanotube sponges as supercapacitor electrodes, Nanoscale. 5 (2013) 8472–8479. https://doi.org/10.1039/c3nr01932b.

[119] M.A. Worsley, S.O. Kucheyev, J.H. Satcher, A. V. Hamza, T.F. Baumann, Mechanically robust and electrically conductive carbon nanotube foams, Applied Physics Letters. 94 (2009) 1–4. https://doi.org/10.1063/1.3086293.

[120] R.D. Kern, K. Xie, H. Chen, A shock tube study of chlorobenzene pyrolysis, Combust. Sci. and Tech. 85 (1992) 77–86.

[121] C.M. Young, K.J. Voorhees, PIC Formation Mechanisms in the thermal decompostion of 1,2-dichlorobenzene, Chemosphere. 23 (1991) 1265–1277.

CONCLUSIONS

Following the main objective and the hypothesis described in the first pages, each chapter contributes in order to obtain a series of results that would help in the accomplishment of these two aspects: the objective and the hypothesis verification.

By the sputtering technique was possible to obtain Co-Cu thin films that work as support and catalyst in a chemical vapor deposition system to grow a variety of carbon nanostructures. The use of a diversity of precursors containing C, S, N, and O plays a crucial role in the type of carbon nanostructure obtained. This knowledge is not new. In literature, it was known that different precursors promote changes over the growth of the carbon nanostructures. However, in this case, a lightly variations of sulfur combined with unstable temperature conditions considerably changes the type of growth leading to the formation of carbon nanoonios, carbon nanotubes, carbon nanofibers, wrinkled carbon nanofibers, and interlaced carbon nanofibers within 30 min of synthesis time. Surprisingly, the interlaced wrinkled carbon nanofibers promote the formation of 3D carbon nanostructures described as wrinkled carbon nanobelts structure (N-CBS) with an increase in synthesis time (240 min).

The N-CBS structure had highly interesting characteristics. It is structured by corrugated graphitic material that grows unidirectional. This graphitic material is full of holes, discontinuous graphitic sections, doped with nitrogen, and functionalized with oxygen. The responsible for the growth of this type of unusual carbon nanostructure is associated with the formation of elongated Cu nanoparticles where Co@Cu semi-spherical nanoparticles are attached. The reduction atmosphere favors the formation of this type of metallic nanostructures. However, this growth mechanism is highly influenced by the Cu interaction with Co and the partial interaction with S and O, which comes from precursors used. When Cu is changed with other metal in the same chemical family-like Ag or Au, the N-CBS structure is not formed, and only thicker interlaced wrinkled carbon nanofibers are observed.

To determinate the influence of Cu, alternative experiments were developed using Cu thin films. Although commonly Cu is used to grow graphene due to the low carbon solubility in the crystal structure, the size, shape, and crystal plane that interacts with carbon its determinant in the variation of growth mechanism in order to obtain carbon nanotubes, carbon nanofibers, and graphene. Not only that, another aspect to have in account is the interaction of intermediary chemical compounds formed during the precursor's pyrolysis. If the atmosphere promotes the diminution of amorphous carbon and a continuous reductive atmosphere, the formation of tubular carbon nanostructures should be observed.

Finally, in order to compare with other growth mechanisms associated with the synthesis of 3D carbon nanostructures, a Fe based catalysts mixed with a variety of precursors was obtained and tested in a chemical vapor deposition system at high temperature. The exciting thing about these experiments was that also for this case, the decomposition mechanism associated with the precursor, as well as the type of heteroatom involved considerably modifies the growth mechanism during the formation of 3D carbon nanostructures named carbon nanotube sponges (CNS). The CNS obtained with a nitrogen-based precursor it is formed of nitrogen-doped carbon nanofibers while using a chloride carbon precursor promotes the formation of iron nanowires carbon nanotube structures. The electronic, magnetic, and physical characteristics vary considerable depending on the precursor used.

Contributions

The main aspect of doing science is to contribute to the development of knowledge, trying to understand the natural laws that dominates the physics or chemistry of things for the development of technology that directly impacts in modern life. All this for the good of humanity. This doctoral thesis intention is to contribute, even in a minimum way, to the development of nanomaterials science especially the focused around the use of carbon nanomaterials.

In this thesis, we have contributed to the development and improvement four principal subjects: 1) CVD technique for the synthesis of 3D carbon materials, 2) Use of bimetallic thin film materials as a catalyst for 3D carbon systems and 3) Understanding in a better way the influence of Co, Cu, and Fe over the develop of 3D carbon arrangements, 4) Role of Cu NPS in the growth of CNT and 3D carbon nanostructured belts.

It was described how precursors play a significant role in the growth of 3D carbon nanostructures. It is known that oxygen and sulfur plays a significant role in the modification of the electronic and structural system in graphitic networks. In this thesis, we introduce a bimetallic catalyst Co-Cu where Co is known by their characteristics to grow CNT and Cu graphene. In an effort to combine all these effects with the intention to create a CNT-graphene hybrid system, a unique growth process took place, and 3D carbon nanostructured belts were grown over thin films.

3D carbon nanostructured belts were catalyzed by a hierarchical process where highly corrugated CNF agglomerates unidirectional and the belt structure take place. One important aspect to grow this type of structure in the synthesis time. After 30 minutes, only wrinkled CNF are obtained. After 2 hours, the 3D carbon nanostructured belts are grown, and after 4 hours of hybrids systems, CNT/N-CBS can be obtained. Due to the use of precursors that contains nitrogen and oxygen, these carbon nanostructured belts are nitrogen-doped, and oxygen functionalized what could help in the development of technology like battery systems and sensors.

One interesting aspect of the growth of 3D carbon nanostructured belts was the role of Cu interaction with Co and Cu NPS formation and posterior influence in the growth of CNT over the surface of 3D carbon nanostructured belts. The understanding of how Cu can nucleate CNT and how the position inside CVD systems influence the growing capacity of Cu films, and Cu NPS was an important contribution of the present thesis work.

In order to improve the growth of 3D carbon nanostructures, the Fe catalyst was employed with different precursors like pyridine and 1,2-dichlorobenzene. The type of 3D carbon nanostructures obtained using this methodology called “carbon nanotube sponge”. These results contribute to the CNF 3D carbon nanostructure development by the use of pyridine and a CNT 3D carbon nanostructure development using 1,2-dichlorobenzene. These two types of carbon nanotube sponge had a highly attractive magnetic characteristic and high charge capacities that can contribute to the development of electrodes, magnetic oil-spill sorbents, and catalysts. An interesting aspect associated with the growth of the pyridine CNF 3D carbon nanostructure is the possibility to obtain a nitrogen functionalized carbon sponge, which could help to develop selective materials. In the case of the 1,2-dichlorobenzene CNT 3D carbon nanostructure, the growth mechanism associated with the influence of Cl radicals and the functionalization with Cl species directly impacts the charge capacity and magnetic saturation.

ANNEX (PUBLICATIONS)

As an Author:

1) *Fajardo-Díaz, J. L., López-Urías, F., & Muñoz-Sandoval, E. (2018). Wrinkled nitrogen-doped carbon belts. Scientific reports, 8(1), 1-9.* **(I.F: 4.1)**

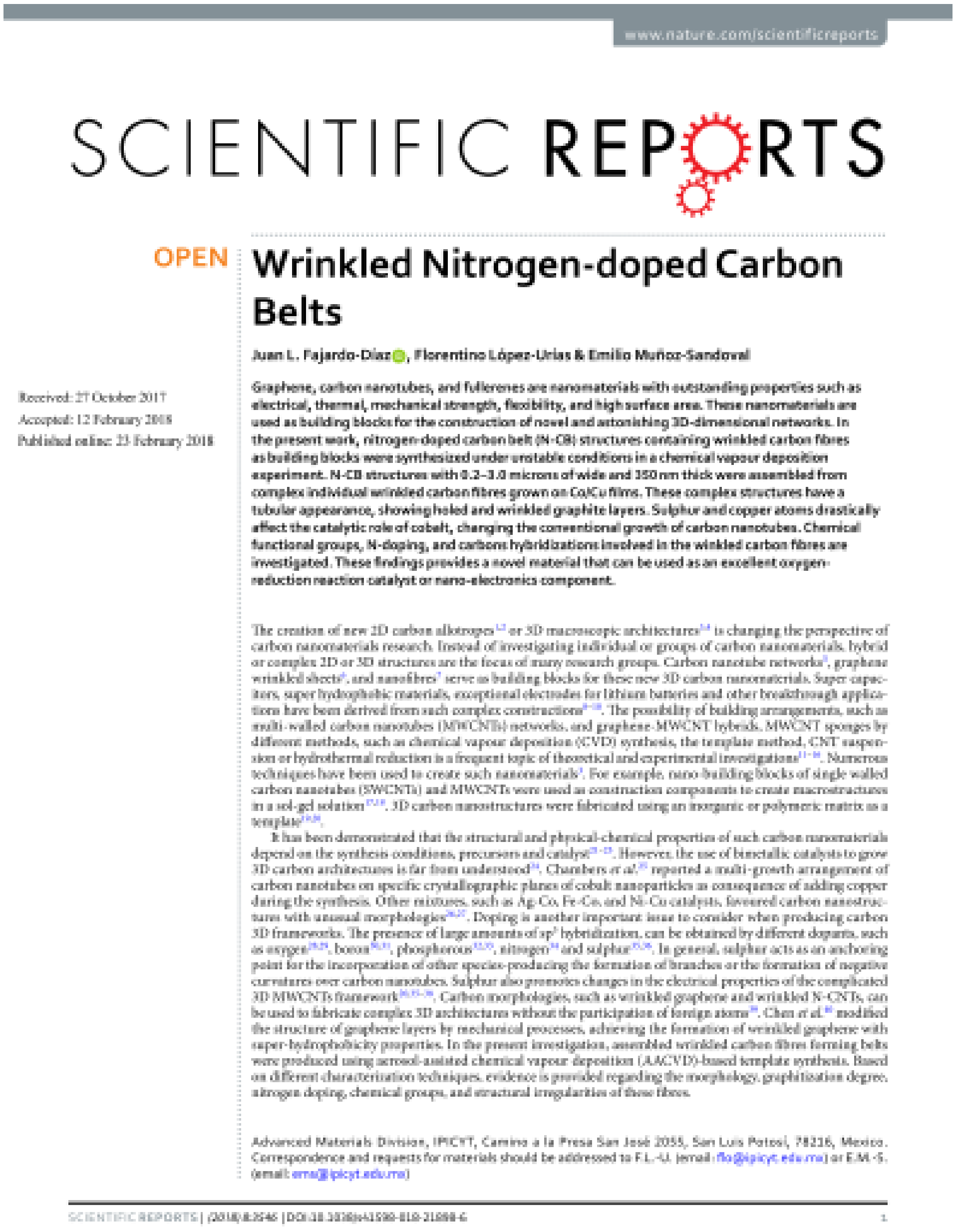

www.nature.com/scientificreports

SCIENTIFIC REPORTS

OPEN

Wrinkled Nitrogen-doped Carbon Belts

Juan L. Fajardo-Díaz, Florentino López-Urías & Emilio Muñoz-Sandoval

Received: 27 October 2017
Accepted: 12 February 2018

Graphene, carbon nanotubes, and fullerenes are nanomaterials with outstanding properties such as electrical, thermal, mechanical strength, flexibility, and high surface area. These nanomaterials are used as building blocks for the construction of novel and astonishing 3D-dimensional networks. In the present work, nitrogen-doped carbon belt (N-CB) structures containing winkled carbon fibres as building blocks were synthesized under unstable conditions in a chemical vapour deposition experiment. N-CB structures with 0.2–3.0 microns of wide and 350 nm thick were assembled from complex individual winkled carbon fibres grown on Co/Cu films. These complex structures have a tubular appearance, showing holed and winkled graphite layers. Sulphur and copper atoms drastically affect the catalytic role of cobalt, changing the conventional growth of carbon nanotubes. Chemical functional groups, N-doping, and carbons hybridizations involved in the winkled carbon fibres are investigated. These findings provides a novel material that can be used as an excellent oxygen-reduction reaction catalyst or nano-electronics component.

The creation of new 2D carbon allotropes[1,2] or 3D macroscopic architectures[3,4] is changing the perspective of carbon nanomaterials research. Instead of investigating individual or groups of carbon nanomaterials, hybrid or complex 2D or 3D structures are the focus of many research groups. Carbon nanotube networks[5], graphene wrinkled sheets[6], and nanofibres[7] serve as building blocks for these new 3D carbon nanomaterials. Super-capacitors, super hydrophobic materials, exceptional electrodes for lithium batteries and other breakthrough applications have been derived from such complex constructions[8–10]. The possibility of building arrangements, such as multi-walled carbon nanotubes (MWCNTs) networks, and graphene-MWCNT hybrids, MWCNT sponges by different methods, such as chemical vapour deposition (CVD) synthesis, the template method, CNT suspension or hydrothermal reduction is a frequent topic of theoretical and experimental investigations[11–16]. Numerous techniques have been used to create such nanomaterials[5]. For example, nano-building blocks of single walled carbon nanotubes (SWCNTs) and MWCNTs were used as construction components to create macrostructures in a sol-gel solution[17,18]. 3D carbon nanostructures were fabricated using an inorganic or polymeric matrix as a template[19,20].

It has been demonstrated that the structural and physical-chemical properties of such carbon nanomaterials depend on the synthesis conditions, precursors and catalyst[21–23]. However, the use of bimetallic catalysts to grow 3D carbon architectures is far from understood[24]. Chambers *et al.*[25] reported a multi-growth arrangement of carbon nanotubes on specific crystallographic planes of cobalt nanoparticles as consequence of adding copper during the synthesis. Other mixtures, such as Ag-Co, Fe-Co, and Ni-Cu catalysts, favoured carbon nanostructures with unusual morphologies[26,27]. Doping is another important issue to consider when producing carbon 3D frameworks. The presence of large amounts of sp^3 hybridization, can be obtained by different dopants, such as oxygen[28,29], boron[30,31], phosphorous[32,33], nitrogen[34] and sulphur[35,36]. In general, sulphur acts as an anchoring point for the incorporation of other species-producing the formation of branches or the formation of negative curvatures over carbon nanotubes. Sulphur also promotes changes in the electrical properties of the complicated 3D MWCNTs framework[16,35–38]. Carbon morphologies, such as wrinkled graphene and wrinkled N-CNTs, can be used to fabricate complex 3D architectures without the participation of foreign atoms[39]. Chen *et al.*[40] modified the structure of graphene layers by mechanical processes, achieving the formation of wrinkled graphene with super-hydrophobicity properties. In the present investigation, assembled wrinkled carbon fibres forming belts were produced using aerosol-assisted chemical vapour deposition (AACVD)-based template synthesis. Based on different characterization techniques, evidence is provided regarding the morphology, graphitization degree, nitrogen doping, chemical groups, and structural irregularities of these fibres.

Advanced Materials Division, IPICYT, Camino a la Presa San José 2055, San Luis Potosí, 78216, Mexico. Correspondence and requests for materials should be addressed to F.L.-U. (email: flo@ipicyt.edu.mx) or E.M.-S. (email: ems@ipicyt.edu.mx)

2) *Fajardo-Díaz, J. L., Durón-Torres, S. M., López-Urías, F., & Muñoz-Sandoval, E. (2019). Synthesis, characterization and cyclic voltammetry studies of helical carbon nanostructures produced by thermal decomposition of ethanol on Cu-foils. Carbon, 155, 469-482.* **(I.F. 7.4)**

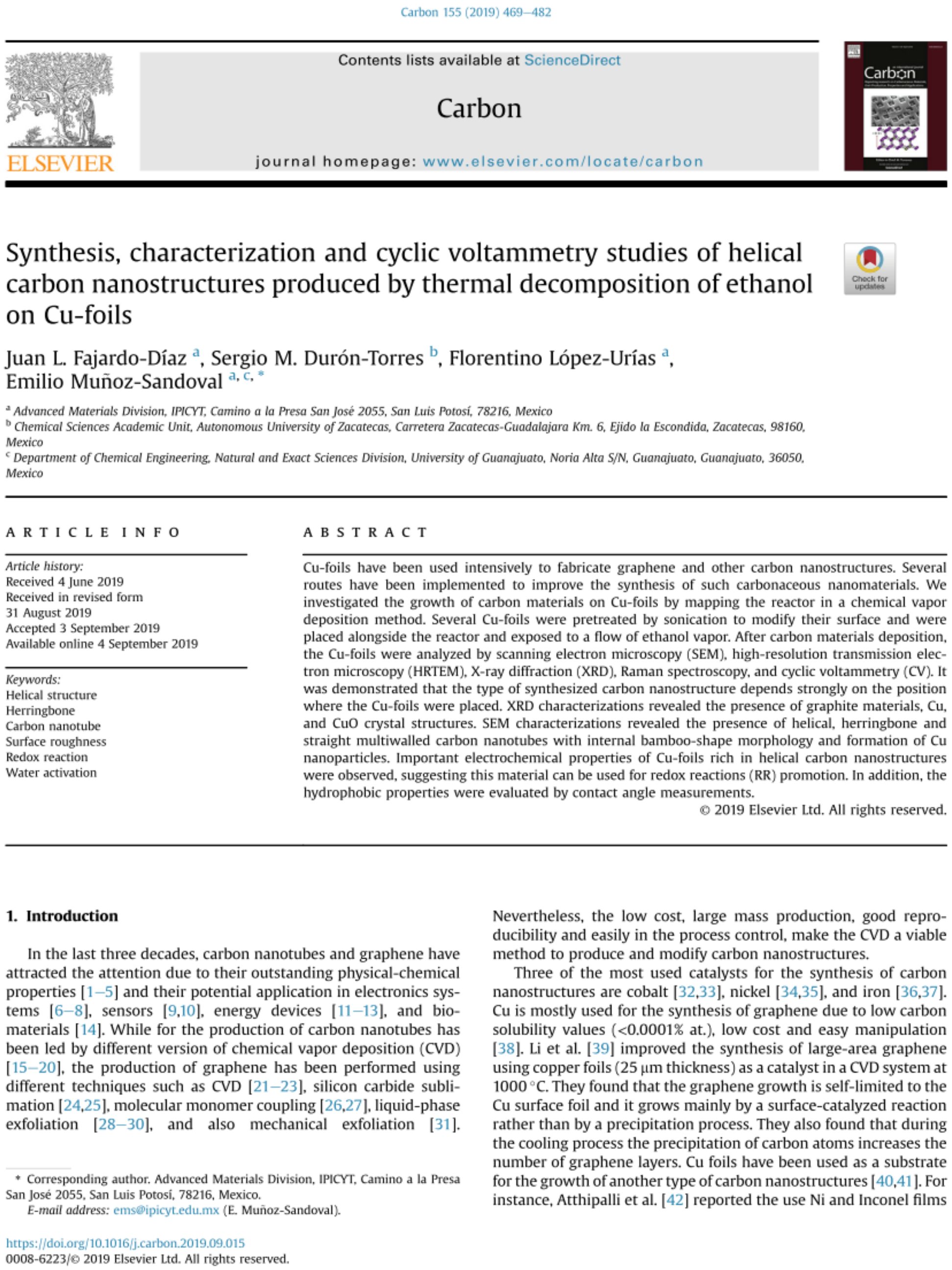

Carbon 155 (2019) 469–482

Contents lists available at ScienceDirect

Carbon

journal homepage: www.elsevier.com/locate/carbon

Synthesis, characterization and cyclic voltammetry studies of helical carbon nanostructures produced by thermal decomposition of ethanol on Cu-foils

Juan L. Fajardo-Díaz [a], Sergio M. Durón-Torres [b], Florentino López-Urías [a], Emilio Muñoz-Sandoval [a, c, *]

[a] Advanced Materials Division, IPICYT, Camino a la Presa San José 2055, San Luis Potosí, 78216, Mexico
[b] Chemical Sciences Academic Unit, Autonomous University of Zacatecas, Carretera Zacatecas-Guadalajara Km. 6, Ejido la Escondida, Zacatecas, 98160, Mexico
[c] Department of Chemical Engineering, Natural and Exact Sciences Division, University of Guanajuato, Noria Alta S/N, Guanajuato, Guanajuato, 36050, Mexico

ARTICLE INFO

Article history:
Received 4 June 2019
Received in revised form
31 August 2019
Accepted 3 September 2019
Available online 4 September 2019

Keywords:
Helical structure
Herringbone
Carbon nanotube
Surface roughness
Redox reaction
Water activation

ABSTRACT

Cu-foils have been used intensively to fabricate graphene and other carbon nanostructures. Several routes have been implemented to improve the synthesis of such carbonaceous nanomaterials. We investigated the growth of carbon materials on Cu-foils by mapping the reactor in a chemical vapor deposition method. Several Cu-foils were pretreated by sonication to modify their surface and were placed alongside the reactor and exposed to a flow of ethanol vapor. After carbon materials deposition, the Cu-foils were analyzed by scanning electron microscopy (SEM), high-resolution transmission electron microscopy (HRTEM), X-ray diffraction (XRD), Raman spectroscopy, and cyclic voltammetry (CV). It was demonstrated that the type of synthesized carbon nanostructure depends strongly on the position where the Cu-foils were placed. XRD characterizations revealed the presence of graphite materials, Cu, and CuO crystal structures. SEM characterizations revealed the presence of helical, herringbone and straight multiwalled carbon nanotubes with internal bamboo-shape morphology and formation of Cu nanoparticles. Important electrochemical properties of Cu-foils rich in helical carbon nanostructures were observed, suggesting this material can be used for redox reactions (RR) promotion. In addition, the hydrophobic properties were evaluated by contact angle measurements.

1. Introduction

In the last three decades, carbon nanotubes and graphene have attracted the attention due to their outstanding physical-chemical properties [1–5] and their potential application in electronics systems [6–8], sensors [9,10], energy devices [11–13], and biomaterials [14]. While for the production of carbon nanotubes has been led by different version of chemical vapor deposition (CVD) [15–20], the production of graphene has been performed using different techniques such as CVD [21–23], silicon carbide sublimation [24,25], molecular monomer coupling [26,27], liquid-phase exfoliation [28–30], and also mechanical exfoliation [31]. Nevertheless, the low cost, large mass production, good reproducibility and easily in the process control, make the CVD a viable method to produce and modify carbon nanostructures.

Three of the most used catalysts for the synthesis of carbon nanostructures are cobalt [32,33], nickel [34,35], and iron [36,37]. Cu is mostly used for the synthesis of graphene due to low carbon solubility values (<0.0001% at.), low cost and easy manipulation [38]. Li et al. [39] improved the synthesis of large-area graphene using copper foils (25 μm thickness) as a catalyst in a CVD system at 1000 °C. They found that the graphene growth is self-limited to the Cu surface foil and it grows mainly by a surface-catalyzed reaction rather than by a precipitation process. They also found that during the cooling process the precipitation of carbon atoms increases the number of graphene layers. Cu foils have been used as a substrate for the growth of another type of carbon nanostructures [40,41]. For instance, Atthipalli et al. [42] reported the use Ni and Inconel films

---

[*] Corresponding author. Advanced Materials Division, IPICYT, Camino a la Presa San José 2055, San Luis Potosí, 78216, Mexico.
E-mail address: ems@ipicyt.edu.mx (E. Muñoz-Sandoval).

https://doi.org/10.1016/j.carbon.2019.09.015
0008-6223/© 2019 Elsevier Ltd. All rights reserved.

3) *Fajardo-Díaz, M. S. J. L., Rodríguez-Corvera, M. S. C. L., Muñoz-Sandoval, P. D. E., & López-Urías, P. D. F. (2020). Furan and Pyran Functional Groups Driven the Surface of Nitrogen-Doped Nanofiber Sponges. ChemNanoMat, 6(4), 672-684.* ***(I.F. 3.4)***

ACES Asian Chemical Editorial Society
DOI: 10.1002/cnma.201900729
CHEMNANOMAT
Full Paper

Furan and Pyran Functional Groups Driven the Surface of Nitrogen-Doped Nanofiber Sponges

M.Sc. Juan L. Fajardo-Díaz, M.Sc. Cristina L. Rodríguez-Corvera, Ph.D. Emilio Muñoz-Sandoval, and Ph.D. Florentino López-Urías*[a]

Abstract: Highly surface oxidized, nitrogen-doped, and nitrogen functionalized carbon nanotube sponge (N-CFS) were produced at 1020 °C using two sprayers approach in an aerosol-assisted chemical vapor deposition (AACVD) experiment. The structure of N-CFS consisted of entangled and corrugated carbon nanofibers of ~200 nm diameter, also showing junctions and knots. TEM characterizations revealed that the carbon nanofiber exhibits stacked graphitic layers in a transversal way with positive curvature. Superficial chemical analysis by XPS showed that the N-CFSs contain an atomic concentration of oxygen and nitrogen of 9.2% and 2.9%, respectively. The high-resolution XPS scans deconvolution-analysis revealed high percentages for C–O bonds, pyrrolic nitrogen doping, NH_3 functionalization, and Si–C interactions. The cyclic voltammetry measurements did not display a redox process despite the high oxygen concentration at the surface. Hydrophobic functional groups containing C–O bonds do not participate in a redox process (furan, pyran, epoxy, methoxy, ethoxy, among others) could mostly determine the electroactivity of N-CFS. Based on density functional theory calculations, we determine that the furans transfer a high amount of electron and promote a positive curvature in thin carbon nanotubes. Graphitic materials with furans, pyrans, and epoxy functional groups could be used as an anode in lithium-ion batteries.

1. Introduction

A way to maintain the material properties of carbon nanostructures at the bulk level is using carbon allotropes as "building blocks" to create 3D carbon frameworks.[1–3] For example, using the single wall and multiwall carbon nanotubes,[4,5] graphene intercalation,[6,7] and other combinations, several nanostructured architectures have been fabricated.[8,9] Dai et al.[10] created a carbon nanotube sponge using a pumped chemical vapor deposition (CVD) device and 1,2-dichlorobenzene, ferrocene on a piece of quartz glass. They found that junctions between carbon nanostructures provide mechanical stability, elasticity, and excellent fatigue resistance. Luo et al.[11] synthesized well-aligned carbon nanotubes (CNT) by a two-step process. First, they produced the CNT by CVD, and subsequently, they mixed them with sodium dodecyl sulfate (SDS) in aqueous solution over sonication to create a CNT-SDS sponge via van der Waals interactions, this material exhibited a low density (<50 mg/cm^{-3}), high porosity ($>99.9\%$) and high conductivity (~1.25 S/cm). He et al.[9] combined a melamine foam matrix impregnated with cobalt and iron solution in a CVD carbonization process to grow a hierarchical porous structure foam of nitrogen-doped CNT with a high capacitance performance. Regarding applications, three-dimensional carbon structures have been used in energy, medicine, material, and environmental sciences.[12,13] For example, Lu et al.[14] synthesized a hybrid sulfur/graphene carbon sponge with a high specific capacitance of 6.0 mAh/cm^2 at the first 11 cycles and stable capacity of 4.53 mAh/cm^2 after 300 cycles. Gui, et al.[15] developed a CNT-sponge with oil absorption capacities of 100 times its weight with the possibility of being used several times after a burning process without losing its absorption capacities.

Another issue for fabricating carbon-bulk nanostructures with exceptional electrical and chemical properties is the introduction of foreign atoms in the carbon network.[16,17] It is known that the incorporation of heteroatoms on the graphitic network induces structural and electronic transport changes. For example, phosphorous over the carbon network increase the surface area and the electrical density with potential application as a supercapacitor electrode.[18] Boron is used to inducing elbows, knees, and corrugated walls into carbon nanotubes and else increases the yield of high-oleophilic carbon nanotube sponges.[19,20] On the other hand, sulfur is used to create Y junctions has been reported that a carbon electrode sulfur and nitrogen co-doped increases the dynamic reaction and the cycling performance of LiS_2 batteries.[21,22] Furthermore, a high concentration of nitrogen promotes bends inwards the graphite layers and the formation of the "bamboo shape" structure.[16,23] Svintsiskiy et al.[24] reported that the nitrogen in carbon nanotubes was at the internal arches as in the external surface of the graphitic wall, while for the nitrogen in platelet carbon nanofibers tend to be at the edges bending the graphitic layers. Additionally, nitrogen pyridinic and pyrrolic doping and amine functionalization on three-dimensional carbon nanostructures are used for the development of metal-free catalysts.[25–27] Recently, nitrogen-doped carbon sponges

---

[a] *M.S. J. L. Fajardo-Díaz, M.S. C. L. Rodríguez-Corvera, P.D. E. Muñoz-Sandoval, P.D. F. López-Urías*
División de Materiales Avanzados, IPICYT, Camino a la Presa San José 2055, Lomas 4a sección, San Luis Potosí, S.L.P., 78216, México
E-mail: flo@ipicyt.edu.mx

Supporting information for this article is available on the WWW under https://doi.org/10.1002/cnma.201900729

ChemNanoMat **2020**, *6*, 672–684 **Wiley Online Library** 672

4) *Fajardo-Díaz, J. L., López-Urías, F., & Muñoz-Sandoval, E. (2020). Chloride functionalized carbon nanotube sponge: High charge capacity and high magnetic saturation. Carbon, 164, 324-336.* **(I.F. 7.4)**

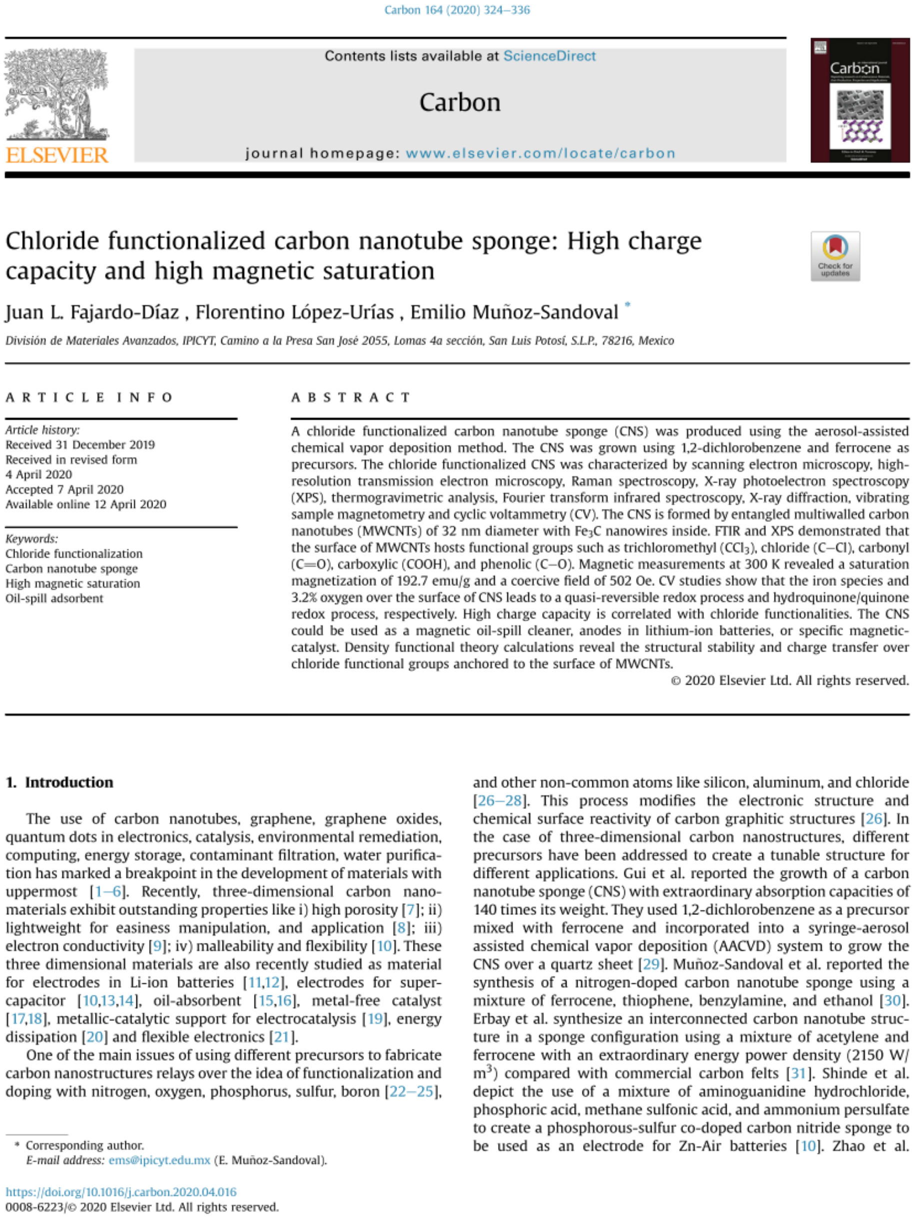

Carbon 164 (2020) 324–336

Contents lists available at ScienceDirect

Carbon

journal homepage: www.elsevier.com/locate/carbon

Chloride functionalized carbon nanotube sponge: High charge capacity and high magnetic saturation

Juan L. Fajardo-Díaz , Florentino López-Urías , Emilio Muñoz-Sandoval *

División de Materiales Avanzados, IPICYT, Camino a la Presa San José 2055, Lomas 4a sección, San Luis Potosí, S.L.P., 78216, Mexico

ARTICLE INFO

Article history:
Received 31 December 2019
Received in revised form
4 April 2020
Accepted 7 April 2020
Available online 12 April 2020

Keywords:
Chloride functionalization
Carbon nanotube sponge
High magnetic saturation
Oil-spill adsorbent

ABSTRACT

A chloride functionalized carbon nanotube sponge (CNS) was produced using the aerosol-assisted chemical vapor deposition method. The CNS was grown using 1,2-dichlorobenzene and ferrocene as precursors. The chloride functionalized CNS was characterized by scanning electron microscopy, high-resolution transmission electron microscopy, Raman spectroscopy, X-ray photoelectron spectroscopy (XPS), thermogravimetric analysis, Fourier transform infrared spectroscopy, X-ray diffraction, vibrating sample magnetometry and cyclic voltammetry (CV). The CNS is formed by entangled multiwalled carbon nanotubes (MWCNTs) of 32 nm diameter with Fe_3C nanowires inside. FTIR and XPS demonstrated that the surface of MWCNTs hosts functional groups such as trichloromethyl (CCl_3), chloride (C–Cl), carbonyl (C=O), carboxylic (COOH), and phenolic (C–O). Magnetic measurements at 300 K revealed a saturation magnetization of 192.7 emu/g and a coercive field of 502 Oe. CV studies show that the iron species and 3.2% oxygen over the surface of CNS leads to a quasi-reversible redox process and hydroquinone/quinone redox process, respectively. High charge capacity is correlated with chloride functionalities. The CNS could be used as a magnetic oil-spill cleaner, anodes in lithium-ion batteries, or specific magnetic-catalyst. Density functional theory calculations reveal the structural stability and charge transfer over chloride functional groups anchored to the surface of MWCNTs.

1. Introduction

The use of carbon nanotubes, graphene, graphene oxides, quantum dots in electronics, catalysis, environmental remediation, computing, energy storage, contaminant filtration, water purification has marked a breakpoint in the development of materials with uppermost [1–6]. Recently, three-dimensional carbon nanomaterials exhibit outstanding properties like i) high porosity [7]; ii) lightweight for easiness manipulation, and application [8]; iii) electron conductivity [9]; iv) malleability and flexibility [10]. These three dimensional materials are also recently studied as material for electrodes in Li-ion batteries [11,12], electrodes for supercapacitor [10,13,14], oil-absorbent [15,16], metal-free catalyst [17,18], metallic-catalytic support for electrocatalysis [19], energy dissipation [20] and flexible electronics [21].

One of the main issues of using different precursors to fabricate carbon nanostructures relays over the idea of functionalization and doping with nitrogen, oxygen, phosphorus, sulfur, boron [22–25], and other non-common atoms like silicon, aluminum, and chloride [26–28]. This process modifies the electronic structure and chemical surface reactivity of carbon graphitic structures [26]. In the case of three-dimensional carbon nanostructures, different precursors have been addressed to create a tunable structure for different applications. Gui et al. reported the growth of a carbon nanotube sponge (CNS) with extraordinary absorption capacities of 140 times its weight. They used 1,2-dichlorobenzene as a precursor mixed with ferrocene and incorporated into a syringe-aerosol assisted chemical vapor deposition (AACVD) system to grow the CNS over a quartz sheet [29]. Muñoz-Sandoval et al. reported the synthesis of a nitrogen-doped carbon nanotube sponge using a mixture of ferrocene, thiophene, benzylamine, and ethanol [30]. Erbay et al. synthesize an interconnected carbon nanotube structure in a sponge configuration using a mixture of acetylene and ferrocene with an extraordinary energy power density (2150 W/m^3) compared with commercial carbon felts [31]. Shinde et al. depict the use of a mixture of aminoguanidine hydrochloride, phosphoric acid, methane sulfonic acid, and ammonium persulfate to create a phosphorous-sulfur co-doped carbon nitride sponge to be used as an electrode for Zn-Air batteries [10]. Zhao et al.

---

* Corresponding author.
E-mail address: ems@ipicyt.edu.mx (E. Muñoz-Sandoval).

https://doi.org/10.1016/j.carbon.2020.04.016
0008-6223/

As coauthor:

1) *Muñoz-Sandoval, E., Cortes-López, A. J., Flores-Gómez, B., Fajardo-Díaz, J. L., Sánchez-Salas, R., & López-Urías, F. (2017). Carbon sponge-type nanostructures based on coaxial nitrogen-doped multiwalled carbon nanotubes grown by CVD using benzylamine as precursor. Carbon, 115, 409-421.* ***(I.F. 7.4)***

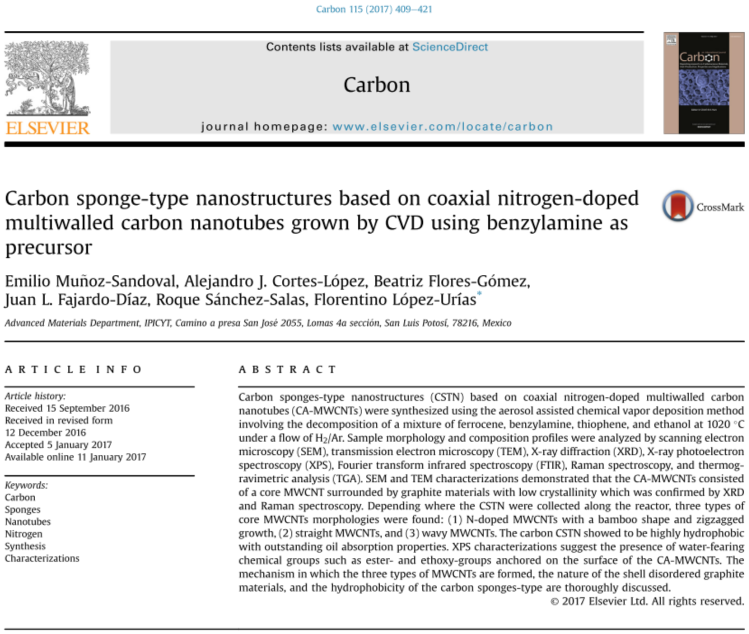

Carbon 115 (2017) 409–421

Contents lists available at ScienceDirect

Carbon

journal homepage: www.elsevier.com/locate/carbon

ELSEVIER

Carbon sponge-type nanostructures based on coaxial nitrogen-doped multiwalled carbon nanotubes grown by CVD using benzylamine as precursor

CrossMark

Emilio Muñoz-Sandoval, Alejandro J. Cortes-López, Beatriz Flores-Gómez,
Juan L. Fajardo-Díaz, Roque Sánchez-Salas, Florentino López-Urías*

Advanced Materials Department, IPICYT, Camino a presa San José 2055, Lomas 4a sección, San Luis Potosí, 78216, Mexico

ARTICLE INFO

Article history:
Received 15 September 2016
Received in revised form
12 December 2016
Accepted 5 January 2017
Available online 11 January 2017

Keywords:
Carbon
Sponges
Nanotubes
Nitrogen
Synthesis
Characterizations

ABSTRACT

Carbon sponges-type nanostructures (CSTN) based on coaxial nitrogen-doped multiwalled carbon nanotubes (CA-MWCNTs) were synthesized using the aerosol assisted chemical vapor deposition method involving the decomposition of a mixture of ferrocene, benzylamine, thiophene, and ethanol at 1020 °C under a flow of H_2/Ar. Sample morphology and composition profiles were analyzed by scanning electron microscopy (SEM), transmission electron microscopy (TEM), X-ray diffraction (XRD), X-ray photoelectron spectroscopy (XPS), Fourier transform infrared spectroscopy (FTIR), Raman spectroscopy, and thermogravimetric analysis (TGA). SEM and TEM characterizations demonstrated that the CA-MWCNTs consisted of a core MWCNT surrounded by graphite materials with low crystallinity which was confirmed by XRD and Raman spectroscopy. Depending where the CSTN were collected along the reactor, three types of core MWCNTs morphologies were found: (1) N-doped MWCNTs with a bamboo shape and zigzagged growth, (2) straight MWCNTs, and (3) wavy MWCNTs. The carbon CSTN showed to be highly hydrophobic with outstanding oil absorption properties. XPS characterizations suggest the presence of water-fearing chemical groups such as ester- and ethoxy-groups anchored on the surface of the CA-MWCNTs. The mechanism in which the three types of MWCNTs are formed, the nature of the shell disordered graphite materials, and the hydrophobicity of the carbon sponges-type are thoroughly discussed.

© 2017 Elsevier Ltd. All rights reserved.

2) *Muñoz-Sandoval, E., Fajardo-Díaz, J. L., Sánchez-Salas, R., Cortés-López, A. J., & López-Urías, F. (2018). Two sprayer CVD synthesis of nitrogen-doped carbon sponge-type nanomaterials. Scientific reports, 8(1), 1-14.* ***(I.F. 4.1)***

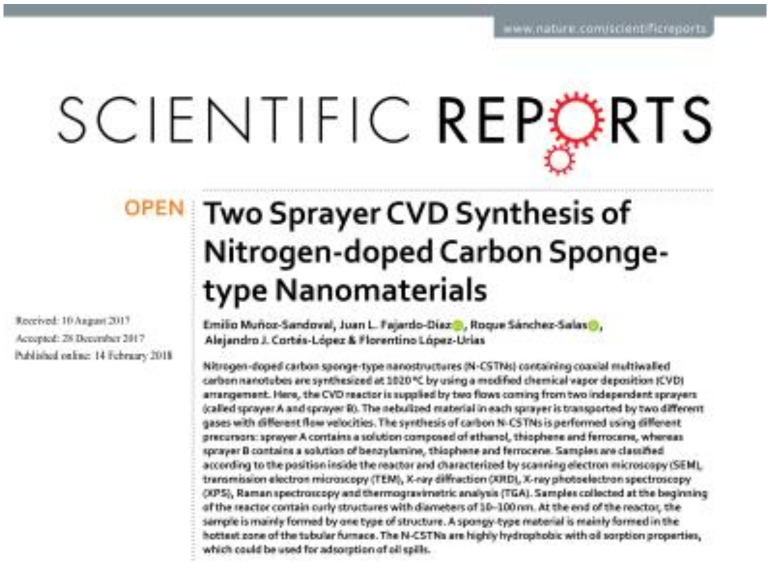

www.nature.com/scientificreports

SCIENTIFIC REPORTS

OPEN

Two Sprayer CVD Synthesis of Nitrogen-doped Carbon Sponge-type Nanomaterials

Received: 10 August 2017
Accepted: 28 December 2017
Published online: 14 February 2018

Emilio Muñoz-Sandoval, Juan L. Fajardo-Díaz, Roque Sánchez-Salas,
Alejandro J. Cortés-López & Florentino López-Urías

Nitrogen-doped carbon sponge-type nanostructures (N-CSTNs) containing coaxial multiwalled carbon nanotubes are synthesized at 1020 °C by using a modified chemical vapor deposition (CVD) arrangement. Here, the CVD reactor is supplied by two flows coming from two independent sprayers (called sprayer A and sprayer B). The nebulized material in each sprayer is transported by two different gases with different flow velocities. The synthesis of carbon N-CSTNs is performed using different precursors: sprayer A contains a solution composed of ethanol, thiophene and ferrocene, whereas sprayer B contains a solution of benzylamine, thiophene and ferrocene. Samples are classified according to the position inside the reactor and characterized by scanning electron microscopy (SEM), transmission electron microscopy (TEM), X-ray diffraction (XRD), X-ray photoelectron spectroscopy (XPS), Raman spectroscopy and thermogravimetric analysis (TGA). Samples collected at the beginning of the reactor contain curly structures with diameters of 10–100 nm. At the end of the reactor, the sample is mainly formed by one type of structure. A spongy-type material is mainly formed in the hottest zone of the tubular furnace. The N-CSTNs are highly hydrophobic with oil sorption properties, which could be used for adsorption of oil spills.

3) *Rodríguez-Corvera, C. L., Fajardo-Díaz, J. L., Cortés-López, A. J., Jiménez-Ramírez, L. E., Muñoz-Sandoval, E., & López-Urías, F. (2019). Nitrogen-doped carbon fiber sponges by using different nitrogen precursors: synthesis, characterization, and electrochemical activity. Materials Today Chemistry, 14, 100200.* ***(I.F. N.A.)***

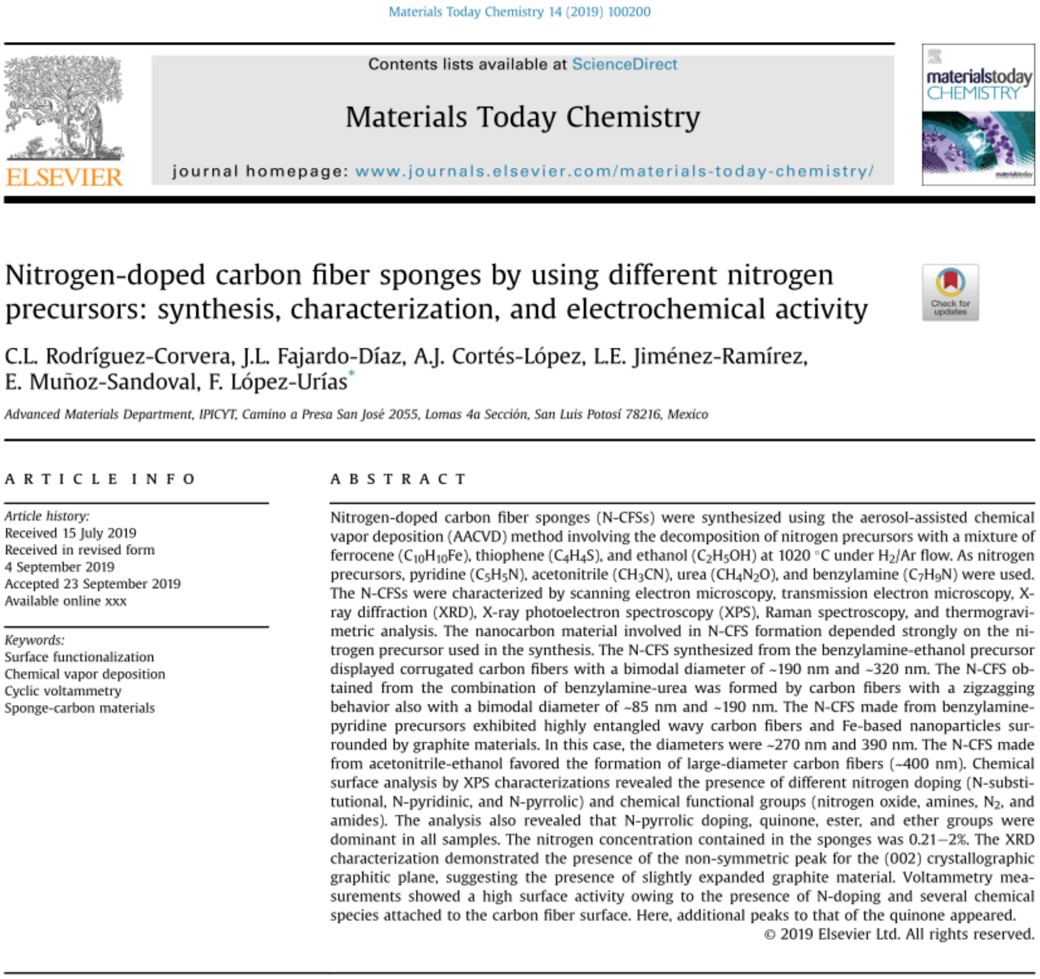

Materials Today Chemistry 14 (2019) 100200

Contents lists available at ScienceDirect

Materials Today Chemistry

journal homepage: www.journals.elsevier.com/materials-today-chemistry/

Nitrogen-doped carbon fiber sponges by using different nitrogen precursors: synthesis, characterization, and electrochemical activity

C.L. Rodríguez-Corvera, J.L. Fajardo-Díaz, A.J. Cortés-López, L.E. Jiménez-Ramírez, E. Muñoz-Sandoval, F. López-Urías*

Advanced Materials Department, IPICYT, Camino a Presa San José 2055, Lomas 4a Sección, San Luis Potosí 78216, Mexico

ARTICLE INFO

Article history:
Received 15 July 2019
Received in revised form
4 September 2019
Accepted 23 September 2019
Available online xxx

Keywords:
Surface functionalization
Chemical vapor deposition
Cyclic voltammetry
Sponge-carbon materials

ABSTRACT

Nitrogen-doped carbon fiber sponges (N-CFSs) were synthesized using the aerosol-assisted chemical vapor deposition (AACVD) method involving the decomposition of nitrogen precursors with a mixture of ferrocene ($C_{10}H_{10}Fe$), thiophene (C_4H_4S), and ethanol (C_2H_5OH) at 1020 °C under H_2/Ar flow. As nitrogen precursors, pyridine (C_5H_5N), acetonitrile (CH_3CN), urea (CH_4N_2O), and benzylamine (C_7H_9N) were used. The N-CFSs were characterized by scanning electron microscopy, transmission electron microscopy, X-ray diffraction (XRD), X-ray photoelectron spectroscopy (XPS), Raman spectroscopy, and thermogravimetric analysis. The nanocarbon material involved in N-CFS formation depended strongly on the nitrogen precursor used in the synthesis. The N-CFS synthesized from the benzylamine-ethanol precursor displayed corrugated carbon fibers with a bimodal diameter of ~190 nm and ~320 nm. The N-CFS obtained from the combination of benzylamine-urea was formed by carbon fibers with a zigzagging behavior also with a bimodal diameter of ~85 nm and ~190 nm. The N-CFS made from benzylamine-pyridine precursors exhibited highly entangled wavy carbon fibers and Fe-based nanoparticles surrounded by graphite materials. In this case, the diameters were ~270 nm and 390 nm. The N-CFS made from acetonitrile-ethanol favored the formation of large-diameter carbon fibers (~400 nm). Chemical surface analysis by XPS characterizations revealed the presence of different nitrogen doping (N-substitutional, N-pyridinic, and N-pyrrolic) and chemical functional groups (nitrogen oxide, amines, N_2, and amides). The analysis also revealed that N-pyrrolic doping, quinone, ester, and ether groups were dominant in all samples. The nitrogen concentration contained in the sponges was 0.21–2%. The XRD characterization demonstrated the presence of the non-symmetric peak for the (002) crystallographic graphitic plane, suggesting the presence of slightly expanded graphite material. Voltammetry measurements showed a high surface activity owing to the presence of N-doping and several chemical species attached to the carbon fiber surface. Here, additional peaks to that of the quinone appeared.

4) *López-Urías, F., Fajardo-Díaz, J. L., Cortés-López, A. J., Rodríguez-Corvera, C. L., Jiménez-Ramírez, L. E., & Muñoz-Sandoval, E. (2020). Edge Chemistry of Armchair Graphene Nanoribbons Containing Sulfur Functional Groups: Towards an Understanding of the Spin-Dependent Electrochemistry. Advanced Theory and Simulations, 3(3), 1900219.* **(I.F. N.A.)**

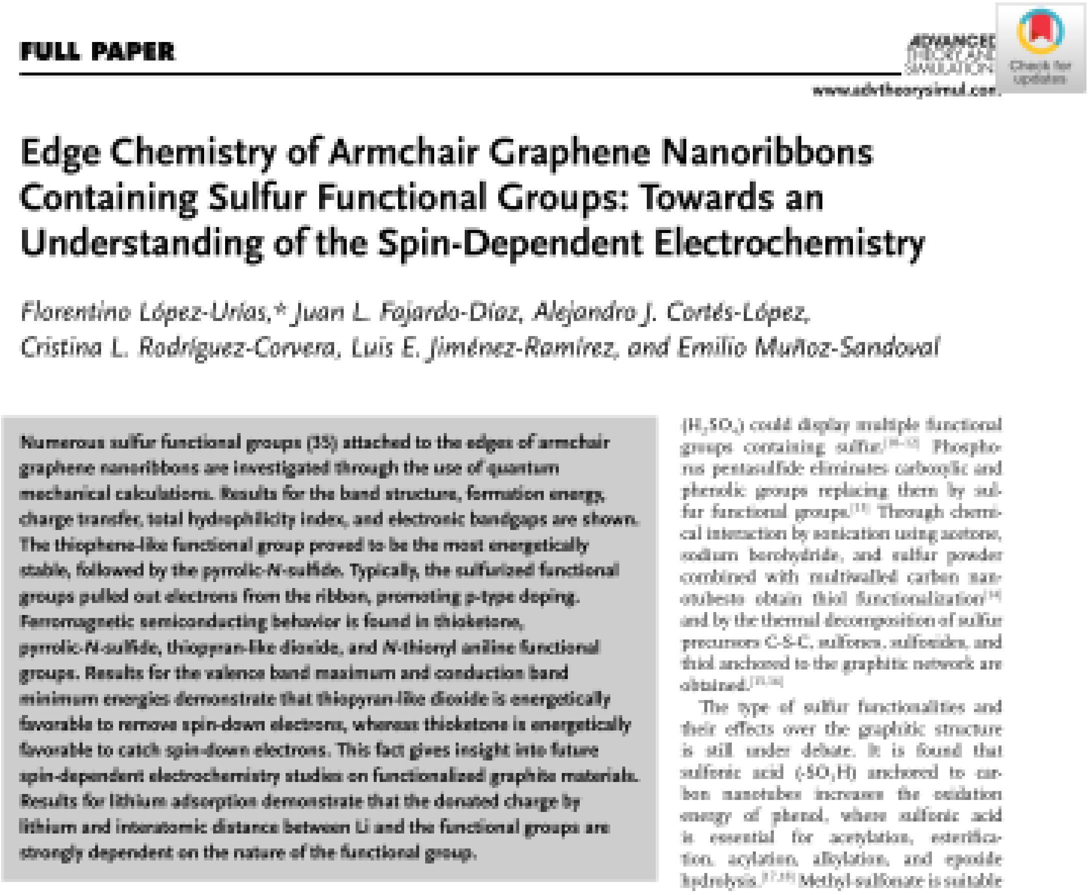

FULL PAPER

www.advtheorysimul.co

Edge Chemistry of Armchair Graphene Nanoribbons Containing Sulfur Functional Groups: Towards an Understanding of the Spin-Dependent Electrochemistry

Florentino López-Urías, Juan L. Fajardo-Díaz, Alejandro J. Cortés-López,*
Cristina L. Rodríguez-Corvera, Luis E. Jiménez-Ramírez, and Emilio Muñoz-Sandoval

Numerous sulfur functional groups (35) attached to the edges of armchair graphene nanoribbons are investigated through the use of quantum mechanical calculations. Results for the band structure, formation energy, charge transfer, total hydrophilicity index, and electronic bandgaps are shown. The thiophene-like functional group proved to be the most energetically stable, followed by the pyrrolic-*N*-sulfide. Typically, the sulfurized functional groups pulled out electrons from the ribbon, promoting p-type doping. Ferromagnetic semiconducting behavior is found in thioketone, pyrrolic-*N*-sulfide, thiopyran-like dioxide, and *N*-thionyl aniline functional groups. Results for the valence band maximum and conduction band minimum energies demonstrate that thiopyran-like dioxide is energetically favorable to remove spin-down electrons, whereas thioketone is energetically favorable to catch spin-down electrons. This fact gives insight into future spin-dependent electrochemistry studies on functionalized graphite materials. Results for lithium adsorption demonstrate that the donated charge by lithium and interatomic distance between Li and the functional groups are strongly dependent on the nature of the functional group.

(H_2SO_4) could display multiple functional groups containing sulfur.[10–12] Phosphorus pentasulfide eliminates carboxylic and phenolic groups replacing them by sulfur functional groups.[13] Through chemical interaction by sonication using acetone, sodium borohydride, and sulfur powder combined with multiwalled carbon nanotubesto obtain thiol functionalization[14] and by the thermal decomposition of sulfur precursors C-S-C, sulfones, sulfoxides, and thiol anchored to the graphitic network are obtained.[15,16]

The type of sulfur functionalities and their effects over the graphitic structure is still under debate. It is found that sulfonic acid (-SO_3H) anchored to carbon nanotubes increases the oxidation energy of phenol, where sulfonic acid is essential for acetylation, esterification, acylation, alkylation, and epoxide hydrolysis.[17,18] Methyl-sulfonate is suitable

5) *López-Urías, F., Fajardo-Díaz, J. L., Cortés-López, A. J., Rodríguez-Corvera, C. L., Jiménez-Ramírez, L. E., & Muñoz-Sandoval, E. (2020). Understanding the electrochemistry of armchair graphene nanoribbons containing nitrogen and oxygen functional groups: DFT calculations. Physical Chemistry Chemical Physics, 22(8), 4533-4543.* ***(I.F. 3.5)***

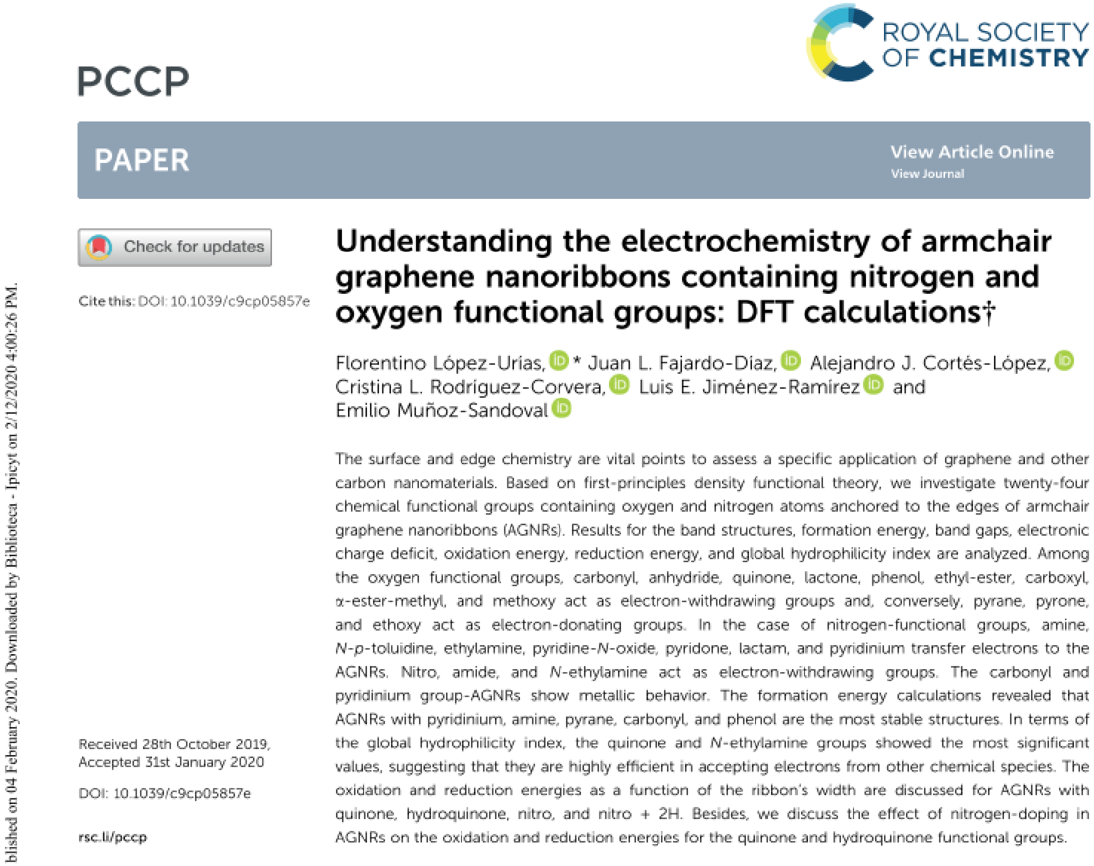

PCCP

ROYAL SOCIETY OF CHEMISTRY

PAPER

View Article Online
View Journal

Check for updates

Cite this: DOI: 10.1039/c9cp05857e

Understanding the electrochemistry of armchair graphene nanoribbons containing nitrogen and oxygen functional groups: DFT calculations†

Florentino López-Urias, * Juan L. Fajardo-Diaz, Alejandro J. Cortés-López, Cristina L. Rodriguez-Corvera, Luis E. Jiménez-Ramírez and Emilio Muñoz-Sandoval

Received 28th October 2019,
Accepted 31st January 2020

DOI: 10.1039/c9cp05857e

rsc.li/pccp

The surface and edge chemistry are vital points to assess a specific application of graphene and other carbon nanomaterials. Based on first-principles density functional theory, we investigate twenty-four chemical functional groups containing oxygen and nitrogen atoms anchored to the edges of armchair graphene nanoribbons (AGNRs). Results for the band structures, formation energy, band gaps, electronic charge deficit, oxidation energy, reduction energy, and global hydrophilicity index are analyzed. Among the oxygen functional groups, carbonyl, anhydride, quinone, lactone, phenol, ethyl-ester, carboxyl, α-ester-methyl, and methoxy act as electron-withdrawing groups and, conversely, pyrane, pyrone, and ethoxy act as electron-donating groups. In the case of nitrogen-functional groups, amine, *N*-*p*-toluidine, ethylamine, pyridine-*N*-oxide, pyridone, lactam, and pyridinium transfer electrons to the AGNRs. Nitro, amide, and *N*-ethylamine act as electron-withdrawing groups. The carbonyl and pyridinium group-AGNRs show metallic behavior. The formation energy calculations revealed that AGNRs with pyridinium, amine, pyrane, carbonyl, and phenol are the most stable structures. In terms of the global hydrophilicity index, the quinone and *N*-ethylamine groups showed the most significant values, suggesting that they are highly efficient in accepting electrons from other chemical species. The oxidation and reduction energies as a function of the ribbon's width are discussed for AGNRs with quinone, hydroquinone, nitro, and nitro + 2H. Besides, we discuss the effect of nitrogen-doping in AGNRs on the oxidation and reduction energies for the quinone and hydroquinone functional groups.

6) *Vega-Diaz, S. M., González, V. J., Morelos-Gomez, A., Tristán-López, F., Labrada-Delgado, G. J., Rivera-Escoto, B. A., ... & Terrones, M. (2020). Pyrrolic nitrogen-doped multiwall carbon nanotubes using ball-milled slag-SiC mixtures as a catalyst by aerosol assisted chemical vapor deposition. Materials Research Express. (**I.F. 1.4**)*

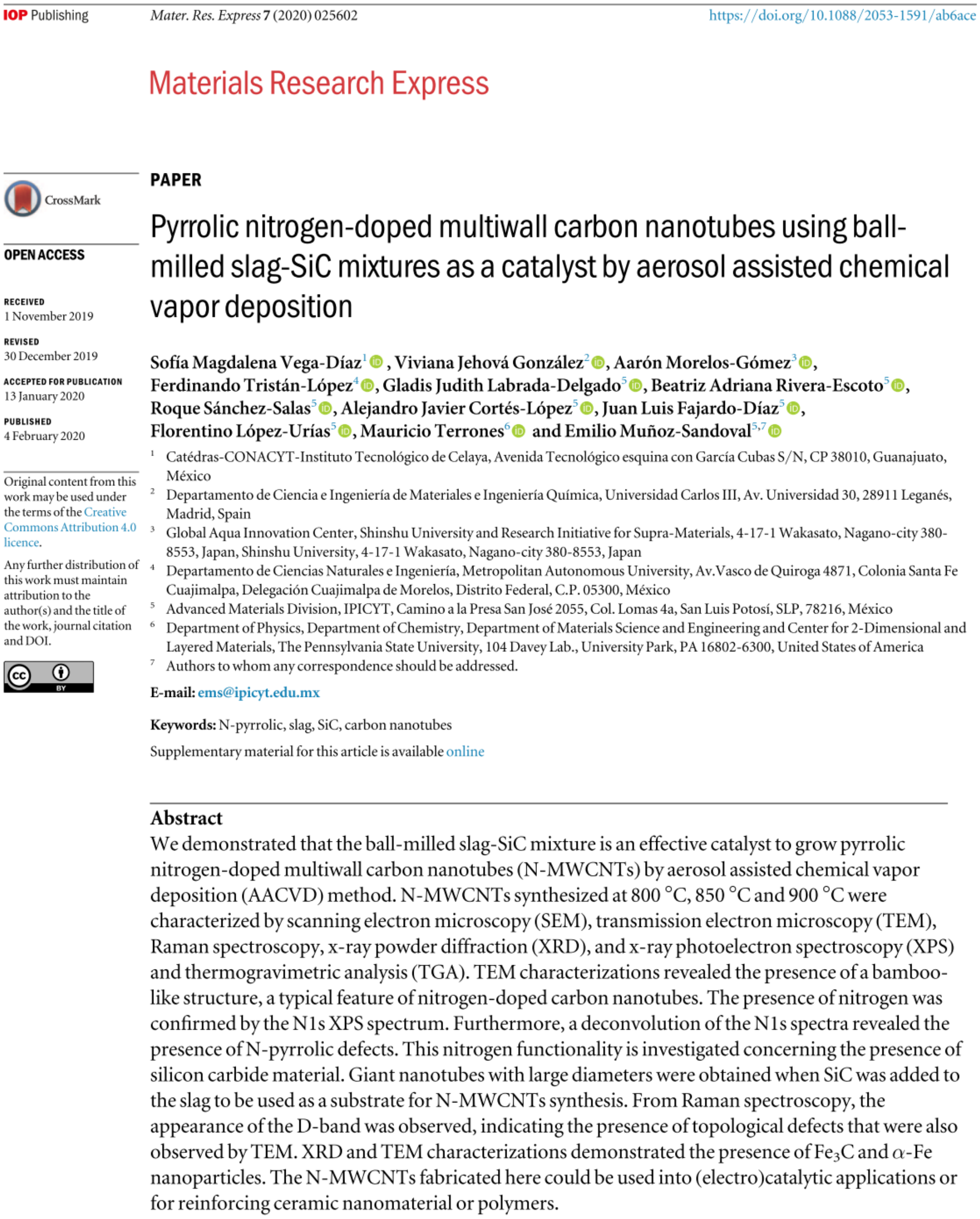

IOP Publishing *Mater. Res. Express* **7** (2020) 025602 https://doi.org/10.1088/2053-1591/ab6ace

Materials Research Express

CrossMark

OPEN ACCESS

RECEIVED
1 November 2019

REVISED
30 December 2019

ACCEPTED FOR PUBLICATION
13 January 2020

PUBLISHED
4 February 2020

PAPER

Pyrrolic nitrogen-doped multiwall carbon nanotubes using ball-milled slag-SiC mixtures as a catalyst by aerosol assisted chemical vapor deposition

Sofía Magdalena Vega-Díaz[1], Viviana Jehová González[2], Aarón Morelos-Gómez[3], Ferdinando Tristán-López[4], Gladis Judith Labrada-Delgado[5], Beatriz Adriana Rivera-Escoto[5], Roque Sánchez-Salas[5], Alejandro Javier Cortés-López[5], Juan Luis Fajardo-Díaz[5], Florentino López-Urías[5], Mauricio Terrones[6] and Emilio Muñoz-Sandoval[5,7]

[1] Catédras-CONACYT-Instituto Tecnológico de Celaya, Avenida Tecnológico esquina con García Cubas S/N, CP 38010, Guanajuato, México
[2] Departamento de Ciencia e Ingeniería de Materiales e Ingeniería Química, Universidad Carlos III, Av. Universidad 30, 28911 Leganés, Madrid, Spain
[3] Global Aqua Innovation Center, Shinshu University and Research Initiative for Supra-Materials, 4-17-1 Wakasato, Nagano-city 380-8553, Japan, Shinshu University, 4-17-1 Wakasato, Nagano-city 380-8553, Japan
[4] Departamento de Ciencias Naturales e Ingeniería, Metropolitan Autonomous University, Av.Vasco de Quiroga 4871, Colonia Santa Fe Cuajimalpa, Delegación Cuajimalpa de Morelos, Distrito Federal, C.P. 05300, México
[5] Advanced Materials Division, IPICYT, Camino a la Presa San José 2055, Col. Lomas 4a, San Luis Potosí, SLP, 78216, México
[6] Department of Physics, Department of Chemistry, Department of Materials Science and Engineering and Center for 2-Dimensional and Layered Materials, The Pennsylvania State University, 104 Davey Lab., University Park, PA 16802-6300, United States of America
[7] Authors to whom any correspondence should be addressed.

E-mail: ems@ipicyt.edu.mx

Keywords: N-pyrrolic, slag, SiC, carbon nanotubes

Supplementary material for this article is available online

Abstract

We demonstrated that the ball-milled slag-SiC mixture is an effective catalyst to grow pyrrolic nitrogen-doped multiwall carbon nanotubes (N-MWCNTs) by aerosol assisted chemical vapor deposition (AACVD) method. N-MWCNTs synthesized at 800 °C, 850 °C and 900 °C were characterized by scanning electron microscopy (SEM), transmission electron microscopy (TEM), Raman spectroscopy, x-ray powder diffraction (XRD), and x-ray photoelectron spectroscopy (XPS) and thermogravimetric analysis (TGA). TEM characterizations revealed the presence of a bamboo-like structure, a typical feature of nitrogen-doped carbon nanotubes. The presence of nitrogen was confirmed by the N1s XPS spectrum. Furthermore, a deconvolution of the N1s spectra revealed the presence of N-pyrrolic defects. This nitrogen functionality is investigated concerning the presence of silicon carbide material. Giant nanotubes with large diameters were obtained when SiC was added to the slag to be used as a substrate for N-MWCNTs synthesis. From Raman spectroscopy, the appearance of the D-band was observed, indicating the presence of topological defects that were also observed by TEM. XRD and TEM characterizations demonstrated the presence of Fe_3C and α-Fe nanoparticles. The N-MWCNTs fabricated here could be used into (electro)catalytic applications or for reinforcing ceramic nanomaterial or polymers.

7) Jimenez-Ramirez, L. E., Kashina, S., Galindo, R., Fuentes-Ramirez, R., Verma, S. K., Fajardo-Diaz, J. L., ... & Muñoz-Sandoval, E. (2020). Synthesis, morphology, magnetic and electrochemical studies of nitrogen-doped multiwall carbon nanotubes fabricated using banded iron-formation as catalyst. *Journal of Alloys and Compounds*, 155200. **(I.F. 4.1)**

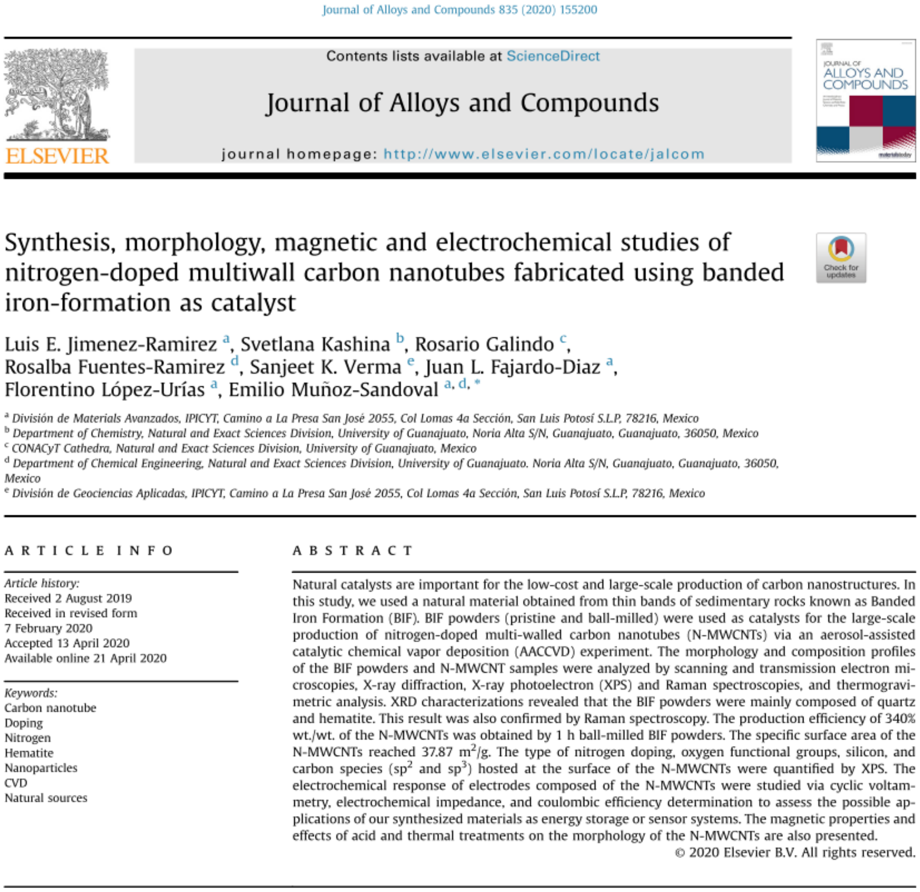

Journal of Alloys and Compounds 835 (2020) 155200

Contents lists available at ScienceDirect

Journal of Alloys and Compounds

journal homepage: http://www.elsevier.com/locate/jalcom

Synthesis, morphology, magnetic and electrochemical studies of nitrogen-doped multiwall carbon nanotubes fabricated using banded iron-formation as catalyst

Luis E. Jimenez-Ramirez [a], Svetlana Kashina [b], Rosario Galindo [c],
Rosalba Fuentes-Ramirez [d], Sanjeet K. Verma [e], Juan L. Fajardo-Diaz [a],
Florentino López-Urías [a], Emilio Muñoz-Sandoval [a, d, *]

[a] *División de Materials Avanzados, IPICYT, Camino a La Presa San José 2055, Col Lomas 4a Sección, San Luis Potosí S.L.P, 78216, Mexico*
[b] *Department of Chemistry, Natural and Exact Sciences Division, University of Guanajuato, Noria Alta S/N, Guanajuato, Guanajuato, 36050, Mexico*
[c] *CONACyT Cathedra, Natural and Exact Sciences Division, University of Guanajuato, Mexico*
[d] *Department of Chemical Engineering, Natural and Exact Sciences Division, University of Guanajuato. Noria Alta S/N, Guanajuato, Guanajuato, 36050, Mexico*
[e] *División de Geociencias Aplicadas, IPICYT, Camino a La Presa San José 2055, Col Lomas 4a Sección, San Luis Potosí S.L.P, 78216, Mexico*

ARTICLE INFO

Article history:
Received 2 August 2019
Received in revised form
7 February 2020
Accepted 13 April 2020
Available online 21 April 2020

Keywords:
Carbon nanotube
Doping
Nitrogen
Hematite
Nanoparticles
CVD
Natural sources

ABSTRACT

Natural catalysts are important for the low-cost and large-scale production of carbon nanostructures. In this study, we used a natural material obtained from thin bands of sedimentary rocks known as Banded Iron Formation (BIF). BIF powders (pristine and ball-milled) were used as catalysts for the large-scale production of nitrogen-doped multi-walled carbon nanotubes (N-MWCNTs) via an aerosol-assisted catalytic chemical vapor deposition (AACCVD) experiment. The morphology and composition profiles of the BIF powders and N-MWCNT samples were analyzed by scanning and transmission electron microscopies, X-ray diffraction, X-ray photoelectron (XPS) and Raman spectroscopies, and thermogravimetric analysis. XRD characterizations revealed that the BIF powders were mainly composed of quartz and hematite. This result was also confirmed by Raman spectroscopy. The production efficiency of 340% wt./wt. of the N-MWCNTs was obtained by 1 h ball-milled BIF powders. The specific surface area of the N-MWCNTs reached 37.87 m^2/g. The type of nitrogen doping, oxygen functional groups, silicon, and carbon species (sp^2 and sp^3) hosted at the surface of the N-MWCNTs were quantified by XPS. The electrochemical response of electrodes composed of the N-MWCNTs were studied via cyclic voltammetry, electrochemical impedance, and coulombic efficiency determination to assess the possible applications of our synthesized materials as energy storage or sensor systems. The magnetic properties and effects of acid and thermal treatments on the morphology of the N-MWCNTs are also presented.

8) *López-Urías, F., Fajardo-Díaz, J. L., Cortés-López, A. J., Rodríguez-Corvera, C. L., Jiménez-Ramírez, L. E., & Muñoz-Sandoval, E. (2020). Spin-Dependent Band-Gap Driven by Nitrogen and Oxygen Functional Groups in Zigzag Graphene Nanoribbons. Applied Surface Science, 146435.* ***(I.F. 5.1)***

Applied Surface Science 521 (2020) 146435

Contents lists available at ScienceDirect

Applied Surface Science

journal homepage: www.elsevier.com/locate/apsusc

Spin-dependent band-gap driven by nitrogen and oxygen functional groups in zigzag graphene nanoribbons

Florentino López-Urías*, Juan L. Fajardo-Díaz, Alejandro J. Cortés-López,
Cristina L. Rodríguez-Corvera, Luis E. Jiménez-Ramírez, Emilio Muñoz-Sandoval

Advanced Materials Department, IPICYT, Camino a Presa San José 2055, Lomas 4a Sección, San Luis Potosí 78216, Mexico

ARTICLE INFO

Keywords:
Carbon
Graphene
Functionalization
Nitrogen
Nanoribbons
Magnetism

ABSTRACT

We investigated the role of nitrogen and oxygen functional groups on the electronic and magnetic properties of zigzag graphene nanoribbons (ZGNRs) using spin-polarized first-principles density functional theory calculations. Twenty four functional groups of nitrogen, oxygen, and nitrogen-oxygen configurations were attached to the edge of ZGNRs. We analyze the band structure, spin-resolved bandgap, charge transfer, magnetic ordering, and binding energy. Similar to the pristine ZGNR, an indirect bandgap semiconducting behavior dominated in functionalized ribbons, except for carbonyl, pyrane, and pyridinium groups, that displays a metallic behavior. Spin-resolved band gap calculations revealed a strong dependence on the functional groups. Carbonyl groups showed a half-metallicity behavior with only spin up states at the Fermi level. In general, the functionalized ribbons displayed ferromagnetic alignment along the edges, but antiferromagnetic alignment between them, resulting in a total null magnetization. We showed some exceptions, the carbonyl, pyrane, lactam, pyridine N-oxide, and pyridinium functional groups induced significant changes in the magnetic arrangement, not only along the edge where they were attached but also to the opposite side. We have also incorporated a pentagon-heptagon pair or a single pentagon defect at the edge to explore the quinone, pyrone, and pyridone functional groups.

9) *García-Betancourt, M. L., Fajardo-Díaz, J. L., Galindo, R., Fuentes-Ramírez, R., López-Urías, F., & Muñoz-Sandoval, E. (2020). Holey Nitrogen-Doped Multiwalled Carbon Nanotubes from Extended Air Oxidation At Low-Temperature. Applied Surface Science, 146546.* ***(I.F. 5.1).***